# Mathematical Modelling and Transcriptional Characterisation of Intratumoral Regulatory T Cell Sub-populations




Itai Muzhingi

Balliol College

University of Oxford

A thesis submitted for the degree of

*Doctor of Philosophy*

Trinity 2023

To my parents and siblings, who have long believed in the transformative power of education even before I did.

# Declaration of Authorship

I declare that no parts of this thesis have been reproduced or accepted for another award or degree at the University of Oxford or any other academic institution. Despite the usage of "we" throughout this thesis, the work presented here is my own, except where otherwise stated, acknowledged and/or referenced.

Itai Muzhingi
Trinity 2023

# Acknowledgements

In Zimbabwe, we have a saying which translates to, *"A big bull was once a suckling calf."* As I write this section, with the surreal feeling of finishing my thesis, the old idiom can not be any more true. First, I would like to express my innermost gratitude to my family, who have propelled me to where I am today. Thank you for placing my needs before yours, and sacrificing even the little that you had so that I could attain excellent education. I can never fully understand how you embraced a life of poverty so that I could stay in school.

I am deeply indebted to my supervisors, the dynamic duo, Professors Mark Coles and Eamonn Gaffney for nurturing my passion for biomedical science. Your unwavering support made me feel comfortable as I entered the unfamiliar territory of computational research. Mark, I have never been mentored by a supervisor who matches your bubbly enthusiasm. I always enjoyed our individual meetings in your office, because they were well-rounded—we talked about everything, from research to life. Eamonn, you have been very patient with me, especially given that I came in with a limited mathematical/computational background. When I was not feeling confident, you were always quick to reassure me and point to the strengths of my work.

To my collaborators, David Withers, Suaad Idris and Zhi Li, this thesis would not have been complete without your support. Thank you very much for your hard work handling the Kaede mice, conducting flow cytometry and generating the scRNA-seq datasets. To my industrial supervisors from Roche, Cristina Santini, Oliver Grimm and Christophe Boetsch, thank you for providing invaluable industrial perspectives on my research outputs. To the friends I made at Oxford, you made my journey memorable. I am especially grateful to David Augustin for helping me set up my parameter estimation environment.

I am extremely grateful to my funding bodies, the Rhodes Trust, Roche and the EPSRC. Without your generosity, it would have been impossible for me to pursue my doctorate studies at the University of Oxford.

Finally, I thank my heavenly Father, for watching over me and guiding my path.

# COVID-19 Statement

Although my thesis was computational, it heavily relied on experimental datasets. These included Treg counts from MC38 and CT26-implanted Kaede mice, as well as single cell datasets. Due to adjustments that had to be adopted during the COVID-19 pandemic, experimental work was heavily impacted. Thus, I experienced delays in getting access to some of the experimental datasets. I received the CT26 photoconversion dataset towards the end of 2021, and the single cell data during the summer of 2022. This partially delayed my publication timeline.

# Abstract

Regulatory T cells (Tregs) suppress harmful immune responses and help prevent autoimmune reactions. However, high densities of Tregs accumulate in solid tumours and contribute to the suppression of anti-tumor responses. The targeting of intratumoral Tregs via antibody-mediated blockade/depletion is a promising cancer treatment strategy but remains ineffective and induces adverse events. Some of these challenges can be addressed by conducting extensive transcriptional profiling of intratumoral Tregs and quantitatively assessing Treg migration dynamics to identify appropriate therapeutic targets and guide the development of safe and effective Treg-targeting therapeutics.

We hypothesised that tumours harbour resident and transient Tregs with distinct transcriptional and migratory profiles. To test our hypothesis, we used photoconvertible Kaede mice to label and quantify Tregs in MC38 and CT26 tumours. We developed a mathematical model to investigate whether the presence of resident and transient tumour Tregs aligns with the observed data and applied Bayesian parameter estimation to infer the rates of intratumoral Treg migration. In both tumours, we confirmed the presence of resident and transient Tregs and found that Tregs egressed from CT26 tumours to lymphoid tissue to a larger extent than MC38 tumours. Single cell analysis of intratumoral Tregs revealed that resident Tregs upregulate Lag3, Tnfrsf18 and Tnfrsf9. To investigate similarities between murine and human intratumoral Tregs, we constructed Treg meta-atlases using public single cell datasets. In mice, we observed that Lag3 and Ccr8 are unique to tumour Tregs and exhausted CD8 T cells. In humans, CCR8 expression was confined to tumour Tregs whereas LAG3 was mainly expressed on exhausted CD8 T cells.

Collectively, our findings outlined the presence of kinetically and transcriptionally distinct intratumoral Treg subpopulations. Furthermore, our Treg meta-atlases exposed key differences in CCR8 and LAG3 expression between mouse models and humans and supported the potential of CCR8 as a target for depleting human intratumoral Tregs.

# Contents

**List of Figures** xiii

**List of Tables** xvi

**List of Abbreviations** xviii

**1 Introduction** 1

1.1 Motivation . . . . . 1

1.2 Tumorigenesis and the hallmarks of cancer . . . . . 3

1.3 The immune system and cancer immunity . . . . . 5

1.3.1 The innate immune system: DCs and NK cells . . . . . 5

1.3.2 The adaptive immune system: CD8 T cells . . . . . 6

1.4 Immunosuppression in the tumour . . . . . 9

1.5 Tumour Tregs – a key immunotherapy target . . . . . 10

1.5.1 The role of Tregs in health and disease . . . . . 12

1.5.2 Treg subsets: nTregs, pTregs and Tr1 Tregs . . . . . 12

1.5.3 Mechanisms of Treg-mediated immunosuppression . . . . . 14

1.6 Therapeutically targeting intratumoral Tregs . . . . . 17

1.6.1 CCR4 . . . . . 18

1.6.2 CD25 . . . . . 18

1.6.3 CCR8 . . . . . 19

1.6.4 LAG3 . . . 20
1.6.5 TNFRSF18 (GITR) . . . 21
1.6.6 TNFRSF9 (4-1BB) . . . 23
1.7 Challenges associated with Treg-targeting . . . 24
1.7.1 Poor mechanistic understanding of intratumoral Treg dynamics 24
1.7.2 Elusive markers – Differences between resident and transient Tregs 27
1.7.3 Knowledge gap in biological differences between resident and transient Tregs . . . 27
1.7.4 Tumour, inter-organ and inter-species Treg heterogeneity . . . 28
1.8 Research questions and hypotheses . . . 29
1.9 Thesis structure and summary . . . 31

**2 Mathematical modelling of intratumoral Treg kinetics 33**

2.1 Introduction . . . 33
2.2 Aims . . . 35
2.3 Materials and Methods . . . 36
2.3.1 Kaede mouse model experiments . . . 36
2.3.2 Structural identifiability assessment . . . 39
2.3.3 Indirect assessment of practical identifiability . . . 41
2.3.4 Bayesian parameter inference . . . 42
2.3.5 Sensitivity analysis with eFAST . . . 49
2.4 Results . . . 55
2.4.1 Qualitative analysis of experimental data . . . 55
2.4.2 Iterative mathematical model development . . . 63
2.4.3 Modelling tumour growth dynamics . . . 77
2.4.4 Modelling the migration profiles of TDLN Tregs . . . 79

2.4.5 CT26 and MC38 tumours harbour resident and transient Tregs 80
2.4.6 CT26 Tregs significantly accumulate in lymphoid organs . . . . 83
2.5 Discussion . . . . . 88

**3 Transcriptional characterisation of intratumoral Tregs 93**
3.1 Introduction . . . . . 94
3.2 Aims . . . . . 96
3.3 Materials and Methods . . . . . 96
3.3.1 CT26 and MC38 scRNA-seq datasets . . . . . 96
3.3.2 Single cell sequencing of MC38 Kaede Tregs . . . . . 98
3.3.3 scRNA-Seq analysis pipeline . . . . . 100
3.3.4 Differential expression analysis . . . . . 101
3.3.5 Gene set enrichment analysis . . . . . 103
3.3.6 Trajectory analysis of red and green Kaede Tregs . . . . . 106
3.3.7 Simulating metabolic reactions from scRNA-seq data . . . . . 110
3.4 Results . . . . . 111
3.4.1 Integrating and clustering MC38 and CT26 Tregs . . . . . 111
3.4.2 CT26 Tregs are distinct from MC38 Tregs . . . . . 114
3.4.3 CT26 Tregs upregulate cell migration markers . . . . . 116
3.4.4 Integrating and clustering Kaede scRNA-seq Treg datasets . . . 119
3.4.5 MC38 tumours harbour mainly activated and Isg15 Tregs . . . 122
3.4.6 Reconstructing Kaede Treg differentiation trajectories . . . . . 125
3.4.7 Differential expression analysis of resident and transient Tregs . 130
3.4.8 Resident and transient Tregs exhibit significant differences in multiple biological pathways . . . . . 137
3.4.9 Resident Tregs display significant metabolic dysfunction . . . . 140

3.5 Discussion . . . 144

3.5.1 Conclusion and future work . . . 149

**4 Treg meta-atlases reveal inter-organ and inter-species heterogeneity 151**

4.1 Introduction . . . 152

4.2 Aims . . . 154

4.3 Methods . . . 154

4.3.1 Murine Treg scRNA-seq datasets . . . 154

4.3.2 Human Treg scRNA-seq datasets . . . 157

4.3.3 Characteristics of scRNA-seq data . . . 159

4.3.4 scRNA-seq analysis pipeline . . . 160

4.3.5 Batch correction using Harmony . . . 168

4.4 Results . . . 169

4.4.1 Integrating mouse Tregs . . . 169

4.4.2 Identifying Treg subpopulations using the mouse Treg meta-atlas 172

4.4.3 Compositional analysis of mouse Tregs . . . 174

4.4.4 Lag3 expression differentiates tumour Tregs from non-lymphoid tissue Tregs . . . 180

4.4.5 Exploring gene expression patterns across T and NK cells . . . 183

4.4.6 Inter-species comparison: Developing a human Treg meta-atlas 186

4.4.7 Identifying human Treg subclusters . . . 188

4.4.8 Compositional analysis of human Tregs . . . 190

4.4.9 Human tumour Tregs highly express CCR8 . . . 194

4.5 Discussion . . . 199

4.5.1 Conclusion and future work . . . 203

**5 Thesis discussion** **205**

5.1 Research summary . . . . . 205

5.2 Context . . . . . 208

5.3 Future work . . . . . 213

5.3.1 Integrating mathematical modelling with transcriptomics . . . . 213

5.3.2 Reducing the level of parameter uncertainty . . . . . 214

5.3.3 Are resident and transient Tregs present in other syngeneic mouse tumour models? . . . . . 214

5.3.4 Experimental validation and spatio-temporal analysis of tumour Tregs . . . . . 215

5.3.5 Can tumour-resident Tregs be metabolically targeted? . . . . . 216

5.3.6 Investigating the role of Lag3 in Tregs . . . . . 216

5.3.7 Is there even a therapeutic window associated with Treg-targeting immunotherapy? . . . . . 217

**Appendices**

**A Mathematical Modelling Appendix** **220**

**B Transcriptional Characterisation Appendix** **225**

**C Treg Meta-atlases Appendix** **227**

**Bibliography** **230**

# List of Figures


1.1 Hallmarks of cancer . . . . . 4

1.2 Mechanisms of NK-cell mediated cytotoxicity . . . . . 6

1.3 The cancer-immunity cycle . . . . . 8

1.4 T cell exhaustion . . . . . 11

1.5 Treg development . . . . . 13

1.6 Mechanisms of Treg-mediated immunosuppression . . . . . 15

1.7 Research questions and hypotheses . . . . . 30

2.1 Kaede model experimental set up. . . . . 38

2.2 Recommended parameter combinations for running eFAST . . . . . 54

2.3 Overview of the MC38 tumour photoconversion dataset . . . . . 56

2.4 Overview of the MC38 TDLN photoconversion dataset . . . . . 58

2.5 Overview of the CT26 tumour photoconversion dataset . . . . . 60

2.6 MC38 and CT26 mathematical models . . . . . 69

2.7 Parameters $\tau$ and $\beta$ have low sensitivity indices . . . . . 70

2.8 MCMC chain convergence. . . . . 72

2.9 Pair-wise joint parameter distributions for the MC38 mathematical model 75

2.10 Pair-wise joint parameter distributions for the CT26 mathematical model 76

2.11 Fitting the mathematical model to tumour growth dynamics . . . . . 78

2.12 Investigating trafficking profiles of Tregs emerging from the MC38 TDLN 79

2.13 Resident and transient Tregs are present in CT26 and MC38 tumours . 80

2.14 Initial conditions and parameters associated with transient Tregs . . . . 82

2.15 CT26 Tregs significantly accumulate in lymphoid organs . . . . . 84

2.16 Identifying parameters that influence dynamics observed in lymphoid compartments . . . . . 86

2.17 Comparing CT26 and MC38 Treg trafficking parameters . . . . . 87

3.1 MC38 and CT26 Treg scRNA-seq extraction and analysis pipeline . . . 98

3.2 Kaede scRNA-seq experimental set up . . . . . 99

3.3 An illustration of how GSEA works . . . . . 105

3.4 Integrating and clustering MC38 and CT26 Tregs . . . . . 113

3.5 CT26 Tregs are transcriptionally distinct from MC38 Tregs . . . . . 115

3.6 CT26 Tregs significantly upregulate T cell trafficking markers . . . . . 117

3.7 Integrating Kaede Treg scRNA-seq datasets . . . . . 119

3.8 Clustering red and green Kaede Tregs . . . . . 121

3.9 Compositional analysis of tumour, TDLN and nDLN Kaede Tregs . . . 124

3.10 Inferring Kaede Treg differentiation trajectories . . . . . 127

3.11 Determining genes that differ in expression along pseudotime . . . . . 129

3.12 Identifying differentially expressed genes between resident and transient Tregs . . . . . 132

3.13 Gene-phenotype and gene-gene correlation analysis . . . . . 135

3.14 Gene set enrichment analysis . . . . . 138

3.15 Simulating metabolic processes in resident and transient Tregs using Compass . . . . . 142

3.16 Multiple metabolic pathways are downregulated in resident Tregs . . . 143

4.1 Overview of how human and mouse scRNA-seq datasets were processed 157

4.2 Illustration of steps taken by the Harmony algorithm . . . . . 170
4.3 Integrating mouse Tregs . . . . . 171
4.4 Clustering the mouse Treg meta-atlas . . . . . 173
4.5 Compositional analysis of mouse Treg meta-atlas . . . . . 175
4.6 Mouse-level compositional analysis . . . . . 177
4.7 Resident and transient signature/module scoring in mice . . . . . 179
4.8 Transcriptional comparison of Tregs across organs . . . . . 182
4.9 Exploring gene expression patterns across T and NK cells . . . . . 185
4.10 Integrating human Tregs . . . . . 187
4.11 Clustering human Tregs . . . . . 189
4.12 Compositional analysis of human Tregs . . . . . 191
4.13 Subject-level Treg compositions . . . . . 193
4.14 CCR8 is highly expressed on human tumour Tregs . . . . . 195
4.15 CCR8 is not highly expressed on conventional T cells . . . . . 197
4.16 Using a human immune cell mega meta-atlas to confirm the specificity of CCR8 on tumour Tregs . . . . . 198

5.1 Mechanism of Treg accumulation and trafficking in the tumour . . . . 212

A.1 Quantification of red and green tumour Tregs . . . . . 220
A.2 Fitting the MC38 Treg mathematical model to all data points . . . . . 222
A.3 Treg trafficking mathematical models without resident Tregs . . . . . 223
A.4 Treg trafficking mathematical models without Treg proliferation . . . . 224

B.1 Mki67 expression in Tregs . . . . . 226
B.2 Micropooling resident and transient Tregs for metabolic simulations . . 226

C.1 Tissue Treg signature/module scoring in mice . . . . . 228
C.2 Human CD4 non-Treg and CD8 T cell meta-atlases . . . . . 229

# List of Tables


1.1 Mathematical models involving intratumoral Treg dynamics . . . . . 26

2.1 Table describing the Kaede photoconversion dataset used in the study . 62

2.2 A summary of observed and unobserved variables or parameters . . . . 65

2.3 Table describing the inferred model parameters . . . . . 73

3.1 Table summarising MC38 and CT26 scRNA-seq datasets . . . . . 97

3.2 Table summarising the MC38 Kaede scRNA-seq experiments . . . . . 99

3.3 Table showing some of the genes that are differentially expressed between CT26 and MC38 Tregs . . . . . 118

3.4 Table showing some of the genes that are differentially expressed between resident and transient Tregs . . . . . 133

3.5 Table showing correlations between genes and the scale of increasing Treg tumour residency. . . . . 136

3.6 Table summarising upregulated and downregulated pathways in resident Tregs. . . . . 139

4.1 Summary of datasets used to generate the murine Treg scRNA-seq meta-atlas . . . . . 156

4.2 Summary of datasets used to generate the human Treg scRNA-seq meta-atlas . . . . . 158

4.3 Exemplar scRNA-seq gene expression matrix . . . . . 159

4.4 Table showing some of the genes that are differentially expressed between Tregs from MC38 tumours and the colon . . . . . 183

A.1 Assessing MCMC chain mixing . . . . . 221

# List of Abbreviations

**ACMC** . . . . . Adaptive Covariance Markov Chain Monte Carlo

**ADCC** . . . . . Antibody Dependent Cellular Cytotoxicity

**BBKNN** . . . . Batch-balanced K-Nearest Neighbours

**BH** . . . . . Benjamini-Hochberg

**bLN** . . . . . Brachial Lymph Node

**BP** . . . . . Biological Process pathways

**CarDEC** . . . . Count-adapted Regularised Deep Embedded Clustering

**CCR7** . . . . . C-C Chemokine Receptor Type 7

**CCR8** . . . . . C-C Chemokine Receptor Type 8

**cDNA** . . . . . Complimentary DNA

**CC** . . . . . Cellular Component pathways

**CRISPR/Cas9** Clustered Regularly Interspaced Short Palindromic Repeats/CRISPR-associated protein 9

**CXCR4** . . . . . C-X-C Chemokine Receptor Type 4

**CTLA4** . . . . . Cytotoxic T-lymphocyte Associated Protein 4

**D$^3$E** . . . . . Discrete Distributional Differential Expression

**DESeq** . . . . . Differential Gene Expression Analysis Based on the Negative Binomial Distribution

**DFMO** . . . . . Difluoromethylornithine

**DIZE** . . . . . Diminazene aceturate

**EdgeR** . . . . . Empirical Analysis of Digital Gene Expression Data in R

**eFAST** . . . . . Extended Fourier Amplitude Sensitivity Test

**ES** . . . . . Enrichment Score

**Fc** . . . . . Fragment crystallisable antibody region

**FDR** . . . . . False Discovery Rate

**GITR** . . . . . Glucocorticoid-induced TNFR-related protein

**GO** . . . . . Gene Ontology pathways

**GSEA** . . . . . Gene Set Enrichment Analysis

**GZMB** . . . . . Granzyme B

**Hif1-$\alpha$** . . . . . Hypoxia-Inducible Factor 1 alpha

**IKZF2** . . . . . Ikaros Zinc Finger Protein 2

**Isg15** . . . . . Interferon-Stimulated Gene 15

**KikGR** . . . . . Kikume Green-Red Photoconvertible Mice

**KNN** . . . . . K-Nearest Neighbours

**LAG3** . . . . . Lymphocyte Activation Gene 3

**LISI** . . . . . Local Inverse Simpson's Index

**LLC** . . . . . Lewis Lung cancer syngeneic tumour model

**LOESS** . . . . . Locally Estimated Scatterplot Smoothing

**LRT** . . . . . Likelihood Ratio Test

**MAST** . . . . . Model-based Analysis of Single-cell Transcriptomics

**MCMC** . . . . . Markov Chain Monte Carlo

**MDSC** . . . . . Myeloid-derived Suppressor Cells

**MF** . . . . . Molecular Function pathways

**MHC** . . . . . Major Histocompatibility Complex

**MLLE** . . . . . Modified Locally Linear Embedding

**mLN** . . . . . Mesenteric Lymph node

**MNN** . . . . . Mutual Nearest Neighbours

**MoE** . . . . . Mixture of Experts model

**mRNA** . . . . . Messenger Ribonucleic Acid

**MST** . . . . . Minimal Spanning Tree

**nDLN** . . . . . Draining/inguinal Lymph Node in naive mice

**NES** . . . . . Normalised Enrichment Score

**NK cell** . . . . Natural Killer cell

**NRP1** . . . . . Neuropilin-1

**ODC1** . . . . . Ornithine Decarboxylase 1

**ODE** . . . . . Ordinary Differential Equation

**PBMC** . . . . . Peripehral Blood Mononuclear Cells/Blood

**PCA** . . . . . Principal Component Analysis

**PD1** . . . . . Programmed Cell Death 1

**PDL1** . . . . . Programmed Cell Death-Ligand 1

**PI3K** $\delta$ . . . . . Phosphoinositide-3-Kinase Delta

**PKPD** . . . . . Pharmacokinetic and Pharmacodynamic models

**pMHC I** . . . . Peptide-Major Histocompatibility class I complex

**pTregs** . . . . . Peripheral Tregs

**SAT1** . . . . . Spermidine/Spermine N1-Acetyltransferase 1

**SCDE** . . . . . Single-Cell Differential Expression Analysis

**scRNA-seq** . . Single cell RNA sequencing

**STREAM** . . . Single-cell Trajectories Reconstruction and Mapping

**TCA** . . . . . Tricarboxylic Acid Cycle

**TCR** . . . . . T Cell Receptor

**TDLN** . . . . . Tumour Draining Lymph Node

**TME** . . . . . Tumour Microenvironment

**Tnfrsf9** . . . . . Tumor Necrosis Factor Receptor Superfamily Member 9 also known as 4-1BB

**Tnfrsf18** . . . . Tumor Necrosis Factor Receptor Superfamily Member 18 also known as GITR

**Tr1** . . . . . Type 1 Regulatory T cell

**Treg** . . . . . Regulatory T cell

**tRNA** . . . . . Transfer Ribonucleic Acid

**TSDR** . . . . . Treg-Specific Demethylated Region

**UMAP** . . . . . Uniform Manifold Approximation and Projection

**VAT** . . . . . Visceral Adipose Tissue

**VEGF** . . . . . Vascular Endothelial Growth Factor

# 1 Introduction

Contents


1.1 Motivation . . . . . 1
1.2 Tumorigenesis and the hallmarks of cancer . . . . . 3
1.3 The immune system and cancer immunity . . . . . 5
1.4 Immunosuppression in the tumour . . . . . 9
1.5 Tumour Tregs – a key immunotherapy target . . . . . 10
1.6 Therapeutically targeting intratumoral Tregs . . . . . 17
1.7 Challenges associated with Treg-targeting . . . . . 24
1.8 Research questions and hypotheses . . . . . 29
1.9 Thesis structure and summary . . . . . 31


## 1.1 Motivation

Cancer is one of the leading causes of death worldwide (Kocarnik et al., 2022; Foreman et al., 2018). Surgery, radiation, and chemotherapy are commonly used to treat cancer, but are not always effective. Immunotherapy, a revolutionary cancer treatment modality, has gained traction in recent years, with immune checkpoint molecules such as CTLA4 and PD1 commonly targeted (Zhang and Zhang, 2020). However, immunosuppressive cells, particularly regulatory T cells (Tregs), which accumulate in

the tumour microenvironment (TME), dampen the clinical benefit associated with immunotherapy (Tie et al., 2022). Thus, targeted depletion/blockade of intratumoral Tregs has the potential to enhance anti-tumour responses and reverse tumour growth.

Tregs exhibit extensive heterogeneity in different tissue (Shevyrev and Tereshchenko, 2020) —specifically targeting tumour Tregs without affecting Tregs in healthy tissue is extremely difficult. Inadvertent targeting of healthy tissue Tregs could induce life-threatening immune-related adverse effects. Furthermore, inter-species differences between mouse models and humans complicate the identification of therapeutic targets in mice that are also relevant for humans. Consequently, numerous experimental cancer drug candidates show good efficacy in mice but exhibit high attrition rates once they reach human clinical trials (Mak et al., 2014). Therefore, defining the therapeutic window of efficacy while accounting for inter-tissue and inter-species Treg variations is a key challenge in the field of immuno-oncology.

We propose that mathematical modelling can be applied to investigate intratumoral Treg dynamics and identify Treg subpopulations that are retained in tumours over time (resident Tregs) in mouse experimental models. Therapeutic markers upregulated on resident but not transient Tregs in mice can then be determined using single cell transcriptomics (scRNA-seq). Through the creation of cross-tissue mouse and human scRNA-seq Treg meta-atlases, potential markers can be assessed for their specificity to tumours and translational relevance in humans. Finally, antibodies targeting the top Treg markers can be evaluated in mice before clinical trials begin.

The aim of this thesis has been to demonstrate how the proposed ideas can be implemented to investigate intratumoral Treg migration mechanisms and identify clinically relevant targets for blocking/depleting tumour Tregs. However, in this introduction, we give a brief overview of tumorigenesis, the role of the immune system in the fight against cancer, Treg-mediated immunosuppression mechanisms, emerging ways of targeting intratumoral Tregs and current challenges associated with the adoption of Treg-targeting as a new cancer treatment modality. We finish the introduction by

exploring potential solutions and hypotheses to address these challenges and setting up the framework in which the work presented in this thesis fits.

## 1.2 Tumorigenesis and the hallmarks of cancer

Cancer refers to a collection of more than 200 diseases characterised by mutated cells that proliferate aggressively (Lambert et al., 2017). Many factors have been attributed to the aetiology of cancer, including carcinogens, radiation, hormones, and viruses. Carcinogens, for example those found in cigarettes, facilitate the onset of lung cancers (CDC, 2010; Blackadar, 2016). Exposure to ionising radiation causes DNA damage, resulting in different forms of cancer (Behjati et al., 2016). Cancers of the breast, endometrium, ovary, testis, and prostate have been associated with hormones suggesting that, in some cases, hormones can behave as natural carcinogens (Henderson and Feigelson, 2000; Blackadar, 2016). Finally, the Human Papilloma Virus (HPV) has been implicated in the development of cervical cancer (Blackadar, 2016; Schiffman et al., 2007).

Cancers are categorised by their tissue of origin. Carcinomas, which constitute about 90% of all human cancers, are characterised by epithelial cell malignancies (Cooper and Hausman, 2000). Sarcomas are relatively rare cancers of the connective tissue, muscle, bone, cartilage, and fibrous tissue. Finally, approximately 8% of human cancers are blood cancers, also known as leukemias and lymphomas, which originate from the hyper-proliferation of blood-borne cells (Cooper and Hausman, 2000). Despite differences between cancer subtypes, most cancers share similar properties that are referred to as the hallmarks of cancer (Fig. 1.1) (Hanahan and Weinberg, 2011).

Understanding these hallmarks is critical for designing cancer therapies. A defining feature of cancer cells is their hyperproliferative capacity. Cancer cells are resistant to regulated cell death and less susceptible to growth suppressors (Fig. 1.1). In the case of solid tumours, the combination of these characteristics allows cancer cells to rapidly grow and form a mass, usually characterised by a poor blood supply network. As a result, the TME is hypoxic and lacks adequate levels of nutrients. However, through

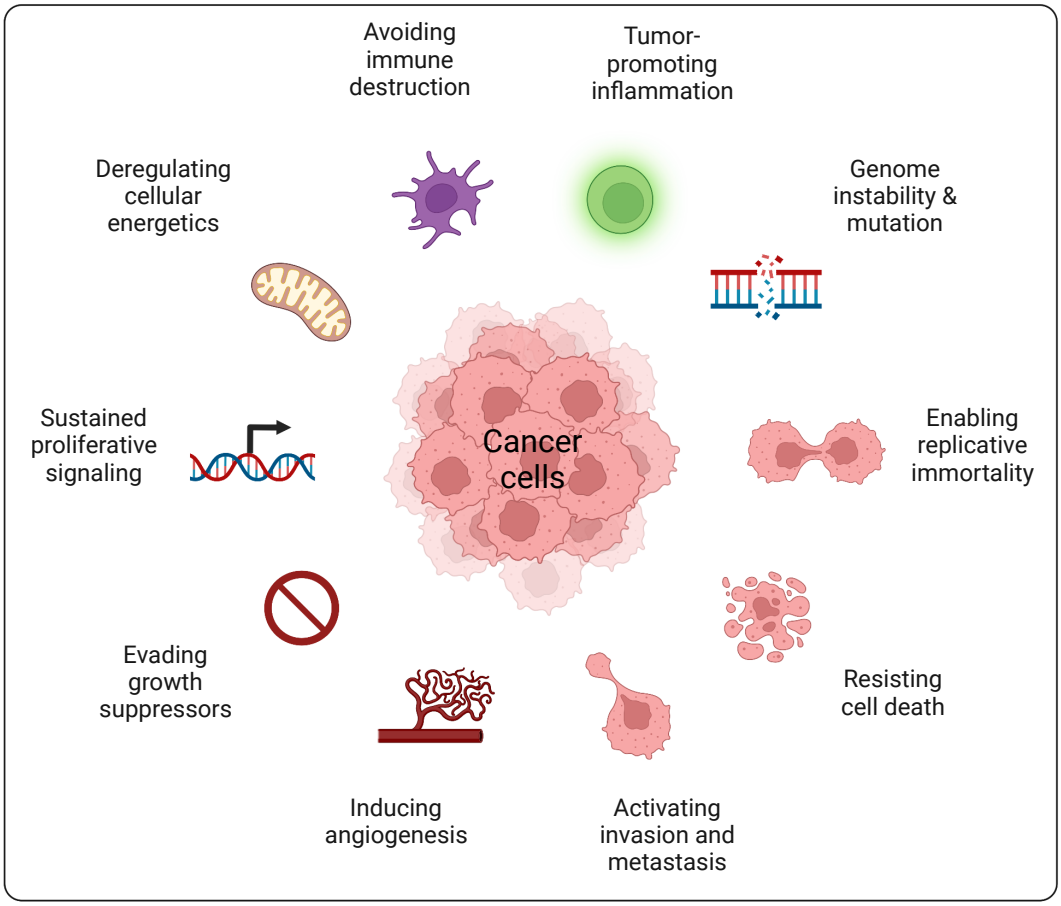



**Figure 1.1: Hallmarks of cancer**. The figure was adopted from Hanahan and Weinberg (2011) and created using Biorender from an existing template.

the secretion of growth factors such as vascular endothelial growth factor (VEGF), cancer cells promote the formation of leaky blood vessels (angiogenesis) that help sustain tumour growth (Verheul and Pinedo, 2000).

Cancer cells have also been shown to undergo extensive metabolic reprogramming (Fig. 1.1). Unlike most normal cells, cancer cells rely heavily on glycolysis and rapidly consume glucose and convert it to lactic acid, even in the presence of oxygen. This is called the Warburg effect (Liberti and Locasale, 2016). The exact reason for this is not yet fully understood. However, by so doing, cancer cells create an acidic environment, which is unfavourable for normal cells. High concentrations of lactic acid within the TME inhibit cancer-clearing immune cells (Wang et al., 2020a). The resulting immune evasion allows the tumour to continue growing and, when sufficiently developed, to

start metastasising to other organs (Cooper and Hausman, 2000).

## 1.3 The immune system and cancer immunity

The immune system plays a critical role in the fight against tumours, although at times it can become overwhelmed. The two main subcomponents of the human immune system are the innate and adaptive immune systems.

### 1.3.1 The innate immune system: DCs and NK cells

The innate immune system refers to an inborn and non-specific type of immunity that serves as the first line of defence against an infection (Marshall et al., 2018). Cells of the innate immune system include Dendritic cells (DCs) and Natural killer cells (NK cells).

Dendritic cells are referred to as professional antigen presenting cells (APCs). They sample the microenvironment and capture fragments (antigens) from bacteria, dead cancer cells, and other hostile agents. APCs then migrate to lymph nodes where they present these antigens to CD8 T cells using the major histocompatibility class I and II molecules (MHC I and II). This primes the adaptive immune system to respond against infection or tumours.

Of particular interest in the field of oncology are NK cells, because of their ability to directly kill cancer cells. A delicate balance between activating and inhibitory signals controls NK cell cytotoxic activity (Fig. 1.2A) (Morvan and Lanier, 2016). Disruption in this balance, for example due to the downregulation of the presentation of self-peptides via MHC class I on cancer cells, activates NK cells, which in turn kill cancer cells by secreting lytic granules. Perforin molecules secreted by NK cells create membrane pores on cancer cells, paving the way for proteases such as Granzyme B (GzmB) to enter cancer cells and induce apoptosis (Fig. 1.2B).

NK cells can also be therapeutically manipulated to induce cell death via a process known as antibody-mediated cellular cytotoxicity (ADCC). Antibodies that bind to

tumour antigens first coat the cancer cells. Using Fc$\gamma$ III receptors on their cell surface, NK cells then bind to the crystallisable fragment (Fc) domains of therapeutic antibodies, resulting in the cross-linking of NK cells with tumour cells and ultimate cancer cell killing (Fig. 1.2C).

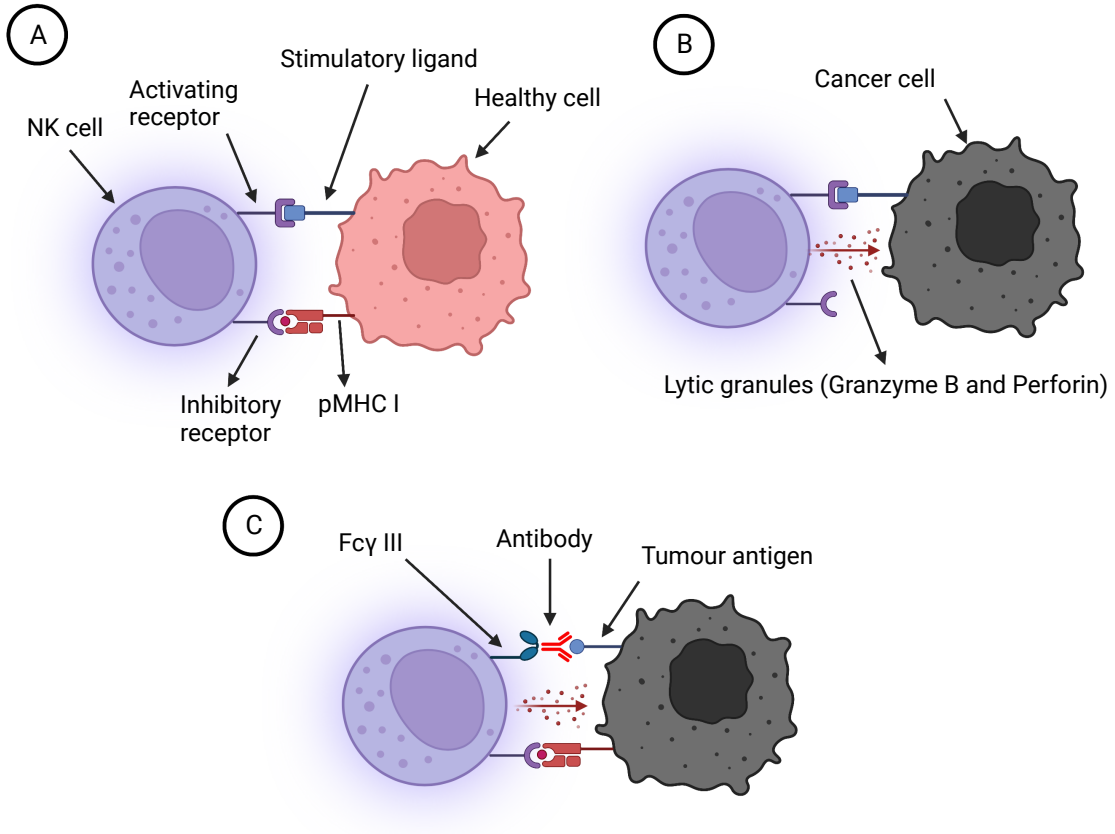



**Figure 1.2: Mechanisms of NK-cell mediated cytotoxicity**. A: NK cells recognise peptide-MHC class I (pMHC I) expressed on healthy cells and refrain from killing them. B: Cancer cells downregulate pMHC I expression resulting in the release of cytotoxic molecules by NK cells which kill cancer cells. C: Antibodies engineered to bind to cancer antigens link NK cells with cancer cells for killing via the antibody-mediated cellular cytotoxicity mechanism (ADCC). The figure was adopted from Morvan and Lanier (2016) and created using Biorender from an existing template. pMHC I – peptide-Major histocompatibility class I complex, Fc$\gamma$ III (CD16) – Fragment crystallisable type III receptors.

### 1.3.2 The adaptive immune system: CD8 T cells

Unlike innate immunity, adaptive immunity is acquired and develops specifically in response to an infection or a developing tumour. The key players of the adaptive immune system are CD4, CD8 T cells and B cells. Cytotoxic CD8 T cells play a

particularly important role in cancer immunity because, much like NK cells, they can directly kill cancer cells.

Naturally, the peptides produced in both healthy and cancer cells are degraded and presented on the cell surface by MHC class I molecules (pMHC I). The peptides presented by normal cells are recognised as "self-peptides" and do not trigger a destructive response from CD8 T cells. On the contrary, cancer cells may present mutated peptides on their MHC class I complexes. Activated cancer-specific CD8 T cells sample these pMHC class I molecules using T cell receptors (TCRs) to form an immune synapse. Signaling via the immune synapse causes CD8 T cells to release lytic molecules such as Granzyme B and Perforin that induce apoptosis in the cancer cell (Fig. 1.3A).

CD8 T cells are central to the cancer-immunity cycle, which is a process that generates immunity against cancer (Chen and Mellman, 2013). In this cycle, dying cancer cells release cancer-associated antigens that are captured by antigen-presenting cells (APCs) (Fig. 1.3B1-2). The APCs then migrate to lymph nodes where they present cancer antigens to naive CD8 T cells (Fig. 1.3B3). CD8 T cells that respond to cancer antigens are activated and expand to generate a clonal population of activated CD8 T cells with potent anti-cancer cytotoxicity. These activated CD8 T cells migrate through the blood and infiltrate the tumour microenvironment, where they recognise and kill cancer cells (Fig. 1.3B4-5). The killing of cancer cells results in the release of more cancer antigens and the cycle repeats (Chen and Mellman, 2013).

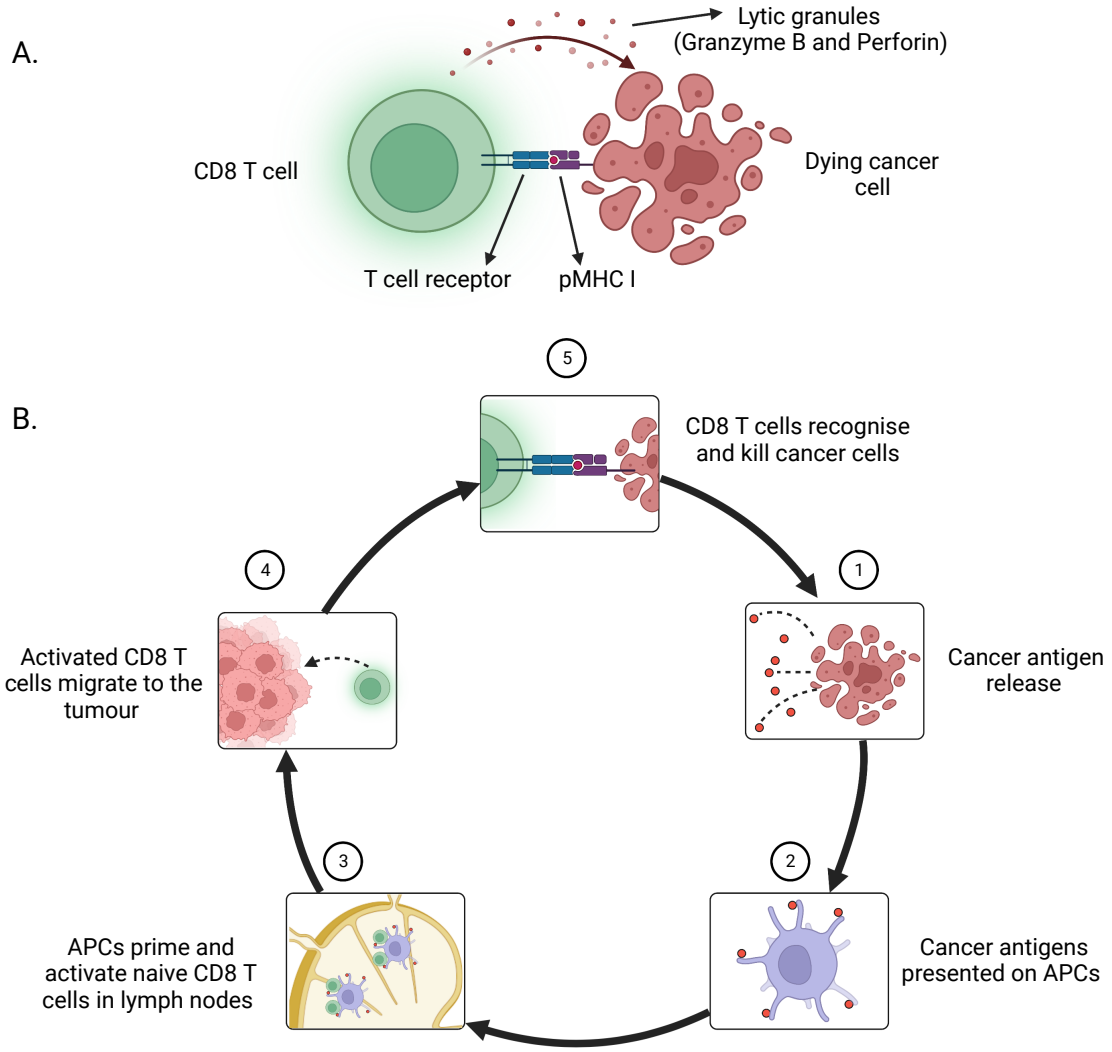



**Figure 1.3: The cancer-immunity cycle**. A: CD8 T cell-mediated cancer killing. B: The cancer-immunity cycle. Dying cancer cells release cancer-associated antigens (1). Antigen presenting cells (APCs) capture and present the cancer antigens on MHC I and II molecules (2). APCs migrate to lymph nodes where they prime and activate naive CD8 T cells to recognise the presented cancer antigens (3). Activated CD8 T cells migrate to the site of the tumour (4) and use their T cell receptors (TCRs) to engage with the pMHC I molecules on cancer cells, leading to the secretion of lytic granules that kill the cancer cells (5). The cycle then repeats. Figure B was adopted from Chen and Mellman (2013) and created using Biorender from an existing template. APC – Antigen presenting cells for example Dendritic cells, pMHC I – peptide-Major histocompatibility class I complex.

## 1.4 Immunosuppression in the tumour

In cancer patients, the cancer-immunity cycle is disrupted in one way or another (Chen and Mellman, 2013). Some patients may have immunologically "cold" tumours that do not express sufficient densities of cancer antigens. In turn, there is a deficiency in antigen presentation by APCs, which leads to poor CD8 T cell priming in the lymph node. Ultimately, cytotoxic CD8 T cells do not effectively infiltrate the tumour microenvironment, resulting in cancer progression (Bonaventura et al., 2019). This disrupts stages 1 through 4 in the cancer-immunity cycle (Fig. 1.3B1-4).

Studies have shown that tumour-infiltrating T cells can become dysfunctional or reach a state of exhaustion. When exhausted, T cells lose their ability to produce cytokines such as interferon gamma (IFN-$\gamma$), tumour necrosis factor alpha (TNF-$\alpha$) and interleukin-2 (IL2), and lytic granules like Granzyme B, which play critical roles in the fight against cancer. Simultaneously, exhausted T cells upregulate inhibitory receptors that include CTLA4, TIGIT, PD1, TIM3, and LAG3, leading to weaker effector functions (Jiang et al., 2015) (Fig. 1.4).

Multiple factors drive T cells to a state of exhaustion. Cancer cells upregulate PD-L1, which binds to PD1 receptors on T cells thereby contributing to T cell exhaustion. Regulatory T cells (Tregs) are an immunosuppressive subset of CD4 T cells that plays a critical role in maintaining immune tolerance (Sakaguchi et al., 1995, 2008). Within the tumour, Tregs inhibit conventional T cells and NK cells (Thornton and Shevach, 2000; Trzonkowski et al., 2004). Plasmacytoid Dendritic cells that develop during cancer growth induce Treg differentiation, which promotes the upregulation of PD-L1 on conventional Dendritic cells (Jiang et al., 2015; Sharma et al., 2007). The resulting tumour-associated Dendritic cells (TADCs) express low levels of costimulatory molecules, but upregulate immunosuppressive markers such as PD-L1 and IDO, which promote T cell exhaustion (DeVito et al., 2019) (Fig. 1.4).

Tumour-associated Macrophages (TAMs) accumulate in tumours. TAMs exhibit an immunosuppressive M2-macrophage phenotype rather than a pro-inflammatory M1-macrophage phenotype (Pan et al., 2020). Previous work has found that, due to their immunosuppressive characteristics, high TAM densities in many types of tumours are negatively correlated with patient prognosis (Lewis and Pollard, 2006). TAMs also produce IL10 and transforming growth factor-beta (TGF-$\beta$) which promote the induction of immunosuppressive Tregs in the tumour, thus suppressing anti-tumour responses (Chen et al., 2019a). Finally, Myeloid-derived Suppressor Cells (MDSCs), which accumulate in tumours, induce T cell exhaustion via the PD-L1/PD1 axis (Kim et al., 2011) (Fig. 1.4).

## 1.5 Tumour Tregs – a key immunotherapy target

To reverse T cell exhaustion in the tumour, a class of immunotherapeutics known as immune checkpoint inhibitors has been developed. The most common include anti-PD1 (Pembrolizumab and Nivolumab) and anti-CTLA4 (Ipilimumab). In the clinic, anti-PD1 has demonstrated positive results in patients with different tumours, including metastatic melanoma, non-small lung carcinoma, metastatic renal cell carcinoma (Brahmer et al., 2010), advanced gastric cancer (Muro et al., 2015) and bladder cancer (O'Donnell et al., 2015). Similarly, anti-CTLA4 has shown clinical benefit in patients with advanced melanoma (O'Day et al., 2010; Wolchok et al., 2010).

Although immune checkpoint inhibitors have shown great promise, not all cancer patients respond to treatment. Various factors such as cytotoxicity and the accumulation of immunosuppressive cells, particularly Tregs, in the tumour dampen the clinical potential of immune checkpoint inhibitors (Sharma et al., 2017).

High intratumoral Treg densities have been observed in head and neck (Schaefer et al., 2005), breast (Liyanage et al., 2002), lung (Wolf et al., 2003), liver (Ormandy et al., 2005), pancreatic (Hiraoka et al., 2006) and ovarian cancer (Curiel et al., 2004). Furthermore, high intratumoral Treg frequencies or low intratumoral T cell (non-Treg):Treg ratios were correlated with a poor prognosis in breast (Bates et al.,

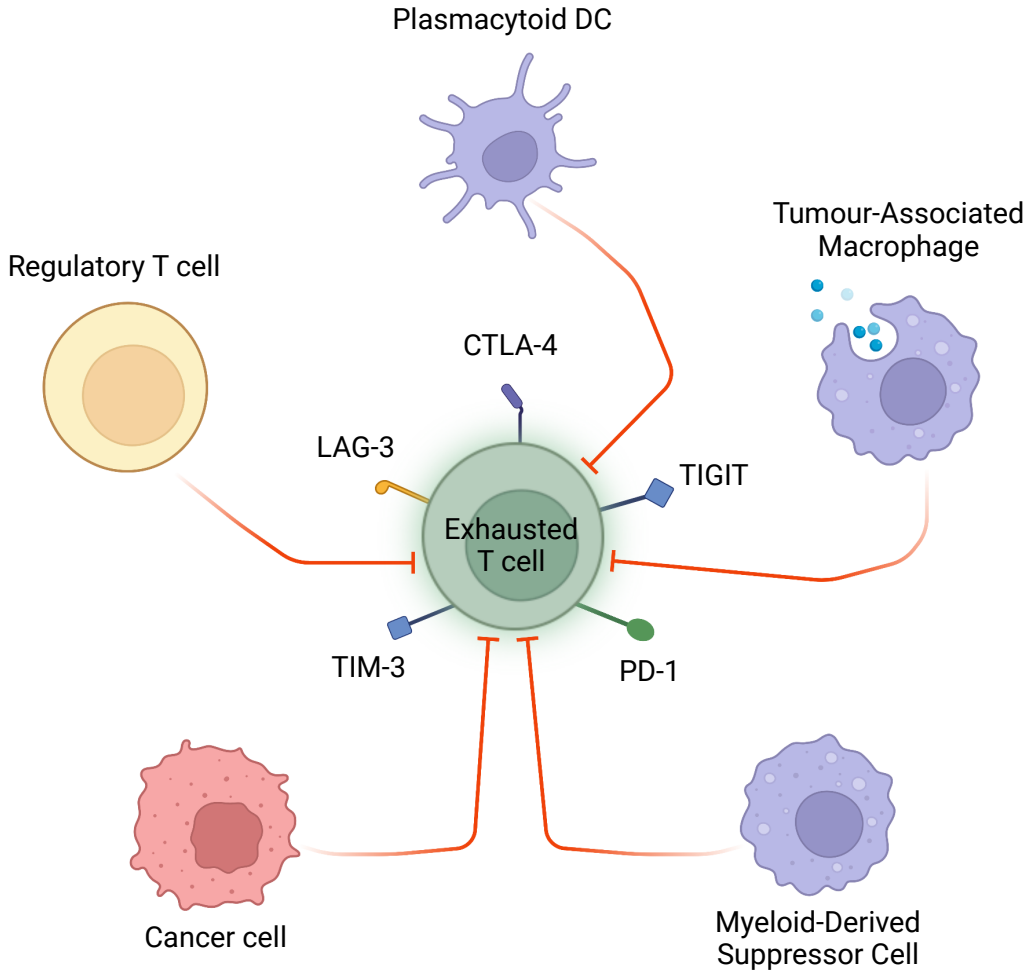



**Figure 1.4: T cell exhaustion**. Tumour infiltrating T cells become exhausted and start expressing inhibitory markers such as CTLA4, LAG3, PD1, TIM3 and TIGIT. Furthermore, immunosuppressive cells that accumulate in tumours contribute to the inhibition of anti-cancer T cell responses. Figure was created using Biorender. DC – Dendritic Cell, LAG3 – Lymphocyte Activation Gene 3 Protein, CTLA4 – Cytotoxic T Lymphocyte Antigen 4, TIM3 – T cell immunoglobulin domain and mucin domain protein 3, PD1 – Programmed Cell Death Protein 1, TIGIT – T cell immunoglobulin and immunoreceptor tyrosine-based inhibitory motif domain.

2006), gastric (Sasada et al., 2003) and ovarian cancer (Curiel et al., 2004). Therefore, interest in blocking/depleting intratumoral Tregs, as a stand-alone therapeutic regimen or in combination with existing immune check point inhibitors, has increased over the past several years. Understanding the role of Tregs in health and disease, the biological development of Treg subsets and tumour-specific Treg markers is critical to inform the development of safe and effective intratumoral Treg-targeting therapeutics.

### 1.5.1 The role of Tregs in health and disease

Tregs are a lineage of CD4 T cells that are immunosuppressive and usually defined by the expression of the forkhead box P3 protein (FOXP3). Typically, about 2-10% of peripheral blood CD4 T cells are Tregs (Dees et al., 2021; Le Bras et al., 2006). Tregs play a critical role in keeping the immune system under control to prevent the development of autoimmune diseases (Sakaguchi et al., 1995). They also reduce inflammation at sites of injury and help promote wound healing (Nosbaum et al., 2016).

Treg dysfunction has been associated with a variety of diseases. Mutations in the FOXP3 gene were found to induce immune dysregulation, polyendocrinopathy, entheropathy, X-linked Syndrome (IPEX) in mice and humans (Brunkow et al., 2001; Bennett et al., 2001). Other conditions associated with impaired Treg function include atopic dermatitis (Verhagen et al., 2006), Sjögren's syndrome (Li et al., 2007), Guillain-barré syndrome (Chi et al., 2007) and Hashimoto's thyroiditis (Hu et al., 2019).

### 1.5.2 Treg subsets: nTregs, pTregs and Tr1 Tregs

There are two broad classes of Tregs namely, natural or thymically derived Tregs (nTregs/tTregs) and peripherally induced Tregs (pTregs). tTregs develop in the thymus after T cell receptor (TCR) stimulation of CD4 single positive (SP) cells by self-antigens presented on medullary thymic epithelial cells (mTECs) or bone-marrow derived antigen presenting cells (BM-APCs) (Lee and Lee, 2018). The subset of CD4 SP cells that binds strongly to ubiquitous self-antigens is eliminated by negative thymic selection. However, CD4 SP subsets that show high affinity for tissue-restricted self-antigens develop to become Treg precursors. Subsequently, the Treg precursors move toward the nTreg lineage after stimulation by IL-2 and IL-15 cytokines (Fig. 1.5A) (Lee and Lee, 2018).

Peripheral Tregs are $CD4^+$ $FOXP3^+$ cells that develop in the periphery. Naive CD4 $FOXP3^-$ T cells are stimulated by non-self antigens presented on Dendritic cells in the presence of cytokines such as TGF-$\beta$ and IL-2, Retinoic acids (RA) and short chain

fatty acids (SCFAs) found in immunosuppressive environments. Non-self antigens may be derived from commensal bacteria or ingested food (Fig. 1.5B) (Lee and Lee, 2018).

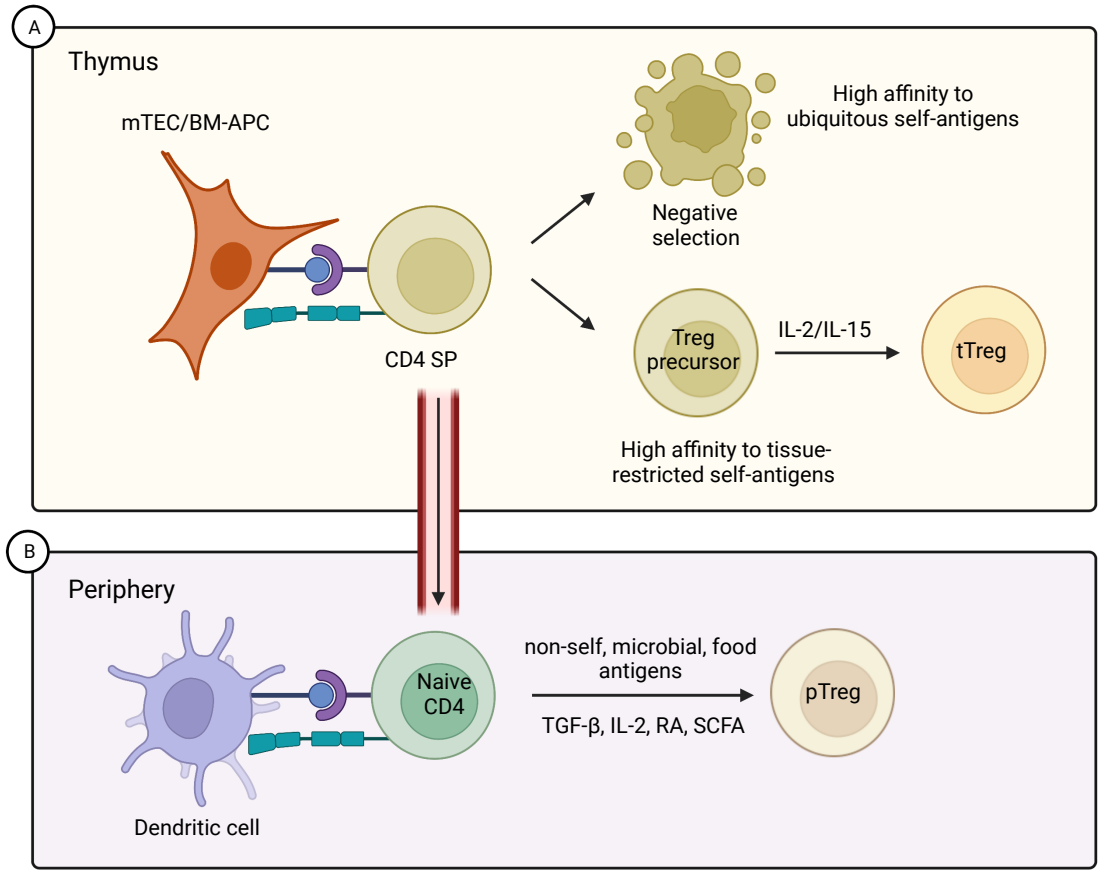



**Figure 1.5: Treg development**. A: In the thymus, CD4 single positive (SP) cells are stimulated by self antigens on medullary thymic epithelial cells (mTECs) or bone-marrow-derived antigen-presenting cells (BM-APCs). If the CD4 SPs exhibit high affinity to ubiquitous antigens, they undergo clonal clearance. However, if CD4 SP cells bind to a subset of tissue-restricted self-antigens, they differentiate towards Treg precursors. Finally, exposure to IL-2 and IL-15 drives precursor Tregs into thymic Tregs (tTreg). B: In the periphery, naive CD4 T cells are stimulated by non-self antigens presented on Dendritic cells. These antigens may come from microbial organisms or food. This leads to the conversion of CD4 T cells into peripherally induced Tregs (pTregs). The figure was adopted from Lee and Lee (2018) and created using Biorender. IL-2 – Interleukin 2, IL-15 – Interleukin 15, TGF-$\beta$ – Transforming Growth Factor $\beta$, RA – Retinoic Acid, SCFA – Short Chain Fatty Acids.

In addition to these two Treg subsets, Type 1 regulatory T cells (Tr1) have also been described. In contrast to nTregs and pTregs, Tr1 cells do not highly express FOXP3, but secrete high levels of immunosuppressive molecules such as IL-10. They are derived from memory T lymphocytes and can be identified by surface expression of LAG3 and the integrin-$\alpha$2 subunit (CD49b) (Gagliani et al., 2013).

Distinguishing between nTregs and pTregs remains a challenge. In humans, there is no widely accepted marker for nTregs. A recent study suggested that GPA33 marks human nTregs though the fraction of GPA33$^{high}$ Tregs isolated from peripheral blood was small (Opstelten et al., 2020). Nrp1 was initially proposed as a marker for mouse nTregs but is not found on Tregs in human blood (Yadav et al., 2012; Milpied et al., 2009). Other studies claimed that Helios (Ikzf2) is a better marker of nTregs because, unlike Nrp1 which is expressed later in the development of nTregs, Ikzf2 is expressed throughout the differentiation of nTregs (Singh et al., 2015). However, further work has found that Helios$^{-}$ Tregs and conventional T cells can be primed to express Ikzf2 upon activation (Akimova et al., 2011; Pratama et al., 2020).

Currently, epigenetic studies looking at the FOXP3 locus are considered a better method of differentiating between nTregs and pTregs. Four conservative noncoding sequences (CNS), namely CNS0, CNS1, CNS2 and CNS4, have been identified in the FOXP3 locus in mouse and human Tregs. CNS2 is also known as the Treg specific demethylation region (TSDR), and its methylation state is believed to mark the stability of FOXP3 expression. Due to their stable and constitutive expression of FOXP3, nTregs are considered to be mostly demethylated in the TSDR while pTregs are methylated (Lee and Lee, 2018).

### 1.5.3 Mechanisms of Treg-mediated immunosuppression

Tregs employ a variety of mechanisms to suppress effector T and NK cell function. Some of the mechanisms involve the direct killing or disruption of biological functions within target cells, while others inhibit cells, such as Dendritic cells, that prime and activate effector T cells. Figure 1.6 highlights markers that are upregulated on Tregs and a few mechanisms that Tregs utilise to directly or indirectly diminish T and NK cell immune responses.

Tregs overexpress the interleukin-2 $\alpha$ receptor (CD25) which binds to IL-2 with high affinity (de la Rosa et al., 2004). As a consequence, Tregs sequester IL-2 from the local environment, thus depriving effector T cells of this valuable cytokine. Without adequate

IL-2, effector T cells do not proliferate and succumb to apoptosis mediated by the Bcl-2 Interacting Mediator of cell death (Bim) (Fig. 1.6A) (Pandiyan et al., 2007).

Similar to effector T cells, Tregs secrete lytic granules such as Granzyme B and Perforin that directly kill target T, B, and NK cells (Zhao et al., 2006; Cao et al., 2007). Perforin molecules create pores in the membranes of target cells, and Granzyme B is a death-inducing protease that kills the target cell (Fig. 1.6B) (Arias et al., 2017).

Through the surface expression of the CD39 and CD79 ectoenzymes, Tregs convert ATP to adenosine. Adenosine promotes the development of induced Tregs and the inhibition of APCs and NK cells. Adenosine also binds to adenosine 2A receptors on T cells, resulting in the suppression of effector T cells (Fig. 1.6C) (Ohta and Sitkovsky, 2014).

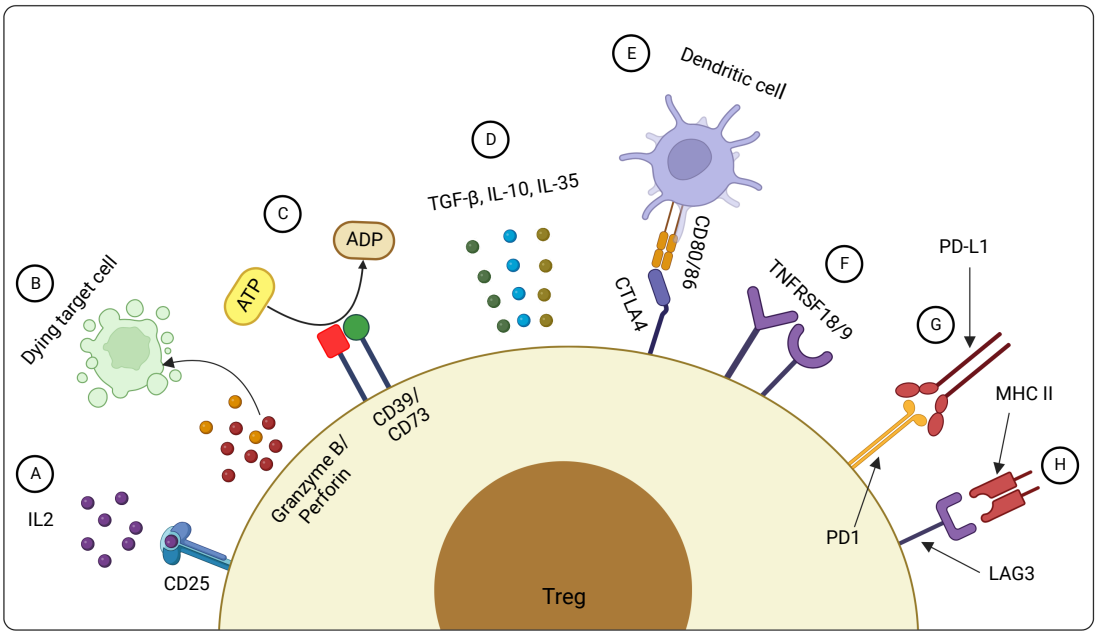



**Figure 1.6: Mechanisms of Treg-mediated immunosuppression**. A: Sequestering of IL2 by CD25. B: Secretion of Granzyme B and Perforin to kill T cells and NK cells. C: Conversion of ATP to adenosine by CD39 and CD73. D: Release of TGF-$\beta$, IL-10 and IL-35. E: Engagement of CTLA4 with CD80 and CD86 molecules on Dendritic cells. F: Expression of TNFRSF18 and 9. Engagement of PD1 with PD-L1 (G) and LAG3 with MHC II (H).The figure was adopted from Chen et al. (2022) and created using Biorender. CD25 – Cluster of Differentiation 25, ATP – Adenosine Triphosphate, ADP – Adenosine Diphosphate.

Tregs secrete different types of anti-inflammatory cytokines such as TGF-$\beta$, IL-10 and IL-35. TGF-$\beta$ plays a role in suppressing effector T and NK cells (Moreau et al., 2022). IL-10 signaling in Tregs has been found to suppress pathogenic T-helper (Th17) cells, resulting in the prevention of colitis (Chaudhry et al., 2011). IL-35 plays a critical role in maintaining Treg immunosuppressive function. Conventional naive CD4 T cells that were engineered to ectopically express IL-35 suppressed T cell proliferation *in vitro* (Fig. 1.6D) (Collison et al., 2007).

The role of CTLA4 in Treg immunosuppression is well documented. During T cell activation, CD80/CD86 molecules on Dendritic cells bind to CD28 on T cells to provide a costimulatory signal. Studies have shown that CTLA4 on Tregs binds to CD80/CD86 molecules on Dendritic cells with higher affinity than CD28. Over time, CD80/CD86 molecules are sequestered from Dendritic cells through a process called trogocytosis (Fig. 1.6E) (Cederbom et al., 2000; Tekguc et al., 2021). As a result, Dendritic cells become anergic resulting in poor T cell costimulation. Furthermore, the engagement of CTLA4 with CD80/CD86 causes Dendritic cells to produce indoleamine 2,3-dioxygenase (IDO) which catabolises tryptophan, a pro-inflammatory amino acid, into immunosuppressive kynurenines (Grohmann et al., 2002; Belladonna et al., 2007).

TNFRSF18 (GITR) and TNFRSF9 (4-1BB), proteins of the tumour necrosis factor receptor superfamily, are highly expressed on Tregs (Fig. 1.6F). The role TNFRSF18 and TNFRSF9 in Tregs is not fully clear. However, previous work has shown that stimulating TNFRSF18 and TNFRSF9 using their agonists results in Treg proliferation and improved survival *in vitro* (Lubrano di Ricco et al., 2020). Furthermore, signaling through various subsets of TNFRSF molecules by their respective ligands maintains lymphoid and non-lymphoid tissue Treg effector function via the Nuclear factor kappa B (NF-$\kappa$B) pathway (Lubrano di Ricco et al., 2020; Vasanthakumar et al., 2017).

PD1 is a surface marker that is highly expressed on Tregs (Fig. 1.6G). Most research has focused on the PD1/PD-L1 axis although PD1 also binds to PD-L2. However, despite years of research, the role of the PD1/PD-L1 axis in Tregs remains unclear (Zhulai and Oleinik, 2022). PD1 deficiency has been shown to induce autoimmune reactions,

suggesting loss of immune tolerance (Wang et al., 2005). Some studies suggest that the PD1/PD-L1 axis plays a critical role in converting memory T cells to induced regulatory T cells (Fanelli et al., 2021). In chronic viral infection, PD1 on Tregs has been shown to engage with PD-L1 on CD8 T cells resulting in CD8 T cell suppression (Park et al., 2015).

Tregs up-regulate LAG3, which strongly binds to pMHC II molecules (Fig. 1.6H) (MacLachlan et al., 2021). Despite limited knowledge about LAG3-mediated Treg immunosuppression, some studies have shown that LAG3 blockade limits the ability of Tregs to suppress T cell proliferation and activation *in vitro* (Huang et al., 2004). LAG3 expression on Tregs is thought to inhibit Dendritic cells from effectively activating T cells (Liang et al., 2008). Finally, LAG3 expressed on effector T cells binds to stable pMHC II, resulting in the reversal of murine autoimmunity and propagation of immune evasion in mouse tumours (Maruhashi et al., 2022).

## 1.6 Therapeutically targeting intratumoral Tregs

High densities of Tregs in solid tumours contribute to the suppression of anti-tumour immunity. To reverse Treg-mediated immunosuppression in the tumour, different types of Treg-targeting therapeutics have either been approved for clinical use or are currently being explored. These therapeutics fall into 2 broad categories, namely Treg-depleting and blocking antibodies.

Depleting antibodies exhibit antibody-dependent cellular cytotoxicity (ADCC). This means that their variable regions bind to a surface molecule that is upregulated on Tregs, whereas their constant domains bind to Fc receptors on NK cells. Consequently, Tregs are brought into close proximity with NK cells, leading to Treg depletion through a mechanism analogous to that illustrated in Figure 1.2C. In contrast, Treg blocking antibodies inhibit the effector function of Tregs, thus reducing Treg-mediated suppression of anti-cancer immunity. Below, we provide a brief overview of relevant intratumoral Treg markers and the antibodies that have been developed to target these markers.

### 1.6.1 CCR4

CCR4, a chemokine receptor for CCL17 and CCL22 chemokines, is highly expressed on various conventional T cell subsets (Duhen et al., 2009) and Tregs (Iellem et al., 2001) in the blood. The expression of CCR4 on Tregs is thought to be involved in their migration towards non-lymphoid tissue, with $Ccr4^{-/-}$ Tregs failing to home to the lung and skin in mice (Sather et al., 2007). In a canine model of bladder cancer, CCR4 blockade inhibited tumour growth and improved overall survival (Maeda et al., 2019). Anti-CCR4 monoclonal antibodies depleted effector Tregs from lung cancer (Kurose et al., 2015a) and melanoma and induced antigen-specific CD4 and CD8 T cells *in vitro* (Sugiyama et al., 2013). Mogamulizumab (humanised anti-CCR4 antibody) was tested in a small-scale clinical trial involving patients with lung and esophageal cancer. Although the study did not evaluate intratumoral Tregs, it found that the antibody not only depleted effector Tregs in the blood, but also induced different types of autoimmune reactions (Kurose et al., 2015b). A follow-up study revealed that Mogamulizumab reduces various T cell subsets in the blood, including effector Tregs and $CCR4^{+}$ CD8 T cells, which may limit its therapeutic benefit against cancer (Maeda et al., 2021). Collectively, these findings suggest that CCR4 is not a unique marker of intratumoral Tregs and the administration of anti-CCR4 antibodies may lead to side effects associated with non-specific T cell depletion.

### 1.6.2 CD25

CD25 was used to identify Tregs long before Foxp3 was discovered (Sakaguchi et al., 1995). However, CD25 expression is not specific to Tregs. Upon activation, conventional T cells can also transiently upregulate CD25 (Boyman and Sprent, 2012). However, Treg depletion using anti-CD25 antibodies disrupted the progression of murine squamous cell carcinoma (Ramos et al., 2012). Intratumoral injection of anti-CD25 antibodies led to improved CD8 T cell responses against 66c14 breast, AB1 mesothelioma and CT26M colon murine cancer models (Onda et al., 2019). In a small-scale clinical study

involving melanoma patients, ONTAK (Denileukin diftitox), an anti-CD25 diphtheria toxin conjugate, depleted peripheral blood Tregs and induced CD8 T cell responses against tumour antigens following vaccination. However, the patients involved in the study developed severe eczema as a result of Treg depletion (Mahnke et al., 2007). Recently, studies have focused on modifying anti-CD25 antibodies to reduce bystander targeting of CD8 T cells. The Fc domain on anti-CD25 antibodies was improved to facilitate stronger binding to Fc receptors, leading to better Treg depletion in the tumour (Vargas et al., 2017). In a recent study conducted by Solomon *et al.*, anti-CD25 depleted Tregs in the tumour, blood and spleen in mice (Solomon et al., 2020). Interestingly, the frequencies of $GzmB^{+}$ CD8 T cells improved after anti-CD25 administration. A similar Treg depletory efficiency was observed in cynomolgus monkeys (Solomon et al., 2020). The most recent study focusing on anti-CD25 utilised CRISPR/Cas9 genome-editing technology to further optimise the Fc domain. The resulting anti-CD25 antibody depleted tumour-resident Tregs and synergised with anti-PD1 therapy in mouse tumour models (Van Elsas et al., 2022).

### 1.6.3 CCR8

Early work involving multiple murine cancer models highlighted that Tregs that infiltrate the tumour exhibit a memory phenotype and upregulate Ccr8 and Cxcr4 (Wang et al., 2012). However, antibody-mediated blockade or genetic ablation of Ccr8 did not reduce the accumulation of Tregs in the tumour (Whiteside et al., 2021; Magnuson et al., 2018) nor did it restrict tumour growth (Bhatt et al., 2021; Campbell et al., 2021). Instead, Treg depletion using anti-CCR8 antibodies with ADCC activity reduced tumour progression in a number of murine cancer models and synergised with anti-PD1 treatment (Bhatt et al., 2021; Campbell et al., 2021; Van Damme et al., 2021; Kidani et al., 2022).

Human studies have shown that in the presence of CCL1 (one of the chemokines that bind to CCR8), about 30% of Tregs in the blood can be induced to upregulate CCR8, CD39, Granzyme B, IL-10 and FOXP3 to become highly immunosuppressive (Barsheshet

et al., 2017). This suggested the possibility of CCR8$^-$ Tregs being converted to a CCR8$^+$ phenotype via antigen stimulation in the tumour.

Plitas *et al.* used bulk RNA sequence data to compare Tregs from breast cancer tissue with Tregs from adjacent healthy breast tissue. The authors found that breast cancer Tregs upregulated CCR8 (Plitas et al., 2016). Consistent with this, a separate study found that CCL1 was highly expressed in human breast cancer and contributed to the accumulation of CCR8$^+$ Tregs in the tumour (Kuehnemuth et al., 2018). CCR8$^+$ Tregs have also been identified in a number of human tumours, including pancreatic ductal adenocarcinoma (Yi et al., 2018), muscle-invasive bladder cancer (Wang et al., 2020b), lung cancer (Haruna et al., 2022) and cutaneous T-cell lymphomas (Giustiniani et al., 2022).

Given these promising studies, Jounce Therapeutics and Gilead have initiated a Phase 1 clinical trial involving GS-1811, a Treg-depleting anti-CCR8 antibody (Weaver et al., 2022), with the first set of results scheduled to be published in 2025.

### 1.6.4 LAG3

Generally, LAG3 suppresses T cell proliferation (Durham et al., 2014) and is considered one of the markers of exhausted T cells. However, the role of LAG3 in Tregs remains enshrouded in mystery (Burnell et al., 2022). Although some studies have shown that Lag3 ablation or blockade impairs Treg immunosuppressive potential (Huang et al., 2004; Workman and Vignali, 2005), other studies did not observe differences in immunosuppressive potential between Lag3$^{-/-}$ and wild-type Tregs (Durham et al., 2014; Sega et al., 2014). More perplexing, other studies have shown that Tregs with Lag3 deletions exhibit higher immunosuppressive capacity that wild-type Tregs in a murine model of autoimmune disease (Zhang et al., 2017). These inconsistent observations make it difficult to fully define the role of Lag3 in Tregs.

Lag3$^+$ Tregs have been identified in various murine tumour models. Using MC38-implanted Kaede mice, Li *et al.* photo-labelled and isolated intratumoral Tregs at

multiple time points. Flow cytometric analysis of these labelled intratumoral Tregs revealed that they upregulated Lag3, suggesting that Lag3 defines Tregs that remain in the tumour over time (Li et al., 2022). Similar studies using the KikGR mouse model highlighted that MC38 tumour-resident Tregs elevated the expression of IL-10, Lag3, GzmB, CD39 and CD25 compared to Tregs that had recently migrated into the tumour (Ikebuchi et al., 2021). Systemic Treg depletion using a PI3K$\delta$ inhibitor resulted in the enrichment of hypoproliferative Mki67$^{lo}$ Lag3$^{+}$ Tregs in 4T1 tumours (Lauder et al., 2021, 2020). Interestingly, Lag3 blockade in the absence of PI3K$\delta$ inhibition did not inhibit tumour growth. This paralleled the findings of a different study in which MC38 tumours progressed to the same extent in wild-type and Lag3$^{-/-}$ mice (Woo et al., 2012). Instead, sequential PI3K$\delta$ inhibition followed by Lag3 blockade restricted 4T1 tumour growth (Lauder et al., 2020). Taken together, the effect of Lag3 blockade on intratumoral Tregs in mice remains unclear.

In humans, a higher fraction of LAG3$^{+}$ Tregs was identified in the blood isolated from patients with colon cancer and melanoma compared to healthy subjects. Furthermore, LAG3 expression defined a subpopulation of Tregs that were enriched in the tumour (Camisaschi et al., 2010). A recent clinical trial, RELATIVITY-047, showed that the combination of Relatlimab (anti-LAG3) and Nivolumab (anti-PD1) confers greater benefit to patients with inoperable melanoma than Nivolumab alone (Tawbi et al., 2022). The drug is believed to block the inhibitory interaction between LAG3 and pMHC II, thus promoting T cell proliferation and cytokine production (Paik, 2022). It remains unknown whether Relatlimab predominately targets intratumoral Tregs, or not.

### 1.6.5 TNFRSF18 (GITR)

TNFRSF18 (GITR) is constitutively expressed on Tregs (Ronchetti et al., 2015) and is considered to be one of the markers of Tregs in both mice (Shimizu et al., 2002) and humans (Tsaknaridis et al., 2003). Its expression is not limited to Tregs, as studies have indicated that after activation, conventional T cells can upregulate GITR (Nocentini et al., 1997). However, in multiple tumour types including Hepatocellular carcinoma, Non-small

cell lung cancer (NSCLC), Renal cell carcinoma and Melanoma, GITR expression was found to be higher in Tregs than in CD4 and CD8 T cells (Vence et al., 2019).

Signaling through TNFRSF18 by its ligand GITRL or an anti-GITR agonist has been found to induce the proliferation, survival (Nocentini et al., 1997) and effector function of CD4 and CD8 T cells (Ronchetti et al., 2004). In Tregs, the effect of GITR/GITRL signaling is not well understood. Generally, studies have associated GITR signaling with improved Treg proliferation (van Olffen et al., 2009) and transient inhibition of Treg function (Ronchetti et al., 2015).

Administration of the GITR agonist, DTA-1, inhibited the growth of CT26 tumours and, to a lesser extent, MC38 tumours. Increased inhibition of CT26 tumours was attributed to intratumoral proportions of CD4 and CD8 T cells that were higher in CT26 tumours than in MC38 tumours (Vence et al., 2019). Another study involving CT26 tumours highlighted that CD4, but not CD8, T cells were critical for anti-GITR-mediated tumour inhibition (Zhou et al., 2007). Furthermore, anti-GITR did not abrogate the immunosuppressive potential of Tregs, but instead induced them to proliferate and produce more IL-10 (Zhou et al., 2007). Similar findings were made using B16 (melanoma) mouse model. Anti-GITR treatment did not inhibit the suppressive potential of Tregs, but destabilised their accumulation in the tumour, leading to higher intratumoral CD8:Treg ratios and tumour restriction (Cohen et al., 2010).

In a different study, Tregs from anti-GITR-treated mice were compared with Tregs from untreated mice. No differences in suppressive potential were observed (Coe et al., 2010). Interestingly, anti-GITR appeared to partially deplete Tregs within MB49 tumours (murine bladder carcinoma), resulting in tumour rejection (Coe et al., 2010). Similarly, anti-GITR was found to not only induce a costimulatory effect but also partially deplete intratumoral Tregs in MC38 (Mahne et al., 2017). Therefore, it was concluded that although anti-GITR was initially thought to be an agonist, it exhibits some level of ADCC activity.

Anti-GITR is currently being tested in humans with solid tumours. So far, early clinical trials have highlighted that anti-GITR as a stand-alone monotherapy or in combination with other antibodies is well tolerated, although the extent of clinical benefit is not yet fully clear (Heinhuis et al., 2020; Piha-Paul et al., 2021; Davar et al., 2022).

### 1.6.6 TNFRSF9 (4-1BB)

TNFRSF9 (4-1BB), another member of the tumour necrosis factor receptor superfamily, is constitutively expressed on Tregs (Tanaka and Sakaguchi, 2019; Zheng et al., 2004) and its ligand is known as 4-1BBL (Alderson et al., 1994). Upon activation, CD4 and CD8 T cells can also upregulate 4-1BB. However, in contrast to CD4 T cells, the activation of 4-1BB in CD8 T cells leads to more significant proliferation and effector responses (Shuford et al., 1997).

In Tregs, the exact influence of 4-1BB signalling is less clear. Studies have shown that a 4-1BB agonist promotes Treg proliferation but does not hinder their ability to suppress CD4 T cells (Zheng et al., 2004). Paradoxically, these 4-1BB-stimulated Tregs produce IFN-$\gamma$, which is typically expressed by pro-inflammatory T cells. The interaction between IFN-$\gamma$ expression and the observed immunosuppression exhibited by these Tregs is not understood (Zhang et al., 2007). Due to its ability to modulate T cell responses, 4-1BB has become an attractive target for cancer immunotherapy.

In the J558-Neo (plasmacytoma) murine tumour model, anti-41BB reversed tumour growth by improving the survival of antigen-experienced CD8 T cells (May Jr et al., 2002). Recent work has shown that, unlike an anti-41BB agonist, an anti-41BB antibody with ADCC activity can deplete intratumoral Tregs and confer enhanced inhibition of CT26 (colon carcinoma), EG7 (thymoma) and NXS2 (neuroblastoma) tumours (Buchan et al., 2018). Sequential administration of a depletory anti-41BB antibody followed by an anti-41BB agonist yielded the best results, prompting the authors to create a new anti-41BB antibody with the dual capacity of depleting Tregs and activating CD8 T cells (Buchan et al., 2018).

Anti-41BB agonists are actively being investigated in humans. In early-stage clinical trials involving advanced solid tumours, high doses of Urelumab (4-1BB agonist) induced transaminitis (Segal et al., 2017). Further clinical development and investigation of the safety profile of anti-41BB is underway (Wang et al., 2022).

## 1.7 Challenges associated with Treg-targeting

Treg-targeting represents a rational approach of enhancing anti-tumour responses by reducing the extent of immunosuppression in the tumour. However, the adoption of this cancer treatment approach is impeded by the potential induction of life-threatening side effects. Therefore, the current priority is to define the therapeutic window of efficacy that confers clinical benefit to patients while minimising adverse events.

The multistep nature of the Treg-targeting drug development pipeline makes it difficult to pinpoint the stages that engender the toxicities seen in clinical trials. However, data-driven approaches can be applied to understand intratumoral Treg dynamics, identify therapeutic markers that are specific to tumour Tregs and assess their translational potential across species. Below, we elaborate on some of the challenges facing Treg-targeting immunotherapy and propose potential solutions that are explored in this thesis.

### 1.7.1 Poor mechanistic understanding of intratumoral Treg dynamics

Similar to many cells of the immune system, Tregs are dynamic. This implies that they are able to migrate from one biological location to another. Understanding the mechanisms of Treg accumulation and emigration from the tumour is critical for informing the development and administration regimens of Treg-targeting immunotherapy.

Currently, intratumoral Treg dynamics, including whether there exist resident and transient Tregs in the tumour, are not well understood. This is, in part, due to the

complexity associated with labelling Tregs *in vivo* and tracking their migration from the primary tumour to other organs.

To our knowledge, only two studies have used photoconvertible mouse models to label Tregs in MC38 tumours and track their migration to the tumour draining lymph node (TDLN) and spleen over time. Ikebuchi *et al.* photo-labelled Tregs in MC38 tumours and observed that after 8-12 hours, a fraction of the labelled Tregs had remained in the tumour (Ikebuchi et al., 2021). Flow cytometric analysis showed that Tregs that remained in the tumour upregulated Lag3, CD25, CD39, IL-10 and Granzyme B, but downregulated Neuropilin-1 (Nrp1) in contrast to Tregs that had recently migrated into the tumour (Ikebuchi et al., 2021). Similarly, Li *et al.* photoconverted MC38 tumours and used flow cytometry to show that there were Lag3-expressing Tregs that remained in the tumour up to 72 hours after photo-labelling (Li et al., 2022). Both these studies suggested that, at any given time, there could be resident and transient Tregs in the tumour. Additional approaches, particularly mathematical modelling, still need to be applied to investigate whether the Treg profile observed in the tumour can be explained by a model of an exponentially decaying transient Treg population or, alternatively, an additive combination of both exponentially decaying (transient) and resident Treg populations. If there are indeed resident and transient Tregs in the tumour, the rates at which transient Tregs migrate out of the tumour would need to be determined. These rates are critical for application in Pharmacodynamic and Pharmacokinetic (PKPD) studies that use mathematical models to study how tumours behave in the presence or absence of a Treg-targeting agent, and are increasingly becoming important in cancer drug development (Sancho-Araiz et al., 2021; Wang and Deisboeck, 2014).

Several mathematical models involving Tregs have been published. However, these models do not infer the rates associated with intratumoral Treg trafficking. Milanez-Almeida *et al.* used mathematical modelling to estimate Treg trafficking rates from the thymus to the spleen and lymph node. As this was a Treg homeostasis model, it lacked a tumour compartment and thus could not infer the kinetics associated with tumour Tregs (Milanez-Almeida et al., 2015). de Pillis *et al.* developed a mathematical model

for cancer and immune cells that describes the effects of a drug called Sunitinib on Renal cell carcinoma. The model described Tregs as a dynamically homogeneous population that accumulates in the tumour over time. However, the model did not account for the possibility of resident and transient Tregs (de Pillis et al., 2013). Many studies have similarly developed mathematical models that involve intratumoral Tregs but did not infer Treg-specific parameters or account for resident and transient Tregs. Table 1.1 gives a summary of some of the mathematical models involving intratumoral Tregs.

**Table 1.1: Mathematical models involving intratumoral Treg dynamics**. ADT – Androgen Deprivation Therapy, ODE – Ordinary differential equations, TNBC – Triple Negative Breast Cancer.

| Author | Model type | Research goal | Research Outcome |
|---|---|---|---|
| Peng et al. (2016) | ODE | Assess the effect of ADT and Treg depletion combination on prostate cancer treatment. | Treg depletion and ADT combination has a beneficial effect towards treatment. |
| Wang et al. (2020c) | ODE | Conduct a virtual clinical trial in which TNBC patients receive different drugs and identify biomarkers that predict positive outcomes. | High intratumoral effector T cell densities and high ratios of effector T cells to Tregs predict positive outcomes. |
| Ma et al. (2020) | ODE | Conduct a virtual clinical trial involving colorectal cancer patients receiving Bispecific T cell engagers. | The model can be used to predict patient-level responses to Bispecific T cell engagers. |
| Coletti et al. (2020) | ODE | Model the therapeutic effect of seven different drugs in treating prostate cancer in a mouse model. | The combination of immune check point inhibitors and cancer vaccines confers the greatest therapeutic benefit. |
| Ji et al. (2023) | ODE | Model the impact of Treg depletion and the enhancement of CD8 T cell effector function after the administration of anti-GITR immunotherapy in CT26 and A20 (B cell lymphoma) tumour models. | The model can reasonably recapitulate observed Treg and CD8 T cell dynamics, serum concentrations of anti-GITR and can be used to aid the further development of anti-GITR immunotherapy. |

### 1.7.2 Elusive markers – Differences between resident and transient Tregs

Single cell or bulk RNA sequencing are some of the approaches that are applied to identify genes that are upregulated on cells of interest. Following similar approaches, studies that focus on identifying therapeutic markers to target tumour Tregs often compare Tregs in the tumour with Tregs in healthy tissue (Plitas et al., 2016; Magnuson et al., 2018). Although this approach can provide valuable information, it assumes that tumour Tregs are a homogeneous population and does not account for dynamically distinct Treg subpopulations within the tumour. This implies that markers associated with tumour Tregs may be confounded by markers present on Treg subsets that are only transiently present in the tumour. Ultimately, this can result in the development of Treg-targeting therapies that are not specific to tumour-resident Tregs but can also impact tumour-transient Tregs that migrate to other tissue.

Photoconvertible mouse models such as Kaede or KikGR mice can be used to isolate tumour-resident, transient, and newly arriving Tregs (Ikebuchi et al., 2021; Li et al., 2022). scRNA-seq can then be used to identify markers that differ between these Treg subsets with greater confidence.

### 1.7.3 Knowledge gap in biological differences between resident and transient Tregs

Due to the paucity of studies that look at resident and transient tumour Tregs, there is a knowledge gap in the biological pathways that differ between the two Treg subpopulations. The few studies that have applied photoconvertible mouse models to investigate intratumoral Treg subpopulations suggest that resident Tregs are more immunosuppressive in contrast to transient or newly arriving Tregs (Ikebuchi et al., 2021; Li et al., 2022). Furthermore, Tregs enriched in 4T1 tumours after systemic Treg depletion were found to be hypoproliferative (Lauder et al., 2020, 2021).

Metabolic remodelling is a key hallmark of cancer. The tumour microenvironment is characterised by nutrient deficiency, high acidity, and low oxygen concentration. Previous work has suggested that the metabolic profile of intratumoral Tregs is transformed to improve their fitness and immunosuppressive potential in the tumour (Yan et al., 2022). Generally, oxidative phosphorylation is thought to play a critical role in sustaining the suppressive function of Tregs. Glycolysis is believed to be important in supporting Treg migration, while fatty acid oxidation enables Tregs to proliferate (Yan et al., 2022). Studies with the MC38 tumour model showed that intratumoral Tregs consumed glucose to the same degree as splenic Tregs. Furthermore, tumour Tregs upregulated genes associated with lipid metabolism (Lim et al., 2021). However, how metabolic pathways differ between tumour-resident and transient Tregs has not yet been investigated.

Photoconvertible mouse models, single-cell sequencing, and bioinformatic approaches can be applied to investigate and generate hypotheses about potential biological pathways that differ between tumour-resident and transient Tregs. Understanding these differences can provide key insights towards the development of intratumoral Treg-targeting cancer therapeutics.

### 1.7.4 Tumour, inter-organ and inter-species Treg heterogeneity

Effective intratumoral Treg-targeting requires the identification of markers that are unique to tumour-resident Tregs. Bystander targeting of other immune cell types and Tregs present in other tissue leads to immune-related adverse events (Kurose et al., 2015b; Mahnke et al., 2007). Furthermore, inter-species differences between organisms used in different stages of drug development can confound effective targeting of intratumoral Tregs in humans (Mak et al., 2014). These challenges suggest the need for conducting inter-tumour, inter-organ and inter-species comparisons of Treg markers to identify appropriate therapeutic targets. However, assessing the gene expression patterns of Tregs in different tumours, organs, and species is time-consuming and expensive.

Fortunately, scRNA sequencing has become cheaper over the past decade. As a result, there is a plethora of publicly accessible scRNA-seq data that can be integrated to create large cell-specific meta-atlases that can be used to investigate different biological questions (Nieto et al., 2021; Rocque et al., 2021). Using similar approaches, public scRNA-seq data can be leveraged to create mouse and human Treg meta-atlases, that can then be used to investigate gene expression patterns of Treg markers across different tissue, tumours, and species.

## 1.8 Research questions and hypotheses

The goal of this thesis has been to address the previously mentioned challenges that need to be explored to inform the development of Treg-targeting cancer immunotherapy. In particular, we examined the following research questions:

- Are there tumour-resident and transient Tregs in MC38 and CT26 murine experimental tumour models? If so, what are the trafficking rates associated with these intratumoral Tregs?
- Does tumour heterogeneity affect intratumoral Treg trafficking dynamics? Do Treg trafficking rates and migration profiles differ between MC38 and CT26 tumours?
- Are there transcriptional differences between tumour-resident and transient Tregs, as well as MC38 and CT26 Tregs? More importantly, which molecular markers are upregulated on resident but not transient Tregs?
- Are tumour-resident Treg markers unique to tumour Tregs or they are also expressed on Tregs found in healthy mouse tissue?
- Can we rely on resident Treg markers identified in mice when designing human clinical trials involving tumour Treg-targeting cancer immunotherapy? How translatable are mouse resident Treg markers to human tumour Tregs?

In Chapter 2, we hypothesise that after Tregs infiltrate MC38 and CT26 tumours, some of them are converted into resident Tregs, while others quickly egress out of the tumour as transient Tregs (Fig. 1.7A mechanism 3). We test this hypothesis by fitting a mathematical model of Treg trafficking to datasets derived from Kaede mouse photoconversion experiments.

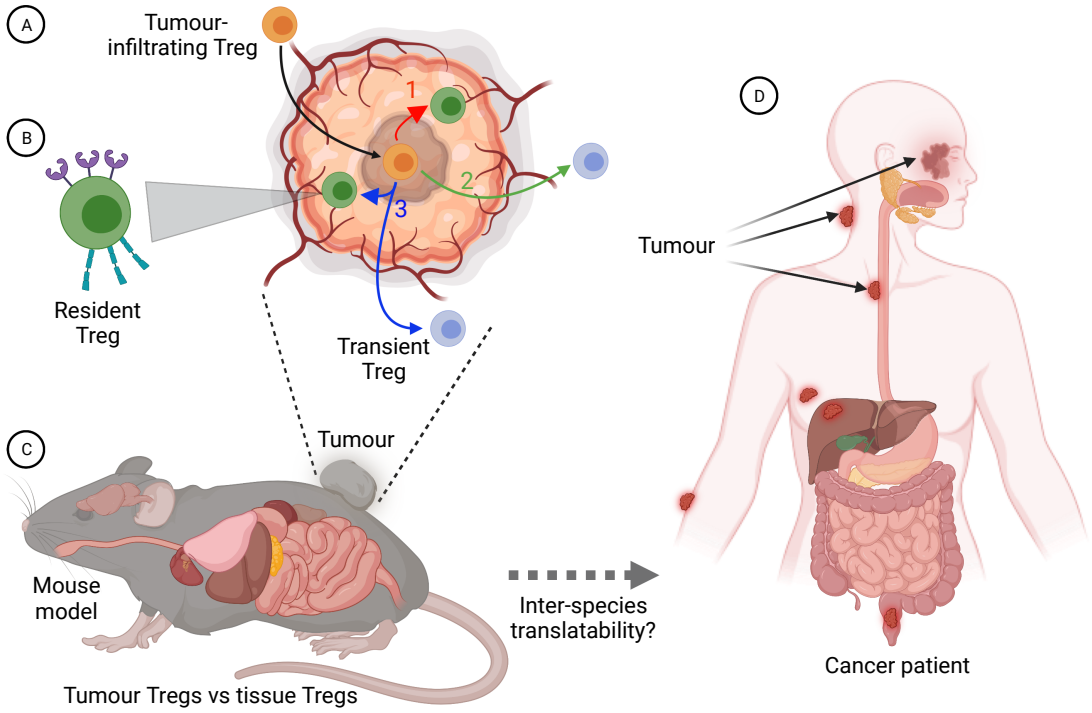



**Figure 1.7: Research questions and hypotheses**. A: Possible mechanisms of intratumoral Treg trafficking. In mechanism 1 (red arrow), all Tregs that infiltrate the tumour remain in the tumour to become resident Tregs (green). In mechanism 2 (green arrow), all Tregs that infiltrate the tumour will egress from the tumour over time. In mechanism 3 (blue arrows), some of the Tregs that infiltrate the tumour become resident while others become transient Tregs (blue) and egress from the tumour over time. B: Molecular markers expressed on resident Tregs. C: Mouse experimental model bearing a subcutaneous tumour, raising the question of whether tumour-resident Tregs differ from healthy tissue Tregs. D: Human cancer patient highlighting the question of inter-species translatability of tumour Treg markers. The figure was created using Biorender.

In Chapter 3, we use scRNA-seq datasets to compare MC38 and CT26, as well as resident and transient Tregs. We hypothesise that Tregs within these two sets exhibit transcriptional differences. In particular, the key aim of Chapter 3 is to bioinformatically explore the biological differences between resident and transient Tregs and ultimately identify therapeutic markers that can be used to deplete/inhibit resident

Tregs (Fig. 1.7B).

In Chapter 4, we hypothesise that, due to Treg heterogeneity across tissue, not all markers that are upregulated on tumour-resident, but not transient, Tregs are unique to tumour Tregs (Fig. 1.7C). Furthermore, due to inter-species differences, potential therapeutic markers identified in mice might not translate well to human tumour Tregs. Therefore, we develop murine and human Treg scRNA-seq meta-atlases to explore the expression characteristics of markers of interest across tumours, organs and species (Fig. 1.7C,D).

## 1.9 Thesis structure and summary

In this chapter, we have given a brief overview of the characteristics of the tumour microenvironment and the role of the immune system in restricting tumour growth. We have highlighted that intratumoral Treg-mediated immunosuppression contributes to the inhibition of anti-tumour immune responses and diminishes the therapeutic benefit of cancer immunotherapy. We have also described specific surface markers on tumour Tregs that have been translated into antibody therapies to target intratumoral Tregs. We finished the chapter by highlighting current challenges associated with targeting intratumoral Tregs, proposing data-driven approaches that can be applied to address some of the challenges and developing hypotheses that we proceed to test in this thesis.

In Chapter 2, we combine mathematical modelling with data from the Kaede experimental mouse system to test whether there are resident and transient Tregs in MC38 and CT26 tumours. Furthermore, we estimate the rates at which transient Tregs egress the tumour and migrate to the tumour draining lymph node (TDLN) and the spleen. Mathematical modelling predicts the presence of resident and transient Tregs in both tumours and suggests that transient Tregs are more proliferative compared to resident Tregs. In addition, we observe dynamical differences in the trafficking behaviour of MC38 and CT26 Tregs, suggesting that Tregs in different tumours may have heterogeneous trafficking profiles.

Chapter 3 builds on the results from Chapter 2. We use internal and publicly available scRNA-seq data to explore gene expression patterns of MC38 and CT26 Tregs, and resident and transient Tregs. We find that CT26 Tregs upregulate markers associated with Treg trafficking to lymph nodes and lymphoid organs in contrast to MC38 Tregs, which explains the observations made in Chapter 2. More importantly, we find that resident Tregs are highly immunosuppressive, responsive to cytokines, metabolically quiescent and, in agreement with the mathematical modelling from Chapter 2, less proliferative than transient Tregs. Furthermore, we identify Lag3, Tnfrsf18 (GITR), Tnfrsf9 (4-1BB) as key surface molecules that are upregulated on resident Tregs.

Chapter 4 further builds on the observations from Chapter 3. With the aim of investigating inter-tissue and inter-species Treg heterogeneity, we construct and analyse mouse and human Treg scRNA-seq meta-atlases. Our analysis reveals that in mice, Lag3 is uniquely expressed in MC38 and CT26 tumour Tregs, while Tnfrsf18 and Tnfrsf9 are also expressed on Tregs in non-lymphoid tissue. However, in humans, we do not observe a high expression of LAG3 in tumour Tregs. Instead, we find that CCR8 is a better marker of human tumour Tregs, suggesting inter-species differences in tumour Treg expression patterns.

Finally, in Chapter 5, we summarise the key findings from this thesis, discuss the implications of our results and propose future directions.

# 2

# Mathematical modelling of intratumoral Treg kinetics

Contents


2.1 Introduction . . . . . 33
2.2 Aims . . . . . 35
2.3 Materials and Methods . . . . . 36
2.4 Results . . . . . 55
2.5 Discussion . . . . . 88


## 2.1 Introduction

Tregs amass in tumours, contributing to the inhibition of beneficial anti-tumour responses (Hiraoka et al., 2006; Curiel et al., 2004). In many tumour types, high Treg densities positively correlate with poor prognoses (Bates et al., 2006; Sasada et al., 2003; Sato et al., 2005). Though promising, attempts at depleting or blocking intratumoral Tregs typically induce severe immune-related adverse events (Mahnke et al., 2007; Kurose et al., 2015b) due to the inadvertent targeting of circulating and tissue-resident Tregs. Thus,

a current challenge in immuno-oncology is to define the safe and effective therapeutic window of efficacy for Treg-targeting immunotherapy (Dees et al., 2021).

Much research has focused on identifying surface markers that are upregulated on intratumoral Tregs which can be used to develop Treg-targeting antibodies (Magnuson et al., 2018; Plitas et al., 2016). However, very little is known about the migration kinetics of intratumoral Tregs. Elucidating the rates at which Tregs accumulate in tumours and whether these Tregs remain resident in the tumour or are dynamic over time can influence Treg-targeting drug administration schedules, dosages and routes. Furthermore, intratumoral Treg migration rates can be used to parameterise Pharmacokinetic and Pharmacodynamic (PKPD) mathematical models for assessing dose-response and identifying the therapeutic window associated with Treg-targeting therapeutics *in silico*.

Up to date, only a handful of studies have investigated intratumoral Treg dynamics. Experimental constraints such as the need to specifically label tumour Tregs and accurately track their movement to other organs over time are some of the reasons for the gap in the field. Using photoconvertible KikGR mice, Ikebuchi *et al.* reported that highly immunosuppressive Tregs remained in MC38 tumours approximately 8 hours after tumour photoconversion (Ikebuchi et al., 2021). Li *et al.* used flow cytometry to quantify Tregs in the tumour, spleen and tumour draining lymph node (TDLN) up to 120 hours post tumour photoconversion using an MC38-implanted Kaede mouse model. Similarly, Tregs that remained in the tumour over time were found to be highly immunosuppressive (Li et al., 2022). However, neither of the studies applied mathematical modelling to quantitatively study intratumoral Treg dynamics in the context of determining Treg trafficking rates.

To our knowledge, there is only one study that determined Treg trafficking rates by fitting an ODE mathematical model to experimental data (Milanez-Almeida et al., 2015). However, this study focused on Treg migration from the thymus to the spleen and lymph node in naive mice (Milanez-Almeida et al., 2015). Therefore, the migration rates of Tregs from the tumour remain unknown. As a consequence, current PKPD studies looking at Treg-immune interactions in the tumour typically describe the accumulation

of Tregs in the tumour without accounting for their egress out of the tumour over time (Sancho-Araiz et al., 2021).

The objective of this study has been to fill the gap in the mathematical understanding of mechanisms underlying intratumoral Treg dynamics and to determine Treg migration rates from the tumour. Motivated by previous work, we hypothesised that there are resident and transient Tregs in both MC38 and CT26 tumour models. Furthermore, because of differences in MC38 and CT26 tumour cell lines, we expected the tumours to give rise to heterogeneous Treg trafficking profiles.

To test these hypotheses, we applied mathematical modelling to temporal Treg datasets. Our results showed that both MC38 and CT26 tumours possess resident and transient Tregs. Additionally, Tregs that leave CT26 tumours accumulate in the TDLN and spleen to a larger extent than MC38 Tregs, indicative of tumour-specific Treg trafficking profiles. Using sensitivity analysis, we showed that the high accumulation of CT26 Tregs in the TDLN and spleen is due to Treg trafficking rates to these organs which are, on average, higher in the CT26 than in the MC38 mathematical model.

## 2.2 Aims

In summary, the aims of this study were as follows:

- Test whether there are tumour-resident and transient Tregs in MC38 and CT26 tumour models through applying mathematical modelling to data that was generated by collaborators using the photoconvertible Kaede experimental mouse model.
- Investigate whether different tumours are predicted to induce heterogeneous Treg trafficking profiles.
- Determine the rates at which Tregs are predicted to migrate out of the tumour to the TDLN, spleen and other organs.

## 2.3 Materials and Methods

### 2.3.1 Kaede mouse model experiments

To study intratumoral Treg trafficking dynamics, we needed an animal model that allowed us to label Tregs originating from the tumour and quantify them as they egressed to other organs over time. Simultaneously, tumour-originating Tregs that accumulated in selected organs needed to be distinguished from tissue-resident Tregs and similarly quantified. Measuring these Treg numbers is essential for creating temporal datasets from which intratumoral Treg trafficking rates can be inferred. However, setting up an experiment that satisfies all these conditions is extremely cumbersome. This is potentially the reason why, to our knowledge, there has been no study that has quantified intratumoral Treg migration rates up to date.

In our study, our collaborators at the University of Birmingham (David Withers' laboratory) made use of the photoconvertible Kaede mouse model to label and quantify Tregs migrating from MC38 and CT26 murine tumours to the inguinal lymph node (TDLN) and the spleen. These mice express a transgenic protein known as Kaede that was cloned from a stony coral species called *Trachyphyllia geoffroyi* (Ando et al., 2002). The protein contains a green chromophore marked by a $\text{His}^{62} - \text{Tyr}^{63} - \text{Gly}^{64}$ tripeptide that can be irreversibly excited to a red chromophore by UV/violet radiation (350-400 nm) (Mizuno et al., 2003).

During the early 2000s, the Kaede complimentary DNA (cDNA) was cloned and transduced into neurons. Upon irradiation with violet light, the red variant of the protein diffused throughout the cytosol and spread to the dendrites, allowing for high resolution visualisation of the neuron under a microscope (Ando et al., 2002). Both the green and red variants were found to be resistant to pH variations and biologically inert. Therefore, the transduction of Kaede into cells is not expected to have drastic effects on normal cellular processes and gene expression (Ando et al., 2002; Li et al., 2022).

Tomura *et al.*, generated Kaede transgenic mice in a C57BL/6 background and used them to study steady-state T cell dynamics in the inguinal lymph node (Tomura et al., 2008). In their study, they photoconverted organs of interest by making small surgical incisions and briefly irradiating them with violet light before closing up the wound. Over time, they sacrificed the mice, homogenised the lymph nodes and quantified the Kaede red lymphocytes using flow cytometry (Tomura et al., 2008).

Following a similar procedure, our collaborators injected either approximately 250 000 MC38 or CT26 cancer cells in the left flanks of Kaede mice. After 11 days, the tumours became palpable and were irradiated with violet light. At 24, 72 and 120 hours post tumour photoconversion, the tumours, TDLNs and spleens were resected, crushed and filtered to harvest cells. Anti-Foxp3 and anti-CD4 antibodies were used to mark Tregs, and flow cytometry was applied to quantify red and green Tregs from the respective organs.

In the MC38 tumour-implanted group, two separate experiments were conducted, one focusing on the photoconversion of the tumour while in the other, the TDLN was photoconverted. In the CT26 group, only the tumours were photoconverted, in part, due to the time-consuming and laborious nature of the Kaede experiments. Figure 2.1 summarises both the biology of the Kaede model and the experimental setup.

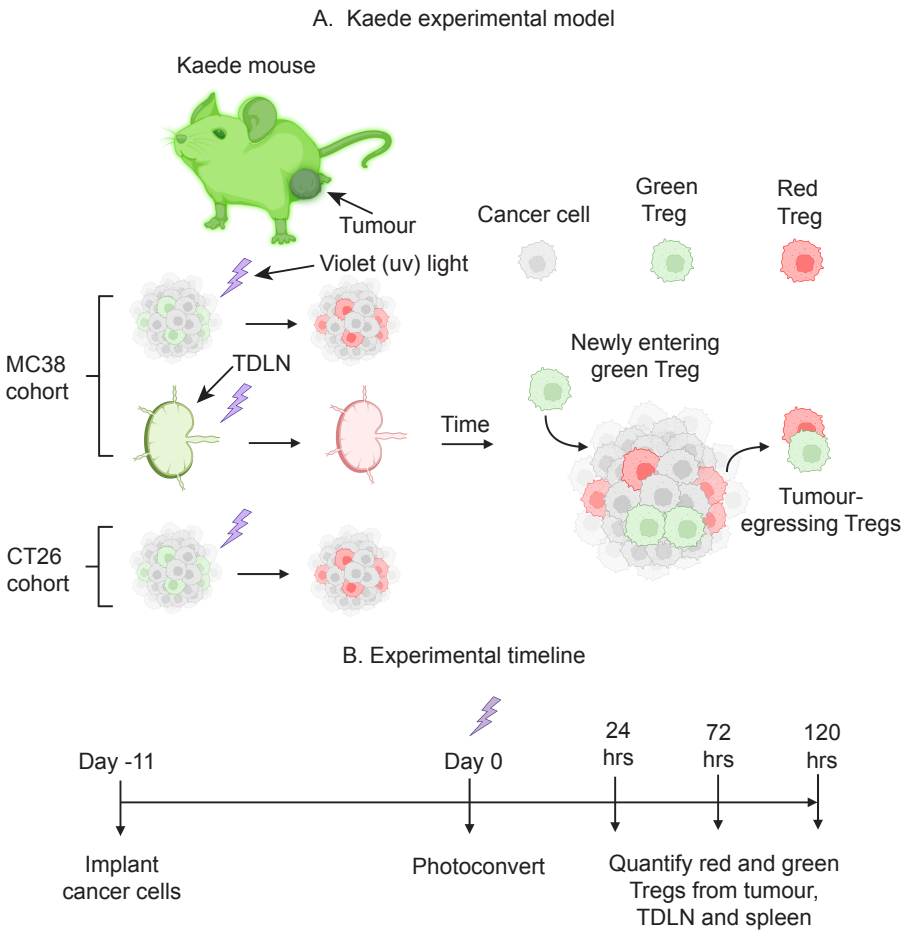



**Figure 2.1: Kaede model experimental set up**. A: The MC38-implanted mouse cohort was split into two groups, each receiving either tumour or TDLN photoconversion respectively. Mice inoculated with CT26 cell lines only had their tumours photoconverted. Note that the cancer cell lines do not express the Kaede protein but are infiltrated by Kaede-expressing host cells as the tumour grows. B: The experimental timeline. At the beginning of the experiment, either MC38 or CT26 cancer cells were implanted in the Kaede mice. Photoconversion occurred 11 days after tumour inoculation. Cell samples were collected from the mice in the tumour, TDLN and spleen at 24, 72 and 120 hours post photoconversion. The figure was created using Biorender.

### 2.3.2 Structural identifiability assessment

To test our hypothesis about the presence of tumour-resident and transient Tregs and to infer the rates at which transient Tregs leave the tumour, we resorted to mathematical modelling using ODEs. The development of the mathematical model is illustrated iteratively along with a qualitative overview of the data in the Results section.

Depending on the complexity of the mathematical model and the resolution of the observed data, it may be impossible to estimate some parameters through fitting the model to the data. When this happens, these parameters are said to be practically unidentifiable. To avoid creating unidentifiable mathematical models, we iteratively performed structural identifiability assessments throughout the development of the mathematical model. This refers to the analysis of the mathematical model to ascertain whether the structure/complexity of the model enables us to reasonably approximate (identify) all unknown parameters given observed data of sufficient quality and resolution (Castro and de Boer, 2020), which is necessary (but not sufficient) for practical identifiability.

Structural identifiability is broken down into global and local identifiability. When a mathematical model is globally identifiable, one unique parameter set can be estimated from the data. On the other hand, a locally identifiable model has multiple parameter combinations or sets that are able to fit the same data set (Castro and de Boer, 2020). Having multiple sets of possible parameter combinations can confound parameter comparison across different experiments. Since we intended to compare Treg trafficking rates from MC38 and CT26 tumours, it was critical for us to develop mathematical models that were complex enough to capture the underlying biological mechanism of Treg trafficking from the tumour yet simple enough to be globally practically identifiable given our limited data.

In this study, we used two different methods to conduct structural identifiability tests. The first method was COMBOS, which uses differential algebra and symbolic computations to determine combinations of identifiable model parameters (Meshkat et al., 2014).

Though the underlying mathematical theory is complex, COMBOS offers a fast and simple web application that allows users to encode the mathematical model, observed variables and parameters (http://biocyb1.cs.ucla.edu/combos/). It then lists parameters and parameter combinations that are structurally identifiable. COMBOS allowed us to quickly assess candidate models leading up to the globally structurally identifiable models presented here. However, to mathematically demonstrate the structural identifiability of the mathematical models used in this study, we made use of a recently developed simple, yet powerful scaling method (Castro and de Boer, 2020). Below, we briefly describe how this method works.

### Structural identifiability analysis using the method of scaling

The method of scaling transformations takes advantage of the fact that there is a direct link between a mathematical model's structural identifiability and the linear dependence of the columns of the model's sensitivity matrix (Jaqaman and Danuser, 2006). For instance, if the sensitivity columns of a pair of model parameters are linearly independent, then the parameters are identifiable. The converse is true.

Suppose we have a mathematical model denoted as:

$$\begin{aligned} \frac{dx_i}{dt} &= f_i(x_1, ..., x_r, x_{r+1}, ..., x_n; \lambda_i, ..., \lambda_m) \qquad i = 1, ..., n, \\ x_i(0) &= x_{i,0} \qquad i = 1, ..., n, \end{aligned} \tag{2.1}$$

where $x_i$ refers to individual ODEs for the dynamical variables in the model, $x_1, ..., x_r$ are the observed/measured variables, $x_{r+1}, ..., x_n$ are the unobserved variables, $x_{i,0}$ are the associated initial conditions and $\lambda_i, ..., \lambda_m$ are the parameters of the model (Castro and de Boer, 2020). Each function, $f_i$, is split into M additive components, $f_{ik}$, as follows:

$$f_i(x_1, ..., x_r, x_{r+1}, ..., x_n; \lambda_i, ..., \lambda_m) = \sum_{k=1}^{M} f_{ik}(\tilde{x}_k, \tilde{\lambda}_k), \tag{2.2}$$

satisfying the condition that $f_{ik}$ is linearly independent of $f_{il}$ for all $k \neq l$. In this equation, $\tilde{x}_k, \tilde{\lambda}_k$ represent the subset of variables and parameters in $f_{ik}$ (Castro and de Boer, 2020).

Next, we scale all parameters and unobserved variables in Equation 2.2 by positive factors, $u$. For example:

$$\begin{aligned} \lambda_i &\mapsto u_{\lambda_i}\lambda_i \qquad i = 1, ..., m, \\ x_j &\mapsto u_{x_j}x_j \qquad j = r+1, ..., n. \end{aligned} \tag{2.3}$$

Each linearly independent function, $f_{ik}$, is then equated to its scaled version:

$$f_{ik}(\tilde{x}, \tilde{\lambda}) = \frac{1}{u_{x_i}} f_{ik}(u_{\tilde{x}}\tilde{x}, u_{\tilde{\lambda}}\tilde{\lambda}). \tag{2.4}$$

and the set of solutions of $u$ that leave the system invariant are determined. Every parameter, $\lambda_i$, with only one solution, $u_i = 1$, is then considered to be structurally identifiable (Castro and de Boer, 2020).

Using this method, we illustrate the structural identifiability of the Kaede Treg trafficking mathematical model in more detail in the Results section as part of our iterative model development strategy. While we do not directly assess practical identifiability in this section, structural identifiability lends confidence to our ability to estimate parameters and thus fit the model and data.

### 2.3.3 Indirect assessment of practical identifiability

While structural identifiability assesses whether the structure of the mathematical model allows for parameter inference, practical identifiability is an assessment of whether the observed data is of sufficient quality to enable precise determination of model parameters (Wieland et al., 2021). Typically, practical identifiability assessment is performed using the Profile Likelihood method before parameter inference is conducted (Wieland et al., 2021). However, in our case, we used Markov Chain Monte Carlo simulations (MCMC) to infer model parameters. MCMC allowed us to visualise the inferred parameters as probability distributions, thereby providing an indirect assessment of the extent to which we were able to precisely identify the parameters of the mathematical model given the quality of the observed data. Thus, the shape of the parameter distributions and the correlations between parameters meant we could indirectly assess practical identifiability without resorting to additional methods such as the Profile likelihood.

### 2.3.4 Bayesian parameter inference

To fit our ODE model to experimental data and to approximate unknown parameters, we resorted to MCMC within the framework of Bayesian estimation. MCMC constitutes a class of probabilistic parameter inference approaches that take into account the variability within experimental data to infer mathematical model parameters as probability distributions. In contrast to other parameter estimation approaches such as sum of squares fitting, MCMC quantifies the level of uncertainty associated with parameters, which is highly informative when working with noisy datasets such as our own.

There are different types of MCMC algorithms that are commonly used to infer model parameters. These include Random Walk Metropolis (Metropolis et al., 1953), Metropolis-Hastings (Hastings, 1970), Adaptive Covariance Markov Chain Monte Carlo (ACMC) (Haario et al., 2001), Hamiltonian Monte Carlo (Duane et al., 1987) and Gibbs Sampling (Geman and Geman, 1984). At their core, they make use of Bayesian statistics to infer model parameters by updating prior hypotheses about the parameters as more data becomes available. Over time, this approach generates probability distributions known as posteriors, which effectively represent model parameter distributions.

Using Bayes' theorem, the conditional probability of model parameters, $\Psi$, given observations, $y$, is denoted as:

$$P(\Psi|y) = \frac{P(y|\Psi)P(\Psi)}{P(y)}. \tag{2.5}$$

In this formula, $P(\Psi|y)$ is typically referred to as the posterior, and is a random variable that reflects the parameters of the model given the observations. $P(y|\Psi)$, the likelihood, is the joint probability of the observed data as a function of model parameters (Lambert, 2018). $P(\Psi)$ is the prior distribution that highlights our prior belief about the distribution of each parameter. Finally $P(y)$ is the evidence, a marginal distribution that normalises the product of the likelihood and prior to make it a valid probability distribution that adds up to 1.

For continuous parameter distributions, $P(y)$ is very difficult to calculate and becomes intractable as the number of model parameters increases (Lambert, 2018). To determine $P(y)$, we have to compute a multidimensional integral depicted below:

$$P(y) = \int_{all\ \Psi_1} ... \int_{all\ \Psi_n} P(y, \Psi_1, ..., \Psi_n) d\Psi_1 ... d\Psi_n, \tag{2.6}$$

for a total of $n$ model parameters. Fortunately, MCMC avoids having to calculate this integral by constructing a Markov chain which stochastically samples from a probability distribution that is proportional to the target distribution:

$$P(\Psi|y) \propto P(y|\Psi)P(\Psi). \tag{2.7}$$

With each iteration, MCMC generates a new candidate distribution describing where the chain may move next based on its current position in parameter space. The proposed transition distribution is then accepted or rejected based on a set of criteria that depend on the specific type of MCMC algorithm being run. Over a number of iterations, the Markov chain converges to an invariant distribution and the history of accepted distributions is used to build a histogram, which is a good approximation of the actual posterior distribution.

### Adaptive Covariance Markov Chain Monte Carlo

Specifically, we used the Adaptive Covariance Markov Chain Monte Carlo (ACMC) (Haario et al., 2001) algorithm implemented in the PINTS package (Clerx et al., 2018) to fit the mathematical model to the observed data. PINTS is a comprehensive Python library that implements many algorithms and can be used to infer parameters from noisy datasets (Clerx et al., 2018). We also made use of Chi, a Python PINTS plugin that was developed for PKPD modelling, to preprocess our data for parameter inference (Augustin, 2021). The mathematical models were then written using the Systems Biology Markup Language (SBML) level 3 version 2, a universal mathematical model writing language that facilitates reproducible model sharing (Hucka et al., 2019).

ACMC is a modification of the Random Walk Metropolis algorithm outlined in Algorithm 1. The acceptance ratio, $r$ is the ratio between the products of the likelihood and prior for current and proposed distributions.

**Algorithm 1: Random Walk Metropolis algorithm**. Here, $\theta$ refers to the parameter distribution while N is the total number of iterations run. $J(\theta^*|\theta_{i-1})$ is a conditional probability distribution describing the next proposed parameter distribution $\theta^*$ given the previous distribution $\theta_{i-1}$ (Lambert, 2018). r is the acceptance ratio that determines whether the proposed distribution will be accepted or not. $U[0,1]$ refers to a uniform distribution ranging from 0 to 1.

Select starting point $\theta_0$
**for** $i \leftarrow 1$ *to* $N$ **do**
  Propose $\theta^* \sim J(\theta^*|\theta_{i-1})$
  Calculate $r = \frac{p(\theta^*|y)}{p(\theta_{i-1}|y)}$
  **if** $r \geq 1$ **then**
    Accept $\theta^*$ and set $\theta_i \leftarrow \theta^*$;
  **else**
    Draw $\alpha \sim U[0,1]$
    **if** $r \geq \alpha$ **then**
      $\theta_i \leftarrow \theta^*$
    **else**
      $\theta_i \leftarrow \theta_{i-1}$
    **end**
  **end**
**end**

ACMC works in a similar way as the Random Walk Metropolis. However, the key difference lies in how ACMC proposes candidate distributions. By definition, Random Walk Metropolis relies on the current position of the chain to determine where it will move next. In contrast, ACMC uses prior knowledge of all the regions in the parameter space that the chain has explored before to propose where it will move next. This adaptive nature results in improved searches within parameter space, leading to fewer function evaluations and quicker chain convergence (Haario et al., 2001). As a result, ACMC is non-Markovian although it still satisfies the ergodicity properties of a typical MCMC simulation (Haario et al., 2001).

Here, we briefly describe how ACMC adapts the search. Suppose at iteration $n-1$, the states sampled by ACMC are $X_0, ..., X_{n-1}$, where $X_0$ is the first state after a chosen

warm-up time. The proposed distribution for the next iteration, $X_n$, is sampled from a Gaussian distribution centered at $X_{n-1}$ with a covariance of $s_d R$. $R$ is the covariance matrix that is calculated from the history of the previously explored distributions of states $X_0, ..., X_{n-1}$. $s_d$ is a scalar that depends on the dimension, $d$, of the covariance matrix (Haario et al., 2001). $s_d$ is set to $\frac{2.4^2}{d}$ (Haario et al., 2001; Gelman et al., 1996).

To initiate the sampling, an arbitrary initial covariance denoted by $C_0$ is applied for an initial warm-up period of time of $t_0$. The covariance at any given time becomes:

$$C_t = \begin{cases} C_0 & t \leq t_0, \\ s_d \text{cov}(X_0, ..., X_{t-1}) + s_d \varepsilon I_d & t > t_0, \end{cases} \tag{2.8}$$

where $\varepsilon$ is a small positive scaling factor and $I_d$ is an identity matrix of dimension $d$ (Haario et al., 2001). Explicitly, $R$ is calculated as:

$$\begin{aligned} R &\equiv \text{covariance matrix of } X_0, X_1, ..., X_t \in \mathbb{R}^d, \\ R &= \text{cov}(X_0, ..., X_t), \\ R = \frac{1}{t}(\sum_{i=0}^{t} X_i X_i^\top - (t+1)\overline{X}_t \overline{X}_t^\top), &\text{ where } \overline{X}_t = \frac{1}{t+1}\sum_{i=0}^{k} X_i. \end{aligned} \tag{2.9}$$

### Setting up parameter inference for the Kaede mathematical model

Two of the most popular paradigms for Bayesian parameter inference are pooled and hierarchical models. In the context of our red Treg dataset, a hierarchical model would infer both individual mouse and population level parameters. This requires hierarchical data consisting of Treg counts per mouse across the observed time scale. Unfortunately, the Kaede experiments require individual mice to be sacrificed to obtain red Treg counts per time point. Thus, we do not observe Treg dynamics in the same mouse across time. As a result, we consider a pooled model over a hierarchical model. The pooled model considers average Treg counts across different mice per time point and infers sample-level parameters.

To set up parameter inference, we started off with the Kaede Treg trafficking mathematical model denoted as a system of ODEs, $\frac{dx}{dt}$, and the initial conditions:

$$\begin{aligned} \frac{dx}{dt} &= f(x, \Psi), \\ x(t = 0, \Psi) &= x_0, \end{aligned} \tag{2.10}$$

where $x \in \mathbb{R}^{\mathcal{D}}$, $\mathcal{D}$ being the number of dynamical variables in the mathematical model while $\Psi$ and $x_0$ represent the set of model parameters and the vector of initial conditions respectively.

In many cases, numerical methods are used to approximate the solution of complex systems of ODEs. We used Myokit, an open source Python package, to solve the system of ODEs (Clerx et al., 2016). For the sake of simplicity, let us assume that our mathematical model can be analytically represented as:

$$x = x(\Psi, x_0, t), \tag{2.11}$$

where the dynamical variable, $x$, can be evaluated at any observed time point, $t$. Suppose the measured values at each time point are represented by $y$, then the expectation of $y$ is defined as:

$$\mathbb{E}(y) = \overline{y}, \tag{2.12}$$

where $\overline{y}$ is the mean at each time point and $y \in \mathbb{R}^{\mathcal{D}}$, for $\mathcal{D}$ compartments/organs. Assuming our mathematical model approximates the biological process underpinning the observed Treg counts, we let the mean of the measured Treg counts at each time point be denoted by:

$$\overline{y} = x(x, \Psi, x_0, t). \tag{2.13}$$

The data acquisition process introduces some variability which could arise from systematic and random errors as well as inter-individual differences across mice. Furthermore, as can be observed from the raw Treg data, time points with greater Treg numbers are also associated with larger variations than time points with low Treg counts. To model

some of this variation, we used a multiplicative error model that scales with the size of the observations. We defined the error model, $\sigma$, as follows:

$$\begin{aligned} \sigma &= \sigma_{base} + \sigma_{rel} \cdot \overline{y}, \\ y = \overline{y} + \sigma \cdot \varepsilon &= \overline{y} + (\sigma_{base} + \sigma_{rel} \cdot \overline{y}) \cdot \varepsilon, \end{aligned} \tag{2.14}$$

where $\varepsilon \sim \mathcal{N}(0, 1)$ and $\overline{y}$ is the mean Treg count at each time point. $\sigma_{base}$ is the base-level precision associated with the measuring instrument. This can also be interpreted as the lowest threshold of Treg counts that the measuring technique can confidently quantify. On the other hand, $\sigma_{rel}$ is the relative error that scales with the size of the measured Treg counts. It can also be referred to as the multiplicative error. Thus, we effectively assumed that the variation at very low cell numbers is $\sigma_{base}$ with an additional multiplicative error model characterised by $\sigma_{rel}$.

In particular, observed cell numbers are relatively large, and an observed trend is that the measurement fluctuation increases with cell number. Hence, the noise associated with the small additive term $\sigma_{base}$ will not significantly feature compared to $\sigma_{rel}$. Furthermore, the scale of $\sigma_{base}$ is assumed small compared to the observed cell numbers in general. Thus, while $\sigma_{base}$ has been set to unity in the ACMC simulation, we do not anticipate that it will have a noticeable effect, as can be confirmed a posteriori. Nonetheless, $\sigma_{base}$ has been included in the model as its absence would suggest that the flow cytometer, which was used to quantify Treg counts, makes perfect measurements for low numbers of Tregs, which is unlikely. We also observed that setting the value of $\sigma_{base}$ to 0 disrupts the evaluation of the log-likelihood function in cases where the initial model prediction was zero such as the TDLN and spleen post tumour photoconversion as can be seen in Equation 2.20. Finally, note that the observed data with this model is normally distributed, with $y \sim \mathcal{N}(\overline{y}, \sigma^2)$.

Applying Bayes' Rule, we have:

$$P(\Psi, \sigma_{rel}|y) = \frac{P(y|\Psi, \sigma_{rel})P(\Psi; \sigma_{rel})}{P(y)} \tag{2.15}$$

where $P(\Psi, \sigma_{rel}|y)$ is the posterior distribution of the parameters, $P(y|\Psi, \sigma_{rel})$ is the likelihood, $P(\Psi; \sigma_{rel})$ is the prior and $P(y)$ is the marginal probability of observing

the evidence/data. As discussed earlier, ACMC does not evaluate $P(y)$ as this is treated as a normalising constant. Thus, the final equation linking the posterior to the prior and likelihood can be simplified to:

$$P(\Psi, \sigma_{rel}|y) \propto P(y|\Psi, \sigma_{rel})P(\Psi; \sigma_{rel}), \tag{2.16}$$

and the likelihood, assumed to be described by a Gaussian distribution, can be explicitly written as:

$$\begin{aligned} P(y|\Psi, \sigma_{rel}, t) &= \frac{1}{\sigma\sqrt{2\pi}} e^{\frac{-(y-\overline{y})^2}{2\sigma^2}}, \\ \sigma &= \sigma_{base} + \sigma_{rel} \cdot \overline{y}, \end{aligned} \tag{2.17}$$

where $\overline{y}$ is a function of $\Psi$ and $t$. Assuming that the $N$ data points in the data set $D = \{y_i, t_i\}_{i=1}^{N}$, are independent because they come from different mice, the likelihood becomes:

$$\mathcal{L} = \prod_{i=1}^{N} P(y_i|\Psi, \sigma_i; t_i). \tag{2.18}$$

Note that $\sigma = \sigma_{base} + \sigma_{rel}.\overline{y}$, so it has $\overline{y}$ dependence and is also indexed by $i$, discrete in time, via $\sigma_i$ as given above. For convenience, we log transform the likelihood function to get a log-likelihood which can be written as a sum:

$$\mathcal{LL} = \sum_{i=1}^{N} \log(P(y_i|\Psi, \sigma_i; t_i)). \tag{2.19}$$

Thus, the final form of the log-likelihood function for $\mathcal{D}$ dynamical variables or compartments in the Kaede mathematical model becomes:

$$\mathcal{LL} = -\sum_{d=1}^{\mathcal{D}} \sum_{i=1}^{N} \frac{1}{2} \log(2\pi\sigma_{i,d}^2) + \frac{(y_{i,d} - \overline{y}_{i,d})^2}{2\sigma_{i,d}^2}. \tag{2.20}$$

By evaluating the sum of the log-likelihood and log-prior, ACMC samples from the posterior distribution and allows us to then approximate the parameters associated with the Kaede mathematical model.

In our analysis, we assigned 5 Markov chains that were randomly initiated at different starting points within uniform prior parameter distributions that we predefined. We ran

ACMC for a total of 200 000 iterations, and used the final 50 000 samples as the final posterior samples. We assessed chain convergence using the Gelman-Rubin convergence statistic also known as $\hat{R}$ (Gelman and Rubin, 1992). This is a diagnostic metric that compares inter- and intra-chain mixing, giving us a quantitative measure of whether the post warm-up ACMC iterations have sufficiently sampled the parameter space and reached an invariant distribution that approximates the posterior distribution. $\hat{R}$ values significantly larger than 1 flag situations in which independent Markov chains fail to mix well, resulting in an improperly sampled parameter distribution. All $\hat{R}$ values that we obtained were less than 1.03, indicative of sufficient chain mixing.

### 2.3.5 Sensitivity analysis with eFAST

In this section, we discuss how we performed sensitivity analysis. The presentation of this section is extensively based on Saltelli et al. (1999) and Marino et al. (2008).

Sensitivity analysis is a method that is used to assess the relative importance of parameters in a mechanistic model. Generally, there are two different measures of sensitivity namely local and global sensitivity. Local sensitivity analysis quantifies how small changes around a fixed parameter value affect the model output. To determine the local sensitivity of a model denoted by $y = g(x_1, ..., x_n)$ for $n$ parameters, with respect to the parameter $x_1$, a small change $\Delta x_1$ is taken while holding other parameters fixed. Following model simulation, local sensitivity, $S_L$, is calculated as follows:

$$\begin{aligned} S_L &= \frac{x_1}{g}\frac{\partial g}{\partial x_1}(x_1, ..., x_n) \\ &\approx \frac{\frac{\Delta g}{g}}{\frac{\Delta x_1}{x_1}}. \end{aligned} \tag{2.21}$$

On the other hand, global sensitivity analysis quantifies the overall effect of the interplay between variations across a given parameter and all model parameters. Mathematically, the global sensitivity of $x_1$ on the outputs can be expressed as follows:

$$\frac{\mathsf{Var}_{x_1}[\mathbb{E}(y|x_1)]}{\mathsf{Var}(y)}, \tag{2.22}$$

where $\mathbb{E}(y|x_1)$ is the expectation of $y$ conditioned on $x_1$ and $\text{Var}_{x_1}$ is the variance taken over all possible values of $x_1$ (Saltelli et al., 1999).

Given considerable uncertainty associated with parameters in biological models, global sensitivity analysis is more quantitatively appropriate than local sensitivity analysis (Marino et al., 2008). Therefore, in our study, we made use of the extended Fourier Amplitude Sensitivity Test (eFAST) (Saltelli et al., 1999, 2004; Saltelli and Bolado, 1998), a global sensitivity analysis method which is an extension of the original FAST method (Cukier et al., 1973).

eFAST makes use of a variance-based decomposition approach to determine sensitivity (Marino et al., 2008). The variation is quantified in a way analogous to variance which is defined as:

$$s^2 = \frac{\sum_{i=1}^{N}(y_i - \overline{y})^2}{N-1}, \tag{2.23}$$

where N is the sample size or the number of times the model is run, $y_i$ is the $i^{th}$ model output and $\overline{y}$ is the sample mean. Once the variance is calculated, eFAST determines the fraction of the variance that can be explained by varying each parameter. This is achieved through sampling parameters at different frequencies and using Fourier analysis to measure the extent to which each parameter's frequency contributes to the model output which then defines the model's sensitivity to that parameter (Marino et al., 2008).

To sample the parameter space at different frequencies, eFAST defines an approximately space-filling sinusoidal search curve, $f$, at a different frequency for each model parameter, $x$. It then creates $N_s$ samples of the given parameter as indicated below:

$$x = f(j), j = 1, 2, ..., N_s. \tag{2.24}$$

Repetitions in parameter samples due to the periodicity of the search curve are avoided by re-sampling the parameters $N_R$ times at a randomly phase-shifted frequency for each parameter. The search curve becomes explicitly defined as:

$$x = \frac{1}{2} + \frac{1}{\pi}\arcsin(\sin(\omega s + \phi)), \tag{2.25}$$

where $\phi$ is a random phase shift that is uniformly distributed in the interval $[0, 2\pi]$ and $s$ is a scalar variable varying over $-\pi < s < +\pi$ (Saltelli et al., 1999). Thus, the total number of simulations that are done equate to $N = N_s \cdot k \cdot N_R$, where $k$ is the number of model parameters plus a dummy variable (Marino et al., 2008).

eFAST simultaneously calculates the first and total-order sensitivity indices for each parameter whereas FAST determines the former. The first-order sensitivity is depicted by $S_i$ and describes how a given parameter influences the model output excluding the effects imposed by interactions with other parameters. To calculate the $S_i$, eFAST determines the $r^{th}$ moment of the model which will be used to calculate the variance. For positive frequency values, Cukier et al.(Cukier et al., 1973) determined that the $r^{th}$ moment of the model is:

$$\overline{y}^{(r)} = \frac{1}{2\pi}\int_{-\pi}^{\pi} g^r(x)dx, \quad \text{where} \quad y = g(x). \tag{2.26}$$

Therefore the variance, $s^2_{total}$, can be inferred as:

$$\begin{aligned} s^2_{total} &= \overline{y}^{(2)} - (\overline{y}^{(1)})^2, \\ &= \frac{1}{2\pi}\int_{-\pi}^{\pi} g^2(x)dx - [\frac{1}{2\pi}\int_{-\pi}^{\pi} g(x)dx]^2, \end{aligned} \tag{2.27}$$

where $y = g(x)$, with $x$ representing the sampled model parameters.

The model output, $g(x)$, can then be expanded using Fourier series:

$$y = g(x) = \sum_{j=0}^{+\infty} A_j \cos jx + B_j \sin jx, \tag{2.28}$$

where the Fourier coefficients $A_j$ and $B_j$ are defined as:

$$\begin{aligned} A_j &= \frac{1}{2\pi}\int_{-\pi}^{\pi} g(x)\cos(jx)dx, \\ B_j &= \frac{1}{2\pi}\int_{-\pi}^{\pi} g(x)\sin(jx)dx, \end{aligned} \tag{2.29}$$

for integer frequencies of $j$ in range $[0, +\infty)$. The power spectrum of the Fourier series for frequency $j$, depicted as $\Lambda_j$, is then calculated as:

$$\Lambda_j = A_j^2 + B_j^2. \tag{2.30}$$

The total variance, $s^2_{total}$, can be approximated by summing up the power spectrum as:

$$s^2_{total} = \sum_{j=1}^{+\infty} \Lambda_j. \tag{2.31}$$

The partial variance, $s^2_i$, arising from the uncertainty in the $i^{th}$ parameter at a frequency of $j$ and its higher order harmonics can then be determined as follows:

$$s^2_i = \sum_{j,2j,3j,\ldots} A^2_j + B^2_j. \tag{2.32}$$

The first-order sensitivity index is calculated as follows:

$$S_i = \frac{s^2_i}{s^2_{total}}. \tag{2.33}$$

The total-order sensitivity, $S_{Ti}$, denotes how the interactions between a given parameter and other parameters influence the model output. To determine $S_{Ti}$, eFAST calculates the combined sensitivity of all the other parameters excluding the parameter of interest defined as $S_{ci}$ (Marino et al., 2008). For example, $S_{ci}$ associated with the first parameter is determined as follows:

$$S_{c1} = \sum_{j=2,3,\ldots} \frac{s^2_j}{s^2_{total}}. \tag{2.34}$$

Thus, the total-order sensitivity of the parameter of interest is then determined as follows:

$$S_{Ti} = 1 - S_{ci}, \tag{2.35}$$

and accounts for higher-order interactions between the parameter of interest and other parameters in the model (Marino et al., 2008).

After running eFAST, statistical comparisons between sensitivity indices can be implemented using a dummy parameter that does not appear in the model. Though the dummy variable's sensitivity indices are non-zero due to interference effects, they are very low such that other sensitivity indices that are in a similar numerical range are considered to be not significantly different from zero (Marino et al., 2008).

### Adjusting eFAST parameters

eFAST allows the user to specify re-sampling times, $N_R$, and the number of parameters including the dummy variable, $k$. It then calculates the frequency to assign the parameter of interest as:

$$\omega_i = \frac{\frac{N}{N_R} - 1}{2Mk}, \tag{2.36}$$

where $M$ is the maximum number of Fourier coefficients used to calculate the partial variance. This value is typically set to either 4 or 6 (Saltelli et al., 1999). Conversely, the maximum allowable frequency for complimentary parameters, defined to be $\omega_i$ for parameter $i$, is calculated as:

$$\max(\omega_{-i}) = \frac{\omega_i}{2M}, \tag{2.37}$$

and complimentary parameters are allowed to take any frequency values within the interval $[1, \max(\omega_{-i})]$. Finally, the number of samples to create for each parameter is then determined as:

$$N_s = 2 \cdot M \cdot \omega_i + 1, \tag{2.38}$$

with the recommended minimum value of $N_s$ being 65 (Saltelli et al., 1999).

Caution has to be taken when adjusting eFAST parameters. In the original eFAST paper, the authors recommend selecting parameters such that the ratio $\frac{\omega_i}{N_R}$ varies between 16 and 64 (Saltelli et al., 1999). The rationale for this requirement is that if $\omega_i$ is low and $N_R$ is high, sampling will be too diffuse. Conversely, if $\omega_i$ is high and $N_R$ is low, the sampling will be highly concentrated in a local region (Saltelli et al., 1999). Therefore, adjusting parameters such that $\omega_i$ and $N_R$ lie in the permitted region illustrated in Figure 2.2 is recommended.

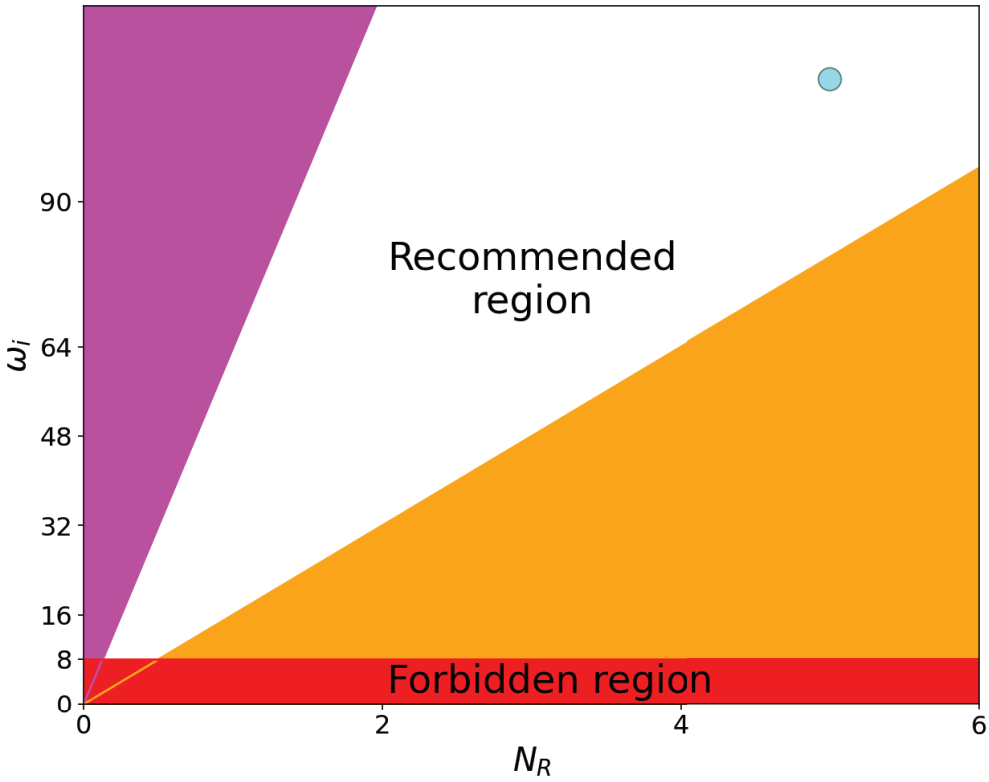



**Figure 2.2: Recommended ranges for selecting the values of $\omega_i$ and $N_R$.** The red region shows the forbidden region while the magenta and orange regions are allowed but not encouraged. Within the recommended region in white, the cyan dot outlines the parameter combination that we used in our sensitivity analyses. Figure reproduced from Saltelli et al. (1999) and ©1999 reprinted by permission of Informa UK Limited, trading as Taylor & Taylor & Francis Group, http://www.tandfonline.com.

### Running eFAST with posterior distributions inferred from the Kaede model

We used the MATLAB implementation of eFAST that was written by Marino *et al.* in their study of HIV dynamics (Marino et al., 2008). The native code assumes that model parameters are uniformly distributed over a small range. However, in our study, we determined model parameters using Markov Chain Monte Carlo simulations. Thus, we substituted the uniformly distributed model parameters in the original eFAST implementation with posterior distributions from our parameter inference.

To accomplish this, we first determined the empirical Cumulative Distribution Function (eCDF) for each parameter distribution. We then used eFAST to draw uniformly distributed samples in the interval $[0, 1]$. Once these were drawn, we mapped them to the

parameter values from the posterior distributions using the eCDFs. Finally, we ran eFAST with $N_R = 5$, $k = 7$ (5 for the CT26 mathematical model), $N_s = 900$, and $M = 4$.

## 2.4 Results

### 2.4.1 Qualitative analysis of experimental data

We performed exploratory data analysis to gain insight on intratumoral Treg dynamics in MC38 and CT26 tumours. These qualitative analyses influenced the structure of the mathematical models that we parameterised with the experimental data.

#### MC38 tumour photoconversion dataset

The first experiment that was conducted involved the photoconversion of MC38 tumours. We refer the reader to Section 2.3.1 for a description of the experiment. Figure 2.3 shows the tumour masses, red and green Tregs that were quantified via flow cytometry from the tumour, TDLN and spleen. Supplementary Figure A.1 illustrates the raw flow cytometry data and the gating strategy that was used. This data was published by our collaborators as part of their *in vivo* intratumoral CD8 T cell dynamics study (Li et al., 2022). However, it has not yet been used in the context of intratumoral Treg migration mathematical modelling.

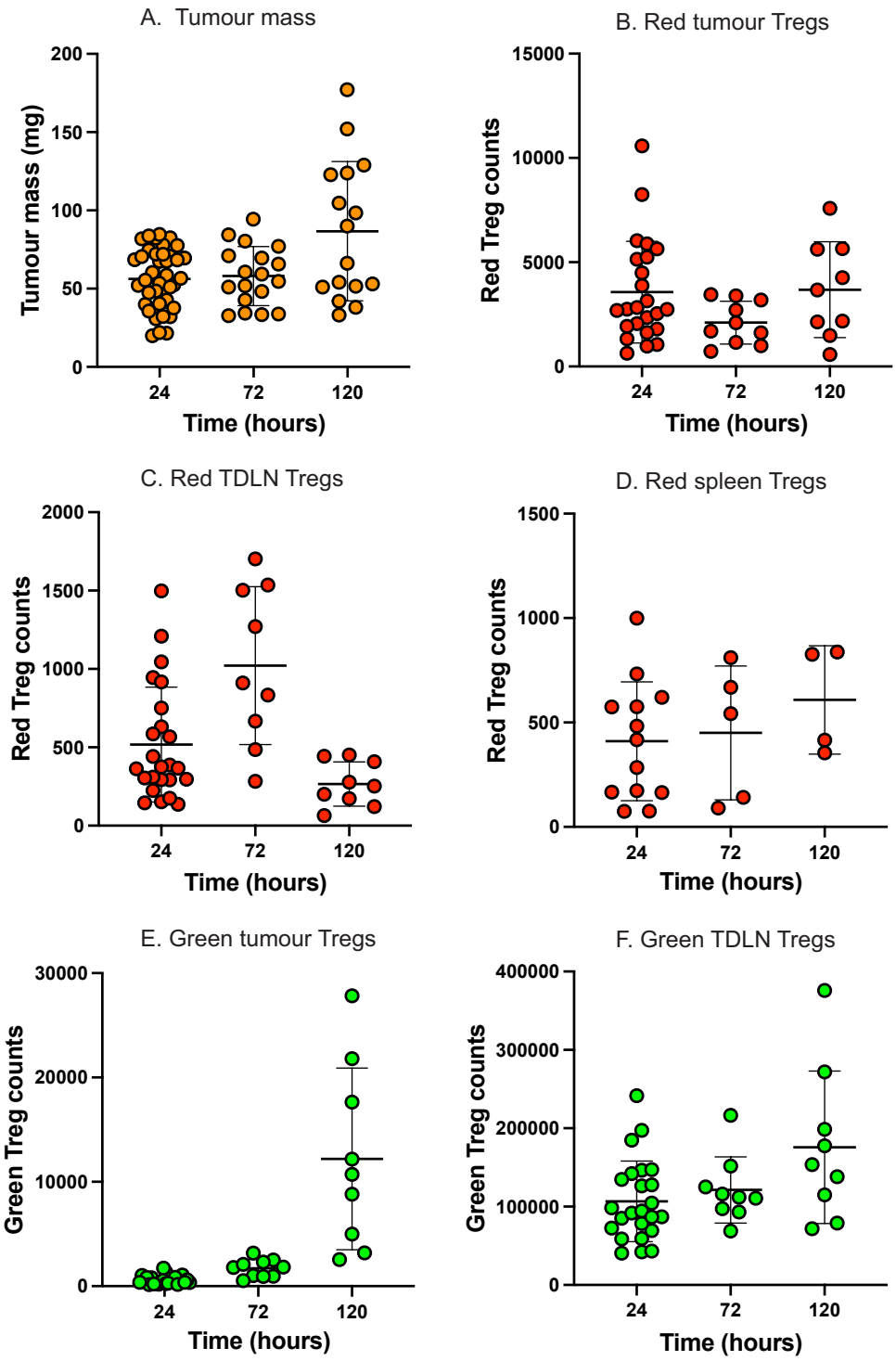



**Figure 2.3: Overview of the MC38 tumour photoconversion dataset**. A: Tumour mass in milligrams. B: Red Treg numbers in the tumour. C: Red Tregs that left the tumour and infiltrated the TDLN. D: Red Tregs that accumulated in the Spleen. E: Green Tregs that accumulated in the tumour after photoconversion. F: Green Tregs that were present in the TDLN. The points depicted here correspond to measurements in independent mice. The origin of the horizontal axis is the time of photoconversion and the rest of the axis refers to hours post tumour photoconversion. Horizontal lines represent the mean and standard deviation. The data set was retrieved from Li et al. (2022).

We observed approximately linear tumour growth dynamics (Fig 2.3A). When we looked at red Tregs in the tumour, we saw unexpected behaviour: Treg numbers appeared to initially drop, only to rise again at the $120^{th}$ hour time point (Fig 2.3B). Such behaviour is less likely to be biological as the Tregs would be required to proliferate at an abnormally high rate contrary to what the single cell data presented in Chapter 3 suggested. Thus, neglecting this $120^{th}$ hour time point for the red MC38 tumour Tregs, we concluded that red Tregs leave the tumour microenvironment over time to populate other organs. In all other datasets, we did not exclude the 120 hour red tumour Treg time point as it did not display drastic variation seen in Figure 2.3B.

We observed that red Tregs exhibited non-monotonic behaviour in the TDLN where their numbers initially rose but fell later in time, indicating a significant egress rate from the TDLN (Fig 2.3C). In contrast, red Tregs exhibited a monotonic increase in the spleen indicative of gradual accumulation over time (Fig 2.3D). Green Tregs steadily accumulated in the photoconverted tumour but exhibited great variation at 120 hours (Fig 2.3E). Finally, green Treg numbers in the TDLN stayed approximately constant over time as would be expected for the TDLN under steady state (Fig 2.3F).

### MC38 TDLN photoconversion dataset

The second set of experiments that were implemented involved the photoconversion of the TDLN in MC38-bearing mice. These experiments were conducted by our collaborators and the data has not yet been published. Figure 2.4 outlines the dataset.

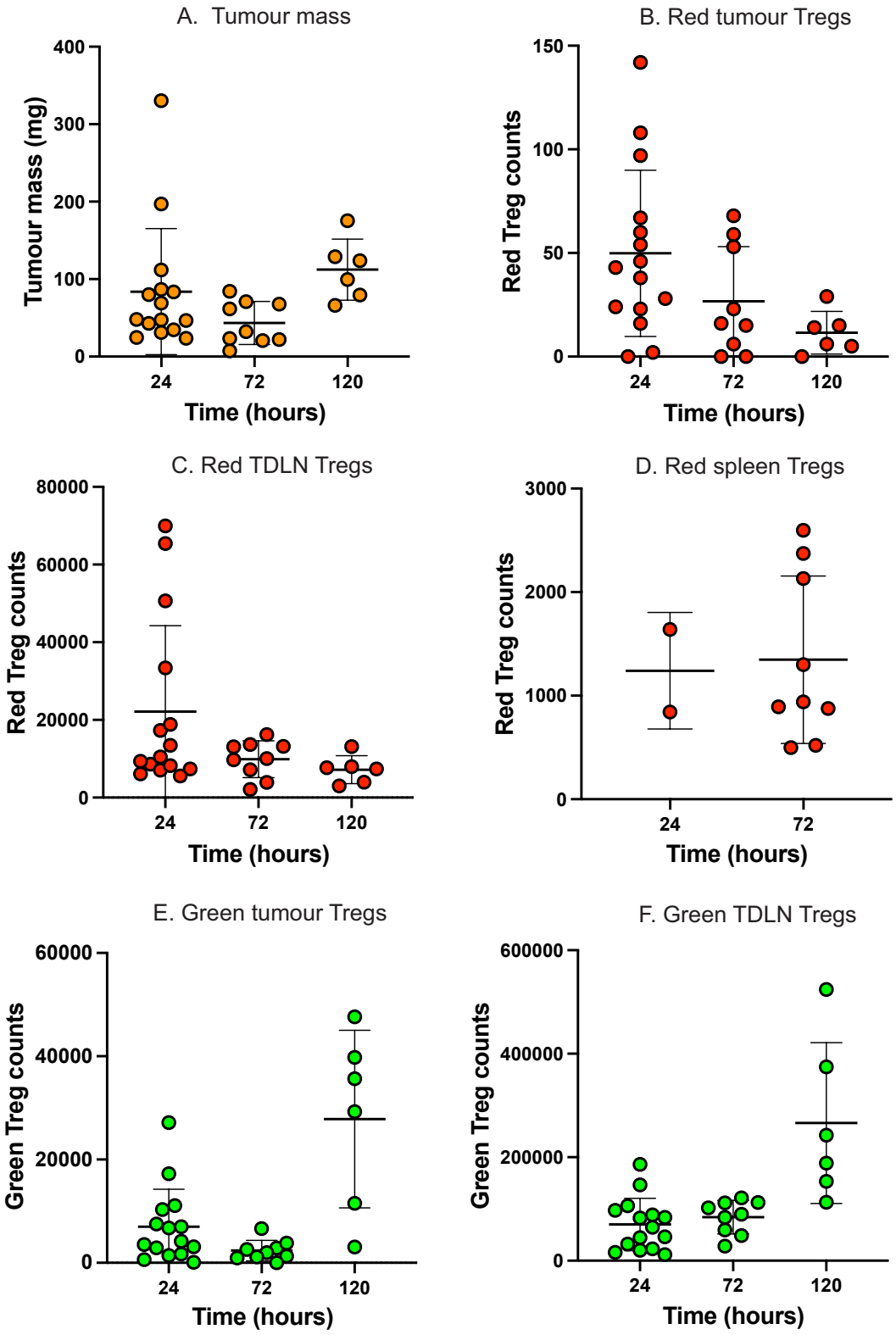



**Figure 2.4: Overview of the MC38 TDLN photoconversion dataset**. A: Tumour mass in milligrams. B: Red Tregs that migrated from the TLDN to the tumour. C: Red Treg numbers in the photoconverted TDLN. D: Red Tregs that accumulated in the Spleen. E: Green Tregs that were found in the tumour. F: Green Tregs that accumulated in the TDLN post TDLN photoconversion. The points depicted here correspond to measurements in independent mice. Horizontal lines represent the mean and standard deviation.

We saw that tumour growth dynamics were approximately linear though the masses of tumours recorded at 72 hours were slightly lower than the masses at 24 hours post TDLN photoconversion (Fig 2.4A). This discrepancy could be attributed to stochastic tumour growth dynamics in independent mice. Few red Tregs reached the tumour, and their numbers peaked at 24 hours before dropping at later time points, suggesting that Tregs from the TDLN exhibit mostly transient behaviour in the tumour (Fig 2.4B). Red Treg dynamics in the photoconverted TDLN displayed a decaying profile as they migrated from the TDLN over time to populate other organs (Fig 2.4C). On average, red Tregs slowly accumulated in the spleen (Fig 2.4D). We observed an inconsistent green Treg profile in the tumour that was characterised by a drop at 72 hours, which may be linked to the lower tumour masses that were recorded at this time point (Fig 2.4E). In the TDLN, green Tregs rapidly increased over time (Fig 2.4F).

### CT26 tumour photoconversion dataset

To investigate the effects of tumour heterogeneity on Treg trafficking, CT26 tumours were photoconverted and red and green Tregs in different organs were quantified as illustrated (Fig 2.5). This data set is not associated with any published study and was generated by our collaborators.

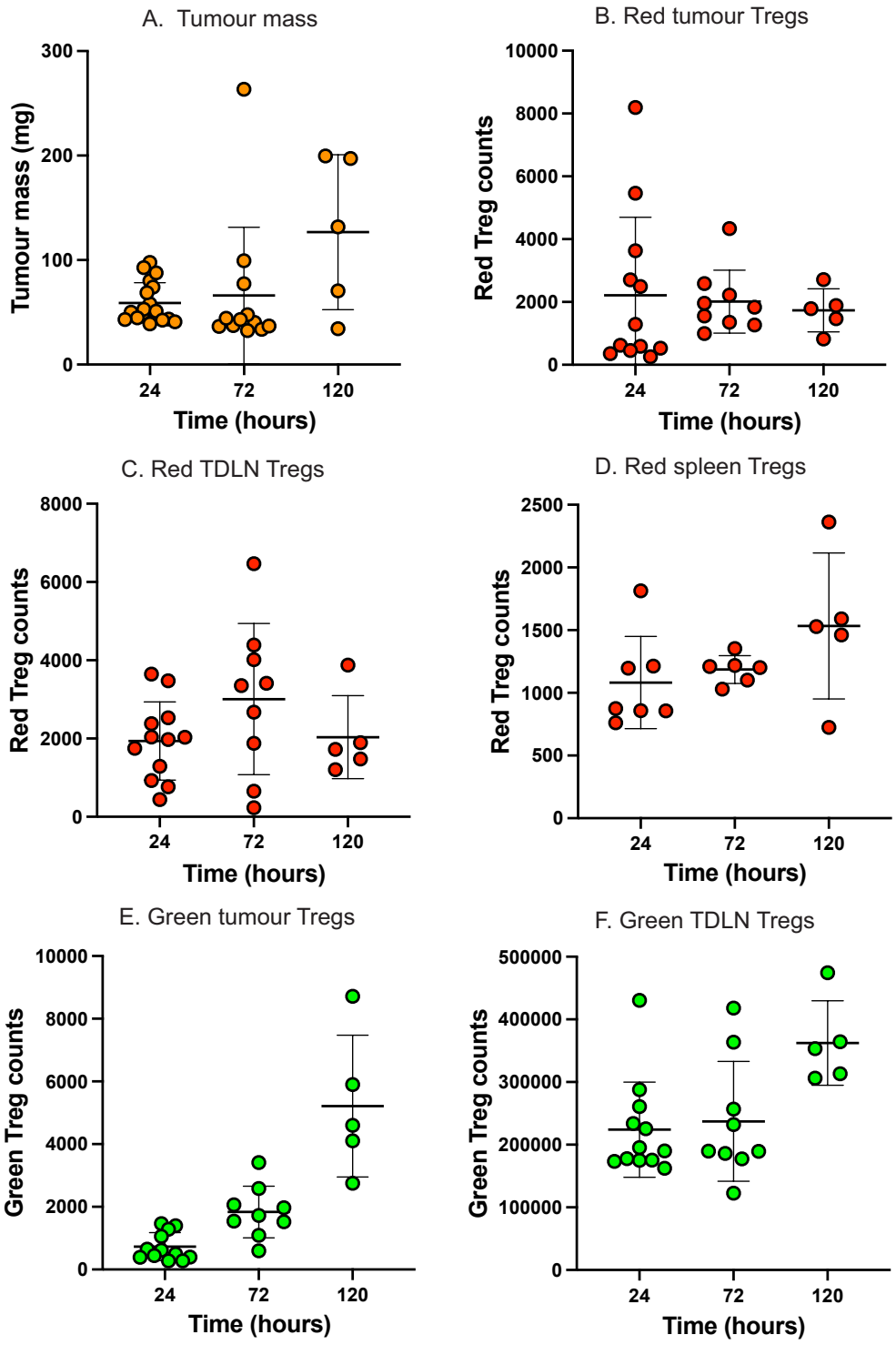



**Figure 2.5: Overview of the CT26 tumour photoconversion dataset**. A: Tumour mass in milligrams. B: Red Tregs in the photoconverted tumour. C: Red Tregs that migrated from the tumour to the TDLN. D: Red Tregs that accumulated in the Spleen. E: Green Tregs that accumulated in the tumour. F: Green Tregs that were present in the TDLN. The points depicted here correspond to measurements in independent mice. Horizontal lines represent the mean and standard deviation. All data points in A-D were used in the mathematical modelling.

CT26 tumours exhibited an approximately linear growth pattern, with unexpectedly lower masses at 72 hours post tumour photoconversion (Fig 2.5A). On average, red Treg numbers in the tumour dropped though they did not reach zero within the experimental time scale (Fig 2.5B). We observed that red Tregs from the tumour accumulated in the TDLN over time, through there was significant variation in Treg numbers at 72 hours (Fig 2.5C). In the spleen, red Tregs steadily increased over time (Fig 2.5D). Green Treg dynamics in the tumour were approximately linear (Fig 2.5E). Finally, the data highlighted approximately constant green Treg dynamics in the TDLN as expected, albeit with slightly higher numbers at 120 hours (Fig 2.5F).

Table 2.1 summarises our datasets.

**Table 2.1: Table describing the Kaede photoconversion dataset used in the study**. For each photoconversion experiment, different datasets were generated with variable numbers of data points per time point. Each data point represents an independent mouse.

| | | Data points per time point | | |
|---|---|---|---|---|
| Photoconverted Tissue | Dataset | 24 hr | 72 hr | 120 hr |
| MC38 | Tumour weight | 41 | 18 | 16 |
| | Tumour Red Tregs | 24 | 10 | 9 |
| | Tumour Green Tregs | 24 | 10 | 9 |
| | TDLN Red Tregs | 24 | 9 | 9 |
| | TDLN Green Tregs | 24 | 9 | 9 |
| | Spleen Red Tregs | 13 | 5 | 4 |
| | Spleen Green Tregs | 13 | 5 | 4 |
| MC38 TDLN | Tumour weight | 15 | 9 | 6 |
| | Tumour Red Tregs | 15 | 9 | 6 |
| | Tumour Green Tregs | 15 | 9 | 6 |
| | TDLN Red Tregs | 15 | 9 | 9 |
| | TDLN Green Tregs | 15 | 9 | 6 |
| | Spleen Red Tregs | 2 | 9 | 0 |
| | Spleen Green Tregs | 2 | 9 | 0 |
| CT26 | Tumour weight | 18 | 12 | 5 |
| | Tumour Red Tregs | 12 | 9 | 5 |
| | Tumour Green Tregs | 12 | 9 | 5 |
| | TDLN Red Tregs | 12 | 9 | 5 |
| | TDLN Green Tregs | 12 | 9 | 5 |
| | Spleen Red Tregs | 7 | 6 | 5 |
| | Spleen Green Tregs | 7 | 6 | 5 |

### 2.4.2 Iterative mathematical model development

We used ordinary differential equations (ODEs) to describe both tumour growth dynamics and the migratory kinetics of intratumoral Tregs. From the exploratory data analysis conducted in the previous subsection, we concluded that tumour mass can be modelled by a linear ODE of the form:

$$\frac{d(\text{mass})}{dt} = \alpha, \tag{2.39}$$

where $\alpha$ is the tumour growth rate per hour.

Next, we considered both the MC38 and CT26 tumour photoconversion datasets, in which the observed variables are red Tregs in the tumour, TDLN and spleen. We restricted our analysis to red Tregs, which we could track from one organ to another, instead of green Tregs, which could not be easily characterised. For instance, we could not infer the rate at which green Tregs were converted from transient to resident Tregs.

The key hypothesis that we wanted to test was the presence of resident and transient Tregs in the tumour. Thus, we modelled the red Tregs in the tumour (Total) as a sum of resident (Res) and transient (Trans) Tregs:

$$\text{Total} = \text{Res} + \text{Trans}. \tag{2.40}$$

The long time dynamics associated with resident Tregs could not be fully described by the dataset, given that measurements were only taken up to 120 hours post tumour photoconversion. Given our poor understanding of resident Treg dynamics, except that they are resident and thus do not turn over quickly, we assumed that resident Treg numbers do not significantly change over the short course of the experiment. Thus, we modelled resident Tregs as a constant population, giving rise to the following equation:

$$\frac{d(\text{Res})}{dt} = 0. \tag{2.41}$$

On the other hand, transient Tregs leave the tumour to populate other organs including the TDLN and spleen. Furthermore, we assumed that transient Treg numbers increase

at an hourly rate of $\eta$ in the tumour due to exposure to cytokines and high antigen densities. For simplicity, $\eta$ accounts for cell proliferation, cell death, and the conversion of CD4 T cells to peripherally-induced Tregs (pTregs). Therefore, transient Treg dynamics are governed by the equation:

$$\frac{d(\text{Trans})}{dt} = \text{Trans}(\eta - \gamma - \delta - \zeta), \tag{2.42}$$

where $\gamma, \delta$ and $\zeta$ are the hourly trafficking rates of transient Tregs to other organs, the TDLN and the spleen respectively.

Using similar reasoning, the observed red Tregs accumulating in the spleen were modelled as:

$$\frac{d(\text{Spleen})}{dt} = \zeta \cdot \text{Trans}, \tag{2.43}$$

where $\zeta$ is the hourly rate at which red Tregs from the tumour accumulate in the spleen. We considered the possibility that red Tregs in the spleen proliferate but this resulted in a predicted exponential increase in splenic Tregs which significantly deviated from the observed dynamics. Furthermore, because we observed monotonically increasing dynamics in the spleen, we assumed that the red Tregs are primarily accumulating but not leaving the spleen at a significant rate within the observed time scale.

Next, we modelled red Tregs in the TDLN as:

$$\frac{d(\text{TDLN})}{dt} = \delta \cdot \text{Trans} + \text{TDLN}(\eta - \rho), \tag{2.44}$$

where $\rho$ is an hourly migration rate describing Tregs that leave the TDLN to go to other organs. We initially modelled TDLN Tregs without proliferation but this resulted in poor model fits suggesting the possibility of a significant Treg proliferation rate in the TDLN. For simplicity, we used the same Treg proliferation/net increase rate of $\eta$. We also observed that red Tregs from MC38 exhibited non-monotonic behaviour in the TDLN characterised by initial increase followed by a drop by 120 hours. This indicated that red Tregs that entered the TDLN also migrated from it to go to other organs. Hence we modelled their exit kinetics to other organs at a rate depicted by $\rho$.

### Structural identifiability assessment

To ensure that the mathematical model was structurally identifiable given our data, we performed structural identifiability assessment using the analytical scaling transformation method (Castro and de Boer, 2020).

Given that we had little data with very few time points, we first searched the literature for parameter values to reduce the number of unknown parameters to be inferred directly from the data. Prior *ex vivo* and *in vitro* cell expansion studies show that mouse Tregs can proliferate at rates of approximately 0.28 and 0.33 per day (Sarkar et al., 2014; Siemasko et al., 2008). Through a combination of mathematical modelling and simulation, additional studies found that murine Tregs can proliferate at a rate between 0.61 and 2 per day and die at a rate of approximately 0.014 per day (Milanez-Almeida et al., 2015; den Braber et al., 2012). Similarly, another study of T cell expansion in the context of viral infection showed that CD4 T cells can expand at rates between 1.07 and 1.59 per day (De Boer et al., 2003). Since CD4 T cell conversion to pTregs can be negligibly low (Milanez-Almeida et al., 2015), we decided not to consider it in the mathematical model.

Consolidating these findings, we fixed the value of $\eta$ at 1 per day, given that it lies within the reasonable order of magnitude reported in the literature. Table 2.2 summarises our knowledge of the variables and parameters in the model.

**Table 2.2: A summary of observed and unobserved variables or parameters**. *The proliferation rate of Tregs was inferred from Sarkar et al. (2014); Siemasko et al. (2008); Milanez-Almeida et al. (2015); De Boer et al. (2003).

| Variables | | Parameters | |
|---|---|---|---|
| Not Observed | Observed | Unknown | Known |
| Res | Total | $\gamma$ | $\eta = 1$ day$^{-1}$* |
| Trans | TDLN | $\delta$ | |
| | Spleen | $\zeta$ | |
| | | $\rho$ | |

To consider structural identifiability, we applied arbitrary scaling transformations, denoted by $u$ to unobserved variables and unknown parameters. Starting off with the total number of Tregs in the tumour, we obtain:

$$\text{Total} = u_{Res}\text{Res} + u_{Trans}\text{Trans}. \tag{2.45}$$

We then identified linearly independent expressions in the equation, which are $u_{Res}$Res and $u_{Trans}$Trans, and equated them to their unscaled forms for all values of Res and Trans (so that degeneracies associated with Res $= 0$ or Trans $= 0$ need not be considered). Then, we checked whether the values of $u$ are uniquely equal to 1, which is indeed the case:

$$\begin{aligned} u_{Res}\text{Res} = \text{Res} \quad &\therefore u_{Res} = 1, \\ u_{Trans}\text{Trans} = \text{Trans} \quad &\therefore u_{Trans} = 1. \end{aligned} \tag{2.46}$$

Noting that spleen Treg numbers are observed and thus not scaled, the spleen compartment equation scales to:

$$\frac{d(\text{Spleen})}{dt} = u_\zeta \zeta u_{Trans}\text{Trans}. \tag{2.47}$$

Equating the scaled equation to the original and noting $u_{Trans} = 1$, we have:

$$u_\zeta \zeta u_{Trans}\text{Trans} = \zeta\text{Trans} \quad \therefore u_\zeta = 1. \tag{2.48}$$

Likewise, we scaled the TDLN compartment as:

$$\frac{d(\text{TDLN})}{dt} = u_\delta \delta u_{Trans}\text{Trans} + (\eta - u_\rho \rho)\text{TDLN}. \tag{2.49}$$

In this equation, the linearly independent expressions are $u_\delta \delta u_{Trans}$Trans and $(\eta - u_\rho\rho)$TDLN. Noting $\eta$ is fixed as known and thus not scaled, and using $u_{Trans} = 1$, we have:

$$\begin{aligned} u_\delta \delta u_{Trans}\text{Trans} = \delta\text{Trans} \quad &\therefore u_\delta = 1, \\ (\eta - u_\rho\rho)\text{TDLN} = (\eta - \rho)\text{TDLN} \quad &\therefore u_\rho = 1. \end{aligned} \tag{2.50}$$

Finally, we examined the Trans compartment. The only independent expression present is:

$$u_{Trans}\frac{d(\text{Trans})}{dt} = (\eta - u_\gamma\gamma - u_\delta\delta - u_\zeta\zeta) \cdot u_{Trans}\text{Trans}. \tag{2.51}$$

We equated the expression above to the original expression in the unscaled equation, and using $u_\zeta = u_\delta = 1$, we have:

$$(\eta - u_\gamma\gamma - u_\delta\delta - u_\zeta\zeta) \cdot u_{Trans}\text{Trans} = (\eta - \gamma - \delta - \zeta) \cdot \text{Trans} \quad \therefore u_\gamma = 1. \tag{2.52}$$

Because all scalings are uniquely unity, we concluded that the proposed model is globally structurally identifiable.

We initially considered inferring $\eta$ from the data. However, we observed that it was not possible to do so uniquely as the mathematical model became structurally unidentifiable (and thus, also practically unidentifiable):

$$\begin{aligned}(u_\eta\eta - u_\gamma\gamma - u_\delta\delta - u_\zeta\zeta)\text{Trans} &= (\eta - \gamma - \delta - \zeta)\text{Trans},\\ (u_\eta\eta - u_\rho\rho)\text{TDLN} &= (\eta - \rho)\text{TDLN}.\end{aligned} \tag{2.53}$$

Since there are independent functions elsewhere in the model where $\delta$ and $\zeta$ appear isolated from $\eta$, we know that both $u_\delta$ and $u_\zeta$ are equal to 1 and hence identifiable. This leaves us with:

$$\begin{aligned}u_\eta\eta - u_\gamma\gamma &= \eta - \gamma,\\ u_\eta\eta - u_\rho\rho &= \eta - \rho,\end{aligned} \tag{2.54}$$

and two equations for the three unknown scalings $u_\eta, u_\gamma, u_\rho$. Hence, these can not be found uniquely and thus, they are not uniquely equal to unity, demonstrating an absence of structural identifiability.

We concluded that the proposed model, with $\eta$ inferred from the literature, would be sufficient to fit the MC38 and CT26 tumour photoconversion data given a sufficient quality of data. However, recall that two different experiments were performed with the MC38 tumour. The additional dataset constituted of red Tregs in the tumour, TDLN and spleen following the photoconversion of the MC38 TDLN. In the case of MC38 TDLN photoconversion dataset, we saw that we could model the trafficking of Tregs from the TDLN to the spleen and the tumour as follows:

$$\begin{aligned}\frac{d(\text{TDLN})}{dt} &= (\eta - \rho - \tau - \beta)\text{TDLN},\\ \frac{d(\text{Spleen})}{dt} &= \beta\text{TDLN},\\ \frac{d(\text{Trans})}{dt} &= \tau\text{TDLN} + (\eta - \delta - \gamma)\text{Trans},\end{aligned} \tag{2.55}$$

where $\tau, \beta$ are rates at which red Tregs arrive in the tumour and spleen respectively. When we combined the MC38 and MC38 TDLN photoconversion data, both $\beta$ and $\tau$ became structurally identifiable by analogous arguments. Incorporating both MC38 datasets, the MC38 mathematical model differed from the CT26 model by having additional terms highlighted in red below:

$$\begin{aligned} \frac{d(\text{TDLN})}{dt} &= (\eta - \rho - \tau - \beta)\text{TDLN}, \\ \frac{d(\text{Spleen})}{dt} &= \zeta\text{Trans} + \beta\text{TDLN}, \\ \frac{d(\text{Trans})}{dt} &= \tau\text{TDLN} + (\eta - \delta - \gamma - \zeta)\text{Trans}. \end{aligned} \tag{2.56}$$

In summary, Figure 2.6 shows that the CT26 mathematical model is essentially a sub-model of the MC38 mathematical model, associated with $\tau = \beta = 0$.

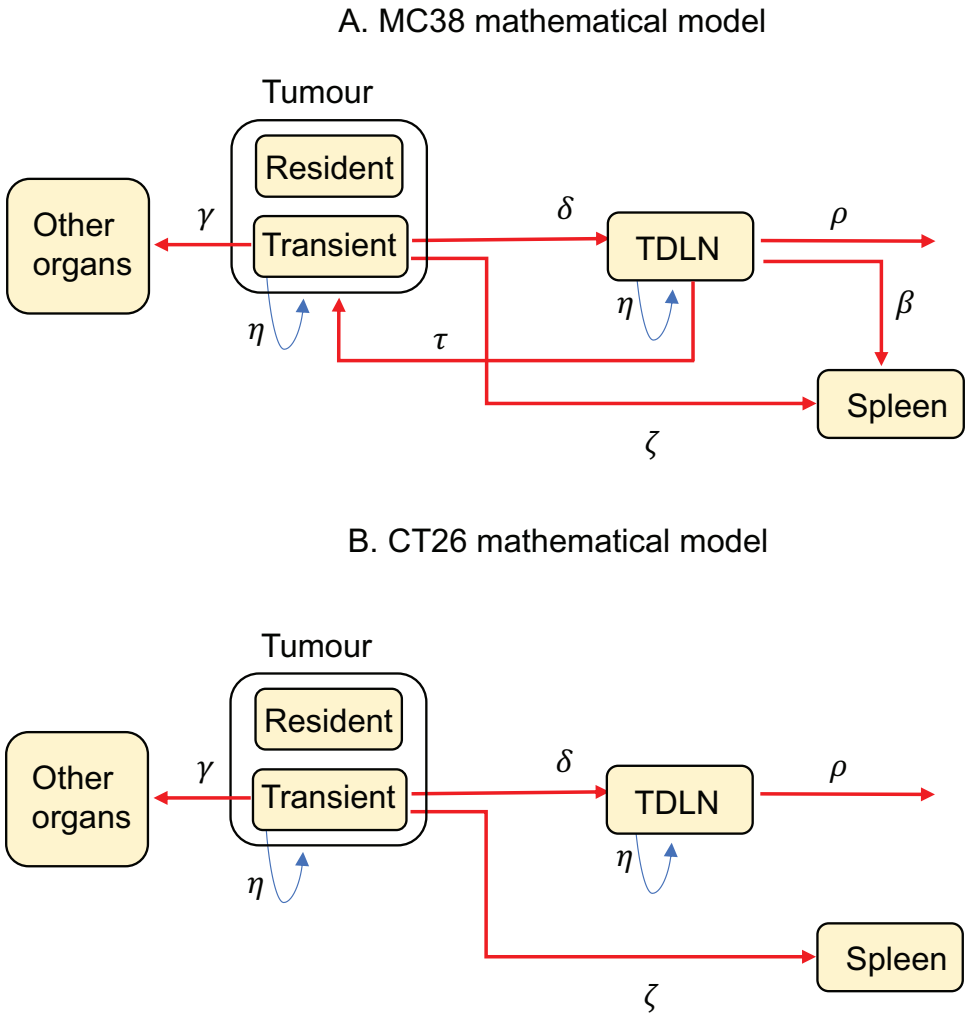



**Figure 2.6: MC38 and CT26 mathematical models**. The presence of the MC38 TDLN photoconversion dataset allowed us to additionally model the trafficking of Tregs from the TDLN to the spleen and the tumour. A sub-model of the MC38 mathematical model was used for fitting the CT26 photoconversion data. The Greek letters denote Treg proliferation and migration rates across the respective organs. Red arrows underscore the migration of red Tregs from each compartment while blue curves signify proliferation.

Though the two mathematical models slightly differed in structure, we showed through sensitivity analysis that the first-order sensitivity indices of $\tau$ and $\beta$ do not differ from those of the dummy variable (Fig 2.7). A similar observation was made when we ran sensitivity analysis for the CT26 mathematical model with $\tau$ and $\beta$ fixed as uniform distributions within the ranges observed in the MC38 mathematical model. The low sensitivity of the parameters justified our ability to compare both the MC38 and CT26 mathematical model parameters after parameter estimation despite the small structural differences in the two mathematical models.

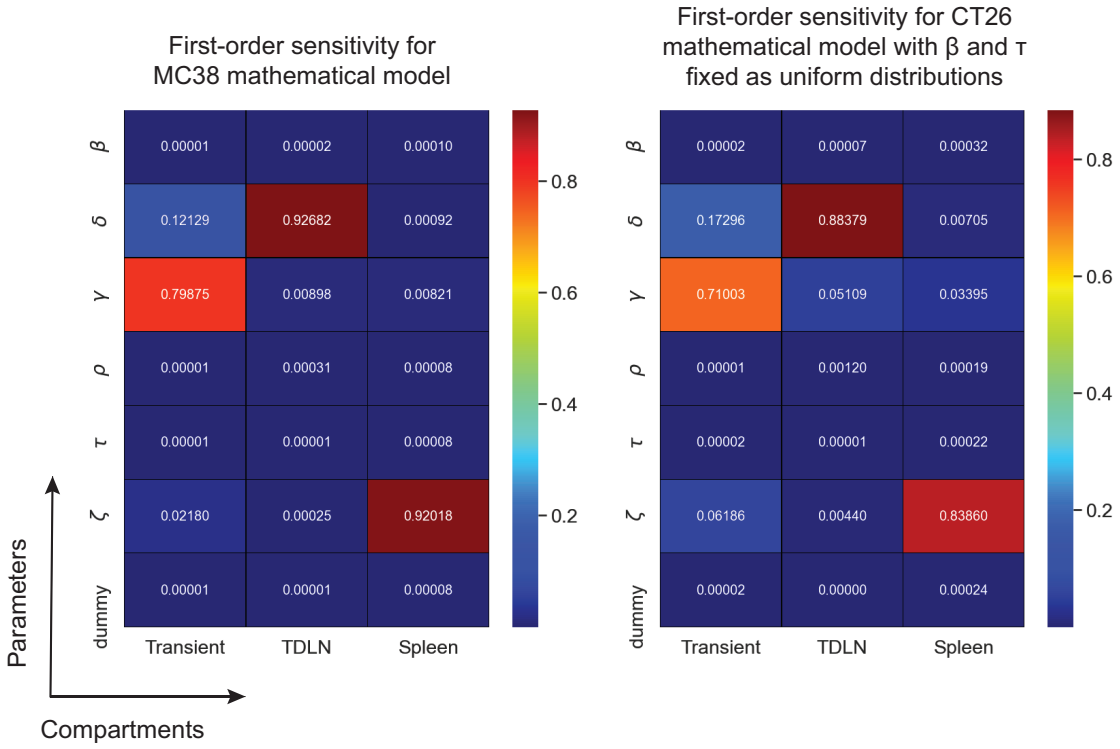



**Figure 2.7: Parameters $\tau$ and $\beta$ have low sensitivity indices.** $\tau$ and $\beta$ inferred from the MC38-TDLN photoconversion data have low first-order sensitivity indices across all compartments. Similarly, when included in the CT26 mathematical model as approximate uniform distributions, both parameters have low first-order sensitivity scores.

### Assessing model practical identifiability using MCMC

Following structural identifiability assessment, we considered if the final models could be used to practically identify parameters from the data. To infer the parameters, we ran MCMC and obtained model parameters as probability distributions. Prior work has demonstrated that MCMC can be used to check if the parameters of a structurally identifiable model are practically identifiable. Cases where the joint posterior distributions are non-trivial and lie only within a suitably small region of parameter space give rise to practical identifiability, as no extreme range of either parameter is consistent with the data (Hines et al., 2014).

We observed that independent Markov chains for all parameters in both the MC38 and CT26 mathematical models converged to approximately invariant distributions which reflected the true posterior distributions (Fig 2.8). The level of chain convergence was assessed using the Gelman-Rubin ($\hat{R}$) convergence statistic. The inferred parameter distributions for MC38 and CT26 mathematical models were associated with $\hat{R}$ values of approximately equal to 1, suggesting sufficient inter- and intra-chain mixing (Supplementary Table A.1). Table 2.3 gives a summary of all model parameters and their definitions.

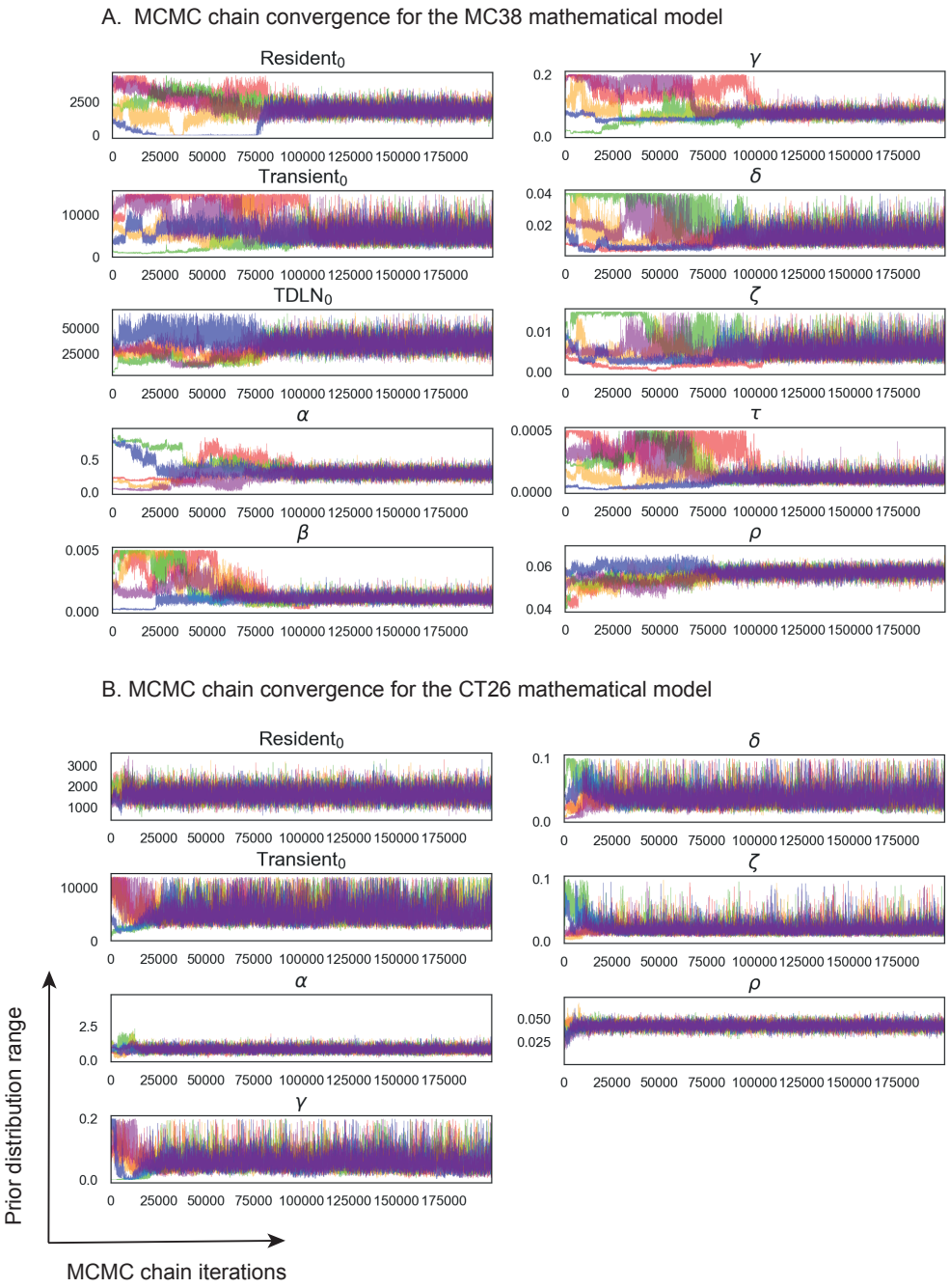



**Figure 2.8: All MCMC chains converged to invariant distributions after about 100 000 iterations**. Different colours show the evolution of 5 different MCMC chains across the 200 000 iterations. Transient$_0$ and Resident$_0$ are the initial distributions of transient and resident Tregs inferred from the data.

**Table 2.3: Table describing the inferred model parameters for both CT26 and MC38**. Uniform distributions were used as priors denoted by $\mathcal{U}$. All inferred parameters are reported as means of the posterior distribution (Post. mean) with standard deviations (S.D). *The proliferation rate of Tregs, $\eta$, was fixed after considering studies from Sarkar et al. (2014); Siemasko et al. (2008); Milanez-Almeida et al. (2015); De Boer et al. (2003). Transient$_0$ and Resident$_0$ are the initial distributions of transient and resident Tregs inferred from the data.

| | | | Tumour | | | | | | |
|---|---|---|---|---|---|---|---|---|---|
| | | | MC38 | | | CT26 | | | |
| Parameter | Definition | Unit | Prior | Post. mean | S.D | Prior | Post. mean | S.D | Source |
| $\alpha$ | Tumour growth rate | mghr$^{-1}$ | $\mathcal{U}$(0,1) | 0.28 | 0.06 | $\mathcal{U}$(0,5) | 0.78 | 0.2 | This study |
| $\beta$ | Treg migration rate from TDLN to Spleen | hr$^{-1}$ | $\mathcal{U}$(0,0.005) | 0.001 | 0.0003 | - | - | - | This study |
| $\gamma$ | Treg migration rate from tumour to Other organs | hr$^{-1}$ | $\mathcal{U}$(0,0.2) | 0.071 | 0.01 | $\mathcal{U}$(0,0.2) | 0.056 | 0.03 | This study |
| $\delta$ | Treg migration rate from Tumour to TDLN | hr$^{-1}$ | $\mathcal{U}$(0,0.04) | 0.013 | 0.005 | $\mathcal{U}$(0,0.3) | 0.046 | 0.014 | This study |
| $\zeta$ | Treg migration rate from Tumour to Spleen | hr$^{-1}$ | $\mathcal{U}$(0,0.015) | 0.0054 | 0.002 | $\mathcal{U}$(0,0.2) | 0.020 | 0.0087 | This study |
| $\rho$ | Treg migration rate from TDLN to Other Organs | hr$^{-1}$ | $\mathcal{U}$(0.04,0.07) | 0.057 | 0.002 | $\mathcal{U}$(0,0.07) | 0.042 | 0.0037 | This study |
| $\tau$ | Treg migration rate from TDLN to Tumour | hr$^{-1}$ | $\mathcal{U}$(0,0005) | 0.0001 | 0.00003 | - | - | - | This study |
| $\eta$ | Treg proliferation rate | hr$^{-1}$ | - | 0.04 | - | - | 0.04 | - | Fixed* |
| Resident$_0$ | Initial Red Resident Tregs | - | $\mathcal{U}$(0,4500) | 1900 | 370 | $\mathcal{U}$(0,4000) | 1600 | 300 | This study |
| Transient$_0$ | Initial Red Transient Tregs | - | $\mathcal{U}$(0,15000) | 5300 | 1900 | $\mathcal{U}$(500,12000) | 5200 | 2000 | This study |

We then visualised the pair-wise joint posterior distributions of the parameters to assess correlations between parameters. As can be observed from the trace plots (Fig. 2.8), the chains reach convergence after about 100 000 iterations. Therefore, we used posterior samples between 150 000 and 200 000 iterations as the final posterior distributions for each parameter.

Ideally, no two parameters should be highly correlated. High correlations between model parameters could indicate redundancy of the parameters in the mathematical model, indicating a lack of practical identifiability and a limit to our capacity to uniquely identify parameter values by fitting. For both the MC38 and CT26 mathematical models, we observed that the joint pair-wise distributions displayed minimal correlations implying that we could confidently identify unique model parameters from the data (Figs 2.9A and 2.10A). Furthermore, we observed that the marginal distributions for inferred initial conditions and parameters had narrow ranges with high probability densities (Figs 2.9B and 2.10B). Regions that accounted for 94% of the probability density for each parameter were well resolved from the posterior distributions. Based on these observations, we concluded that our models were practically identifiable.

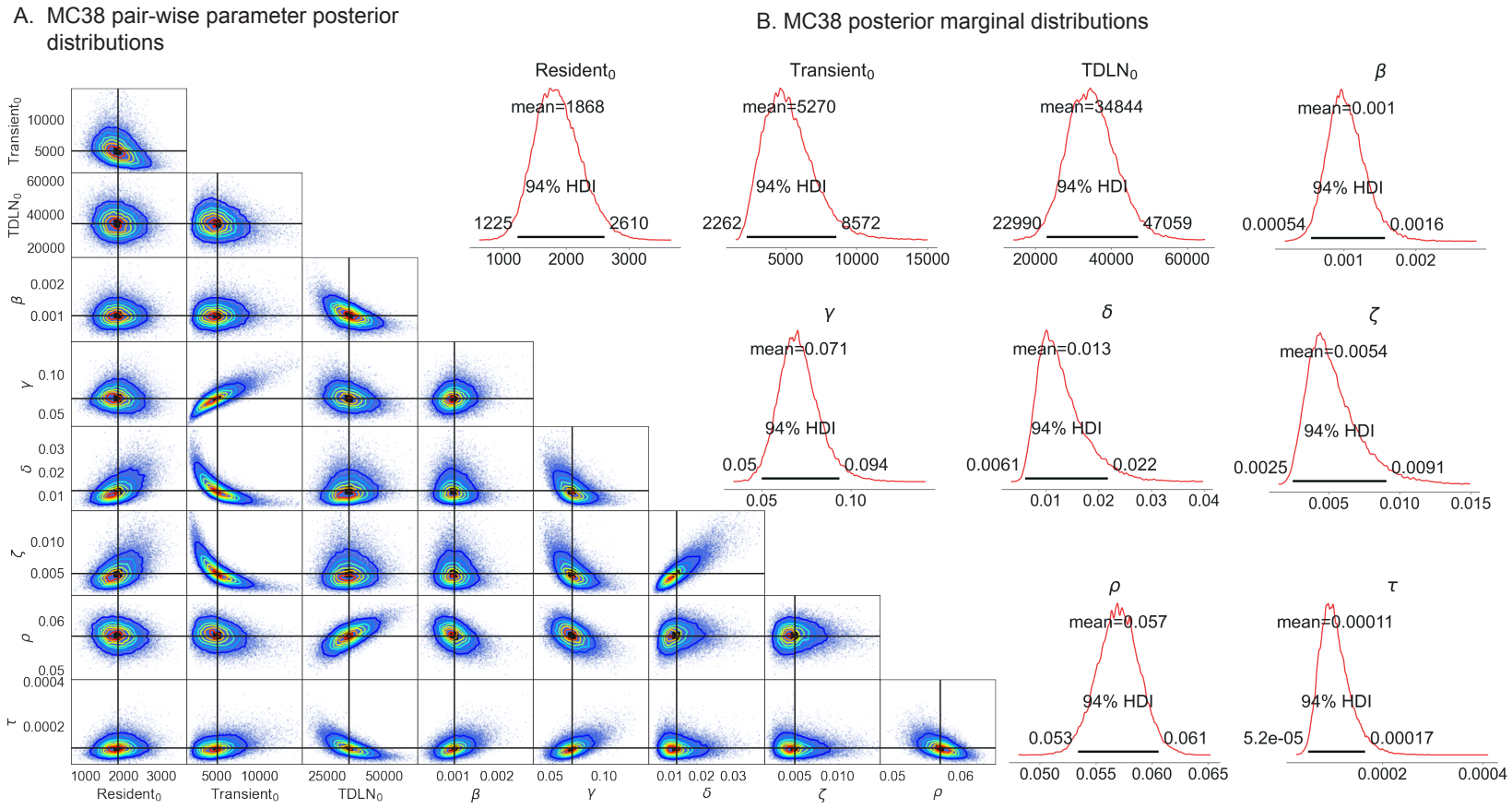



**Figure 2.9: Pair-wise joint parameter distributions for the MC38 mathematical model**. A: Pair-wise joint parameter distributions for the MC38 mathematical model. Red regions highlight joint distribution peaks while the blue colour shows lower joint distribution density regions. B: Marginal distributions for the initial resident, transient and TDLN numbers, and inferred Treg trafficking parameters. Transient$_0$ and Resident$_0$ are the initial distributions of transient and resident Tregs inferred from the data. HDI refers to the highest density interval.

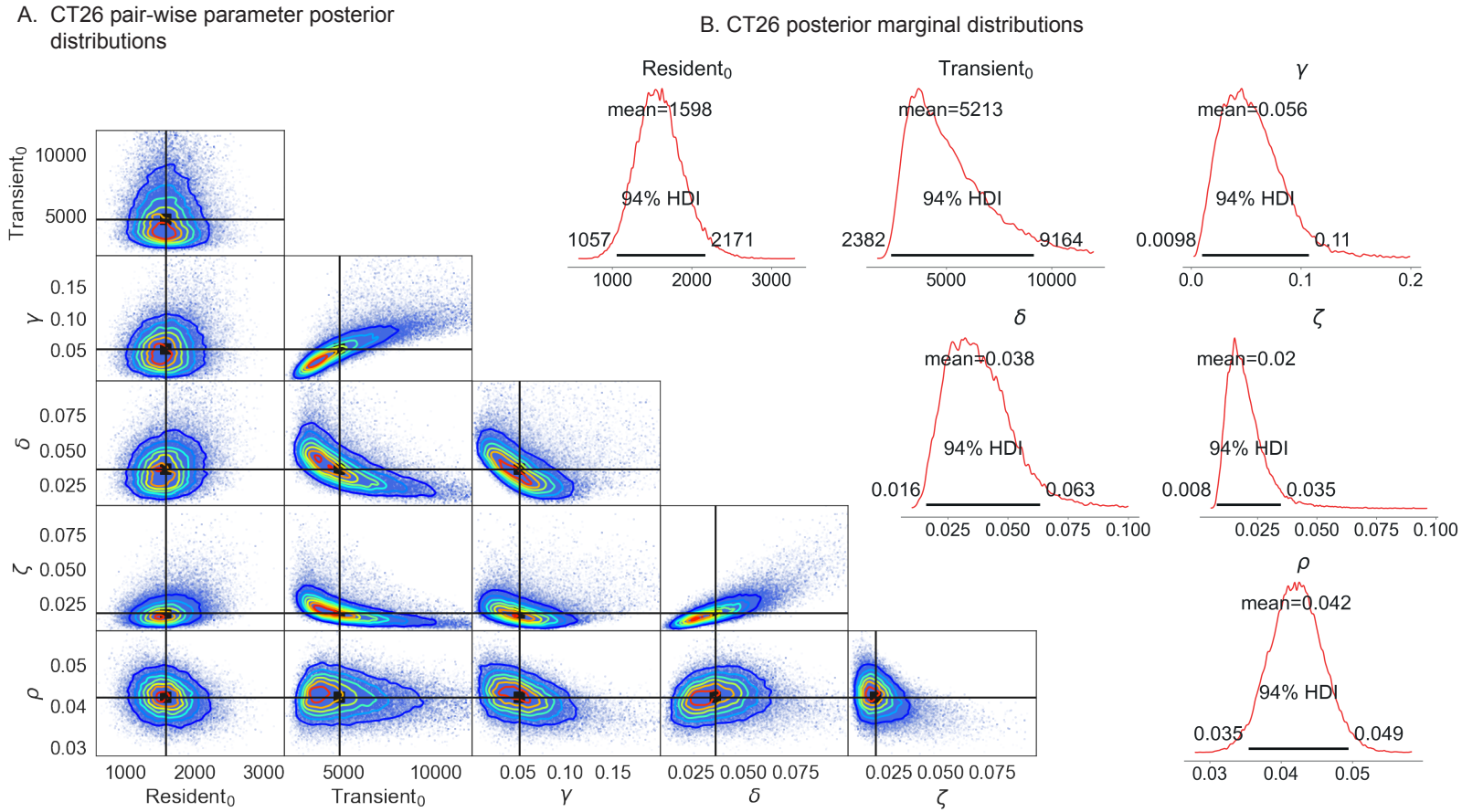



**Figure 2.10: Pair-wise joint parameter distributions for the CT26 mathematical model**. A: Pair-wise joint parameter distributions for the CT26 mathematical model. Red regions highlight joint distribution peaks while the blue colour shows lower joint distribution density regions. B: Marginal distributions for the initial resident and transient Treg numbers, and inferred Treg trafficking parameters. Transient$_0$ and Resident$_0$ are the initial distributions of transient and resident Tregs inferred from the data. HDI refers to the highest density interval.

### 2.4.3 Modelling tumour growth dynamics

We explored the growth dynamics of the MC38 and CT26 tumours by fitting the mathematical model to tumour masses (Fig 2.11). Our results indicated that both MC38 and CT26 tumours exhibited approximately linear growth dynamics during the 120 hours of experimentation (Fig 2.11A-C). However, we observed some differences in the predicted initial tumour masses and growth rates which could indicate tumour heterogeneity. First, tumours from the MC38-TDLN photoconversion group were predicted to have a higher initial tumour mass distribution than tumours from the MC38 tumour photoconversion group, with greater variation in tumour size seen at 24 hours (Fig 2.11C). Secondly, CT26 tumours had lower initial masses than MC38 tumours (Fig 2.11D). Interestingly, the predicted growth rate of CT26 tumours was higher than that of MC38 tumour for the remainder of the experiment (Fig 2.11E).

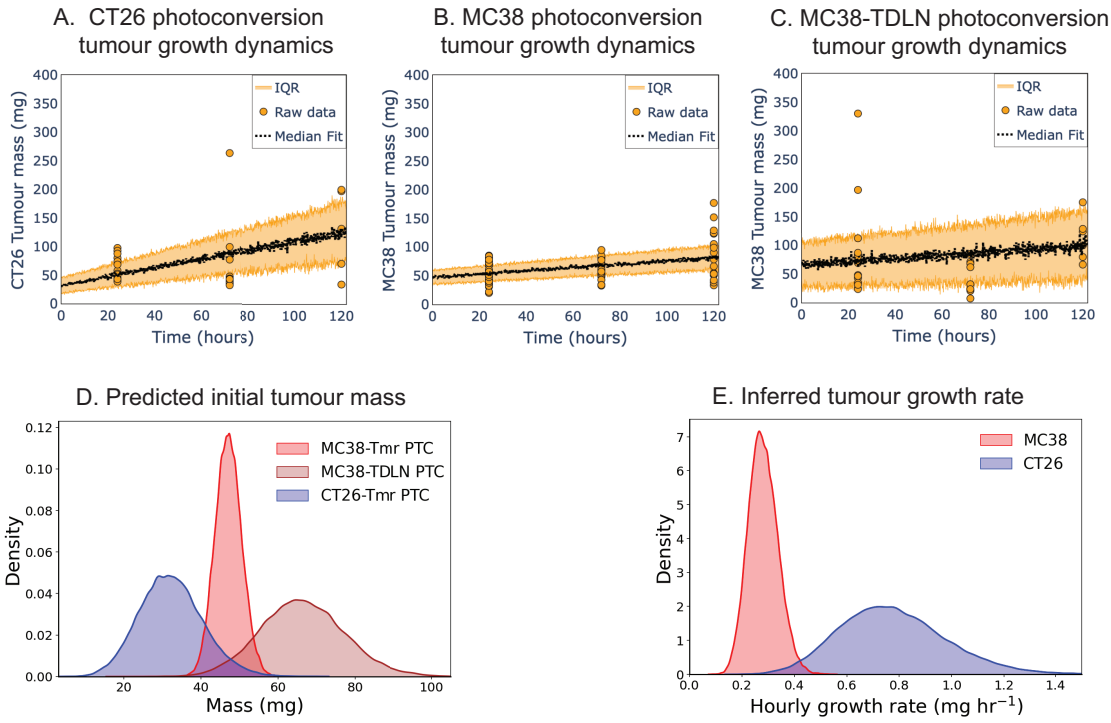



**Figure 2.11: Fitting the mathematical model to tumour growth dynamics**. A-C: Both MC38 and CT26 tumours express linear growth patterns. D: The initial masses of MC38 tumours are slightly higher than those of CT26. E: CT26 tumours display a higher growth rate than MC38 tumours. Orange points correspond to tumour masses recorded per individual mouse while the orange shaded region reflects the inter-quartile range (IQR) of the model fit. Black curves highlight the median of the model fit for a total of 300 samples from the posterior distribution. Abbreviations Tmr and PTC refer to tumour and photoconversion respectively.

### 2.4.4 Modelling the migration profiles of TDLN Tregs

The MC38 TDLN photoconversion dataset enabled us to assess whether a large fraction of TDLN Tregs migrated to the tumour. Following the photoconversion, TDLN Tregs rapidly exited from the TDLN (Fig 2.12A). This predicted that, over time, negligible amounts of red Tregs would be retained in the TDLN. Very few red Tregs from the TDLN migrated to the tumour but exhibited transient behaviour (Fig 2.12B). The inferred rate at which TDLN Tregs migrated to the tumour was minuscule (Fig 2.12D). The transient behaviour of TDLN Tregs in the tumour could imply that most of the Tregs that are seen in the MC38 tumour originate from organs other than the TDLN. Substantial red Tregs accumulated in the spleen (Fig 2.12C) at a rate of approximately $0.001 \pm 0.0003$ per hour (Fig 2.12E).

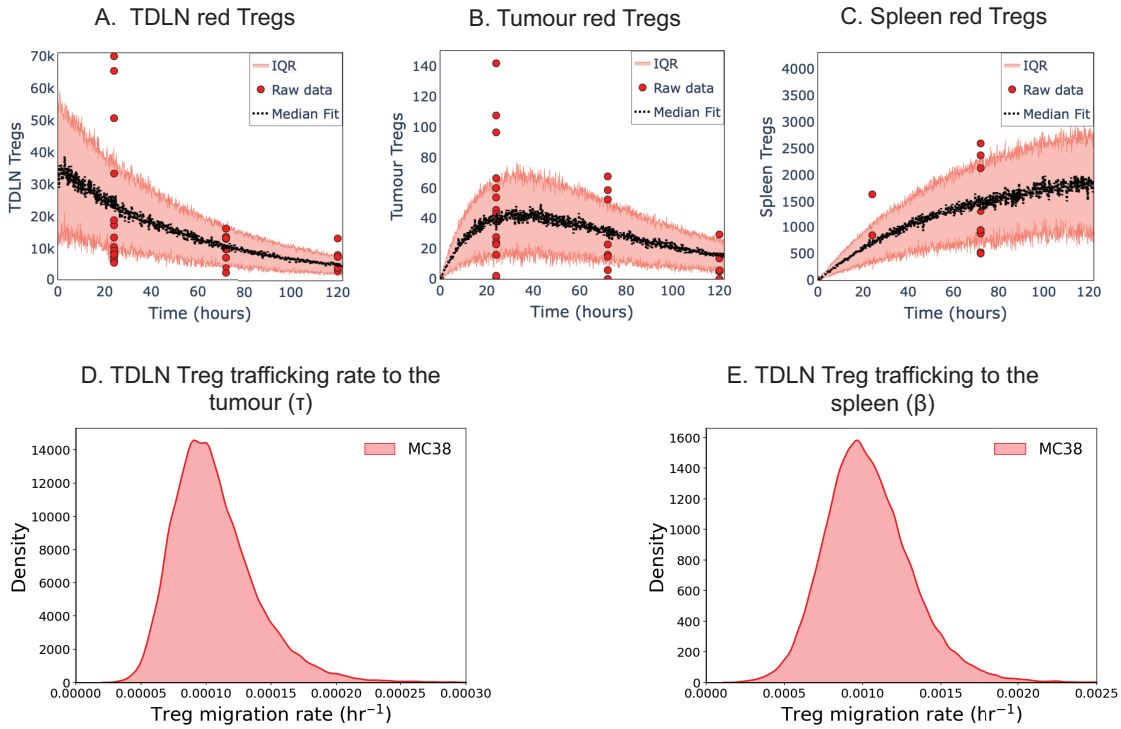



**Figure 2.12: Investigating profiles of Tregs emerging from the MC38 TDLN**. A: Red Tregs leaving the photoconverted TDLN. B: Few red Tregs transiently pass through the tumour. C: Substantial numbers of red Tregs accumulate in the spleen. D: The posterior distribution for the rate at which Tregs from the TDLN migrate to the tumour. E: The rate at which TDLN Tregs migrate to the spleen. The red dots reflect red Tregs that were measured in the organs of individual mice. Black curves are the median fits of the model and the red shaded region in A-C is the inter-quartile range (IQR) for a total of 300 samples from the posterior distribution.

### 2.4.5 CT26 and MC38 tumours harbour resident and transient Tregs

As previously observed, TDLN Tregs rapidly emigrated the TDLN without leaving behind a significant TDLN-resident Treg population. We considered if tumour Tregs exhibited a similar complete egress from the tumour. Thus, we commenced to test whether both resident and transient Tregs are found in both CT26 and MC38 tumours. To do so, we fit the mathematical model to the temporal red Treg counts and observed that the mathematical model was able to capture red Treg dynamics in both tumours. This suggested that the observed dynamics could be, in reality, a combination of resident and transient Treg profiles that could not be separately observed from the data (Fig 2.13).

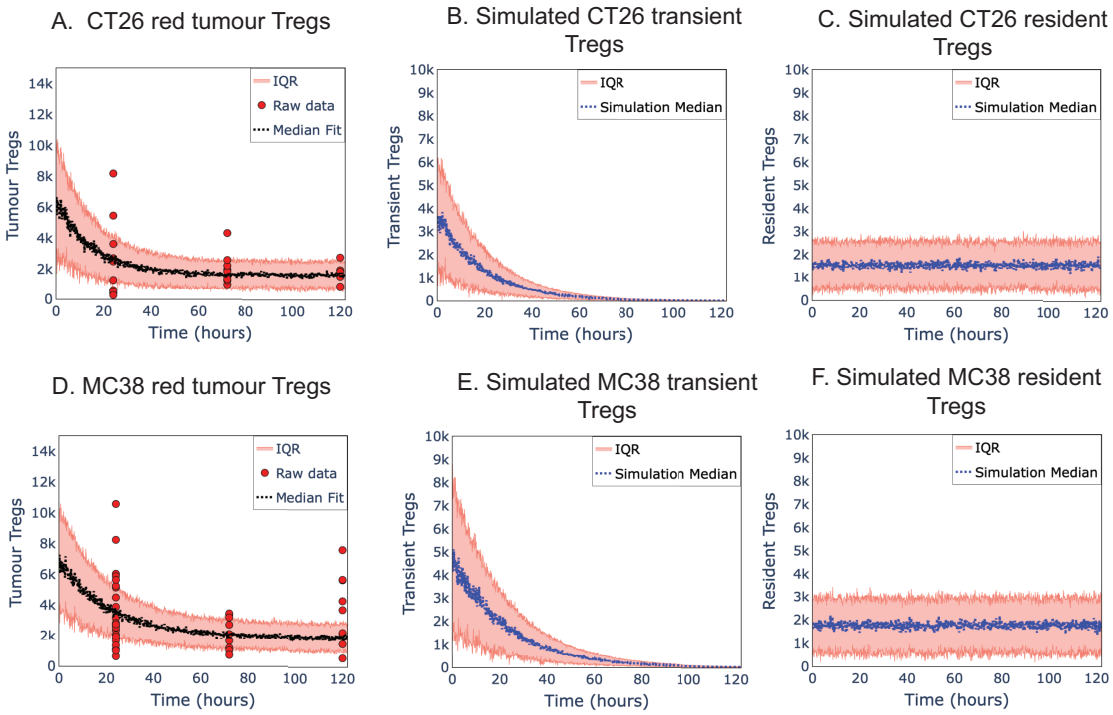



**Figure 2.13: Resident and transient Tregs are present in CT26 and MC38 tumours.** A: Model fit for the red Tregs in the CT26 tumour. B-C: Simulations showing the predicted dynamics associated with transient and resident Tregs in CT26 tumours respectively. D: Model fit for red Tregs in the MC38 tumour, with the 120 hour time point excluded from the MCMC run. E-F: Model simulations showing transient and resident Treg profiles in MC38 tumours respectively. The red points show raw red Treg counts quantified per mouse and the red shaded region depicts the inter-quartile range (IQR) for either the model output or the simulations. Black or blue curves are the median fits of the model/simulation for a total of 300 samples from the posterior distribution.

Recall that we excluded the 120 hour MC38 red Treg time point when running MCMC as discussed in Section 2.4.1. When we attempted to infer parameters with the 120 hour time point included, we observed that the fit was biased towards the 120 hour time point and failed to capture the more biologically plausible 72 hour time point (Supplementary Fig. A.2B). Such a fit overestimated the numbers of resident Tregs in the MC38 tumours.

MC38 and CT26 Treg trafficking mathematical models that did not account for resident Tregs failed to fit to the data (Supplementary Fig. A.3). Similarly, mathematical models that did not consider the proliferation of transient and TDLN Tregs did not fit the observed data well. Without Treg proliferation, the CT26 mathematical model predicted a very high number of initial red Tregs in the tumour (Supplementary Fig. A.4A, B). Running MCMC with an MC38 Treg trafficking mathematical model that lacked Treg proliferation resulted in lack of chain convergence (Supplementary Fig. A.4C, D).

To independently visualise resident and transient Treg profiles, we ran simulations with the parameterised mathematical models. We observed that transient Tregs quickly exited from both tumours. By the 72 hour time point, most transient Tregs had left the tumour. This implies the prediction that the red Tregs that are observed at 72 and 120 hours in the tumours are likely to be resident Tregs. We noted that transient Tregs appeared to leave CT26 tumours slightly faster than MC38 tumours (Fig 2.13B and E), suggesting heterogeneous Treg trafficking kinetics between the tumours.

Interestingly, both tumours had similar distributions of initial transient and resident Tregs (Fig 2.14A-B). This may have been due to the fact that CT26 and MC38 tumours of roughly similar sizes, with possibly similar cell numbers, were used in the experiments. Posterior distributions of Treg trafficking rates from the tumour to the TDLN and spleen were higher in the CT26 rather than the MC38 mathematical models (Fig 2.14C and E). In contrast Treg trafficking rate to other organs was higher in the MC38 mathematical model (Fig 2.14D). Finally, the MC38 Tregs egressed the TDLN faster than CT26 Tregs (Fig 2.14F). Collectively, these results highlighted trafficking differences between MC38 and CT26-derived Tregs.

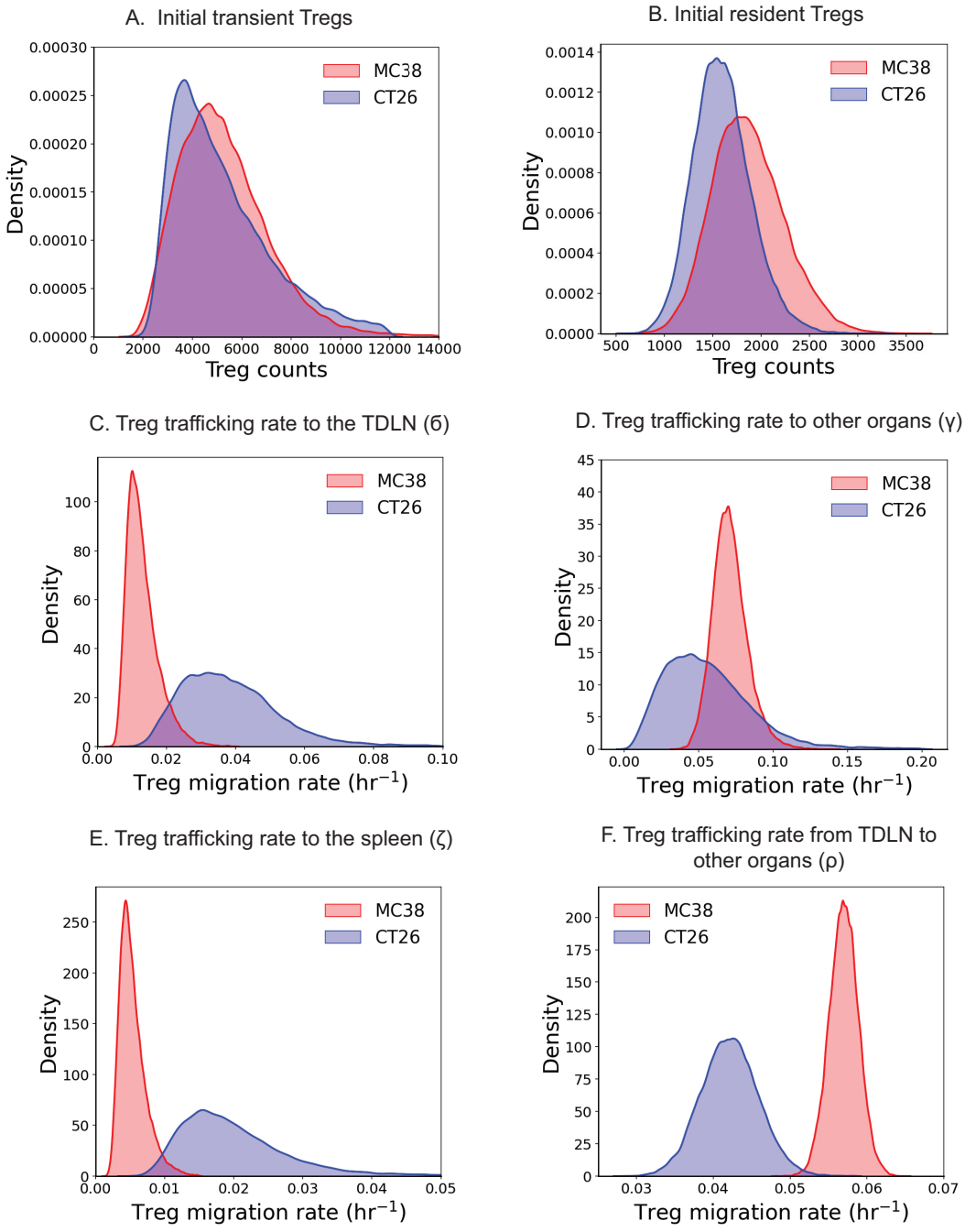



**Figure 2.14: Initial conditions and parameters associated with transient Tregs**. A-B: Initial transient and resident Treg distributions in CT26 and MC38 tumours respectively. C-E: Posterior distributions representing the rates of transient Treg trafficking from the tumour to the TDLN, other organs and the spleen respectively. F: Rates of trafficking of Tregs from the TDLN to other organs.

### 2.4.6 CT26 Tregs significantly accumulate in lymphoid organs

We previously used the mathematical model to predict the initial distributions of red transient Tregs in CT26 and MC38 tumours. Figure 2.14A highlights that initial transient Treg distributions in CT26 and MC36 tumours do not significantly differ. Thus, to assess the effect of tumour heterogeneity on Treg trafficking profiles, we evaluated how CT26 and MC38 Tregs differed in their accumulation in the TDLN and spleen (Fig 2.15).

CT26 Treg numbers rapidly accumulated in the TDLN (Fig 2.15A-B) while MC38 Tregs exhibited transient behaviour characterised by an initial increase followed by a drop by 120 hours (Fig 2.15C). Across the experimental time scale, there were more CT26 Tregs in the TDLN than MC38 Tregs (Fig 2.15B-C).

Similarly, CT26 Tregs accumulated in the spleen to a larger extent than MC38 Tregs (Fig 2.15 D-F). From this analysis, we concluded that Tregs emerging from CT26 and MC38 tumours have heterogeneous trafficking profiles. In particular, CT26 Tregs significantly accumulate in lymphoid organs in comparison to MC38 Tregs.

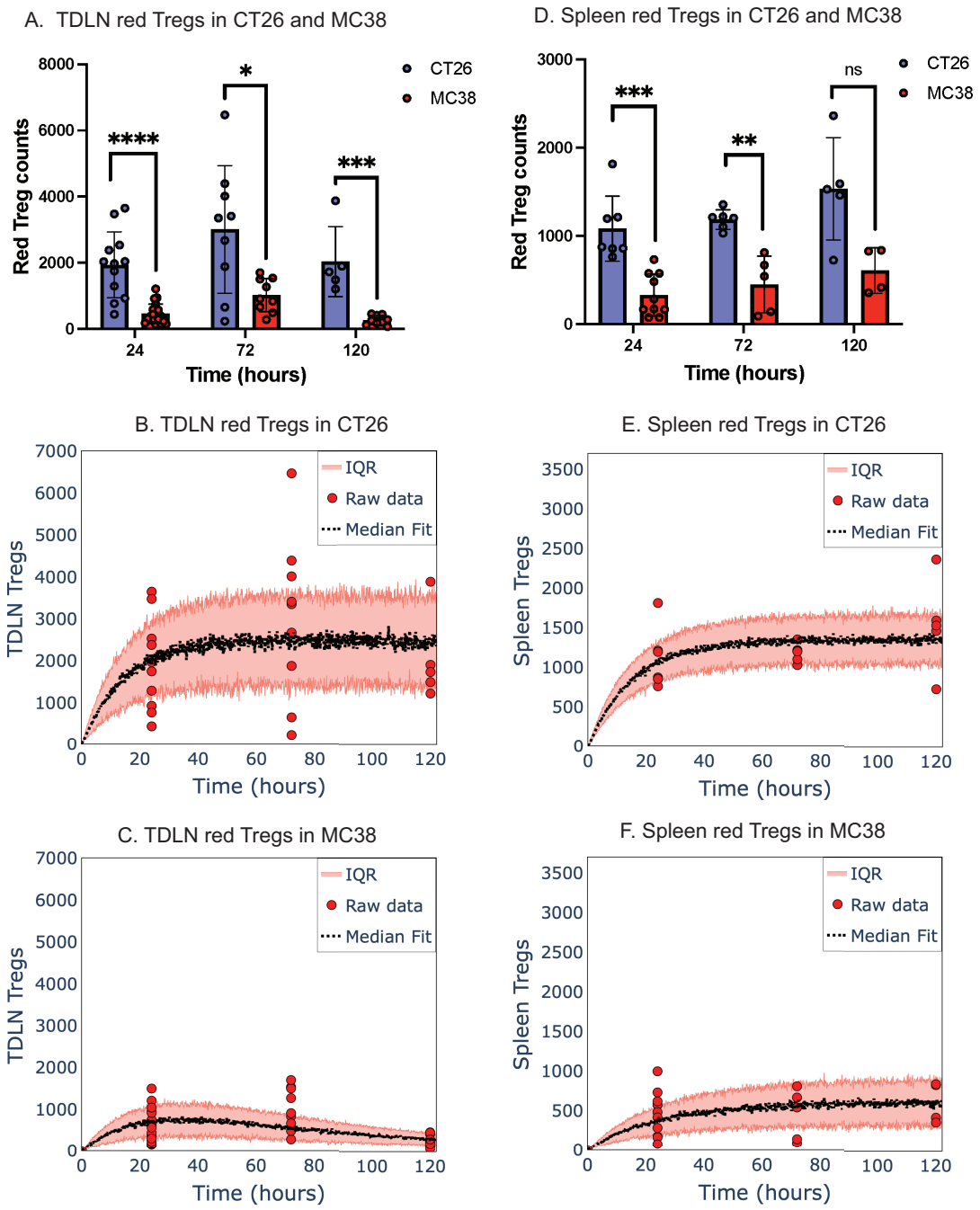



**Figure 2.15: CT26 Tregs significantly accumulate in lymphoid organs**. A: More red Tregs from the CT26 tumour accumulate in the TDLN in contrast to MC38 Tregs (horizontal lines within bars depict the mean and standard deviation). B-C: The mathematical model fits to the red Tregs that accumulate in the TDLNs from CT26 and MC38 tumours respectively. D: Tregs from CT26 tumours accumulate in the spleen to a larger extent than MC38 Tregs (horizontal lines within bars depict the mean and standard deviation). E-F: The dynamical profiles of red Tregs accumulating in the spleen from CT26 and MC38 tumours respectively. The colored dots represent Treg numbers from each mouse. Black curves are the median fits of the model and the red shaded region is the inter-quartile range (IQR) for a total of 300 samples from the posterior distribution. The Mann-Whitney U-test was used to compare C26 and MC38 Treg numbers in the TDLN and spleen. Calculated p-values were as follows: *$p < 0.05$, **$p < 0.01$, ***$p < 0.001$, ****$p < 0.0001$.

### Investigating heterogeneous Treg trafficking using sensitivity analysis

To investigate how the differences between CT26 and MC38 Treg mathematical model parameters could explain the observed differences in Treg accumulation in lymphoid organs, we applied sensitivity analysis using eFAST. We determined both first and total-order sensitivity indices with the aim of identifying parameters that influence the dynamics in the TDLN and spleen (Fig 2.16).

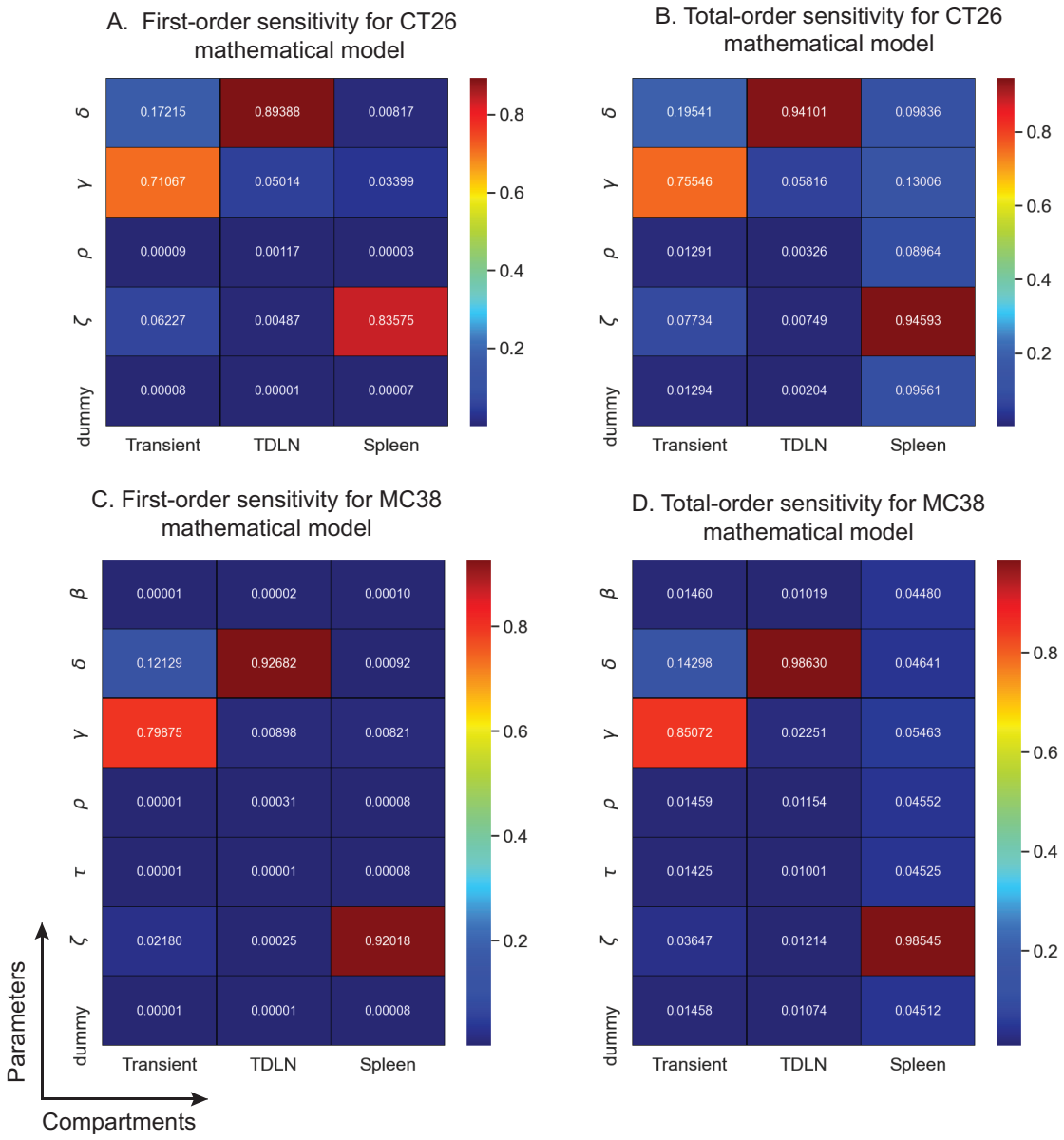



**Figure 2.16: Identifying parameters that influence dynamics observed in lymphoid compartments**. A-B: First and total order sensitivity indices derived from the CT26 mathematical model parameter distributions. C-D: First and total order sensitivity indices determined using the MC38 mathematical model parameter distributions.

Our analysis revealed that for both MC38 and CT26, the parameters $\delta$ and $\zeta$ are critical for the accumulation of red Tregs in the TDLN and spleen respectively (Fig 2.16). Next, we compared the inferred CT26 and MC38 posterior distributions for $\delta$ and $\zeta$. We observed that both parameters were significantly higher for the CT26 mathematical model in contrast to the MC38 model (Fig 2.17). Thus, we concluded that the significant accumulation of CT26 Tregs in lymphoid tissue arises in the mathematical model due to higher parameter values of $\delta$ and $\zeta$ that govern the trafficking of red Tregs to the TDLN and spleen respectively.

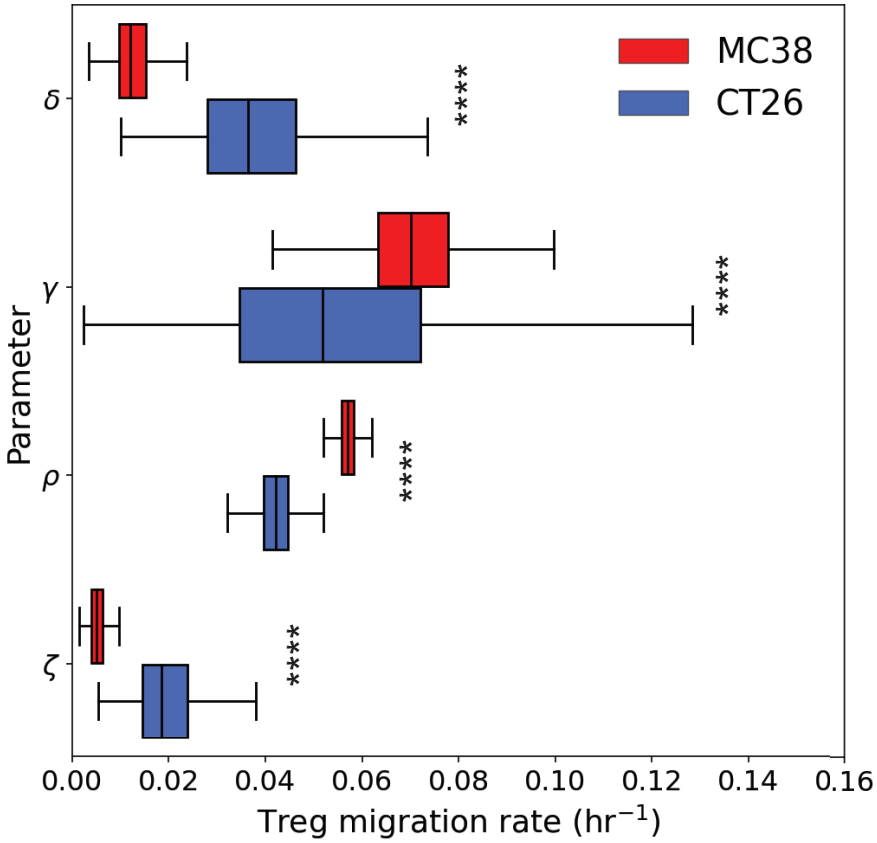



**Figure 2.17: Comparing CT26 and MC38 Treg trafficking parameters**. We compared the inferred MC38 and CT26 Treg trafficking parameter distributions and saw statistically significant differences. The boxes show the $25^{th}$, median and $75^{th}$ percentiles. Whiskers show the rest of the distribution. The Mann-Whitney U-test was used to compare averages between MC38 and CT26 parameters. Calculated p-values were as follows: *p $<$ 0.05, **p $<$ 0.01, ***p $<$ 0.001, ****p $<$ 0.0001.

## 2.5 Discussion

Extensive research on the TME has revealed that Tregs contribute to the inhibition of beneficial anti-cancer responses, leading to resistance against immunotherapy (Kamada et al., 2019) and tumour progression (Nishikawa and Sakaguchi, 2014; Cinier et al., 2021). Targeting intratumoral Tregs via antibody-mediated blockade or cellular ablation is a promising strategy for next-generation immunotherapy. Therefore, establishing deep understanding of intratumoral Treg migration characteristics is pivotal for improving Treg-targeting therapeutics and informing effective administration dosages, regimens and routes. However, due to experimental constraints, little work has been done to quantitatively model intratumoral Treg dynamics.

The objective of this chapter was to characterise intratumoral Tregs both qualitatively and quantitatively by applying mathematical modelling and Bayesian parameter inference to time-course Treg data derived from CT26 and MC38 syngeneic experimental models. Our aim has been to investigate the presence of resident and transient Tregs in the tumour and assess how different tumour types are predicted to affect Treg trafficking profiles.

Assessment of MC38 and CT26 tumour growth dynamics indicated that within the experimental time frame, both tumour types exhibited approximately linear growth. This was not surprising, particularly because only 120 hours of tumour growth post tumour photoconversion were observed. Therefore, the linear model appeared to be a reasonable and simple description of the observed tumour growth patterns. The broadly similar tumour sizes that were used for both tumour types allowed us to easily perform comparative analysis of Treg dynamics between tumours. However, in reality, MC38 and CT26 tumours exhibit approximately exponential growth patterns over long time as has been extensively studied (Taylor et al., 2019).

To investigate the distribution of TDLN Tregs across the spleen and the tumour, we leveraged the MC38 TDLN photoconversion dataset. Our mathematical model predicted an exponential drop in red TDLN Tregs over time. This was consistent with prior work that demonstrated a 76% drop in inguinal lymph node T cells 24 hours post

lymph node photoconversion (Tomura et al., 2008). Over time, the model predicted that virtually all red Tregs egress the TDLN without leaving behind a significant TDLN-resident Treg population.

As red TDLN Tregs traverse the mouse body, a tiny fraction of TDLN Tregs homes to the tumour, resulting in very few red Tregs accumulating in the tumour. This finding was expected given that the tumour is very small compared to the rest of the mouse body. Interestingly, the few Tregs that infiltrated the tumour exhibited transient behaviour. This suggested that the majority of Tregs that establish residency in the tumour likely originate from other organs apart from the TDLN. Furthermore, TDLN Tregs may be transcriptionally distinct from tumour Tregs resulting in transient behaviour that is observed in the tumour. In contrast, substantial numbers of Tregs from the TDLN infiltrated the spleen. Assuming that the red TDLN Tregs express lymph node and lymphoid tissue homing markers such as Ccr7 (Schneider et al., 2007), we would expect that a significant fraction of Tregs that leave the TDLN would end up in lymphoid organs such as the spleen as observed in the data.

In contrast to TDLN Tregs, we observed that Tregs in both MC38 and CT26 tumours consist of resident and transient Tregs. This indicates that tumour Tregs are heterogeneous in their migratory profiles. Prior work has qualitatively pointed out the possibility of both resident and transient Tregs in MC38 tumours (Ikebuchi et al., 2021). Furthermore, the original publication from which part of the MC38 dataset was taken has indicated that some Tregs remain in MC38 tumours long after photoconversion (Li et al., 2022).

However, unlike the investigations in this chapter, prior studies have not applied mathematical modelling to quantify the rates at which transient Tregs leave the tumour and mathematically demonstrate the necessity for a resident Treg population to explain the observed dynamics. The knowledge of Treg migration rates from the tumour is critical for the development of cellular analogues of Pharmacokinetic and Pharmacodynamic models that can be used to simulate dose-response, investigate the therapeutic window of efficacy and direct the development of immunotherapy (Gueorguieva et al., 2014).

Due to their differences in migration profiles, the two intratumoral Treg sub-populations likely exhibit significant transcriptional differences. Using flow cytometry, prior work has demonstrated that Tregs that remain in the tumour more than 8 hours post tumour photoconversion are highly immunosuppressive (Ikebuchi et al., 2021; Li et al., 2022). Thus, it is clear that tumour-resident Tregs are more immunosuppressive than transient Tregs and are therefore a key target for blockade or depletion. This implies that experimental methods that first filter away transient Tregs from the tumour, such as photoconvertible systems, need to be applied to reduce the confounding effect of transient Tregs when identifying therapeutic markers that are unique to tumour-resident Tregs.

Given inter-species differences between mouse syngeneic tumour models and human tumours (Zhong et al., 2020), it is not clear but possible that there may be resident and transient Tregs in humans. Due to ethical and practical considerations, it may be infeasible to investigate the presence of tumour-resident and transient Tregs in humans using similar approaches used in this study. However, characterisation of intratumoral Tregs in humans using methods such as scRNA-seq could identify Treg subsets with different expression levels of immunosuppressive molecules to indirectly infer the possibility of tumour-resident and transient Tregs in the context of human tumours.

One of the main challenges in treating human tumours is the extensive heterogeneity that the tumours exhibit across different patients and tumour types. Therefore, it is critical to investigate how different tumour types affect Treg trafficking characteristics. Prior work has highlighted significant longitudinal immune cell dynamical differences between CT26 and MC38 tumours. For instance, over time Treg numbers in CT26 tumours drop while those in MC38 tumours remain stable (Taylor et al., 2019). To investigate the effect of tumour type on Tregs kinetics, we compared the migration patterns of Tregs originating from CT26 and MC38 tumours.

We observed that MC38-derived Tregs peaked in the TDLN early but exhibited transient behaviour with time. This agreed with prior work that demonstrated that T cells entering the TDLN from the LLC tumour model peaked at 24 hours post tumour photoconversion but gradually dropped over time (Torcellan et al., 2017). Interestingly,

CT26-derived Tregs deviated from this behaviour. Instead, they accumulated in the TDLN and spleen. These distinct mechanisms could form a basis for heterogeneous responses to Treg-targeting immunotherapy. As the TDLN is an immunologically important organ where T cells are primed, the accumulation of tumour Tregs in the TDLN could result in immunosuppression thereby attenuating the extent to which conventional naive T cells are primed to restrict tumours.

While the destination of CT26 Tregs appears to be lymphoid tissue, it remains unclear where MC38 Tregs are migrating to. Transcriptionally characterising MC38 Tregs using scRNA-seq and experimentally assessing additional organs for the red Tregs following MC38 photoconversion may provide further insight into where MC38 Tregs tend to localise.

Inevitably, mathematical modelling involves extensive simplification of the underlying biology. Therefore, while it gives us useful insight, our mathematical modelling framework is not perfect. Firstly, our dataset is not only noisy, but also has limited time points. This resulted in inferred parameter distributions with significant levels of uncertainty.

Secondly, we had an unequal number of datasets between the two tumour experimental models. The MC38 dataset consisted of two independent datasets, one involving the photoconversion of the tumour and the other, TDLN photoconversion. This allowed us to additionally model the trafficking of TDLN Tregs to the spleen and the tumour in the context of the MC38 but not CT26 experimental model. Therefore, the MC38 mathematical model had two additional parameters in contrast to the CT26 mathematical model and this imbalance may have affected the comparison between MC38 and CT26 Treg trafficking parameters. However, sensitivity analysis showed that the models are insensitive to the two additional parameters, justifying the structure of the CT26 mathematical model and allowing us to compare parameters from the two mathematical models.

Thirdly, the red Tregs were quantified from both tumours consisting of resident and transient Tregs. It is not possible to tell which of the red Tregs are resident and which

are transient from the raw data alone, apart from observing transient Tregs populating the TDLN and the spleen. Therefore, modelling the exact dynamics associated with resident Tregs was not possible. Long timescale red Treg data could have enabled us to define the dynamics of resident Tregs, which start dominating a long time after tumour photoconversion. However, the red Kaede signal decays over time making it impossible to distinguish between green and red Tregs at later time points. These limitations ultimately led us to assume that, due to the short experimental time scale we are considering, resident Treg numbers may not be significantly changing and could be modelled as a constant population.

However, despite these limitations, the study provides mechanistic insights into the different intratumoral Treg sub-populations and their heterogeneous trafficking profiles, which can inform future studies. To our knowledge, it is also the first study that has quantified the rates at which tumour Tregs migrate to lymphoid tissue and demonstrated the presence of resident and transient Tregs in tumours using mathematical modelling.

### Conclusion and future work

In this chapter, we hypothesised that there are resident and transient Tregs in CT26 and MC38 experimental tumour models. Through applying mathematical modelling, we showed that a significant fraction of tumour Tregs leaves both tumours in order to reproduce the dynamics seen in the TDLN and spleen. This implies that the Tregs that are still observed at later time points in the tumours constitute a tumour-resident population. Furthermore, our study highlighted that Tregs from CT26 tumours significantly accumulate in lymphoid organs. Given trafficking differences between resident and transient Tregs as well as MC38 and CT26 Tregs, we hypothesised that these Treg subsets are transcriptionally different. Therefore, the aim of the proceeding chapter has been to characterise Treg subsets using scRNA-seq datasets.

# 3

# Transcriptional characterisation of intratumoral Tregs

Contents


3.1 Introduction . . . . . 94
3.2 Aims . . . . . 96
3.3 Materials and Methods . . . . . 96
3.4 Results . . . . . 111
3.5 Discussion . . . . . 144


In Chapter 2, we used mathematical modelling to quantify the migration kinetics of Tregs from MC38 and CT26 tumours. Mathematical modelling estimated Treg migration rates and predicted the presence of resident and transient Tregs in both tumours. CT26 Tregs were found to accumulate in the TDLN and spleen to a greater extent than MC38 Tregs, suggesting intertumoral heterogeneity in Treg trafficking behaviour. Based on these findings, we hypothesised that there are significant differences in gene expression patterns between MC38 and CT26 Tregs, as well as tumour-resident and transient Tregs. Therefore, the objective of this chapter has been to explore these transcriptional differences using scRNA-seq datasets.

## 3.1 Introduction

The contributions of intratumoral Tregs in suppressing immune responses and promoting tumour growth are well documented (Bates et al., 2006; Kang et al., 2013; Watanabe et al., 2019; Tao et al., 2012; Ménétrier-Caux et al., 2012). Due to potential applications in cancer treatment, the characterisation and therapeutic targeting of intratumoral Tregs have become active areas of research. However, extensive Treg heterogeneity has been observed both inter- and intratumorally, complicating the rapid adoption of Treg blockade/depletion as a strategy for cancer immunotherapy.

Taking into account intertumoral differences, mouse models such as CT26 and MC38 respond differently to treatment and exhibit significant differences in immune cell infiltrate densities (Goggi et al., 2020; Taylor et al., 2019). In contrast to MC38, CT26 Treg densities peak early during tumour development, but rapidly drop with time. Paradoxically, other immune cells such as CD8 T cells continue to accumulate in CT26 tumours over time (Taylor et al., 2019). This suggests that the extent to which intratumoral Tregs facilitate immune escape probably differs between murine syngeneic tumour models. Caution should be taken when timing the administration and evaluating the effect of Treg-targeting immunotherapy in murine tumour models (Taylor et al., 2019).

Although divergent dynamics in MC38 and CT26 Tregs have been experimentally observed, the molecular drivers of this behaviour have not been fully studied. To our knowledge, no transcriptional characterisation of MC38 and CT26 Tregs has been performed. Differences in the degree to which MC38 and CT26 Tregs differentiate towards a tumour-resident phenotype and the differential expression of chemokine receptors may lead to the observed dynamical differences.

Considering intratumoral Treg heterogeneity, different subpopulations of Tregs have been transcriptionally identified in syngeneic tumour models (Li et al., 2022; Bhatt et al., 2021). Emerging research, including our own, has shown that intratumoral Treg subsets exhibit different migration behaviour. In particular, Ikebuchi *et al.* have used flow

cytometry and photoconvertible KikGR mice to show that the Tregs that are retained in MC38 tumours 8 hours after tumour photoconversion upregulate Lag3, Gzmb, Cd25, Il10, and Cd39. Interestingly, the expression of Ctla4, which is typically associated with immunosuppressive Tregs, did not differ between resident and transient Tregs. On the other hand, transient Tregs were shown to upregulate Nrp1 (Ikebuchi et al., 2021). Similarly, Li *et al.* used flow cytometry and photoconvertible Kaede mice to show that Lag3 is one of the genes that define Tregs retained in the MC38 tumour model (Li et al., 2022). Although both studies identified some of the markers associated with resident Tregs, more characterisation of tumour-resident and transient Tregs needs to be performed using scRNA-seq data to expand the arsenal of potential therapeutic targets. Furthermore, biological pathways that differ between tumour-resident and transient Tregs still need to be explored to develop deeper mechanistic understanding.

It is well known that the TME is characterised by diminished metabolites, and a poor blood supply which leads to hypoxia. Cancer cells are glycolytic, favouring the rapid metabolism of glucose to produce lactic acid, which in turn, acidifies the TME (Hanahan and Weinberg, 2011). These conditions suppress effector T cells but, interestingly, allow Tregs to maintain their suppressive capacity. Prior work has shown that, unlike conventional T cells, Tregs are capable of modifying their metabolism to adapt to the TME. They metabolise lactic acid and use it as an alternative fuel source. Lactic acid not only stabilises Tregs over time, but also induces them to be more immunosuppressive (Watson et al., 2021). Hypoxia in the TME promotes Hif1a expression in Tregs, which similarly increases their immunosuppressive capacity (Ben-Shoshan et al., 2008). Therefore, it is possible that tumour-resident and transient Tregs differ not only in their immunosuppressive capacity but also metabolically.

The objective of this study has been to transcriptionally explore the heterogeneity of intertumoral and intratumoral Tregs using MC38 and CT26 syngeneic tumour models. Inspired by the results of Chapter 2, we hypothesised that the extent of Treg activation and chemokine expression account for the differences in Treg dynamics between MC38 and CT26 Tregs. Considering tumour-resident and transient Tregs, we hypothesised that

resident Tregs exhibit an effector Treg phenotype required to promote immunosuppression in the tumour while transient Tregs have a naive-like phenotype, expressing markers such as Ccr7, which are associated with migration out of the tumour and towards lymph nodes. Furthermore, because tumour-resident Tregs are sustained in the hypoxic and poorly nourished TME, we hypothesised that there are significant metabolic differences between tumour-resident and transient Tregs.

## 3.2 Aims

To summarise, the aims of the study were as follows:

- Use scRNA-seq data analysis to compare MC38 and CT26 Tregs for differences in Treg activation and expression of cell migration markers.
- Transcriptionally compare tumour-resident and transient Tregs to identify resident Treg markers, that can potentially be used to inform the development of Treg-targeting cancer immunotherapy.
- Bioinformatically explore biological pathways that differ between tumour-resident and transient Tregs.

## 3.3 Materials and Methods

### 3.3.1 CT26 and MC38 scRNA-seq datasets

We investigated gene expression differences between CT26 and MC38 Tregs using public scRNA-seq datasets. The CT26 dataset was obtained from Qu *et al.*'s study that focused on identifying immune cells that promote response to Avelumab (anti-PDL1) treatment (Qu et al., 2020). In summary, the authors bilaterally implanted CT26 tumours on the left and right flanks of 6 to 8-week-old female Balb/c mice. They then resected tumours from the left flanks 8 days after tumour implantation, leaving

behind tumours on the right flanks (Qu et al., 2020). Next, they isolated $CD45^+$ cells from resected tumours and performed scRNA sequencing. Qu *et al.* proceeded to treat the mice with Avelumab and stratified them into responders and nonresponders based on the outcome of the treatment (Qu et al., 2020). Finally, using scRNA-seq data of tumour-infiltrating immune cells prior to treatment, the authors identified a pro-inflammatory $F480^+MHCII^+Ly6C^{lo}$ Cxcl9-producing macrophage population that was present in the TME of responders before treatment (Qu et al., 2020).

We identified MC38 scRNA-seq data from Bhatt *et al.*'s study on T cell dynamics and therapeutic interventions in various tumour models (Bhatt et al., 2021). To generate this dataset, the authors subcutaneously implanted MC38 tumours in 4 C57BL/6 female mice between 6-8 weeks of age. 16 days after tumour inoculation, $CD3^+$ T cells were isolated from tumours, TDLNs, blood and spleens and used to perform scRNA sequencing. Through scRNA-seq analysis, they identified $Ccr8^+$ intratumoral Tregs and demonstrated the therapeutic benefit of Treg-depleting anti-CCR8 antibodies in CT26 tumours and the synergy between anti-CCR8 and anti-PD1 treatment in MC38 tumours (Bhatt et al., 2021).

Table 3.1 summarises the two scRNA-seq datasets that we used to investigate differences between Tregs derived from MC38 and CT26 tumours. Figure 3.1 highlights the analysis pipeline that was applied to the MC38 and CT26 scRNA-seq datasets.

**Table 3.1: Table summarising the MC38 and CT26 scRNA-seq datasets**. The count matrices for both datasets were generated after aligning the raw reads with the mm10 genome build to eliminate batch effects that could potentially arise from aligning the reads to different genome builds.

| Tumour | Number of mice | Total Tregs | Genome build | Source |
|---|---|---|---|---|
| CT26 | 30 | 6739 | mm10 | Qu et al. (2020) |
| MC38 | 4 | 2704 | mm10 | Bhatt et al. (2021) |

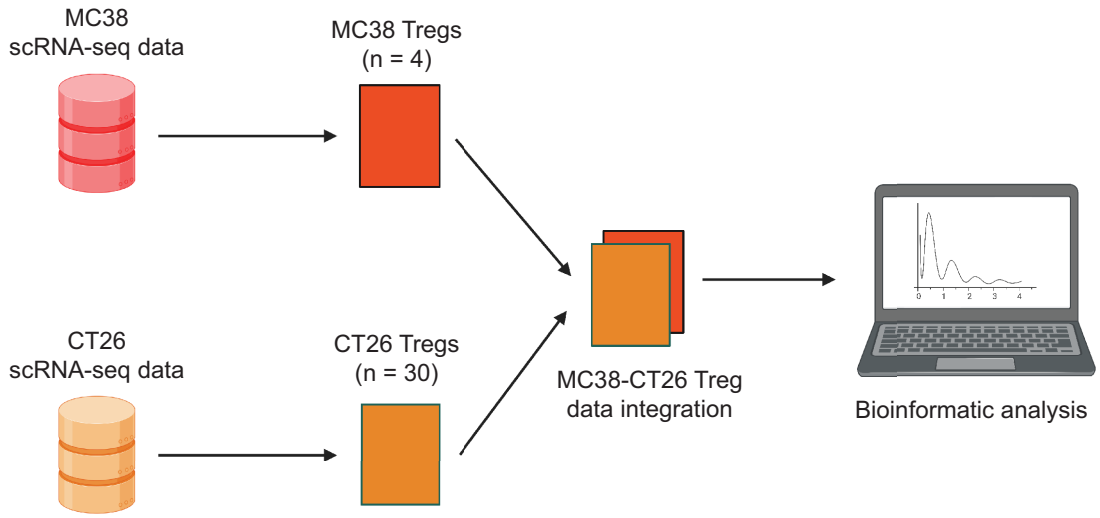



**Figure 3.1: MC38 and CT26 Treg scRNA-seq extraction and analysis pipeline**. Tregs were isolated from the public MC38 and CT26 scRNA-seq datasets and integrated together to perform bioinformatic analysis. The figure was created using Biorender.

### 3.3.2 Single cell sequencing of MC38 Kaede Tregs

To investigate the transcriptional differences between intratumoral Treg subsets in the Kaede experimental model, we applied scRNA-seq analysis. Two independent experiments were carried out to generate the scRNA-seq data. The first experiment was carried out by our collaborators as part of their published study on CD8 T cell dynamics in MC38 (Li et al., 2022).

In this study, C57BL/6 Kaede mice were inoculated with 250 000 MC38 cancer cells and tumours were grown for 11 days as previously described in the Methods section of Chapter 2. On the $11^{th}$ day, the tumours were photoconverted and tumours of similar size were extracted at 24 and 72 hours after tumour photoconversion. After tumour homogenisation, the red and green tumour-infiltrating lymphocytes were sorted as live $CD45^{+}Ter119^{-}CD11b^{-}$ cells using flow cytometry (Li et al., 2022). The 10X Genomics 3' version 2 kit was used for library preparation and the CellRanger pipeline (Zheng et al., 2017) was used to generate scRNA-seq count matrices (Li et al., 2022).

The second Kaede scRNA-seq dataset was also generated by our collaborators, but it has not yet been published. Similarly, Kaede mice were implanted with MC38

tumours that were later photoconverted after 11 days of tumour growth. Red and green lymphocytes were isolated from tumours of similar size at 48 hours after tumour photoconversion. Additionally, red lymphocytes were collected in the TDLN 48 hours after tumour photoconversion. As a control, green lymphocytes were harvested from inguinal lymph nodes from tumour-naive Kaede mice. Figure 3.2 and Table 3.2 summarise the Kaede scRNA-seq experiments.

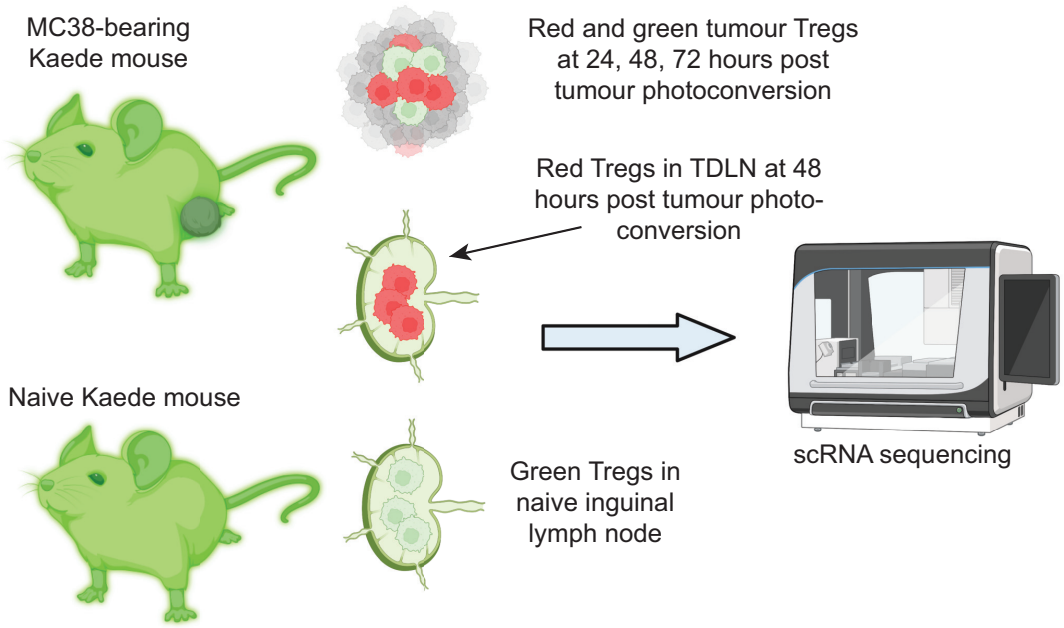



**Figure 3.2: Kaede scRNA-seq experimental set up (n = 19)**. Red and green T cells were isolated from MC38 tumours at 24, 48 and 72 hours post tumour photoconversion. In addition, tumour-transient T cells (red) were harvested from the TDLN at 48 hours post tumour photoconversion. Finally green lymphocytes were collected from inguinal lymph nodes of naive Kaede mice. The figure was created using Biorender.

**Table 3.2: Table summarising the MC38 Kaede scRNA-seq experiments**. Tregs were isolated from 13 and 6 mice in the first and second experiments, respectively. nDLN refers to the normal draining lymph node/inguinal lymph node in tumour-naive mice.

| Dataset | Total mice | Total Tregs | Genome build | Source |
|---|---|---|---|---|
| Tumour Tregs 24, 72 hours | 13 | 911 | mm10 | Li et al. (2022) |
| Tumour, TDLN, nDLN Tregs 48 hours | 6 | 2494 | mm10 | David Withers' lab |

### 3.3.3 scRNA-Seq analysis pipeline

The scRNA-seq data described in previous sections is high-dimensional. Therefore, it is almost impossible to draw insights from it in its raw form. To gain biological insight from the scRNA-seq data, we made use of Scanpy, a Python framework developed for the analysis of scRNA-seq data (Wolf et al., 2018). In this section, we briefly describe the Scanpy scRNA-seq analysis pipeline that we adopted. For a more detailed description, we refer the reader to the Methods section of Chapter 4, where we demonstrate the development of murine and human Treg scRNA-seq meta-atlases.

The scRNA-seq sub-datasets from different experiments were first concatenated as annotated tables (Wolf et al., 2018). Genes that were unique to one sub-dataset were filtered out as they could give rise to non-biological effects during downstream analyses. Next, quality control was performed by removing cells expressing less than 250 genes or filtering out genes present in fewer than 3 cells. Cells with mitochondrial transcripts that represented more than 10% of the total genes were removed as they were likely to have been compromised during sample preparation. Next, library size normalisation was performed to correct for skewed gene counts in independent sub-datasets. The gene matrices were then logarithmically transformed to reduce the numerical range of gene expression profiles.

To improve scRNA-seq data visualisation, genes that varied significantly across cells were determined and used to perform Principal Component Analysis (PCA). Cell cycle scoring was performed followed by doublet removal using Scrublet (Wolock et al., 2019). Sources of unwanted variation, including the fraction of mitochondrial genes and the cell cycle stage of individual cells, were regressed followed by batch correction, which was performed at the PCA level using Harmony (Korsunsky et al., 2019a). The extent of data integration achieved using Harmony was assessed through calculating the Local Inverse Simpson's Index (LISI) distribution, which is peaked at a low value for poorly corrected data and shifted towards higher values in the case of well integrated data (Korsunsky et al., 2019a). Finally, cell communities with similar gene expression profiles

were identified and visualised on a Uniform Manifold Approximation and Projection plot (UMAP) (McInnes et al., 2018).

### 3.3.4 Differential expression analysis

To identify sets of genes that differ between MC38 and CT26 Tregs, and tumour-resident and transient Kaede Tregs, we performed differential gene expression analysis. This method was designed to assess whether the difference in gene counts observed between two conditions/treatments is statistically significant. Traditionally, differential gene expression analysis has been applied to microarray and bulk RNA sequencing data. The advent of scRNA-seq has necessitated the need for new differential expression analysis methods that are suitable for the zero inflated, bimodal expression patterns seen in scRNA-seq datasets (Finak et al., 2015).

Some of the methods that have been developed specifically for analysing scRNA-seq data include MAST (Finak et al., 2015), SCDE (Kharchenko et al., 2014) and $D^3E$ (Delmans and Hemberg, 2016). In addition to these methods, bulk differential expression analysis tools such as DESeq2 (Love et al., 2014) and EdgeR (Robinson et al., 2010) have been recommended for pseudo-bulked scRNA-seq data (Squair et al., 2021). Pseudo-bulking refers to the summation and averaging of scRNA-seq counts across different samples to create a modified gene expression matrix that resembles bulk RNA-seq data. Ultimately, the design of the scRNA-seq experiment dictates which method would be used to perform differential expression analysis, as highlighted in the following sections.

#### Identifying differentially expressed genes from Kaede Treg scRNA-seq data

To find differentially expressed genes between tumour-resident and transient, as well as red and green Kaede Tregs, we used a tool called Model-Based Analysis of Single Cell Transcriptomics (MAST) (Finak et al., 2015). We accessed MAST through Libra (Squair et al., 2021), an R package that provides an easy interface to different differential expression analysis tools with minimal programming requirements. Our

rationale behind using MAST instead of first pseudo-bulking the data and using more common tools like EdgeR was that the Kaede scRNA-seq experiments were pooled. Thus, it was not possible to connect individual cells to their mouse of origin, which is a key requirement for pseudo-bulking.

MAST uses a hurdle model to perform differential expression analysis between two conditions of interest or cell populations. A hurdle model is a statistical framework that models a random variable using two parts (Cragg, 1971). The first part models whether a given gene is expressed or not, which addresses the zero-inflated nature of single-cell data, using logistic regression. The second part models non-zero gene expression counts using a Gaussian linear model (Finak et al., 2015).

Following the fitting of the model, MAST determines the likelihood of the data under the assumption that there are no differences in gene expression between the two test conditions (null hypothesis). In addition, it determines the likelihood of the data assuming there are differences in gene expression between test conditions (alternate hypothesis) (Finak et al., 2015). Finally, differentially expressed genes are identified using the likelihood ratio test (LRT) outlined below:

$$R = -2 \cdot \ln\left(\frac{\text{likelihood under null hypothesis}}{\text{likelihood under alternate hypothesis}}\right). \tag{3.1}$$

$R$ follows a $\chi^2$ distribution, and can be used to determine p-values for significance testing. The Benjamini-Hochberg (BH) method is used to adjust the p-values for multiple hypothesis testing (Benjamini and Hochberg, 1995; Finak et al., 2015).

### Identifying differentially expressed genes between MC38 and CT26 Tregs

Unlike Tregs in the Kaede dataset that were pooled, public MC38 and CT26 Tregs were stratified according to the mouse of origin. This allowed us to create a pseudo-bulked gene expression dataset to which we could apply robust bulk RNA-seq methods such as EdgeR or DESeq2 to identify differentially expressed genes. As previous work has

demonstrated the superior performance of EdgeR's likelihood ratio test (LRT) on pseudo-bulked scRNA-seq data (Squair et al., 2021), we decided to use EdgeR to elucidate the transcriptional differences between MC38 and CT26 Tregs.

EdgeR attempts to model both the biological and technical variations in pseudo-bulked scRNA-seq/RNA-seq data using the Gamma and Poisson distributions, respectively (Chen et al., 2014; Robinson et al., 2010). The combination of the two gives rise to a Negative Binomial modelling approach. Using generalised linear models (GLMs), EdgeR is capable of running differential expression analysis for complicated experimental designs, with nested conditions or cell types. Then an empirical Bayes approach is applied to reduce the bias caused by small numbers of samples in the data (Chen et al., 2014). Finally, analogous to MAST, EdgeR performs significance testing using the LRT test. The resulting p-values are adjusted for the false discovery rate using the Benjamini-Hochberg (BH) test (Benjamini and Hochberg, 1995).

### 3.3.5 Gene set enrichment analysis

The differential gene expression analysis methods we have discussed so far identify individual genes that differ significantly in expression between two conditions. However, it is difficult to infer which biological mechanisms are perturbed between conditions of interest by looking at differentially expressed genes alone. To investigate the biological pathways that differ between intratumoral Treg subsets reported in this chapter, we made use of Gene Set Enrichment Analysis (GSEA) (Subramanian et al., 2005) using the clusterProfiler R package (Yu et al., 2012).

The input of GSEA is a gene list $L$, that is obtained after performing differential expression analysis. As a first step, the genes in the list, $g_i$, are ranked in descending order according to their logarithmic fold changes, $r_i$. Thus, $L$, with a total of $N$ genes, can be denoted as:

$$L = \{g_1, g_2, ..., g_N\}, \text{ with log fold changes denoted by } r(g_j) = r_j. \tag{3.2}$$

GSEA then compares the ranked gene list with an established gene set, $S$, which corresponds to a specific biological pathway (for example, cell proliferation), with the

goal of evaluating whether the genes in $S$ appear either at the top or at the bottom of the ranked gene list, $L$ (Subramanian et al., 2005). If most of the genes appear on top of the ranked gene list, then these genes, along with their associated pathway, are upregulated between the conditions of interest. If most genes are found towards the lower end of the list, then the pathway is downregulated. Otherwise, if the genes are unspecifically scattered all over the ranked list, the associated pathway does not differ between the two conditions of interest.

For a comprehensive coverage of biological pathways, we set clusterProfiler to use gene sets in Cellular component (CC), Biological process (BP), and Molecular function (MF) databases, which collectively constitute the Gene Ontology (GO) pathways (Blake et al., 2001). In the following section, we briefly delineate the key steps that constitute GSEA.

### Enrichment score calculation

The Enrichment score ($ES$) summarises the extent to which genes in a given gene set, $S$ (with a total of $N_H$ genes), are skewed towards the top or bottom of the ranked gene list (Subramanian et al., 2005). To determine $ES$, GSEA walks down the genes in $S$ and increments a running-sum statistic when it finds a matching gene in the ranked gene list or reduces it if no matching gene is seen. This creates a Kolmogorov-Smirnov-like statistic whose maximum height represents the $ES$. The subset of genes that drive the $ES$ is referred to as the leading-edge genes (Subramanian et al., 2005). Figure 3.3 summarises the key steps involved in GSEA.

The fraction of hits $P_{hit}(S, i)$, up to the $i^{th}$ gene in L, is weighted by their corresponding logarithmic fold changes as follows:

$$P_{hit}(S, i) = \sum_{g_j \in S,\ j \leq i} \frac{|r_j|^p}{N_R} \quad \text{where} \quad N_R = \sum_{g_j \in S} |r_j|^p. \tag{3.3}$$

The parameter $p$ is referred to as the weighting exponent which is, by default, set to unity (Subramanian et al., 2005). The weighted fraction of misses $P_{miss}(S, i)$, up

to the $i^{th}$ gene in $L$, is denoted as:

$$P_{miss}(S,i) = \sum_{g_j \notin S,\ j \leq i} \frac{1}{N - N_H}, \tag{3.4}$$

where $i$ is the $i^{th}$ position of a gene in the ranked gene list, $N$ is the total number of genes in the gene list and $N_H$ is the total number of genes in the gene set, $S$, that defines the biological pathway (Subramanian et al., 2005). One can show that $ES$ is mathematically equivalent to the maximum difference from zero of $P_{hit} - P_{miss}$ (Subramanian et al., 2005).

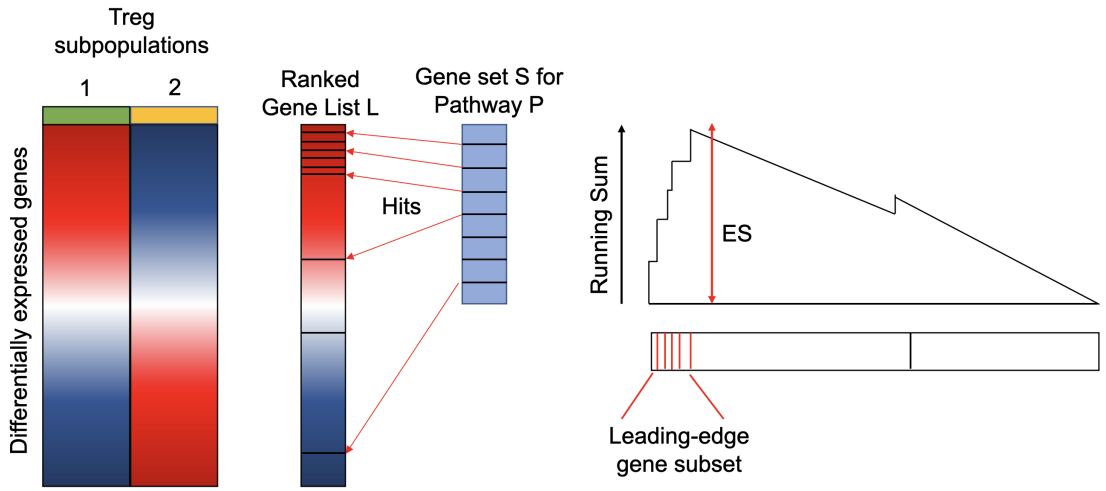



**Figure 3.3: An illustration of how GSEA works**. Differential gene expression analysis between Treg sub-populations 1 and 2 yields a list of differentially expressed genes. The list is then ranked by decreasing log fold values to give rise to $L$. Genes expressed in $L$ are queried against a candidate gene set, $S$, associated with a biological pathway, $P$, to check whether the genes in $S$ appear either at the top or bottom of $L$. The genes that appear in both $L$ and $S$ (referred to as hits here) are used to construct a running sum statistic, whose largest deviation from 0 becomes the $ES$. The genes that are skewed to one end of $L$, which contribute to the $ES$, are the leading-edge genes. The higher the $ES$ value for a given biological pathway, the more likely that pathway is enriched in the ranked gene set. In this figure, the red shade corresponds to genes with high log fold changes while genes with low log fold changes are in blue. Figure reproduced from (Subramanian et al., 2005; Tan et al., 2016) with adaptions, Copyright (2005) National Academy of Sciences.

#### Estimating Enrichment score significance level

To determine the significance level of the $ES$, GSEA performs a permutation test to generate samples that will be used for the null hypothesis, $ES_{null}$. This is achieved by randomly swapping genes along with their logarithmic fold changes between the conditions of interest 1000 times, reranking the gene list, and recomputing $ES$. The p-value is then determined by comparing $ES$ with $ES_{null}$ (Subramanian et al., 2005).

#### Multiple hypothesis testing correction

In practise, GSEA is used to test whether multiple biological pathways are enriched between conditions of interest. This results in the generation of multiple hypotheses, necessitating the need for multiple hypothesis testing correction. To do so, GSEA first normalises $ES$ based on the size of the respective gene set to generate a Normalised Enrichment Score ($NES$). Finally, the false discovery rate (FDR) (Benjamini et al., 2001; Reiner et al., 2003) is used to control for the contribution of false positives to each $NES$ (Subramanian et al., 2005).

### 3.3.6 Trajectory analysis of red and green Kaede Tregs

The most common scRNA-seq analysis method, clustering, categorises cells into distinct clusters in low-dimensional space based on their shared gene expression patterns. Although extremely useful, clustering assumes discrete cellular groupings; yet in reality, cellular processes such as differentiation are dynamic and lie along a continuous trajectory. The need to capture these continuous biological processes has given rise to a class of bioinformatic analysis methods, called pseudotime or trajectory analyses. In general, these methods trace the changes in cellular states along a continuous numerical variable known as pseudotime, which highlights how far the cells are along their differentiation pathway. We adopted pseudotime analysis to trace the developmental trajectories associated with tumour-resident and transient Kaede Tregs.

### Single cell Trajectories Reconstruction, Exploration and Mapping (STREAM)

Multiple trajectory analysis methods have been developed, such as Monocle (Trapnell et al., 2014; Qiu et al., 2017a,b; Cao et al., 2019), PAGA (Wolf et al., 2019), Slingshot (Street et al., 2018) and STREAM (Chen et al., 2019b). However, the vast majority of these methods still fall short on providing more informative visualisations of distinct cell sub-populations along pseudotime particularly for large datasets (Chen et al., 2019b). Furthermore, most of the current tools require raw rather than preprocessed single cell datasets from which to infer trajectories. This requirement is particularly problematic when working with meta-atlases, such as the ones we have been developing, that have significant batch effects, which need to be first corrected before carrying out downstream analysis.

In our search, we found that a trajectory analysis method known as Single Cell Trajectory Reconstruction, Exploration, and Mapping (STREAM) integrated well with our single cell analysis pipeline and could efficiently infer trajectories from raw or preprocessed single cell data (Chen et al., 2019b).

For each gene in all cells, STREAM calculates the mean and standard deviation and fits a nonparameteric local regression (LOESS) curve to the relationship between the mean and standard deviation (Guo et al., 2016). Genes that lie above the curve and are significantly different from the rest are kept as highly variable genes. This process partially reduces the dimensionality of the cell by gene single cell matrix. STREAM further reduces the dimensionality of the dataset by projecting cells in a low-dimensional space using the Modified Locally Linear Embedding (MLLE) method, summarised in Ghojogh et al. (2020).

MLLE follows three basic steps. The first step is to generate a low-dimensional k-NN graph using the K-Nearest Neighbours algorithm. Thus, for each cell, $x_i$, the set of its nearest neighbours $[x_{i1}, ..., x_{ik}]$ is determined. Next, weights that use the k-Nearest

Neighbours to map the low-dimensional embedding back to its original high-dimensional space are determined through running the following constrained optimisation scheme:

$$\begin{aligned} \text{minimise}(\tilde{w}) &:= \sum_{i=1}^{n} \left\| x_i - \sum_{j=1}^{k} \tilde{w}_{ij} x_{ij} \right\|_2^2, \\ \text{Subject to} \quad & \sum_{j=1}^{k} \tilde{w}_{ij} = 1, \forall i \in \{1, ..., n\}, \end{aligned} \tag{3.5}$$

where $j$ is $x_i$'s $j^{th}$ nearest neighbour and $\tilde{w}_{ij}$ is the weight that maps $x_{ij}$ to $x_i$ (Ghojogh et al., 2020). Following this optimisation, a further optimisation using the resulting weights to determine n vectors in a lower, $p < n$, dimensional space generates an embedding of the data points onto this lower dimensional space.

By default, STREAM uses a neighbourhood size of approximately $10\%$ of the original data when running the k-NN algorithm. Furthermore, $p = 3$ components are used in MLLE as they can capture the overall structure of the data, although this number can be changed for more complex trajectories (Chen et al., 2019b).

Following reduction in dimensionality, STREAM creates a Minimum Spanning Tree (MST), a non-cyclic graph structure that highlights the loose connectivity between cells (Chen et al., 2019b). The MST is then used as the initial starting point for an Elastic Principal Graph (ElPiGraph), which is a tool that is used to learn nonlinear geometries and topologies from high-dimensional data sets using gradient descent approaches (Albergante et al., 2020).

To learn trajectory topologies, ElPiGraph mimics physical springs with potential elastic energy. The algorithm minimises the mean square distance between the graph vertices and the data points to determine the finer structures. Elastic potential energy is then calculated to penalise spurious stretching and bending of learned branches (Chen et al., 2019b). Additional modifications such as pruning branches, shifting, and extending nodes can be applied as necessary using biological knowledge from the dataset. The learned trajectories can be visualised in 2-dimensional space as a Flat tree plot or along pseudotime as a Stream map plot (Chen et al., 2019b).

### Detecting diverging, transition and leaf genes

A key application of trajectory analysis is the identification of genes that are differentially expressed at different events along pseudotime. To this end, STREAM can detect diverging, transition and leaf genes. Diverging genes are defined as genes that mark branching points along pseudotime, whereas transition genes are genes with expression patterns that correlate with pseudotime. Finally, leaf genes are genes that are upregulated along individual branches (Chen et al., 2019b). Below, we briefly describe how STREAM determines diverging genes.

Let us consider a pair of branches, $B_a$ and $B_b$ with gene expression across branch cells defined as $G_a$ and $G_b$ respectively. STREAM standardises the gene expression to be bounded in the interval $[0, 1]$. Next, the mean and standard deviations are determined for each gene. A log2-fold change of greater than 0.25 is used as a cut-off to remove genes that are not significantly different between the two branches. Using the remaining genes in each branch, STREAM applies the Mann-Whitney U test to assess whether $G_a > G_b$ or vice versa. The U statistic is then normalised by Z-scoring and a Z-score difference threshold of 2 is applied to identify diverging genes between two branches (Chen et al., 2019b).

Transition genes are determined in a similar manner. For each branch, $B_i$, the gene expression matrix, $G_i$, is scaled so that the expression values lie in $[0, 1]$. Individual genes are assessed for gene expression differences at the beginning and the end of pseudotime within $B_i$ using log2-fold change. If log2-fold change is greater than 0.25, STREAM calculates the Spearman's rank correlation between the inferred pseudotime and gene expression. Genes with Spearman's rank correlation of greater than 0.4 are reported as transition genes within the branch (Chen et al., 2019b).

Finally, STREAM calculates leaf genes by first scaling the expression of each gene, $E$, in all leaf branches to lie in the interval $[0, 1]$. Mean gene expression is determined and then Z-scored. If there is a leaf branch with a Z-score value greater than 1.5, it is selected as the candidate branch for downstream analysis. The Kruskal-Wallis H

test and post hoc pairwise Conover tests are then sequentially applied to identify leaf genes associated with the candidate branch (Chen et al., 2019b).

### 3.3.7 Simulating metabolic reactions from scRNA-seq data

We used the Compass algorithm (Wagner et al., 2021) to simulate metabolic reactions in tumour-resident and transient Tregs at steady state. Compass uses Recon2, which is a mathematical model that encodes metabolic reactions (Thiele et al., 2013). Using normalised scRNA-seq data, Compass simplifies metabolic modelling by applying Flux Balance Analysis (FBA), a computationally tractable method for simulating metabolism from genome-wide metabolic networks. The scRNA-seq matrix is converted into a reaction matrix in which each row corresponds to an individual metabolic reaction and each column denotes an individual cell. The reaction matrix is then processed to generate reaction penalties that are inversely proportional to the scRNA counts that encode metabolic enzymes. Next, Compass uses linear optimisation to identify the metabolic flow distribution that minimises reaction penalties and generates a matrix of reaction scores, which highlight the occurrence likelihood of each metabolic reaction (Wagner et al., 2021).

Compass takes about 30 minutes to compute metabolic reaction scores per single cell. This implied that the Kaede subdataset, consisting of 1136 resident and transient Tregs, would take 24 days to process on a local machine. For large datasets, Wagner *et al.* recommends reducing the size of the dataset through micropooling (Wagner et al., 2021).

To micropool the Kaede Treg dataset, we first library normalised the dataset so that all transcripts added up to 10,000. Next, we ran PCA to reduce the dimensionality of the dataset and applied the k-Nearest Neighbour (k-NN) algorithm to subcluster the dataset into 45 micropools with approximately 25 Tregs in each. Finally, we confirmed that each micropool consisted of approximately 100% tumour-resident or transient Tregs before

running Compass on the reduced dataset. Statistical comparisons between tumour-resident and transient Treg metabolic reactions were then determined by computing Wilcoxon adjusted p-values and Cohen's d statistic (Wagner et al., 2021).

## 3.4 Results

### 3.4.1 Integrating and clustering MC38 and CT26 Tregs

We started our analysis by investigating the differences between the MC38 and CT26 Tregs using public scRNA-seq data. To explore the sources of technical variation, we analysed the data without performing batch correction. We observed that Tregs separated according to the study of origin. LISI score distributions for both the complete and the downsampled datasets were centered at 1 indicating that Tregs from either study were almost exclusively surrounded by neighbouring Tregs from the same study in low-dimensional space (Fig 3.4A). These batch effects were recapitulated on UMAP as two separate clusters with Tregs from the CT26 and MC38 studies (Fig 3.4B). An additional prominent batch effect that appeared in the data was the cell cycle stage of the Tregs. Highly proliferating Tregs, expressing Mki67, clustered separately from the rest (Fig 3.4C). In summary, exploratory data analysis before batch correction highlighted that we needed to account for cell cycle stage and study batch effects to integrate both datasets.

After batch correction using Harmony (Korsunsky et al., 2019a), the range of LISI distributions for both the full and down-sampled datasets extended to 2 (Fig 3.4D). However, there was still a peak at 1 even after batch correction suggesting that there could be extensive biological differences between the MC38 and CT26 Tregs that tend to group these Tregs separately in low-dimensional space. When visualising the Tregs on a UMAP, we observed that there was an improvement in the mixing of the MC38 and CT26 Tregs in contrast to what we observed before batch correction (Fig 3.4E).

We then clustered the integrated data to identify Treg communities. Clustering revealed 3 main Treg subsets. These were Isg15$^{+}$ Tregs that upregulated cytokine response genes

such as Stat1, Ifit1 and Isg15, naive/central memory Tregs that upregulated Ccr7, and activated Tregs characterised by Lag3 and Il10 expression. A small cluster consisted of proliferating Tregs and was characterised by the expression of Mki67 (Fig 3.4F-G).

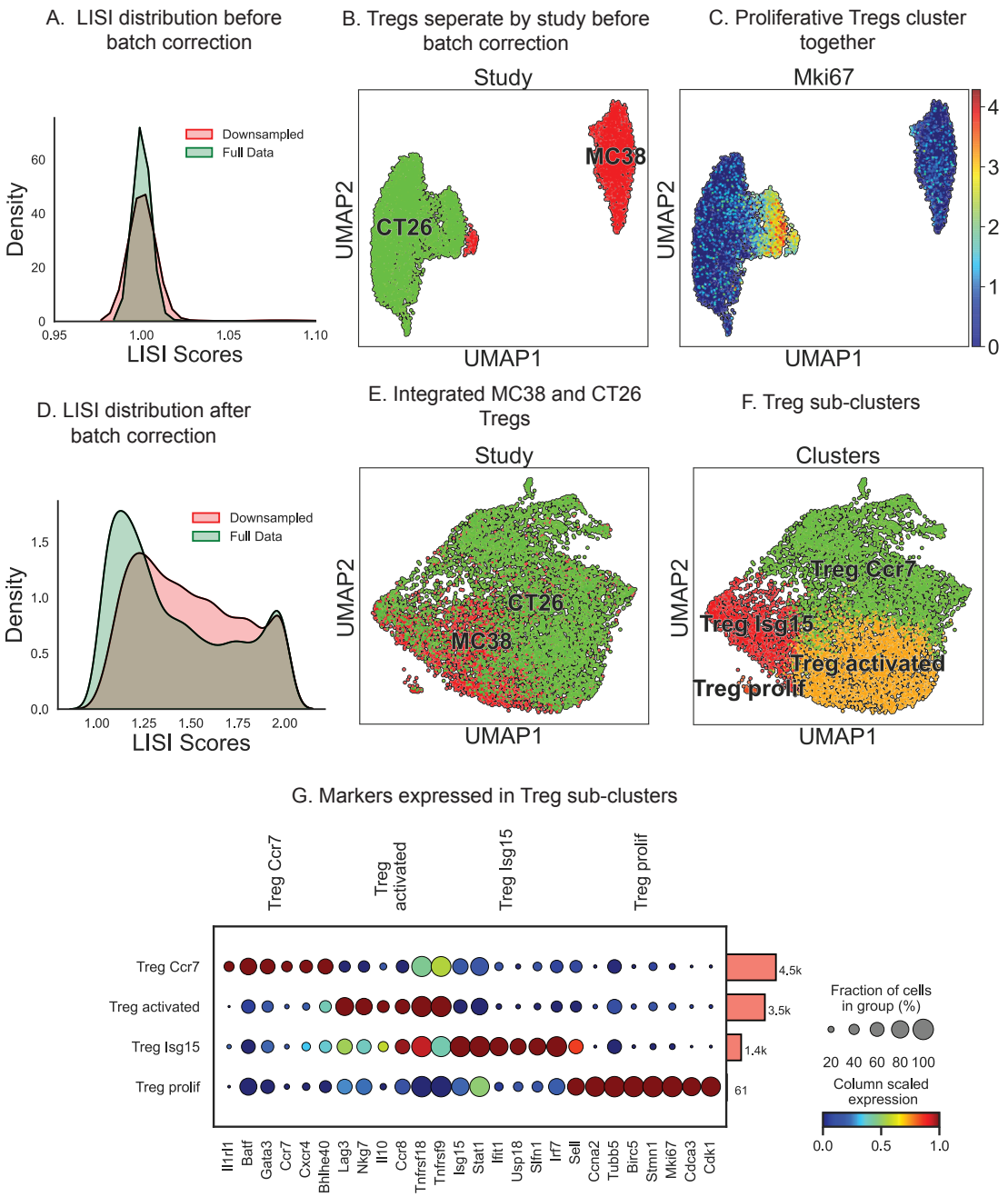



**Figure 3.4: Integrating and clustering MC38 and CT26 Tregs**. A: LISI score distributions for both the full and downsampled datasets before batch correction. Downsampling was performed to ensure that there were equal Treg numbers (2704) in both MC38 and CT26 Tregs to effectively interpret data integration using LISI distributions. UMAPs illustrating that study (B) and cell proliferation (C) are batch effects in the data. D: LISI score distributions for both the full and downsampled datasets after batch correction using the Harmony algorithm. E: UMAP showing MC38 and CT26 Tregs after data integration. F: Treg clusters identified after community detection. G: Dot plot showing markers expressed in different Treg clusters as well as numbers of Tregs per cluster (vertical bar plot on the right of the dot plot).

### 3.4.2 CT26 Tregs are distinct from MC38 Tregs

We visualised the densities of batch-corrected MC38 and CT26 Tregs in UMAP space and saw that CT26 Tregs were located primarily in the activated and Ccr7$^+$ Treg cluster regions (Fig. 3.5A). In contrast, MC38 Tregs clustered densely in the activated and Isg15$^+$ Treg compartments (Fig 3.5B). The separation of MC38 and CT26 Tregs was also found at the level of individual mice, as shown by mouse-specific Treg centroids that formed two separate clusters (Fig. 3.5C). In summary, these findings suggested that there are differences in the compositions and transcriptional profiles of MC38 and CT26 Tregs.

To explore compositional differences, we downsampled the Treg datasets to have equal numbers of MC38 and CT26 Tregs. We then quantified the fractions of MC38 and CT26 Tregs within each of the Treg subclusters. We found that the Ccr7$^+$ Treg cluster consisted mostly of CT26 Tregs while the other subclusters were enriched for MC38 Tregs (Fig. 3.5D). To confirm these differences using all Treg data and not just the downsampled dataset, we determined the fractions of Ccr7$^+$, activated and Isg15$^+$ Tregs of all Tregs in individual mice. The analysis highlighted a significantly higher fraction of Ccr7$^+$ Tregs in CT26 mice than in MC38-bearing mice (Fig. 3.5E). On the contrary, the proportions of activated and Isg15$^+$ Tregs were higher in MC38 than in CT26-implanted mice (Fig. 3.5F-G). Consolidating these findings, we concluded that MC38 and CT26 Tregs have different phenotypic compositions.

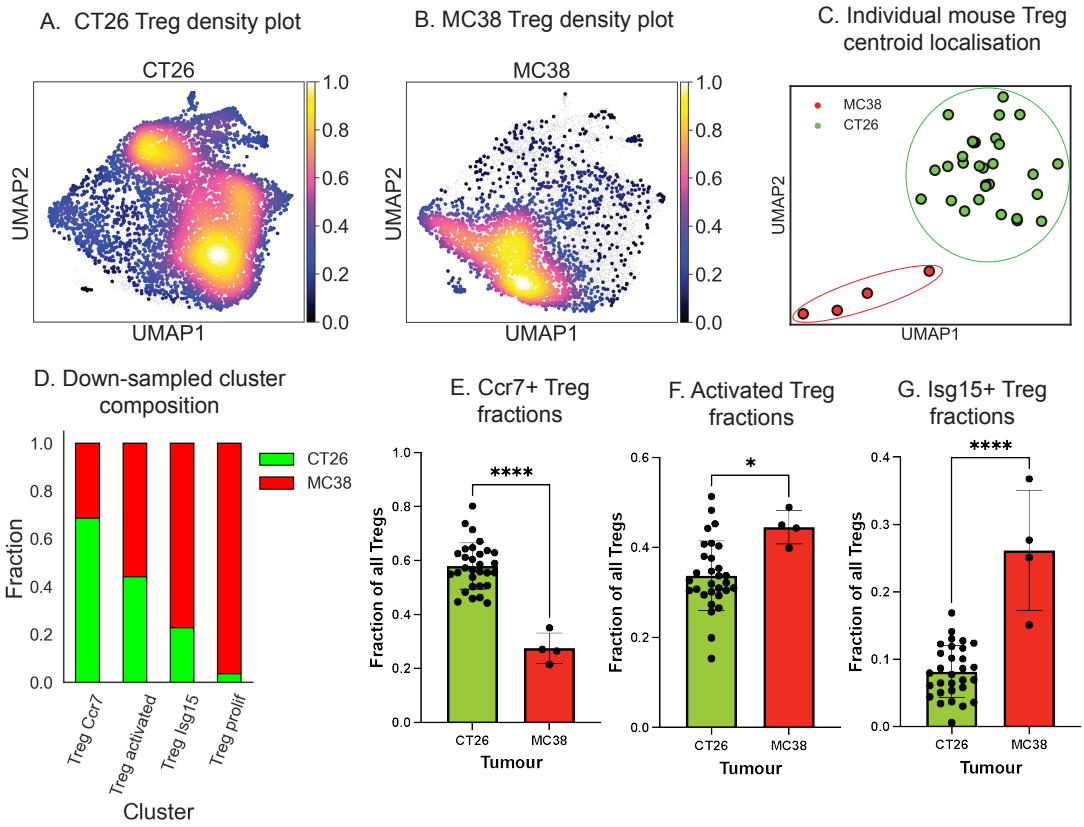



**Figure 3.5: CT26 Tregs are transcriptionally distinct from MC38 Tregs**. CT26 and MC38 Tregs separate in UMAP space indicative of distinct transcriptional programs (A-B). C: Centroids corresponding to where Tregs from individual mice bearing either MC38 or CT26 tumours collectively localise on a UMAP. D: Composition of Treg clusters split by tumour type in a down-sampled dataset in which there are equal MC38 and CT26 Tregs. Fractions of $Ccr7^{+}$, activated and $Isg15^{+}$ Tregs of all Tregs in tumours from individual mice (E, F and G respectively). The error bars represent the standard deviation. The Mann-Whitney U-test was used to compare CT26 and MC38 Treg fractions. Calculated p-values were as follows: *$p < 0.05$, **$p < 0.01$, ***$p < 0.001$, ****$p < 0.0001$.

### 3.4.3 CT26 Tregs upregulate cell migration markers

To explore differences in gene expression patterns between MC38 and CT26 Tregs, we proceeded to perform differential gene expression analysis. We compared Tregs from the 4 MC38-bearing mice (2706 Tregs) with Tregs from 4 selected CT26 mice (1554 Tregs) with comparable Treg numbers. We found that CT26 Tregs upregulated markers associated with a quiescent or stem-like phenotype such as Bach2 and Tcf7 (Grant et al., 2020). They upregulated Ccr7, which marks naive/central memory T cells and is associated with the trafficking of Tregs to lymph nodes (Menning et al., 2007). Cxcr4, which is associated with Treg trafficking to the bone marrow, was also upregulated in CT26 Tregs (Zou et al., 2004). On the contrary, MC38 Tregs upregulated Nt5e, the ecto-5′-nucleotidase which is associated with Treg-mediated immunosuppression (Antonioli et al., 2013) and Ass1, which is involved in arginine metabolism (Sun and Zhao, 2022) (see Figure 3.6A and Table 3.3).

Using the resultant list of differentially expressed genes, we ran GSEA to identify biological pathways that differ between MC38 and CT26 Tregs. Although we did not find pathways that were enriched in MC38 Tregs, CT26 Tregs upregulated pathways associated with cell migration (Fig. 3.6B-C). Some of the genes involved in these pathways included chemokine receptors, in particular Ccr7 and Cxcr4, which are involved in Treg trafficking to lymph nodes and lymphoid organs, respectively (Fig. 3.6D).

Summing these findings together, we concluded that MC38 and CT26 Tregs exhibit distinct transcriptional profiles. CT26 Tregs show a more quiescent phenotype and upregulate chemokine receptors involved in Treg trafficking to lymphoid organs in contrast to MC38 Tregs. This finding gave a transcriptional explanation for the increased accumulation of CT26 Tregs in the TDLN and spleen that was observed in Chapter 2.

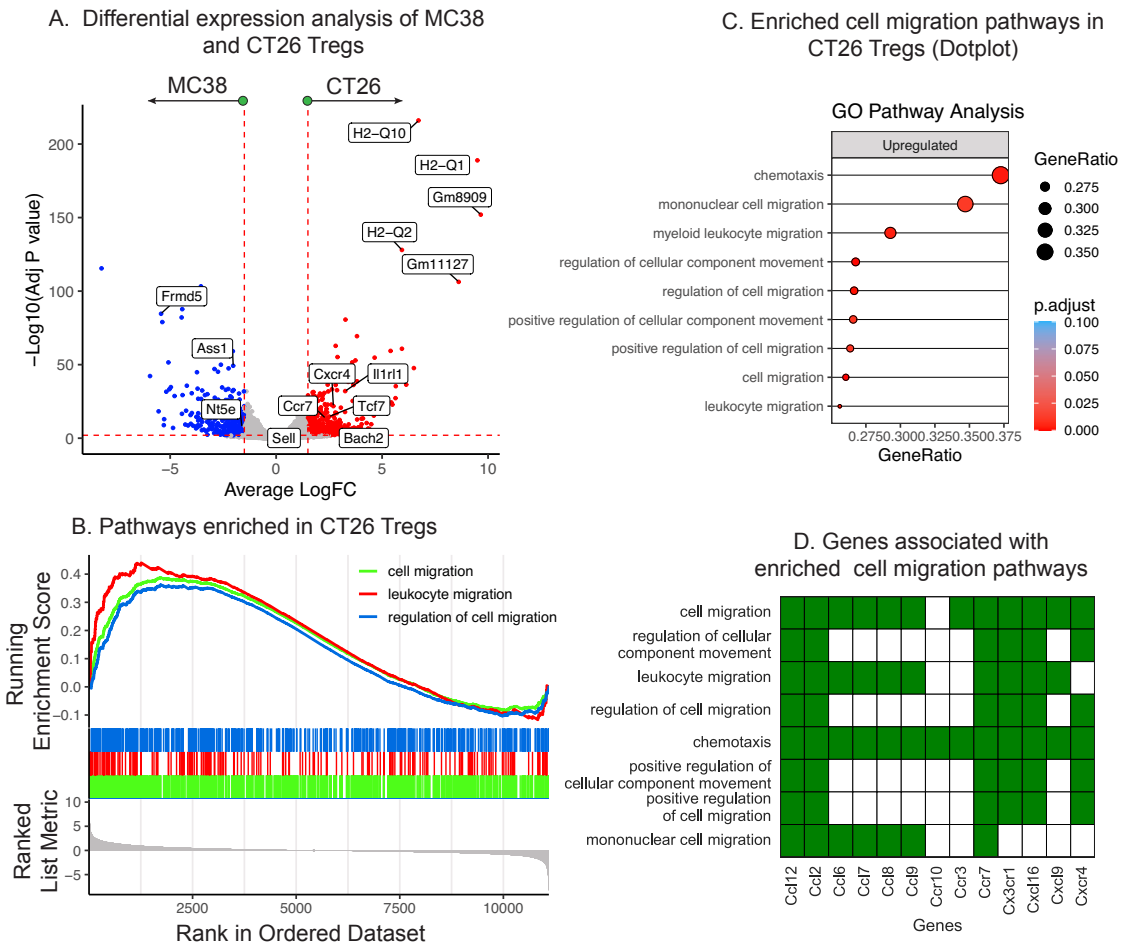



**Figure 3.6: CT26 Tregs significantly upregulate T cell trafficking markers**. A: Volcano plot showing genes that significantly differ between MC38 and CT26 Tregs. Adjusted p-values show the extent to which gene expression differs between MC38 and CT26 Tregs. B: Barcode plot from GSEA showing biological pathways that are enriched in CT26 Tregs. C: Dot plot showing pathways that are enriched in CT26 Tregs along with the gene ratios, which give a measure of the fraction of genes detected in the data out of all genes defined for a given pathway. The False discovery rate (FDR) adjusted p-values (p.adjust) show the extent to which a given pathway is upregulated in CT26 Tregs in contrast to MC38 Tregs D: Heatmap showing the overlap of detected genes across the enriched pathways associated with cell migration. Green boxes indicate the presence of a gene whereas white boxes show the absence of respective genes in the pathway. Average LogFC – average logarithmic fold change in base 2.

**Table 3.3: Table showing some of the genes that are differentially expressed between CT26 and MC38 Tregs**. Genes that are positively regulated in CT26 are ordered by decreasing average LogFC while negatively regulated genes are ordered by increasing average LogFC. The adjusted p-values reflect the significance level of the difference in gene expression between MC38 and CT26 Tregs. Average LogFC – average logarithmic fold change in base 2.

| Genes upregulated in CT26 Tregs | | | Genes downregulated in CT26 Tregs | | |
|---|---|---|---|---|---|
| Gene | Average LogFC | Adjusted p-val | Gene | Average LogFC | Adjusted p-val |
| Gm8909 | 9.656754 | 9.946278e-153 | Hist1h2ap | -5.541421 | 5.408769e-19 |
| H2-Q1 | 9.502089 | 1.061737e-189 | Frmd5 | -5.435919 | 2.288931e-85 |
| Gbp2b | 6.501018 | 2.150391e-48 | Gda | -5.037304 | 5.679476e-34 |
| Gm8730 | 5.936072 | 1.532920e-61 | Bmp7 | -4.217518 | 2.212524e-36 |
| Esm1 | 5.629787 | 6.762305e-28 | Clybl | -3.976113 | 7.577785e-18 |
| Cd24a | 5.571542 | 1.358949e-48 | Akap2 | -3.761494 | 2.671520e-15 |
| Arntl2 | 4.772805 | 1.056662e-19 | Arhgap31 | -3.737754 | 1.347530e-45 |
| Gzma | 4.610188 | 4.947326e-16 | Fam129c | -3.673185 | 9.833379e-13 |
| Gng4 | 4.268781 | 4.986343e-11 | Apobec3 | -3.551650 | 5.170759e-104 |
| Ddx43 | 4.249762 | 9.386498e-22 | Cxx1b | -3.541313 | 2.063837e-27 |
| Gm10020 | 3.826468 | 2.157444e-39 | Acss2 | -3.245134 | 1.270842e-30 |
| Ccl8 | 3.792331 | 9.646544e-22 | Ggt7 | -3.162818 | 9.563406e-11 |
| Gm29243 | 3.612001 | 5.071998e-26 | F2rl2 | -2.963817 | 3.890717e-23 |
| Atrnl1 | 3.588191 | 2.918338e-52 | Bcl2a1b | -2.930114 | 5.729537e-62 |
| Bmpr2 | 3.399137 | 5.849383e-39 | Cd74 | -2.916190 | 1.043782e-47 |
| Ahr | 3.271284 | 2.760975e-81 | Cpe | -2.843124 | 2.881595e-14 |
| Ece1 | 3.097193 | 3.315041e-43 | Fam132a | -2.826119 | 2.971147e-63 |
| Dhrs3 | 2.874997 | 1.027518e-11 | Gm6793 | -2.748376 | 7.772579e-11 |
| Cd9 | 2.873729 | 2.380074e-33 | Gm4070 | -2.699677 | 2.612690e-19 |
| H60b | 2.845221 | 8.538324e-18 | Cd37 | -2.612395 | 8.991229e-51 |
| Abhd17c | 2.763680 | 4.526474e-14 | Gapdh | -2.545580 | 2.543857e-35 |
| Cxcr4 | 2.699949 | 1.379945e-22 | Aarsd1 | -2.481745 | 4.020460e-14 |
| Ccr7 | 2.323358 | 2.156924e-14 | Hmgn3 | -2.333978 | 3.754697e-15 |
| Grb7 | 2.189633 | 1.435012e-29 | Farp1 | -2.325301 | 5.816097e-13 |
| Arhgef10 | 2.164706 | 6.428383e-27 | Cbx7 | -2.271960 | 1.001963e-26 |
| Emb | 2.106680 | 9.535800e-22 | Gm26510 | -2.223221 | 8.891077e-11 |
| Bcl2l11 | 2.080832 | 4.247868e-13 | Gm4951 | -2.181613 | 6.325304e-19 |
| Cd7 | 1.994880 | 7.127385e-11 | Gng10 | -2.156827 | 3.382716e-29 |
| H2-Ab1 | 1.939210 | 1.117351e-15 | Eno1 | -2.046926 | 5.997975e-60 |
| Ctsl | 1.907544 | 7.039694e-17 | Ass1 | -2.025310 | 5.750817e-50 |
| Dennd5a | 1.770932 | 6.772132e-12 | Bcl2a1d | -1.955161 | 1.101667e-15 |
| Chd7 | 1.769621 | 4.605191e-30 | Alg9 | -1.897210 | 3.457855e-19 |
| Egln3 | 1.719978 | 8.562278e-32 | Decr1 | -1.896763 | 1.232421e-11 |
| Cx3cr1 | 1.717312 | 4.929411e-14 | Gm28053 | -1.852761 | 1.241386e-12 |
| Acsl3 | 1.679429 | 4.220771e-14 | Calcrl | -1.800857 | 1.769238e-12 |
| H2-Q6 | 1.678753 | 4.508653e-15 | Cpne1 | -1.745095 | 6.604552e-14 |
| Arl5c | 1.674466 | 9.214808e-26 | Ebi3 | -1.727152 | 5.057781e-27 |
| Ankrd55 | 1.624601 | 2.273593e-22 | F2r | -1.712200 | 4.187287e-21 |

### 3.4.4 Integrating and clustering Kaede scRNA-seq Treg datasets

In the next set of analyses, we focused on the transcriptional characterisation of tumour-resident and transient Tregs from the Kaede experiments involving MC38 tumours. Given that the Kaede scRNA-seq datasets came from two independent experiments (see Table 3.2), we performed exploratory data analysis for batch effects. Before batch correction, the LISI distributions with the full or downsampled datasets were centered at 1, indicative of poor integration between the two datasets (Fig. 3.7A). This was similarly reflected on the UMAP on which the 24-72 and 48 hour datasets formed separate clusters (Fig. 3.7B). Following batch correction, the LISI distribution shifted to 2 and both datasets were well integrated in the UMAP embedding (Fig. 3.7C-D).

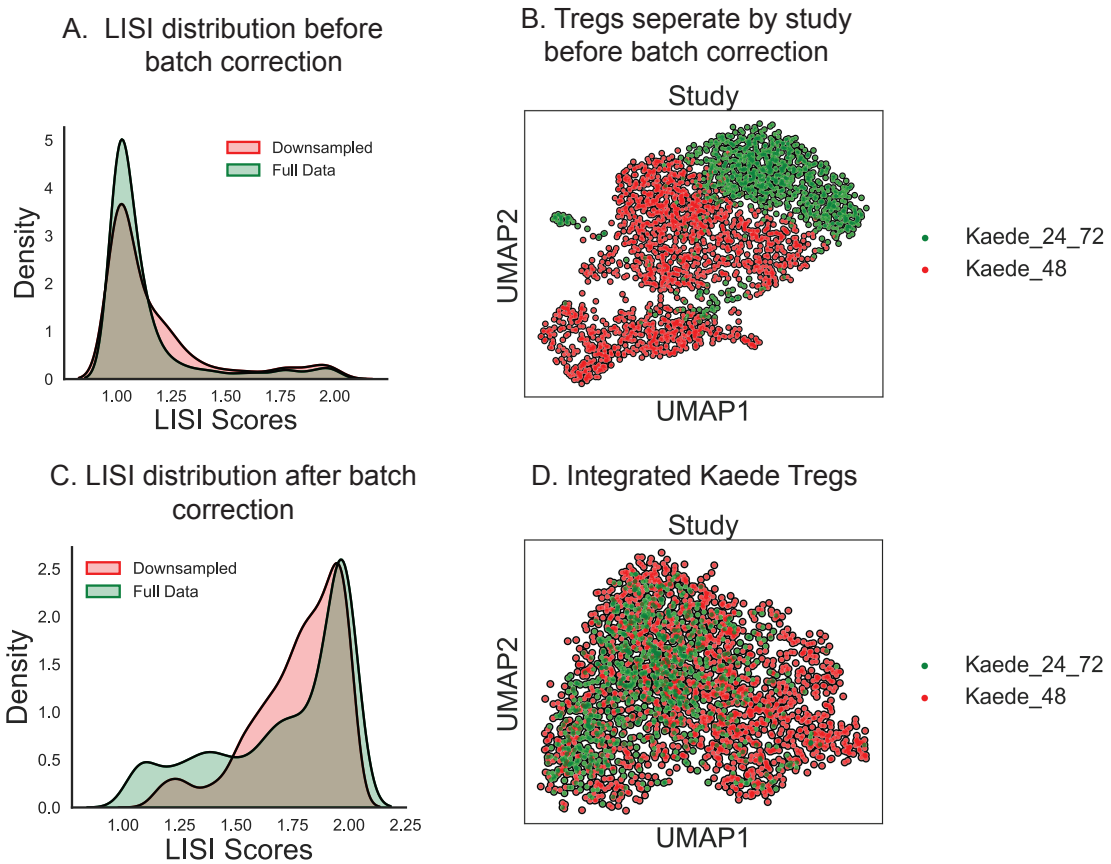



**Figure 3.7: Integrating Kaede Treg scRNA-seq datasets**. A: LISI distributions for full and down-sampled Kaede Treg datasets before batch correction. B: UMAP embedding of the 24-72 and 48 hour Treg datasets that were derived from two separate studies with the Kaede mouse experimental model. C: LISI distributions after batch correction. D: Well mixed UMAP embedding of 24-72 and 48 hour Kaede Treg datasets.

Using the batch-corrected low-dimensional embeddings, we clustered the Kaede Tregs. Consistent with the clusters identified from the MC38 and CT26 Treg datasets (Fig. 3.4), we identified activated, Ccr7$^{+}$ and Isg15$^{+}$ Treg sub-clusters (Fig. 3.8A). Ccr7$^{+}$ Tregs exhibited a naive/central memory phenotype marked by the upregulation of Ccr7 and Tcf7. Activated Tregs displayed an effector Treg signature and expressed Il10 and Lag3. Isg15$^{+}$ Tregs expressed many cytokine response genes such as Ifit1, Isg20 and Isg15 (Fig. 3.8B-E). Finally, we investigated whether the green Tregs that had recently infiltrated the tumour differed from the red Tregs that had been in the tumour for longer time. The red and green Tregs did not separate in the UMAP space, suggesting a lack of a definitive relationship between the Treg colour and the transcriptional characteristics (Fig. 3.8F).

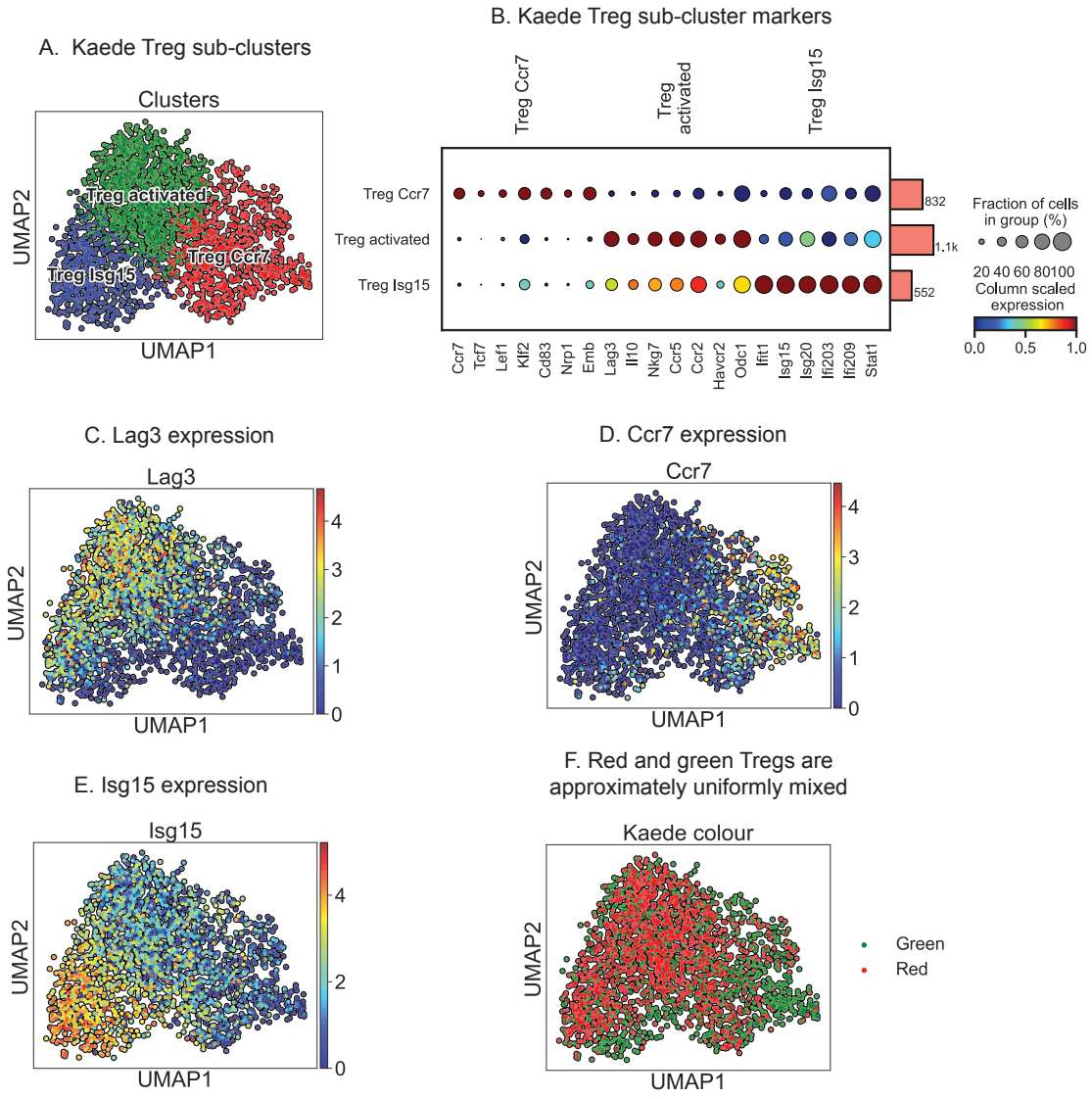



**Figure 3.8: Clustering red and green Kaede Tregs**. A: UMAP showing Treg sub-clusters. B: Dotplot showing genes upregulated in each Treg cluster along with the numbers of Tregs per cluster. UMAPs showing the Tregs expressing Lag3, Ccr7 and Isg15 respectively (C-E). F: UMAP showing the localisation of red and green Tregs.

### 3.4.5 MC38 tumours harbour mainly activated and Isg15 Tregs

After clustering Kaede Tregs, we investigated whether there was a difference between Tregs in MC38 tumours and the draining lymph nodes. Stratifying Tregs according to their origin, we observed that MC38 Tregs separated from draining lymph node Tregs (Fig. 3.9A). This observation was further supported by origin-specific Treg density plots that highlighted that tumour Tregs were mostly localised in the activated and Isg15$^+$ Treg cluster regions (Fig. 3.9B). On the contrary, the TDLN and nDLN Tregs were localised in the Ccr7$^+$ Treg cluster (Fig. 3.9C-D). These findings suggested that there are significant transcriptional differences between Tregs in the tumour and draining lymph nodes.

Next, we explored the composition of Tregs in different samples which differed according to colour, time, and origin. Across time, the fractions of activated Tregs within the green tumour Treg samples increased while the fractions of Ccr7$^+$ Tregs decreased. On the other hand, Isg15$^+$ Treg fractions did not significantly change (Fig. 3.9E). The red Treg samples had higher fractions of activated Tregs and lower proportions of Ccr7$^+$ Tregs than green Tregs (Fig. 3.9E). The red Tregs that infiltrated the TDLN at 48 hours after tumour photoconversion consisted mostly of Ccr7$^+$ Tregs, although a small fraction of activated Tregs could be seen. Finally, the green Tregs in the draining lymph nodes from tumour-naive mice were almost entirely Ccr7$^+$ Tregs (Fig. 3.9E).

We then determined the compositions of each Treg cluster. Activated Tregs consisted mainly of red and green tumour Tregs at different times, while Ccr7$^+$ Tregs consisted mainly of nDLN and 48 hour red Tregs from the TDLN. Isg15$^+$ Tregs consisted almost exclusively of Tregs from the tumour (Fig. 3.9F).

Finally, we investigated the collective compositions of red and green tumour Tregs, red TDLN Tregs, and green nDLN Tregs. We found that most of the red tumour Tregs, approximately 60%, were activated Tregs, 27% were Isg15$^+$ Tregs and 13% were Ccr7$^+$ Tregs (Fig. 3.9G). Similarly, most of the green tumour Tregs were activated Tregs, although this fraction was lower for green Tregs than for red Tregs. Furthermore, the green tumour Tregs contained a higher fraction of Ccr7$^+$ Tregs than the red Tregs

(Fig. 3.9H). The 48-hour red TDLN Tregs were mainly Ccr7$^+$, and approximately 24% of these Tregs had an activated phenotype (Fig. 3.9I). Finally, as previously observed, close to 100% of green inguinal lymph node Tregs from tumour-naive mice were Ccr7$^+$ (Fig. 3.9J).

Collectively, we concluded that Tregs from MC38 tumours exhibited extensive compositional differences in contrast to Tregs from the TDLN and nDLN. In particular, tumour Tregs consisted of mostly activated and Isg15$^+$ Tregs.

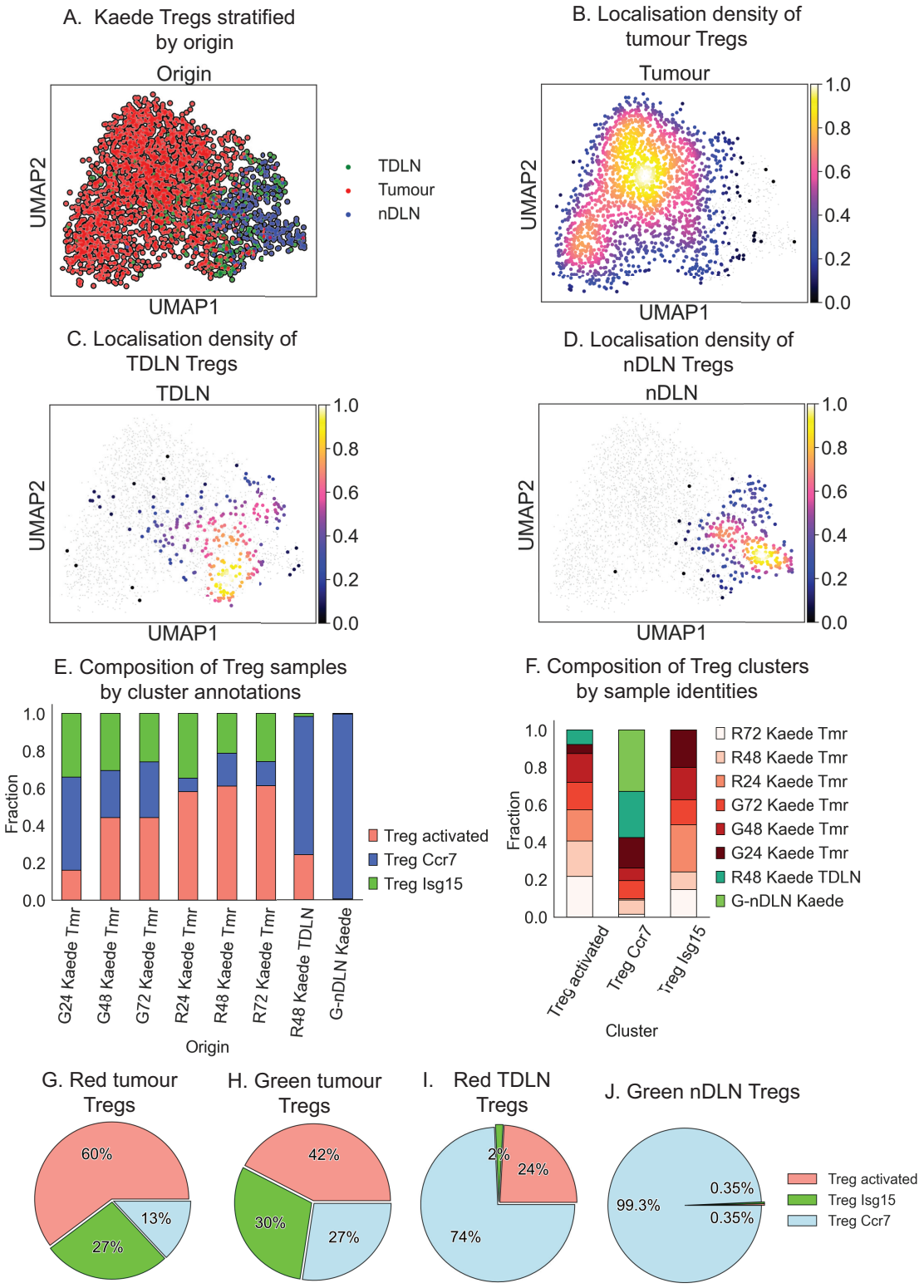



**Figure 3.9: Compositional analysis of tumour, TDLN and nDLN Kaede Tregs**. UMAP and UMAP density plots showing Kaede Tregs separated by origin (A-D). Sample and cluster level compositional analysis (E-F). Pie charts showing the compositions of red and green tumour Tregs (G-H), red TDLN Tregs (I) and green nDLN Tregs (J).

### 3.4.6 Reconstructing Kaede Treg differentiation trajectories

In the previous sections, we clustered Kaede Tregs into discrete subclusters based on gene expression profiles. However, cells are complex entities and are on continuous differentiation trajectories. In this section, we employed pseudotime analysis to reconstruct possible Treg trajectories and provide a more biologically consistent understanding of Kaede Treg characteristics. To do this, we used the STREAM package (Chen et al., 2019b) to perform trajectory analysis.

Using the batch-corrected UMAP embedding, STREAM identified a bifurcating trajectory with nodes S0, S1, S2 and S3 (Fig. 3.10A). S1 originated in the Ccr7$^{+}$ cluster, S0 and S2 were embedded in the activated Treg cluster and S3 was found in the Isg15$^{+}$ Treg cluster (Fig. 3.10A-B). However, STREAM could not predict the root of the trajectory representing where Treg differentiation originates. Typically, trajectory analysis involves the use of prior biological knowledge to infer the node that represents the root of the trajectory. In our analysis, we picked node S1 as the root. The rationale behind this selection was that S1 consisted of Ccr7$^{+}$ with an undifferentiated naive/central memory phenotype. Therefore, we would expect other Ccr7$^{-}$ Tregs seen in the tumour to be more differentiated than Ccr7$^{+}$ Tregs.

With S1 as the root, we inferred the positions of the rest of the Tregs along pseudotime, which is a latent time dimension assigned by STREAM (Fig. 3.10C). We then visualised where Tregs from the tumour and healthy tissue (TDLN and nDLN) localised. We found that Tregs from healthy tissue appeared early in pseudotime while Tregs from tumours dominated later in pseudotime. Furthermore, tumour Tregs exhibited a bifurcating trajectory later in pseudotime (Fig. 3.10D-E). Most of the Ccr7$^{+}$ Tregs clumped early in pseudotime, while activated, and the Isg15$^{+}$ Tregs separated into two different trajectories later in pseudotime (Fig. 3.10F).

Finally, we visualised the trajectories followed by individual Treg samples within our dataset. The trajectory analysis highlighted that the green nDLN and the red Tregs in the TDLN at 48 hours were mainly restricted towards the beginning of the trajectory,

suggesting that they are less differentiated than the rest of the Tregs in the dataset (Fig. 3.10G). Interestingly, we observed that all other tumour Tregs, regardless of their colour and the time at which they were collected, formed a continuous spectrum starting from the middle of the trajectory going all the way to each of the branches at the end of pseudotime. There were no noticeable differences between the red and green tumour Tregs in terms of the extent to which they spanned the differentiation trajectory (Fig. 3.10G). This suggested that both red and green Tregs had, on average, comparable Treg compositions as previously observed (see Fig. 3.9E).

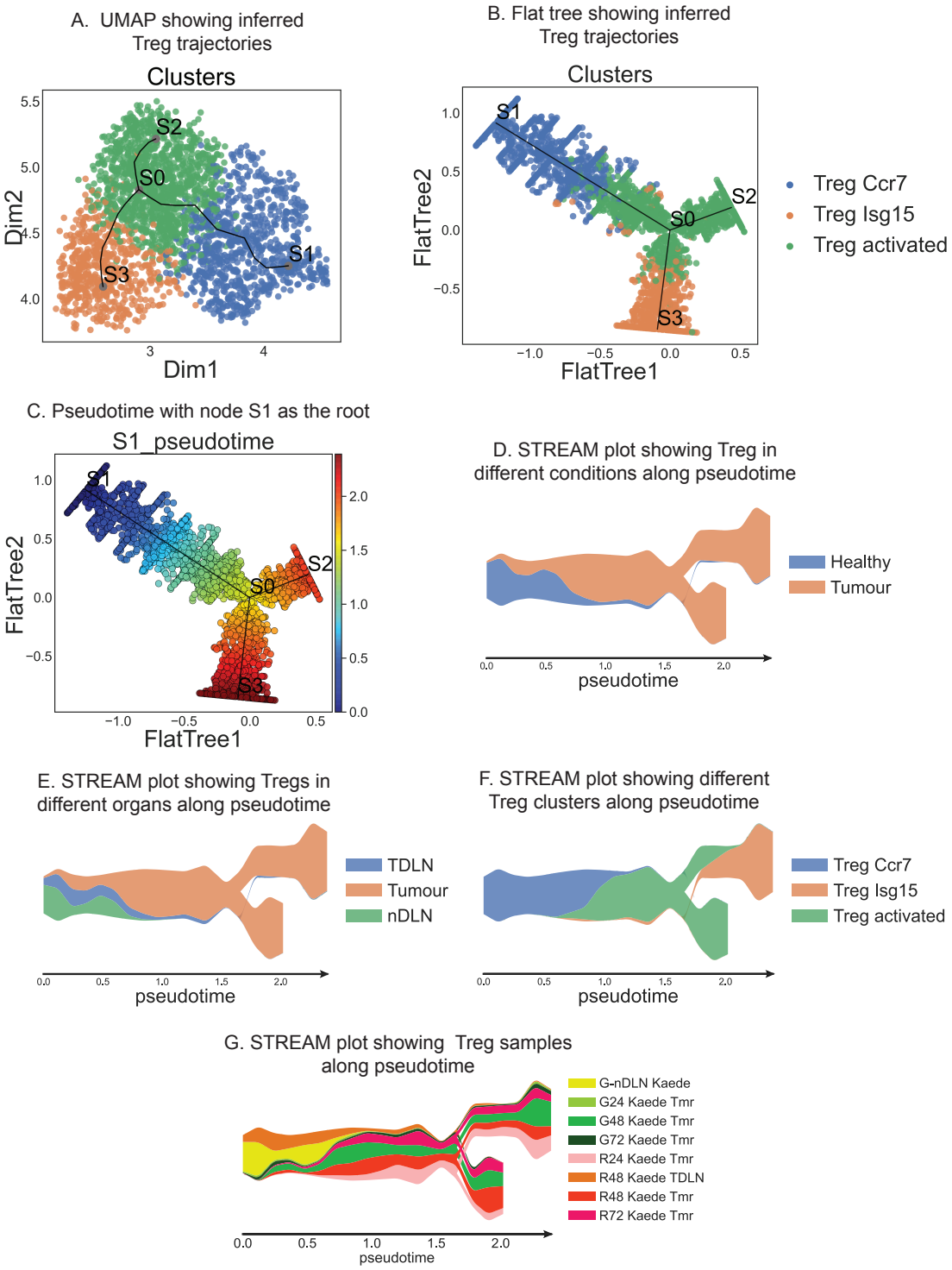



**Figure 3.10: Inferring Kaede Treg differentiation trajectories**. UMAP (A) and Flat tree (B) embeddings showing the inferred Treg trajectory nodes. C: Flat tree embedding showing the grouping of Tregs in pseudotime using S1 as the root node. STREAM plots illustrating Treg trajectories stratified by Treg origin (D-E), cluster (F) and samples (G).

We further characterised Kaede Tregs by identifying genes that are correlated with pseudotime within each trajectory branch depicted in Figure 3.11A. Also known as transition genes, these genes shed light on the transcriptional changes that took place as Tregs became more differentiated.

Tregs upregulated Ccr5, Lag3, and Isg15 as they transitioned from node S1 to the middle of the trajectory. At the same time, Ccr7, Tcf7 and Nrp1 were downregulated (Fig. 3.11B). This highlighted that Tregs were differentiating from a naive/central memory phenotype to an effector and cytokine responsive Treg phenotype. We observed less significant transcriptional differences between nodes S0 and S2 as indicated by higher adjusted p-values compared to the previous trajectory (Fig. 3.11C). However, from S0 to S3, there was an increased upregulation of Ifit3, Isg15 and a downregulation of Lag3, suggesting that the Tregs were adopting an interferon response signature while becoming less immunosuppressive (Fig. 3.11D).

The results above were supplemented by STREAM plots showing that Tregs differentiated from having $Ccr7^{+}$ phenotype to a branching point that was enriched for Lag3 expression (Fig. 3.11E-F). The Tregs then bifurcated into two separate trajectories characterised by Lag3 and Isg15 expression as expected (Fig. 3.11F-G).

To sum up, trajectory analysis allowed us to characterise differences between Tregs in the tumour and lymph nodes along a reconstructed differentiation trajectory — a treatment that is closer to the biology than discrete cell clustering.

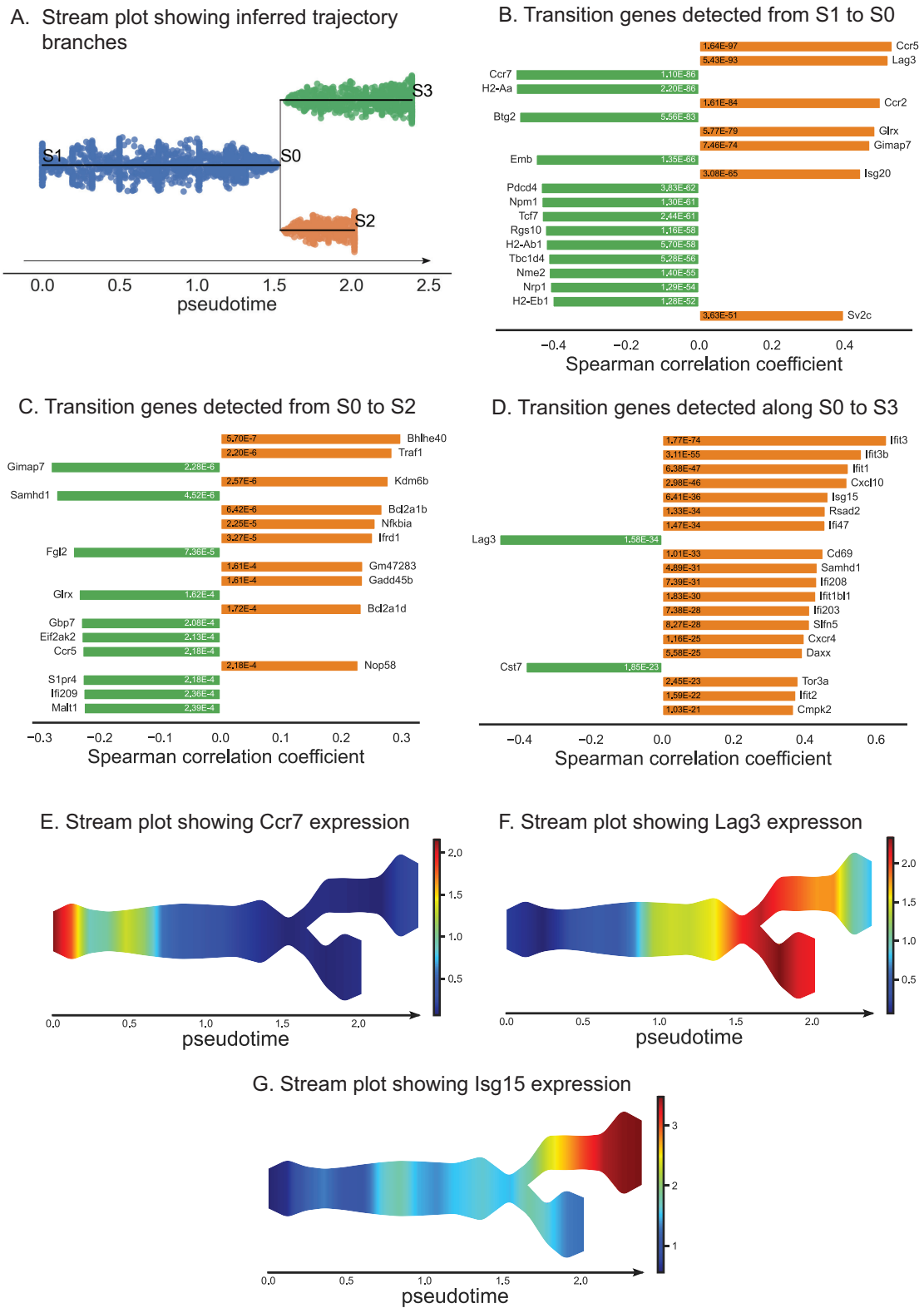



**Figure 3.11: Determining genes that differ in expression along pseudotime**. A: Identified trajectory branches. Genes that are correlated with pseudotime along S1-S0 (B), S0-S2 (C) and S0-S3 (D). Adjusted p-values, reflecting the extent to which gene expression differs between nodes, are written within each bar. STREAM plots showing the expression of Ccr7 (E), Lag3 (F) and Isg15 (G). Colour bars show gene expression levels.

### 3.4.7 Differential expression analysis of resident and transient Tregs

Mathematical modelling revealed that there are resident and transient Tregs in both MC38 and CT26 tumours (see the Results section of Chapter 2). To identify genes that differ significantly in expression between tumour-resident and transient Tregs, we used the MAST package (Finak et al., 2015) to perform differential gene expression analysis.

Anticipating that incoming green Tregs exhibit a less activated state compared to red Tregs that have been in the tumour for a longer time, we compared red (1255 cells) and green (731 cells) tumour Tregs. However, we did not observe drastic differences between red and green Tregs, with the exception of a few genes that were upregulated between the two (Fig. 3.12A). Green Tregs upregulated Ccr7 suggesting the presence of a naive/central memory signature. On the other hand, red Tregs upregulated Il10, which is a marker of an effector Treg phenotype (Fig. 3.12A). Interestingly, Tnfrsf9, which is typically associated with highly immunosuppressive Tregs, was slightly upregulated in green Tregs, suggesting that they were probably a mixture of naive/central memory and activated Tregs, as previously shown through compositional and trajectory analyses (see Figures 3.9E and 3.10G).

More drastic differences in gene expression were observed when we compared tumour-resident Tregs (867 cells) with transient Tregs (267 cells). In this analysis, we considered red 48 and 72 hour tumour Tregs as resident Tregs and red 48 hour TDLN Tregs as transient Tregs. Our reasoning was that the red Tregs from the tumour found after 24 hours post tumour photoconversion consist mainly of resident Tregs, as the mathematical model in Chapter 2 revealed. Furthermore, the red 48-hour Tregs in the TDLN are truly transient because before migrating into the TDLN, they were in the tumour.

Differential expression analysis underscored that tumour-transient Tregs upregulate the naive/central memory marker, Ccr7, proliferation markers such as Stmn1 and Mki67 and Areg, which is associated with Treg-mediated musculoskeletal tissue repair (Burzyn et al., 2013)(Fig. 3.12B). On the contrary, tumour-resident Tregs upregulated genes

associated with Treg-mediated immunosuppression such as Gzmb and tumour necrosis factor receptor superfamily genes, Tnfrsf18 (GITR), Tnfrsf9 (4-1BB), Tnfrsf4 (OX40). They highly expressed T cell exhaustion markers such as Lag3, cytokine response genes such as Ifit1, the Hypoxia inducible factor 1-$\alpha$, Hif1a, which is upregulated in cells under hypoxic conditions (Wang et al., 1995), and Odc1, an enzyme that plays a critical role in polyamine metabolism (Pendeville et al., 2001). Finally, tumour-resident Tregs upregulated the expression of GTPase of immunity-associated proteins (GIMAPs). These included Gimap1, Gimap3, Gimap4, Gimap5, Gimap6, Gimap7, Gimap8 and Gimap9, most of which have been implicated in maintaining T cells through inhibiting apoptosis, with the exception of the pro-apoptotic Gimap4 (Ho and Tsai, 2017; Yano et al., 2014; Datta et al., 2017; Schnell et al., 2006) (see Figure 3.12B and Table 3.4 which show the expression of some of the genes discussed here).

To further explore gene expression patterns on a sample-level basis, we ordered the Kaede Treg samples on a scale of an approximately increasing tumour residency phenotype defined by the length of time each Treg sample has been in the tumour (Fig. 3.12C). For each sample, we then plotted the normalised expression of some of the genes that were identified via differential expression analysis, particularly, Lag3, Tnfrsf18, Tnfrsf9, Ccr7 and Tcf7 (Fig. 3.12D-H). The expression of Lag3 increased as Tregs adopted an increasingly resident phenotype, suggesting that Lag3 is a marker of tumour residency (Fig. 3.12D). Similarly, Tnfrsf18 and Tnfrsf9 were upregulated in all tumour Treg samples (Fig. 3.12E-F). In contrast, the expression of Ccr7 and Tcf7 dropped along the residency scale (Fig. 3.12G-H).

In summary, these results indicated that genes that were either upregulated or downregulated between tumour-resident and transient Tregs were also positively or negatively correlated, respectively, with tumour residency. Lag3 was found to be significantly upregulated as Tregs adopted an increasingly tumour-resident phenotype.

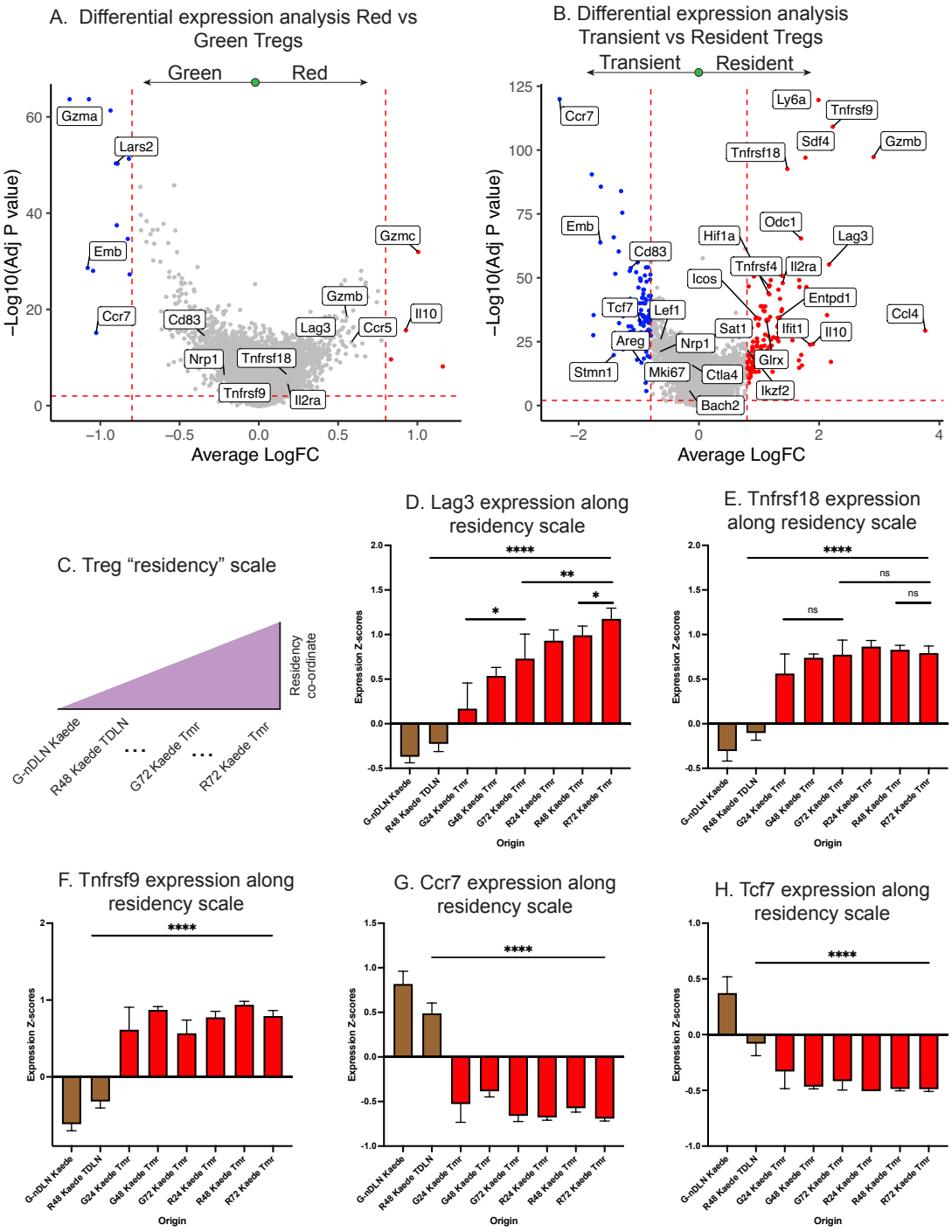



**Figure 3.12: Identifying differentially expressed genes between resident and transient Tregs**. Volcano plots showing genes that significantly differ between red and green Tregs (A) and tumour-resident and transient Tregs (B). The adjusted p-values show the extent to which each gene differs in expression between red and green, and resident and transient Tregs. C: A schematic showing Treg samples ordered in increasing tumour residency. Scaled expression of Lag3 (D), Tnfrsf18 (E), Tnfrsf9 (F), Ccr7 (G) and Tcf7 (H) along the scale of increasing tumour residency. The error bars highlight the 95% confidence interval. The Mann-Whitney U-test was used to compare inter-sample gene expression. Calculated p-values in D-H were as follows: *p $<$ 0.05, **p $<$ 0.01, ***p $<$ 0.001, ****p $<$ 0.0001. Average LogFC – average logarithmic fold change in base 2.

**Table 3.4: Table showing some of the genes that are differentially expressed between resident and transient Tregs**. Positively regulated genes are ordered by decreasing average LogFC while negatively regulated genes are ordered by increasing average LogFC. Adjusted p-values reflect the significance level of differences in gene expression between resident and transient Tregs. Average LogFC – average logarithmic fold change in base 2.

| Genes upregulated in resident Tregs | | | Genes downregulated in resident Tregs | | |
|---|---|---|---|---|---|
| Gene | Average LogFC | Adjusted p-val | Gene | Average LogFC | Adjusted p-val |
| Ccl4 | 3.764481 | 4.772621e-30 | Ccr7 | -2.317197 | 1.215228e-120 |
| Gzmb | 2.902255 | 5.802297e-98 | Nme2 | -1.781707 | 3.351092e-91 |
| Tnfrsf9 | 2.226757 | 7.427363e-110 | Hmgb2 | -1.750922 | 3.991182e-36 |
| Lag3 | 2.164064 | 5.687734e-56 | Emb | -1.639837 | 1.478769e-64 |
| Nkg7 | 2.128981 | 3.991182e-36 | Npm1 | -1.334871 | 5.438501e-61 |
| Ccr5 | 1.823555 | 1.560557e-44 | Itgb1 | -1.327060 | 5.698431e-33 |
| Gzmc | 1.785709 | 3.975738e-47 | Arhgdib | -1.292016 | 1.073760e-84 |
| Isg20 | 1.776246 | 4.596293e-55 | S100a10 | -1.259693 | 1.220478e-35 |
| Sdf4 | 1.770445 | 9.674912e-98 | Btg2 | -1.250460 | 6.834023e-39 |
| Odc1 | 1.697042 | 4.210751e-66 | Pdcd4 | -1.248946 | 1.993276e-38 |
| Irf7 | 1.671974 | 4.012080e-47 | Hspe1 | -1.176883 | 2.507482e-36 |
| Bst2 | 1.668377 | 8.694454e-50 | Hmgn2 | -1.172784 | 9.649081e-32 |
| Isg15 | 1.554365 | 2.657883e-26 | Crip1 | -1.166918 | 2.221751e-28 |
| Tnfrsf18 | 1.470159 | 2.378539e-93 | Ass1 | -1.145328 | 1.383314e-29 |
| Il2ra | 1.391851 | 1.208794e-48 | Junb | -1.140715 | 1.683310e-42 |
| Maf | 1.386984 | 1.797563e-51 | Cd83 | -1.138072 | 1.725723e-54 |
| Gimap7 | 1.380075 | 1.961378e-38 | Rgs10 | -1.126172 | 1.088697e-31 |
| Mdfic | 1.373697 | 1.209135e-37 | Ighm | -1.088690 | 1.896680e-30 |
| Fgl2 | 1.360851 | 1.831247e-28 | Eif4a1 | -1.049700 | 6.818829e-42 |
| Entpd1 | 1.341466 | 2.972364e-35 | Hmgn1 | -1.005734 | 6.823290e-47 |
| Parp14 | 1.326494 | 3.631552e-29 | H2afz | -0.984825 | 5.333037e-34 |
| Ddit4 | 1.325629 | 7.068525e-26 | Gm2000 | -0.981998 | 8.784390e-41 |
| Ifi27l2a | 1.321909 | 4.311802e-46 | Arl5c | -0.979835 | 1.421939e-36 |
| Rtp4 | 1.319693 | 2.594981e-32 | Rasgrp2 | -0.979062 | 1.672448e-50 |
| Itgav | 1.312908 | 4.379203e-35 | Hspa8 | -0.969578 | 1.482813e-49 |
| Slfn8 | 1.287526 | 3.739758e-27 | Phgdh | -0.959147 | 2.242124e-29 |
| Ifngr1 | 1.283151 | 1.701942e-53 | Bzw2 | -0.933851 | 3.702142e-36 |
| Nedd9 | 1.239732 | 1.808088e-27 | Eef1b2 | -0.932263 | 4.418109e-43 |
| Npc2 | 1.177013 | 1.022981e-47 | Cct5 | -0.926039 | 1.758219e-44 |
| Tnfrsf4 | 1.168264 | 3.089611e-47 | H2afv | -0.918229 | 2.279962e-26 |
| Hif1a | 1.157581 | 1.155905e-44 | Eif3i | -0.908126 | 2.296165e-33 |
| Mxd1 | 1.154988 | 6.781590e-28 | B3gnt2 | -0.899179 | 5.200198e-35 |
| Glrx | 1.124307 | 2.957646e-34 | Pfn1 | -0.898174 | 1.245317e-51 |
| Stat1 | 1.103054 | 1.580561e-39 | Cct2 | -0.896425 | 1.076336e-40 |
| Gimap4 | 1.090493 | 1.334136e-37 | Nr4a1 | -0.888606 | 2.672015e-34 |
| Crem | 1.052689 | 1.461282e-39 | Lsp1 | -0.886637 | 2.110000e-42 |
| Gimap6 | 1.006142 | 9.712546e-35 | Ndufa4 | -0.843776 | 3.995636e-34 |
| Pld3 | 0.988262 | 1.506808e-32 | Cnn2 | -0.837593 | 3.999498e-33 |
| Icos | 0.961111 | 3.206158e-35 | Cxcl16 | -0.810985 | 4.524859e-50 |
| Gimap3 | 0.870836 | 4.056568e-31 | Cacnb3 | -0.808275 | 5.526338e-52 |

The correlations we observed between gene expression and tumour residency implied that we could formally rank all genes in the dataset by correlation coefficients with tumour residency. Given that for some genes, expression reaches saturation as Tregs adopt a more tumour-resident phenotype, we decided to calculate Spearman's $\rho$ rather than Pearson's $\rho$ (see Figure 3.13A and Table 3.5). Consistent with differential expression analysis, genes such as Tnfrsf9, Gzmb, Tnfrsf18, Lag3 and Hif1a were positively correlated with tumour residency. As expected, Ccr7, Cd83 and Nrp1 were negatively correlated (Fig. 3.13A).

We then calculated gene-gene expression correlations and performed hierarchical clustering to isolate distinct gene clusters. Two clusters representing resident (top left) and transient (bottom right) profiles were identified (Fig. 3.13B). We observed that Odc1, Smox and Sat1 were positively correlated with the resident Treg signature, while Ass1, Amd1, Srm and Sms were negatively correlated, suggesting that tumour-resident Tregs exhibit a downregulation/defect in polyamine (spermine and spermidine) metabolism in contrast to transient Tregs (Casero and Marton, 2007) (Fig. 3.13B). Compared to transient Tregs, tumour-resident Tregs appeared to be enriching for the production of putrescine instead of spermine/spermidine (Fig. 3.13C).

In summary, analysis of gene expression correlations suggested significant differences in biological pathways in tumour-resident and transient Tregs. In particular, it revealed that tumour-resident Tregs adopt a hypoxia adaptation signal and are potentially defective in polyamine metabolism.

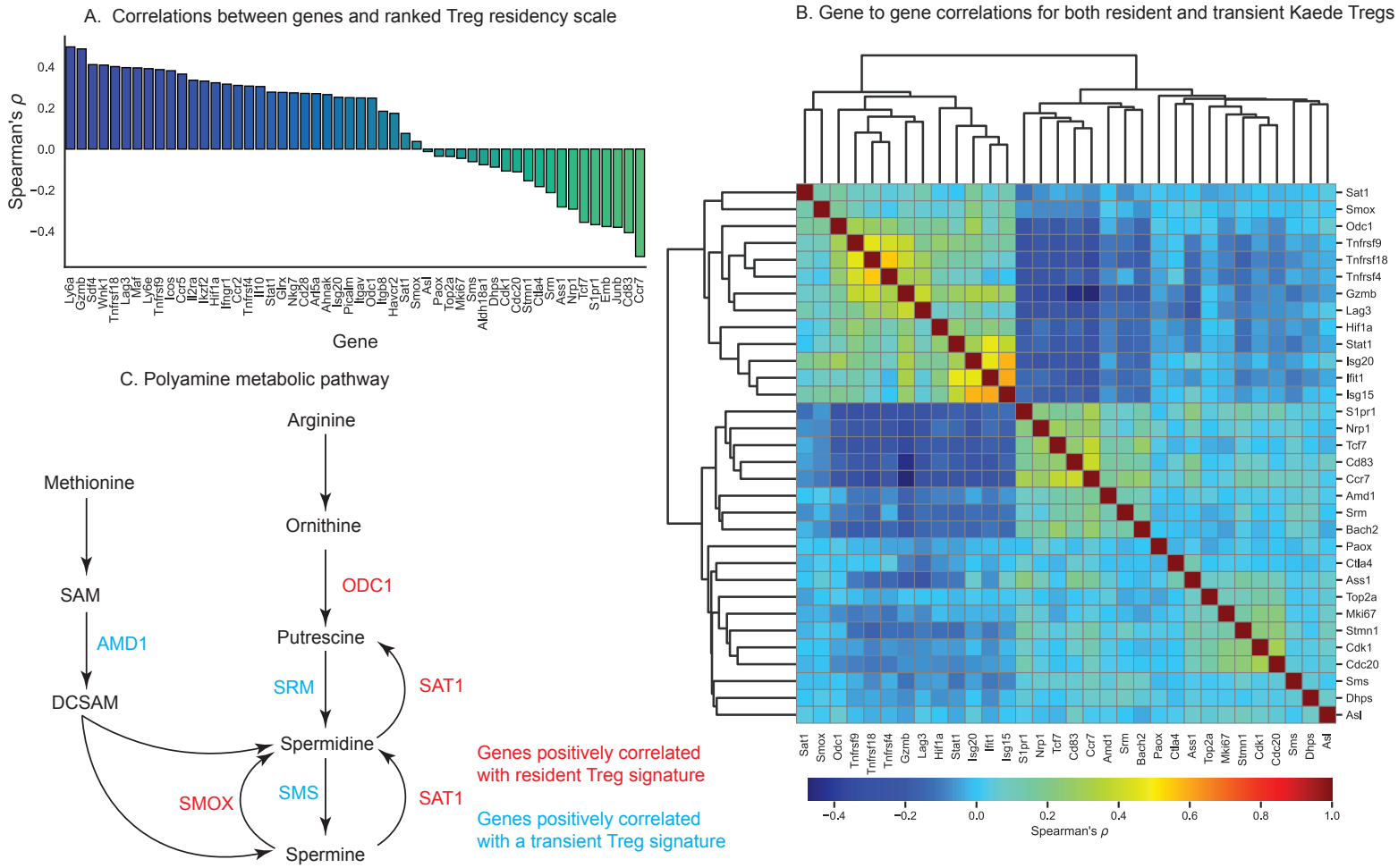



**Figure 3.13: Gene-phenotype and gene-gene correlation analysis**. A: Barplot showing Spearman's $\rho$ for top genes that are either positively or negatively correlated with tumour residency. B: Gene-gene correlation matrix for both resident and transient Tregs. C: Genes involved in the polyamine metabolic pathway.

**Table 3.5: Table showing correlations between genes and the scale of increasing Treg tumour residency**. We determined the Spearman's $\rho$ correlation coefficient for each gene after ordering the Kaede samples by tumour residency.

| Top 31 positively correlated genes | | Top 31 negatively correlated genes | |
|---|---|---|---|
| Gene | Spearman's $\rho$ | Gene | Spearman's $\rho$ |
| Ly6a | 0.497 | Btf3 | -0.349 |
| Gzmb | 0.488 | Rnaset2b | -0.349 |
| Sdf4 | 0.411 | Tomm6 | -0.356 |
| Wnk1 | 0.409 | Tcf7 | -0.357 |
| Tnfrsf18 | 0.402 | Sub1 | -0.367 |
| Lag3 | 0.397 | S1pr1 | -0.368 |
| Maf | 0.395 | Eif4a1 | -0.370 |
| Ly6e | 0.392 | Coro1a | -0.371 |
| Tnfrsf9 | 0.387 | Npm1 | -0.375 |
| Icos | 0.381 | Emb | -0.377 |
| Ccr5 | 0.365 | Junb | -0.380 |
| Vmp1 | 0.351 | Ppia | -0.384 |
| Gimap4 | 0.336 | Hmgn1 | -0.390 |
| Il2ra | 0.335 | Hspa8 | -0.391 |
| Cd2 | 0.334 | Rgs10 | -0.397 |
| Ikzf2 | 0.331 | Tbc1d4 | -0.399 |
| Hif1a | 0.323 | Naca | -0.401 |
| B2m | 0.318 | Cd83 | -0.407 |
| Ifngr1 | 0.316 | Arhgdib | -0.409 |
| Ccr2 | 0.310 | Pfn1 | -0.410 |
| Tnfrsf4 | 0.310 | Slamf6 | -0.411 |
| Il10 | 0.305 | H3f3a | -0.412 |
| Parp14 | 0.300 | Actb | -0.427 |
| Gimap7 | 0.300 | Srsf7 | -0.432 |
| Mdfic | 0.288 | Snrpg | -0.440 |
| Trim30a | 0.288 | Eaf1a1 | -0.446 |
| Npc2 | 0.285 | Gm11808 | -0.455 |
| Stat1 | 0.277 | Uba52 | -0.470 |
| Igtp | 0.277 | Nme2 | -0.495 |
| Glrx | 0.276 | Tmsb10 | -0.508 |
| Nkg7 | 0.274 | Ccr7 | -0.523 |

### 3.4.8 Resident and transient Tregs exhibit significant differences in multiple biological pathways

From the previous section, we observed that tumour-resident Tregs upregulate genes that are associated with Treg-mediated immunosuppression and cytokine response. They downregulate proliferation markers such as Stmn1 and Mki67 (Fig. 3.12B and Supplementary Fig. B.1). Furthermore, gene-gene correlation analysis revealed that tumour-resident Tregs potentially downregulate polyamine metabolism (Fig. 3.13B). To robustly characterise the biological pathways that differ between tumour-resident and transient Tregs, we performed gene set enrichment analysis (GSEA).

We identified two biological pathways that were enriched in tumour-resident Tregs. These included the negative regulation of leukocyte activation and response to type I interferon (Fig. 3.14A). On the other hand, multiple pathways were downregulated. Cellular metabolism was suppressed in tumour-resident Tregs, including oxidative phosphorylation and the tricarboxylic acid cycle (TCA). Furthermore, the degree to which tumour-resident Tregs oxidise organic compounds to derive energy was decreased in contrast to transient Tregs (Fig. 3.14B). In particular, amide metabolism was downregulated (Fig. 3.14C). A closer look at the genes involved in this pathway highlighted that a disproportionate number of amminoacyl-tRNA synthetase-encoding genes including Farsb, Eprs1, Gars, Hars1, Lars, Mars, Nars, Rars, Sars and Wars were downregulated. This indicated a low level of peptide synthesis at the translation level, which culminated in diminished peptide metabolism. As peptides and polyamines are critical for cell proliferation, we expected tumour-resident Tregs to be less proliferative than transient Tregs. In fact, we found that tumour-resident Tregs downregulated cell division and exhibited a defect in the synthesis of purines and pyrimidines, bases that are essential for DNA synthesis prior to cell division (Fig. 3.14D). In summary, GSEA enabled us to identify biological pathways that provide mechanistic insight into tumour-resident and transient Tregs (summarised in Figure 3.14E and Table 3.6). In particular, tumour-resident Tregs were predicted to be less proliferative and metabolically quiescent than transient Tregs, possibly due to restrictions in nutrient and oxygen levels in the TME.

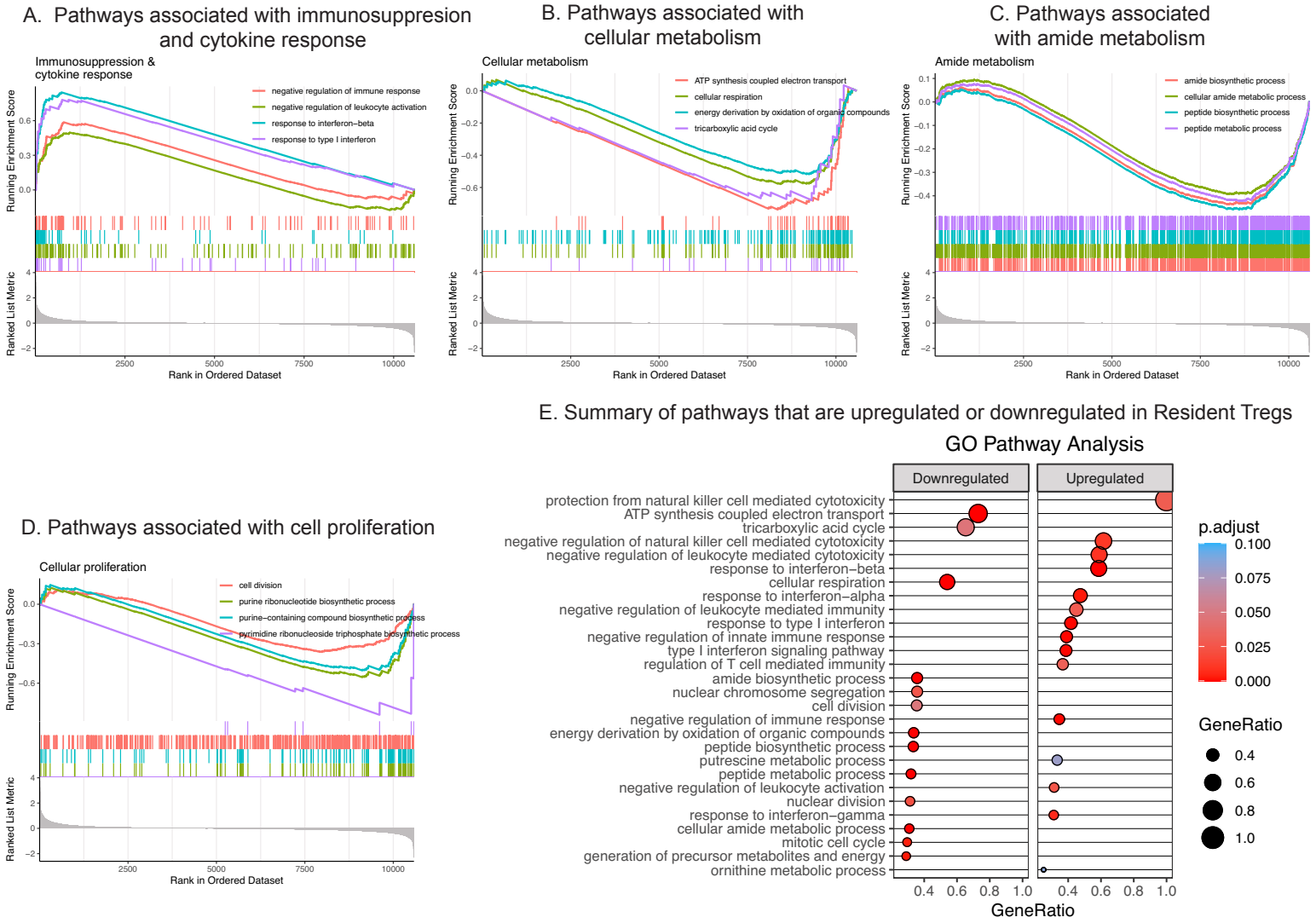



**Figure 3.14: Gene set enrichment analysis**. A: Barcode plots showing pathways that are enriched (A) and suppressed (B-D) in resident Tregs. E: A summary of pathways that differ between resident and transient Tregs reported together with significance level and gene ratios. p.adjust – False discovery rate (FDR) adjusted p-values depicting the extent to which pathways differ between resident and transient Tregs.

**Table 3.6: Table summarising upregulated and downregulated pathways in resident Tregs**. The set size is the number of genes in a predefined pathway. ES and NES refer to Enrichment score and Normalised Enrichment Score, respectively. NES normalises ES to take into account different gene set sizes across different pathways. False discovery rate (FDR) adjusted p-values indicate the extent to which pathways differ between resident and transient Tregs. Different colours denote different pathways identified namely, Cyan – immunosuppression, Magenta – cytokine response, Green – putrescine/polyamine metabolism, Yellow – cell division, Orange – amide metabolism, Light red – cellular metabolism.

| Pathway | Set size | ES | NES | p-value | Adjusted p-value | Gene ratio |
|---|---|---|---|---|---|---|
| Negative regulation of innate immune response | 41 | 0.732 | 2.116 | $7.588\times10^{-6}$ | 0.0007 | 0.39 |
| Negative regulation of immune response | 104 | 0.587 | 1.950 | $1.323\times10^{-5}$ | 0.00116 | 0.346 |
| Regulation of T cell mediated immunity | 60 | 0.571 | 1.737 | 0.000932 | 0.0325 | 0.367 |
| Regulation of immune effector process | 279 | 0.417 | 1.559 | 0.000209 | 0.010 | 0.204 |
| Negative regulation of leukocyte activation | 127 | 0.498 | 1.697 | 0.000703 | 0.0263 | 0.315 |
| Negative regulation of leukocyte mediated immunity | 40 | 0.647 | 1.861 | 0.000800 | 0.0288 | 0.45 |
| Protection from natural killer cell medicated cytotoxicity | 6 | 0.933 | 1.710 | 0.000834 | 0.0300 | 1 |
| Negative regulation of natural killer cell mediated cytotoxicity | 13 | 0.853 | 1.913 | 0.000262 | 0.0119 | 0.615 |
| Response to interferon-beta | 46 | 0.845 | 2.476 | $1.334\times10^{-11}$ | $8.00\times10^{-9}$ | 0.587 |
| Response to type I interferon | 36 | 0.781 | 2.182 | $5.014\times10^{-6}$ | 0.0005 | 0.417 |
| Type I interferon signaling pathway | 31 | 0.78 | 2.114 | $9.392\times10^{-9}$ | 0.0009 | 0.387 |
| Response to interferon-alpha | 19 | 0.826 | 2.030 | $5.204\times10^{-5}$ | 0.00349 | 0.474 |
| Response to interferon-gamma | 93 | 0.560 | 1.837 | 0.000135 | 0.00737 | 0.312 |
| Putrescine metabolic process | 3 | 0.971 | 1.543 | 0.00339 | 0.0810 | 0.334 |
| Ornithine metabolic process | 4 | 0.945 | 1.605 | 0.00378 | 0.0872 | 0.25 |
| Mitotic cell cycle | 646 | -0.362 | -1.423 | $7.011\times10^{-5}$ | 0.00442 | 0.296 |
| Cell division | 449 | -0.364 | -1.400 | 0.00160 | 0.0485 | 0.354 |
| Nuclear division | 284 | -0.399 | -1.470 | 0.000611 | 0.0236 | 0.313 |
| Nuclear chromosome segregation | 199 | -0.432 | -1.541 | 0.000719 | 0.0268 | 0.357 |
| Peptide metabolic process | 535 | -0.424 | -1.643 | $8.192\times10^{-8}$ | $1.819\times10^{-5}$ | 0.320 |
| Peptide biosynthetic process | 452 | -0.459 | -1.767 | $2.80\times10^{-9}$ | $9.466\times10^{-7}$ | 0.334 |
| Amide biosynthetic process | 524 | -0.437 | -1.691 | $1.333\times10^{-8}$ | $3.331\times10^{-6}$ | 0.357 |
| Cellular amide metabolic process | 685 | -0.393 | -1.555 | $1.434\times10^{-7}$ | $2.818\times10^{-5}$ | 0.309 |
| Generation of precursor metabolites and energy | 275 | -0.443 | -1.625 | $3.881\times10^{-5}$ | 0.00286 | 0.291 |
| Cellular respiration | 124 | -0.579 | -1.948 | $1.606\times10^{-7}$ | $3.105\times10^{-5}$ | 0.540 |
| Tricarboxylic acid cycle | 26 | -0.679 | -1.770 | 0.00152 | 0.0471 | 0.654 |
| Energy derivation by oxidation of organic compounds | 173 | -0.518 | -1.810 | $2.453\times10^{-6}$ | 0.000297 | 0.335 |
| ATP synthesis coupled electron transport | 48 | -0.738 | -2.122 | $1.279\times10^{-7}$ | $2.599\times10^{-5}$ | 0.729 |

### 3.4.9 Resident Tregs display significant metabolic dysfunction

GSEA revealed that amide metabolic processes were downregulated in tumour-resident Tregs, yet, unexpectedly, putrescine/ornithine metabolic processes appeared to be upregulated (Fig. 3.14E). Upon closer examination, we observed that putrescine and ornithine metabolic processes had small gene set sizes of 3 and 4 genes, respectively. Therefore, it became clear that the reported enrichment of the putrescine/ornithine metabolic process was based on only one gene, Odc1, which was over-expressed in tumour-resident Tregs. Furthermore, slightly higher FDR adjusted p-values (approximately 0.08) also indicated that the GSEA results associated with these two pathways should be interpreted with caution (Table 3.6).

In summary, these observations hinted at the limitations associated with using gene expression to infer biological pathways such as metabolism via GSEA. A more accurate bioinformatic analysis would consider the relative abundance of metabolites and associated metabolic enzymes to infer whether respective metabolic processes are enriched between conditions. To this end, we used Compass (Wagner et al., 2021) to simulate metabolic reactions in tumour-resident and transient Tregs. To reduce the dimensionality of the dataset and computational run time, we ran Compass on tumour-resident and transient Treg micropools instead of individual cells (Supplementary Fig. B.2).

Upon running Compass, we observed that the tumour-resident Tregs were defective in oxygen-dependent metabolic processes. While gylcolysis did not appear to be different between tumour-resident and transient Tregs (Fig. 3.15A), the tricarboxylic acid cycle (Fig. 3.15B), oxidative phosphorylation (Fig. 3.15C) and fatty acid oxidation (Fig. 3.15E) were downregulated in resident Tregs. In agreement with GSEA, tumour-resident Tregs exhibited an overall dysfunction in amino acid metabolism. However, unlike the GSEA results, Odc1 activity (ornithine decarboxylase 1) was negatively regulated in resident Tregs (Fig. 3.15D). Thus, despite the upregulation of Odc1 gene expression in tumour-resident Tregs, the deficit of precursor metabolites due to the downregulation of

amide metabolism as a whole potentially leads to low activity of ornithine decarboxylase 1, as Compass predicts via simulation (Fig. 3.15D).

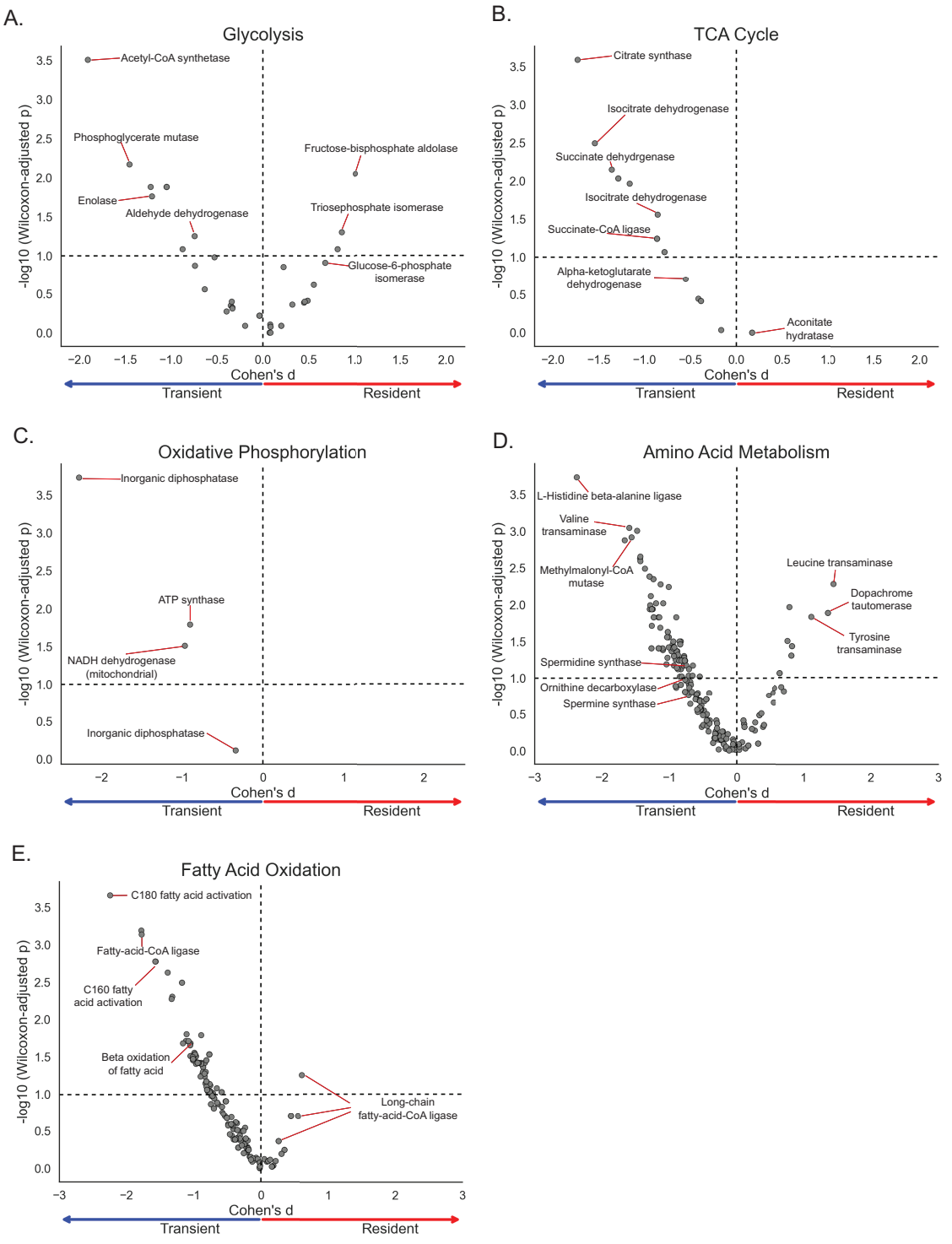



**Figure 3.15: Simulating metabolic processes in resident and transient Tregs using Compass**. Volcano plots showing the extent to which metabolic reactions within Glycolysis (A), the Tricarboxylic acid cycle (B), Oxidative Phosphorylation (C), Amino acid metabolism (D) and Fatty acid Oxidation (E) differ between resident and transient Tregs. Each dot represents a metabolic reaction rather than gene expression. Cohen's d measures the effect size difference per reaction between resident and transient Tregs. The p-values reflect the significance level associated with the difference in metabolic reactions between resident and transient Tregs. The Benjamini-Hochberg (BH) method was used for multiple-hypothesis adjustment.

Indeed, when we visualised Compass simulation results, we observed that multiple amide metabolic processes were predicted to be suppressed in tumour-resident Tregs including arginine, proline, glycine, serine, alanine and threonine, valine, leucine, isoleucine, aspartate, and tryptophan metabolism. The Urea cycle that clears ammonia, a byproduct of amine metabolism, was also predicted to be negatively regulated in tumour-resident Tregs, possibly as a result of reduced amide metabolism. Finally, the synthesis of purines and pyrimidines was predicted to be negatively regulated, making it less likely that tumour-resident Tregs would be highly proliferative (Fig. 3.16). Therefore, on the basis of these results, we concluded that tumour-resident Tregs are defective in polyamine metabolism, a model which fits well with their low proliferative capacity.

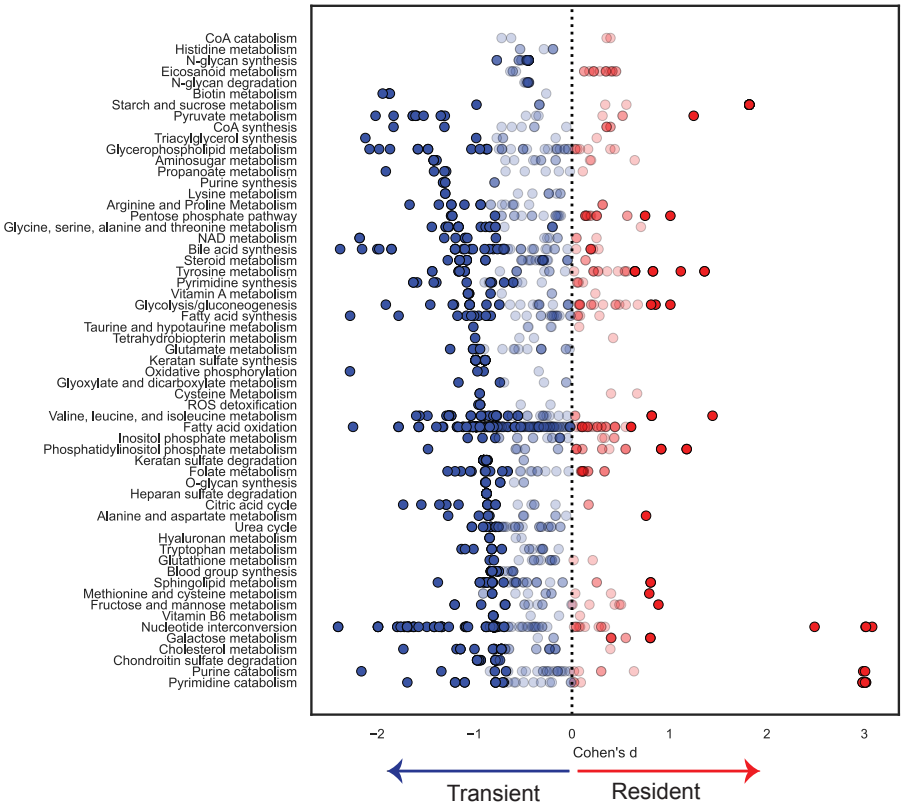



**Figure 3.16: Multiple metabolic pathways are downregulated in resident Tregs**. A scatter plot comparing differences in metabolic reactions between resident and transient Tregs. Blue and red dots denote reactions that are upregulated in transient and resident Tregs respectively. Lightly shaded dots highlight reactions with Benjamini-Hochberg (BH)-adjusted p-values $> 0.1$ while dark dots are reactions with BH-adjusted p-values $< 0.1$. The p-values reflect the significance level associated with the difference in metabolic reactions between resident and transient Tregs.

## 3.5 Discussion

In the previous chapter, we observed that the MC38 and CT26 Tregs exhibit different migration patterns. CT26 Tregs appeared to rapidly exit the tumour and migrate to lymphoid tissue (TDLN and spleen) to a greater extent than MC38 Tregs. We also observed that MC38 and CT26 Tregs consist of resident and transient subpopulations. Both findings implied significant heterogeneity within inter- and intratumoral Treg subsets.

In this chapter, we analysed public and in-house transcriptomics datasets to establish a basis for the differences between Treg subpopulations within and across different tumours. The aim of first part of this chapter has been to compare and contrast gene expression profiles in MC38 and CT26 Tregs to explain the observed differences in Treg dynamics. We then devoted the rest of the chapter towards investigating gene expression differences between tumour-resident and transient Kaede Tregs in MC38-implanted mice with the aim of identifying surface markers that can be translated into tumour-resident Treg-inhibiting/depleting cancer therapeutics. Finally, we investigated the biological pathways that differ between tumour-resident and transient Kaede Tregs to shed light on the mechanisms that underlie tumour residence.

The transcriptional characterisation of MC38 and CT26 Tregs revealed three main Treg phenotypes. We identified Tregs with a naive/central memory (Ccr7$^{+}$) phenotype, highly immunosuppressive (activated) Tregs and cytokine responsive (Isg15$^{+}$) Tregs, which are protected from cytokine-mediated death. Naive/central memory Tregs upregulated Ccr7 and Cxcr4, chemokine receptors that facilitate the homing of Tregs to lymph nodes (Menning et al., 2007) and the bone marrow (Zou et al., 2004), respectively. These Tregs most likely represent newly arriving central Tregs that have not yet been stimulated by neo-antigens and are less differentiated to become highly immunosuppressive/activated intratumoral Tregs. Activated Tregs expressed markers that have been shown to mark highly immunosuppressive intratumoral Tregs, for instance, Lag3, Il10 and Ccr8 (Whiteside et al., 2021; Van Damme et al., 2021; Rubtsov et al., 2008). On the other hand, Isg15 Tregs over expressed cytokine response genes such as Isg15, Stat1,

Ifit1 and Isg20 which protect Tregs from cytokine-mediated cellular death (Pacella et al., 2016; Gangaplara et al., 2018; Pacella et al., 2020), thus allowing them to survive the TME. They could represent Tregs that have been in the tumour for a long time and have been constantly exposed to cytokines, resulting in the stable upregulation of cytokine response genes.

Further analysis indicated that CT26 Tregs display distinct transcriptional and compositional fingerprints from MC38 Tregs. In particular, CT26 Tregs consisted of significantly higher fractions of $Ccr7^{+}$ Tregs than MC38 Tregs. On the contrary, the proportions of activated and $Isg15^{+}$ Tregs were higher in MC38 tumours. Differential expression analysis showed that MC38 Tregs had increased expression of Nt5e, which plays a role in immunosuppression (Antonioli et al., 2013), while CT26 Tregs upregulated Ccr7, Cxcr4, and Bach2, suggesting that CT26 Tregs have a more quiescent profile (Grant et al., 2020). Given that Ccr7 and Cxcr4 are associated with lymphoid tissue homing, we expected CT26 Tregs to upregulate pathways associated with migratory behaviour. Indeed, GSEA revealed that CT26 Tregs upregulate cell migration pathways to a greater extent than MC38 Tregs. Therefore, these findings provided a transcriptional explanation for the previously observed increased accumulation of CT26 Tregs in lymphoid tissue compared to MC38 Tregs.

The widespread use of mouse tumour models to investigate immune checkpoint therapy warrants proper selection of experimental tumour models. Only recently, studies that compare immune cell dynamics in different murine tumour models have begun to highlight that the immune cell dynamics of MC38 and CT26 tumours differ. In particular, Treg numbers have been observed to decrease while CD8 T cell numbers increase as CT26 tumours grow (Taylor et al., 2019; Yu et al., 2018). However, in MC38 tumours, Treg numbers remain stable as the tumour mass increases (Taylor et al., 2019). As our study suggests, the lower densities of Tregs in CT26 tumours over time may be explained by their quiescent transcriptional profile which favours lymphoid tissue homing rather than tumour residence.

Compared to MC38 tumours, CT26 tumours typically have lower Treg infiltrates and a lower ratio of Treg to CD4 T cells (Vence et al., 2019; Fu et al., 2021; Selby et al., 2016). Upon the administration of antibodies that affect Treg numbers in tumours, CT26 tumours undergo higher increases in CD8 T cell/Treg ratios than MC38 tumours, but this does not necessarily result in a more significant tumour restriction (Selby et al., 2016). The naturally low densities of Tregs in CT26 tumours as a result of their accelerated egress to lymphoid tissue raise the question of whether Treg-mediated immunosuppression is a significant driver of CT26 tumour progression. Although Treg-mediated immunosuppression may be a key mechanism involved in the progression of MC38 tumours, CT26 tumours may be less dependent on Treg-mediated immune escape mechanisms. Instead, T cell exhaustion or differences in the extracellular matrices of the tumours may be more relevant mechanisms driving CT26 tumour growth (Yu et al., 2018). Great care should be taken when studying Treg blocking or depleting therapeutics using murine tumour models such as CT26 (Taylor et al., 2019). Furthermore, similar differences in Treg migration may be found in different human tumours, and should be explored as they might reveal key mechanisms underlying immune resistance and tumour heterogeneity.

To investigate Treg heterogeneity within MC38 tumours and TDLNs, we analysed scRNA-seq data from Kaede mice. As expected, we identified Ccr7$^{+}$, activated and Isg15$^{+}$ Treg subsets. Compositional analysis revealed that the tumour Tregs consisted mainly of activated and Isg15$^{+}$ Treg subsets, while the TDLNs were composed mainly of central/naive memory Tregs. Activated Treg fractions increased from green to red Tregs over time. This suggested that tumour infiltrating naive/central memory Tregs rapidly differentiated to adopt a highly immunosuppressive tumour-resident Treg signature, possibly due to exposure to neo-antigens in the tumour (Koizumi and Ishikawa, 2019). Naive/central memory Tregs that were not converted to activated/Isg15$^{+}$ Tregs became transient Tregs and egressed the tumour to accumulate in the TDLN via Ccr7-mediated chemotaxis. Consistent with this view, trajectory analysis reconstructed potential Treg differentiation routes and showed that Tregs bifurcate from a naive/central memory phenotype to either activated or Isg15$^{+}$ Tregs. Interestingly, there were no significant

differences in differentiation patterns between green and red tumour Tregs, indicating that the differentiation of green Tregs from naive/central memory phenotype to activated and Isg15$^+$ Tregs occurs rapidly, within 24 hours after tumour entry.

Differential expression analysis highlighted the absence of significant transcriptional differences between red and green MC38 Kaede Tregs. There were weak naive/central memory and activated Treg signatures in green and red Tregs respectively. As discussed before, this indicated that newly arriving naive/central memory green Tregs rapidly differentiated into activated and Isg15$^+$ phenotypes.

When we compared tumour-resident and transient Tregs, we observed significant differences in gene expression patterns. Transient Tregs upregulated naive/central markers such as Ccr7 and Tcf7. This suggested that tumour Treg subsets that do not differentiate into effector Tregs end up adopting a transient phenotype. Resident Tregs upregulated markers associated with an effector Treg signature such as Gzmb, Lag3, Il2ra, Il10, Tnfrsf18, and Tnfrsf9. Surprisingly, they did not express Ccr8, which has been shown to be upregulated in highly immunosuppressive tumour Tregs (Van Damme et al., 2021; Whiteside et al., 2021; Bhatt et al., 2021). We could not definitively explain this discrepancy, but we speculated that it could be due to differences in MC38 cell lines and the Kaede experimental system. However, the absence of Ccr8 expression in tumour-resident Tregs indicated that Ccr8 is not required for Treg tumour infiltration, as previous work has found (Whiteside et al., 2021). Ccr8 could serve as a redundant tumour retention signal or bystander activation marker.

Given their long occupancy in the TME, we anticipated that tumour-resident Tregs would upregulate genes associated with cellular adaptation to hypoxic environments. Consistent with this hypothesis, tumour-resident Tregs upregulated Hypoxia-inducible factor 1$\alpha$, Hif1a, supporting their residency in the oxygen-deficient TME (Wang et al., 1995).

Surface markers that can be targeted using antibody therapy, namely Lag3, Tnfrsf18, and Tnfrsf9 were not only upregulated in tumour-resident Tregs, but also positively correlated with tumour residency. These observations were consistent with previous work that, aided

by flow cytometry, demonstrated the upregulation of Lag3 in tumour Tregs (Li et al., 2022; Ikebuchi et al., 2021). The upregulation of Lag3 in tumour-resident Tregs could also explain the observed accumulation of Lag3$^+$ Tregs in 4T1 tumours after systemic Treg depletion with agents such as PI3K$\delta$ inhibitors (Lauder et al., 2021). Depending on dose, PI3K$\delta$ inhibitors likely deplete circulating naive/central memory Tregs, which have a transient phenotype, thus enriching the tumour for resident Lag3$^+$ Tregs. Pathway enrichment analysis revealed that tumour-resident Tregs upregulated the biological pathways associated with immunosuppression and cytokine response, as expected. Interestingly, tumour-resident Tregs downregulated metabolic processes such as the tricarboxylic cycle and amide biosynthesis. Additionally, they suppressed cell division.

Previous work has shown that Th17 and induced Tregs exhibit metabolic differences, indicating that metabolic changes are associated with T cell differentiation (Wagner et al., 2021). The metabolic differences/defects that we observed between tumour-resident and transient MC38 Kaede Tregs could possibly be explained by high lactate levels and the deficit of oxygen within the poorly vascularised TME. Therefore, tumour-resident Tregs would be expected to undergo drastic metabolic changes to adapt to the TME (Yan et al., 2022; Sasidharan Nair et al., 2021). Indeed, prior work has shown that Tregs shift their metabolism to consume lactate and metabolise it as an energy source in the TME. Lactate consumption also correlated with Treg immunosuppressive potential (Watson et al., 2021), which partially explains why tumour-resident Tregs are more immunosuppressive than transient Tregs.

GSEA appeared to suggest that putrescine production, which is involved in the polyamine metabolic process, was upregulated in tumour-resident Tregs. However, this result was potentially spurious as it was based on the expression of only one gene, Odc1, and did not consider the abundance of precursor-metabolites present in tumour-resident Tregs. To further explore amide metabolism, we simulated metabolic reactions in tumour-resident and transient Tregs using Compass. The simulation results indicated that polyamine metabolism was, in fact, downregulated in tumour-resident Tregs. This was a reasonable conclusion because polyamines are essential for cell proliferation

(Pendeville et al., 2001; Nishimura et al., 2002; Pegg, 2016). Thus, downregulation of amide/polyamine metabolism in tumour-resident Tregs was well correlated with their predicted low proliferative capacity.

Despite the in-depth transcriptional analysis conducted in this chapter, it is important to note that our study has some drawbacks. scRNA-seq data may not directly correlate well with protein expression, therefore differentially expressed genes we identified need to be experimentally validated using flow cytometry. Validating the downregulated metabolic processes in tumour-resident Tregs is likely to be cumbersome as it requires the quantification of metabolites and associated enzymes present in tumour-resident and transient Tregs. However, to our knowledge, this chapter represents the first study to provide an extensive bioinformatic characterisation of resident and transient Kaede Tregs in MC38 tumours and a transcriptional comparison between MC38 and CT26 Tregs.

### 3.5.1 Conclusion and future work

In this chapter, we have transcriptionally profiled Tregs within and between tumours. This has allowed us to explain differences in Treg trafficking kinetics across tumour types and identify markers that are upregulated in tumour-resident Tregs. We showed that, compared to MC38 Tregs, CT26 Tregs upregulate chemokine receptors, Ccr7 and Cxcr4, which promote their egress to lymphoid organs. This partially explained the dynamical differences between MC38 and CT26 Tregs observed in Chapter 2.

Comparison of tumour-resident and transient MC38 Kaede Tregs revealed that resident Tregs are highly immunosuppressive, responsive to cytokines, metabolically quiescent, and less proliferative. Considering defects in metabolism, it would be interesting to investigate whether metabolic manipulation, for example giving tumour-bearing Kaede mice polyamine and lipid supplements, can reduce resident Treg numbers and slow down tumour growth.

Though our analysis identified many interesting and unexpected pathways that differed between tumour-resident and transient Tregs, our main goal was to identify surface

markers that can potentially be targeted to deplete or inhibit resident Tregs. In alignment with this goal, we found that tumour-resident Tregs upregulate Lag3, Tnfrsf18, and Tnfrsf9. However, whether these markers are specific to tumour Tregs or are also expressed in Tregs that reside in other organs remains to be examined. In addition, it would be critical to investigate if human tumour Tregs also significantly upregulate these markers, which would shed light on the potential of targeting these markers in the clinic.

Given extensive Treg heterogeneity across organs, we hypothesised that some of the tumour-resident Treg markers are not unique to tumour Tregs, but are also expressed in Tregs in other mouse organs. We also hypothesised that given interspecies differences between mice and humans, some of the markers identified in tumour-resident mouse Tregs may not be expressed in human tumours. Thus, the goal of the next chapter has been to generate mouse and human Treg meta-atlases to investigate the expression patterns of Lag3, Tnfrsf18, and Tnfrsf9 across tumours, healthy organs, and species.

# 4

# Treg meta-atlases reveal inter-organ and inter-species heterogeneity

Contents


4.1 Introduction . . . . . 152
4.2 Aims . . . . . 154
4.3 Methods . . . . . 154
4.4 Results . . . . . 169
4.5 Discussion . . . . . 199


In Chapter 3, we transcriptionally profiled MC38 and CT26 Tregs, as well as tumour-resident and transient Tregs from the Kaede experimental model. We found that, compared to MC38 Tregs, CT26 Tregs consisted of a higher fraction of naive/central memory Tregs and upregulated Ccr7 and Cxcr4. This explained their increased migration to lymphoid organs and the drop in Treg densities that has been observed in CT26 tumours over time (Taylor et al., 2019). In comparison to transient Tregs, tumour-resident Tregs in MC38 Kaede mice upregulated pathways associated with immunosuppression and cytokine response but downregulated cellular metabolism, proliferation and amide metabolism. They also upregulated Lag3, Tnfrsf18 and Tnfrsf9, surface markers that can be leveraged to therapeutically target tumour-resident Tregs.

However, because the Kaede study did not consider Tregs in healthy mouse tissue and in humans, we could not tell which of the surface markers were specific to mouse tumours and translatable to human tumours for clinical application. We hypothesised that, due to extensive inter-organ Treg heterogeneity, some of the identified markers of tumour-resident Tregs are not unique to tumour Tregs. Furthermore, due to inter-species differences, some of the markers of tumour-resident Tregs found in mice may not translate well to human tumours. Therefore, the objective of the study in this chapter has been to generate mouse and human Treg scRNA-seq meta-atlases to explore Treg heterogeneity in tumours and healthy tissue in both mice and humans to identify clinically relevant markers of tumour Tregs.

## 4.1 Introduction

Tregs are critical for establishing a tolerogenic immune environment and preventing the onset of autoimmune disease (Sakaguchi et al., 1995, 2008). Although they constitute only 5-10% of all CD4 T cells in the blood (Baecher-Allan et al., 2004), Tregs are a highly heterogeneous cell population. Part of this heterogeneity arises from the significant reprogramming that Tregs undergo as they adapt to different tissues (Li et al., 2021; Burzyn et al., 2013; Delacher et al., 2020). Due to their significant contribution towards immunosuppression in the tumour, Tregs have become a target for next generation cancer immunotherapy. However, specifically depleting/blocking intratumoral Tregs without impacting circulating or tissue-resident Tregs and consequently inducing immune-related adverse effects is extremely challenging.

Over the past couple of years, many studies have focused on identifying molecular markers that are upregulated on intratumoral Tregs. Some of the markers that have been identified and targeted in humans include CCR4, CTLA4 and CD25. Apart from that, ongoing trials are exploring the potential therapeutic benefit of targeting CCR8 (Campbell et al., 2021), LAG3, TNFRSF18 (GITR), TNFRSF9 (4-1BB) on mouse and human intratumoral Tregs (Kim et al., 2020a).

Anti-CCR4 antibodies with antibody-dependent cellular cytotoxicity (ADCC) activity have been tested in patients with non-small lung cancer, lung cancer and esophageal cancer (Kurose et al., 2015b,a). However, anti-CCR4 immunotherapy was found to induce significant side-effects (Kurose et al., 2015b) and negatively affect CD8 T cells, thus limiting its efficacy (Maeda et al., 2021). Similarly, side-effects have been observed following Treg depletion using anti-CD25 antibodies (Mahnke et al., 2007). Ongoing research has focused on modifying the fragment crystallisable region (Fc domain) of anti-CD25 antibodies to limit unintended side-effects (Vargas et al., 2017).

There are mixed opinions on the therapeutic mechanism of anti-CTLA4, one of the pioneering immune checkpoint inhibitors. Some studies suggest that anti-CTLA4 achieves efficacy by partially depleting intratumoral Tregs (Vargas et al., 2018) in addition to blocking CD8 T cell exhaustion, while other studies have not observed significant anti-CTLA4-mediated Treg depletion (Sharma et al., 2019). However, it is well known that anti-CTLA4 induces significant side-effects (Karimi et al., 2021).

Recently, much attention has been placed on targeting CCR8, a chemokine receptor, that has been shown to be upregulated on murine and human tumours (Wang et al., 2012; Plitas et al., 2016; Villarreal et al., 2018; Van Damme et al., 2021; Whiteside et al., 2021; Bhatt et al., 2021; Campbell et al., 2021; Weaver et al., 2022; Kidani et al., 2022; Haruna et al., 2022). However, it remains unknown whether CCR8-mediated Treg depletion will be tolerated in humans.

Historically, many cancer treatments that have succeeded in mice have failed once they reached clinical trials due to inter-species differences (Mak et al., 2014). Furthermore, studies investigating markers that are upregulated on tumour Tregs often compare tumour samples with blood or healthy tissue adjacent to the tumour (Plitas et al., 2016). Highly heterogeneous Tregs resident in other tissues are not profiled due to experimental limitations but can contribute to immune-related adverse events seen in clinical trials.

To profile immune cells in different organs, scRNA-seq datasets that have become widely available over the past decade can be harnessed by creating and analysing meta-atlases

(Nakayama and Yamamoto, 2021; Nieto et al., 2021; Rocque et al., 2021; Swamy et al., 2021; Bosi et al., 2020). In light of side-effects associated with Treg targeting immunotherapy, the objective of this study has been to explore the expression of surface markers identified in mouse tumour-resident Tregs from Chapter 3, namely Lag3, Tnfrsf9, Tnfrsf18 and Ccr8 across different mouse organs and in humans. In particular, taking into account the results of Chapter 3, we hypothesised that due to the extensive heterogeneity of Tregs in different tissues, some of the surface markers of tumour-resident Tregs may also be expressed in Tregs resident in other mouse tissue. Furthermore, due to inter-species differences, not all mouse tumour-resident Treg markers translate well to human tumour Tregs. Thus, our objective has been to use data-driven approaches to rationally identify markers that are specific to tumour Tregs and also translatable to humans, increasing confidence in their potential clinical applications.

## 4.2 Aims

In summary, the objectives of the study have been as follows:

- To develop a mouse Treg scRNA-seq meta-atlas to explore the expression of therapeutically relevant Treg markers across different mouse tumour models and healthy tissue.
- To generate a human Treg scRNA-seq meta-atlas to assess the extent to which tumour-resident Treg markers identified in mouse models are relevant for human tumour Tregs.

## 4.3 Methods

### 4.3.1 Murine Treg scRNA-seq datasets

We developed a mouse Treg meta-atlas to explore Treg heterogeneity across conditions and organs. The scRNA-seq datasets were obtained from the sources listed in Table 4.1.

In summary, the datasets consisted of immune cells from tumours and healthy tissue. In the selected studies, $CD45^+$, $CD4^+$ or $Foxp3^+$ T cells were isolated to enrich for Tregs, which are typically a rare population. All Tregs were from treatment-naive or placebo-treated mice. Tregs were directly isolated from the tumour, other tissue within the same tumour-implanted mouse, or from tumour-naive mice. For example, tissue annotated as MC38 Spleen refers to Tregs that were obtained from the spleens of MC38-implanted mice (Table 4.1).

All studies used 10X Genomics technology to perform scRNA sequencing. The resulting raw sequencing reads were then aligned to the Mus musculus 10 (mm10) genome build to generate a gene expression matrix. As not all datasets included cellular annotations, we performed preliminary scRNA-seq analysis to isolate Tregs which were defined as $CD4^+$ $Foxp3^+$ cells. Finally, we concatenated the Tregs to generate a mouse scRNA-seq Treg meta-atlas.

**Table 4.1: Summary of datasets used to generate the murine Treg scRNA-seq meta-atlas**. TDLN – tumour draining lymph node, nDLN – inguinal lymph node from naive mice, PBMC – blood, TC1 – murine lung cancer model, MC38 and CT26 – murine colon cancer models, bLN – brachial lymph node, mLN – mesenteric lymph node, LLC OVA – Lewis Lung carcinoma expressing ovalbumin, B16F10 OVA – murine melanoma expressing ovalbumin, Figshare* – https://figshare.com/projects/Treg_scRNA-seq/38864.

| Tissue | Mouse Strain | Number of mice | Cell enrichment | Aligned Genome Build | Sequencing chemistry | Original Annotations | GEO/ArrayExpress Identifier | Source |
|---|---|---|---|---|---|---|---|---|
| MC38 | C57BL/6 | 4 | $CD45^+$ | mm10 | 10X 3'V3 | Present | GSE168944 | Bhatt et al. (2021) |
| MC38 PBMC | C57BL/6 | 4 | $CD45^+$ | mm10 | 10X 3'V3 | Present | GSE168944 | Bhatt et al. (2021) |
| MC38 Spleen | C57BL/6 | 4 | $CD45^+$ | mm10 | 10X 3'V3 | Present | GSE168944 | Bhatt et al. (2021) |
| MC38 TDLN | C57BL/6 | 4 | $CD45^+$ | mm10 | 10X 3'V3 | Present | GSE168944 | Bhatt et al. (2021) |
| Skin 1 | C57BL/6 | 3 | – | mm10 | 10X 3'V3 | – | GSE149121 | Liu et al. (2020) |
| Intestine | BALB/CJ | 10 | – | mm10 | 10X | – | GSE124880 | Xu et al. (2019) |
| TC1 | C57BL/6 | 7 | $CD4^+$ | mm10 | 10X 5' | – | GSE152022 | Son et al. (2020) |
| TC1 Lung | C57BL/6 | 10 | $CD4^+$ | mm10 | 10X 5' | – | GSE152022 | Son et al. (2020) |
| CT26 | BALB C | 30 | $CD45^+$ | mm10 | 10X 3'V3 | Present | GSE150970 | Qu et al. (2020) |
| bLN | Foxp3-IRES GFP | 16 | $CD4^+$ | mm10 | 10X 5' | – | Figshare* | Miragaia et al. (2019) |
| mLN | Foxp3-IRES GFP | 16 | $CD4^+$ | mm10 | 10X 3'V2 | – | Figshare* | Miragaia et al. (2019) |
| Skin 2 | Foxp3-IRES GFP | 16 | $CD4^+$ | mm10 | 10X 3'V2 | – | Figshare* | Miragaia et al. (2019) |
| Spleen | Foxp3-IRES GFP | 16 | $CD4^+$ | mm10 | 10X 3'V2 | – | Figshare* | Miragaia et al. (2019) |
| Colon | Foxp3-IRES GFP | 16 | $CD4^+$ | mm10 | 10X 3'V2 | – | Figshare* | Miragaia et al. (2019) |
| Thymus | Foxp3-GFP | 10 | $Foxp3^+$ | mm10 | 10X 3'V2 | – | GSE134902 | Hemmers et al. (2019) |
| LLC OVA | C57BL/6 | 5 | $CD45^+$ | mm10 | 10X V2 | – | GSE162621 | Van Damme et al. (2021) |
| B16F10 OVA | C57BL/6J | 3 | $Foxp3^+$ | mm10 | 10X 5'V2 | – | GSE166149 | Eschweiler et al. (2022) |
| Kaede 48 (MC38, TDLN and nDLN) | C57BL/6 | 6 | $CD45^+$ | mm10 | 10X 3'V2 | Present | In-house | – |
| Kaede 24-72 (MC38) | C57BL/6 | 13 | $CD45^+$ | mm10 | 10X 3'V2 | Present | E-MTAB-10176 | Li et al. (2022) |

### 4.3.2 Human Treg scRNA-seq datasets

To investigate Treg heterogeneity in humans and subsequently perform inter-species comparison, we generated a human Treg meta-atlas. Table 4.2 summarises the constituent datasets used to develop the human Treg meta-atlas. The atlas consisted of Tregs isolated from tumours, adjacent healthy tissue, and normal tissue from tumour-free subjects. To reduce confounding effects, we carefully selected datasets from patients who were not under treatment at the time of cell isolation.

Most datasets used in the human Treg meta-atlas came from $CD45^+$, $CD3^+$ and $CD4^+$ and $CD8^+$-enriched experiments. In the case of the Zheng *et al.* dataset (Zheng et al., 2021), we isolated Tregs from the $CD4^+$ enriched dataset and later used the $CD8^+$ dataset to compare Tregs with CD8 T cells. Tregs were defined as $CD4^+$ $FOXP3^+$ cells which implies that other Treg subsets such as Type 1 Tregs (Tr1), could not be analysed in this dataset. However, this exclusion of Tr1 Tregs can be justified by the fact that these $FOXP3^-$ Treg subsets tend to be rare and thus, difficult to detect in large numbers from scRNA-seq datasets. All datasets were aligned to the GRCh38 genome build.

Figure 4.1 gives a brief overview of how human/mouse scRNA-seq datasets were processed. Individual data analysis steps are described in full detail in the following section.

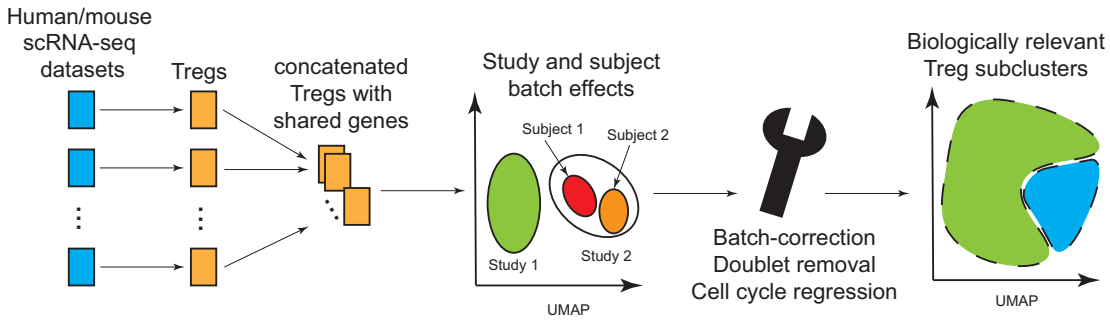



**Figure 4.1: Overview of how human and mouse scRNA-seq datasets were processed.** Tregs were isolated from public scRNA-seq datasets and concatenated. Preliminary clustering was conducted to identify batch effects or confounding variables in the datasets. This was followed by data correction, resulting in the identification of biologically relevant Treg subpopulations.

**Table 4.2: Summary of datasets used to generate the human Treg scRNA-seq meta-atlas**. All Tregs came from subjects who were not under treatment at the time of cell isolation. PBMC – blood, LN – lymph node, Server[1] – https://artyomovlab.wustl.edu/immune-aging/explore.html and Server[2] – https://www.tissuestabilitycellatlas.org

| Tissue | Number of subjects | Cell enrichment | Aligned Genome Build | Sequencing chemistry | Original Annotations | GEO/ArrayExpress Identifier | Source |
|---|---|---|---|---|---|---|---|
| Breast cancer | 2 | $CD3^+$ | GRCh38 | 10X 3' | – | GSE110686 | Savas et al. (2018) |
| Hepatic LN | 3 | $CD45^+$ | GRCh38 | 10X | Present | GSE140228 | Zhang et al. (2019) |
| Hepatocellular Carcinoma | 5 | $CD45^+$ | GRCh38 | 10X | Present | GSE140228 | Zhang et al. (2019) |
| Colorectal Cancer | 6 | – | GRCh38 | 10X 3'V3 | – | GSE188711 | Guo et al. (2022) |
| Healthy Colon | 8 | $CD3^+$ | GRCh38 | 10X 5'V3 | – | GSE144469 | Luoma et al. (2020) |
| Colorectal cancer liver metastases | 3 | – | GRCh38 | 10X V2 | – | GSE178318 | Che et al. (2021) |
| PBMC | 21 | – | GRCh38 | 10X 5' | – | Server[1] | Mogilenko et al. (2021) |
| Spleen | 5 | – | GRCh38 | 10X 3'V2 | Present | Server[2] | Madissoon et al. (2020) |
| Lung Cancer | 11 | $CD3^+$ | GRCh38 | 10X 3'V2 | – | GSE162500 | Gueguen et al. (2021) |
| Healthy Lung | 2 | $CD3^+$ | GRCh38 | 10X 3'V2 | – | GSE162500 | Gueguen et al. (2021) |
| Head and Neck Cancer | 12 | $CD45^+$ | GRCh38 | 10X 3'V2 | – | GSE164690 | Kürten et al. (2021) |
| Normal Lung | 11 | – | GRCh38 | 10X 3' | Present | GSE131907 | Kim et al. (2020b) |
| Brachial Lymph Node | 10 | – | GRCh38 | 10X 3' | Present | GSE131907 | Kim et al. (2020b) |
| Uveal Melanoma | 11 | – | GRCh38 | 10X 3'5' | – | GSE139829 | Durante et al. (2020) |
| Basal Cell Carcinoma | 2 | $CD4^+$ and $CD8^+$ | GRCh38 | 10X 5' | Present | GSE156728 | Zheng et al. (2021) |
| Esophageal Cancer | 7 | $CD4^+$ and $CD8^+$ | GRCh38 | 10X 5' | Present | GSE156728 | Zheng et al. (2021) |
| Healthy Esophagus | 6 | $CD4^+$ and $CD8^+$ | GRCh38 | 10X 5' | Present | GSE156728 | Zheng et al. (2021) |
| Ovarian Cancer | 1 | $CD4^+$ and $CD8^+$ | GRCh38 | 10X 5' | Present | GSE156728 | Zheng et al. (2021) |
| Pancreatic Cancer | 6 | $CD4^+$ and $CD8^+$ | GRCh38 | 10X 5' | Present | GSE156728 | Zheng et al. (2021) |
| Renal Cell Carcinoma | 6 | $CD4^+$ and $CD8^+$ | GRCh38 | 10X 5' | Present | GSE156728 | Zheng et al. (2021) |
| Healthy Kidney | 6 | $CD4^+$ and $CD8^+$ | GRCh38 | 10X 5' | Present | GSE156728 | Zheng et al. (2021) |
| Thyroid Cancer | 10 | $CD4^+$ and $CD8^+$ | GRCh38 | 10X 5' | Present | GSE156728 | Zheng et al. (2021) |
| Healthy Thyroid | 8 | $CD4^+$ and $CD8^+$ | GRCh38 | 10X 5' | Present | GSE156728 | Zheng et al. (2021) |
| Uterine Cancer | 9 | $CD4^+$ and $CD8^+$ | GRCh38 | 10X 5' | Present | GSE156728 | Zheng et al. (2021) |
| Healthy Uterus | 8 | $CD4^+$ and $CD8^+$ | GRCh38 | 10X 5' | Present | GSE156728 | Zheng et al. (2021) |

### 4.3.3 Characteristics of scRNA-seq data

Each of the scRNA-seq datasets used in the meta-atlases consisted of a matrix of gene expression. The rows of the matrix correspond to barcoded cells, while the columns contain unique transcripts detected in the cells. Thus, the matrix is populated with integer counts representing the frequency of individual mRNA molecules (messenger Ribonucleic acid/genes) that are expressed in each cell. Table 4.3 illustrates an exemplar scRNA-seq expression matrix with a total of $i$ cells and $n$ genes.

| | Gene 1 | Gene 2 | Gene 3 | ... | Gene $n$ |
|---|---|---|---|---|---|
| Cell 1 | 0 | 10 | 1 | ... | 5 |
| Cell 2 | 0 | 2 | 0 | ... | 0 |
| Cell 3 | 0 | 1 | 0 | ... | 0 |
| ... | ... | ... | ... | ... | ... |
| Cell $i$ | 0 | 0 | 0 | ... | 14 |

**Table 4.3: Exemplar scRNA-seq gene expression matrix**.

scRNA-seq data is extremely noisy due to various factors. These include the stochastic nature of transcription, biological effects such as divergent cell cycle stages across cells, and amplification bias during the experimental stages of sequencing (Kim et al., 2015). All of these factors result in high variation in gene expression across cells.

The expression matrix is also zero-inflated. This implies that it is characterised by a disproportionate frequency of genes with raw counts of zero, a phenomenon that is particularly common for genes with low expression profiles (Kim et al., 2015).

Genes that are moderately expressed in one cell may have zero expression in another cell of the same cell type, giving rise to technical artefacts referred to as drop-outs. As a result of zero-inflation and drop-outs, gene expression follows complex multimodal distributions which are challenging to statistically model.

Finally, scRNA-seq data is characterised by batch effects arising from nonlinear interactions between biological and technical differences between experiments (Luecken

et al., 2022). These batch effects confound the identification of biologically meaningful signals in the data, complicating downstream analysis such as clustering. Therefore, to mitigate the extent of batch effects in the downstream analysis, we ensured that all datasets that were used in the mouse or human Treg meta-atlas had been generated using similar sequencing technology and aligned to the same genome build, as illustrated in Tables 4.1 and 4.2.

### 4.3.4 scRNA-seq analysis pipeline

Several tools have been developed to facilitate the analysis of scRNA-seq data and address some of the challenges outlined above. The most popular are Seurat (Satija et al., 2015), which is an R package, and Scanpy (Wolf et al., 2018), a Python package.

We started our scRNA-seq analysis using Seurat, but had to switch to Scanpy because Seurat took a long time to process atlas-level scRNA-seq datasets on a local machine. On the contrary, Scanpy implements novel annotated data matrices (Virshup et al., 2021) that are optimised to handle large datasets in memory, allowing us to easily analyse extremely large data matrices in reasonable time.

The scRNA-seq analysis pipelines adopted by Seurat and Scanpy are similar. Although we followed standard preprocessing steps (Chen et al., 2019c), we incorporated slight modifications to make the analysis relevant for atlas-level or integrative data analysis. Below, we highlight the key steps that we took to robustly analyse the single cell datasets and generate the Treg meta-atlases presented here.

#### Amalgamating Treg data from different studies

We separately analysed datasets from individual studies to isolate Tregs. Finally, we pooled the different Treg subsets together to generate 2 Treg meta-atlases, one for humans and the other for mice. We observed that Treg expression matrices from different studies did not cover the same set of genes. This variation in gene coverage

can contribute to batch effects, which cause the data to separate by study rather than biological Treg subsets upon clustering.

To eliminate the contribution of study-specific gene sets towards batch effects, we excluded genes that were not present in all datasets, thus creating a data matrix with shared genes across different studies. This approach is commonly used in integrative scRNA-seq analysis and has been adopted in prior studies (Bosi et al., 2020).

### Filtering and quality control

Some of the genes in the integrated matrix were expressed at low levels and present in very few cells. Furthermore, some cells only expressed very few genes. As part of the prepossessing pipeline, we filtered cells that expressed less than 250 genes and genes that were only found in less than 3 cells.

We then determined the level of expression of mitochondrial genes in the filtered matrix. High proportions of mitochondrial genes highlight low-quality or even dead cells that may have burst open at some stage before the actual sequencing was started. As a result, these cells would have lost cytoplasmic mRNA through holes in the cell membrane, but they retained mitochondria that, being quite large, do not easily pass through the ruptures in the cell membrane (Lun et al., 2016). For both human and mouse atlases, we observed that the percentage of mitochondrial gene expression was less than 0.1, indicating that high-quality cells were analysed.

### Library size normalisation and logarithmic transformation

Gene expression patterns in different studies differ due to sequencing technology, amplification bias, reagents, and other factors. For example, in two independent studies that involve exactly the same cell type under the same conditions, raw gene expression counts may be proportional rather than equivalent to each other. If not corrected, these variations can confound the ultimate interpretation of cell states.

To address this challenge, we applied library size normalisation to remove the effect of extreme values and ensure that cells had similar gene expression patterns. Equation 4.1 illustrates how the library normalisation was performed. Taking into account a scRNA-seq gene expression matrix with $n$ total genes,

$$\tilde{x}_i = \frac{x_i}{n} \cdot 10000, \tag{4.1}$$

where $x_i$ is the $i$th gene expressed in a given cell and $\tilde{x}_i$ is the library size normalised expression value for gene $x_i$ (Wolf et al., 2018; Satija et al., 2015).

After library normalisation, the data was transformed to eliminate large numerical ranges in gene expression and improve visualisation. This was done by applying the following transformation, element-wise on X:

$$X_T = \ln(X + 1), \tag{4.2}$$

where $X$ is the original gene expression matrix and $X_T$ is the log-transformed matrix.

### Identification of highly variable genes

Distinct cell subsets express genes that are different from those expressed by the rest of the cells. Identifying these highly variable genes is critical for dimensionality reduction and provides a basis for running Principal Component Analysis (PCA).

To determine highly variable genes, Scanpy fits a nonparametric Locally Estimated Scatterplot Smoothing (LOESS) curve to the relationship between the mean log-transformed expression and variance of each gene across different cells. It divides genes into 20 bins based on their mean expression (Satija et al., 2015). For each bin, a standard count, $SC$, is then determined as follows:

$$SC = \frac{X_{G,C} - \overline{X}_G}{\sigma_G}, \tag{4.3}$$

where $X_{G,C}$ is the log transformed expression of a gene $G$ in cell $C$ and $\overline{X}_G$ is the mean log transformed expression of gene X across different cells. $\sigma_G$ is the standard

deviation of the log transformed expression of gene $G$, which is predicted by the LOESS curve. Finally, genes with a standard count that is larger than 0.5 are kept as highly variable genes while the rest are discarded from the main data matrix (Satija et al., 2015). This process partially reduces the dimensionality of the data matrix. However, since all normalised genes are required during downstream cell cycle regression, an instance of whole matrix with all normalised and scaled genes is stored in a different slot of the annotated data object that Scanpy uses.

### Scaling and running PCA on highly variable genes

When analysing uniform scRNA-seq data from a single study, it is common to regress out additional sources of variation such as the cell cycle stage from the log-transformed matrix of highly variable genes before scaling the data. However, in our analysis pipeline for data from multiple studies, we skipped this step. This was a deliberate step that enabled us to see how the cells clustered together before any batch correction had been attempted and rationally investigate the categorical variables to use when we eventually performed batch correction. Therefore, we proceeded to scale or standardise the expression of highly variable genes so that the mean expression in all cells was 0 and the variance was 1. This was achieved through subtracting the mean log transformed gene expression from the log transformed gene expression and dividing the result by the standard deviation of the log transformed gene expression.

Next, we performed PCA to identify the directions that captured most of the variance in the data. For both the mouse and human Treg meta-atlases, we selected the top 50 principal components for downstream analysis.

Multiple methods have been developed to select the number of principal components, including the most commonly used elbow method (Thorndike, 1953). However, the Scanpy documentation recommends using a high number of principal components, as relying on the elbow method may result in the exclusion of some principal components that may contain a reasonable amount of information.

### UMAP visualisation and community detection

As a result of the complexity associated with scRNA-seq data, it is not always possible to easily identify clusters of cells with similar gene expression patterns on a 2-dimensional PCA plot. This is mainly due to the fact that, for complex datasets, the first 2 principal components may not significantly explain most of the variation in the data. To address this challenge, additional dimensionality reduction methods such as t-Distributed Stochastic Neighbour Embedding (t-SNE) (Van der Maaten and Hinton, 2008) or Uniform Manifold Approximation and Projection (UMAP) (McInnes et al., 2018) are often applied to the principal components.

UMAP is preferred over t-SNE due to its scalability to large datasets and its ability to more accurately capture the global structure of the underlying data (McInnes et al., 2018). Thus, the principal components calculated in the previous step were fed into the UMAP algorithm, which then projected the data onto a 2-dimensional graph based on the similarity between the gene expression patterns of the cells. In this low-dimensional graph, cells are depicted as nodes, while the edges give a measure of the level of similarity between the cells.

To group Tregs into communities with shared gene expression patterns, we used the Leiden algorithm (Traag et al., 2019) which iteratively moves nodes between communities, refines, aggregates the nodes, and assesses their connectivity until convergence is reached.

### Identifying sources of batch-effects

When we plotted the mouse and human Treg meta-atlases on a UMAP embedding, we observed significant batch effects. In particular, mouse data was separated mainly by study, while human data was separated based on study and individual subjects within each study. Furthermore, proliferating cells that expressed high levels of MKI67 clustered together in both datasets.

To quantitatively assess the extent of batch effects present in the datasets, we made use of a metric known as the Local Inverse Simpsons Index (LISI) (Korsunsky et al., 2019a). Briefly, LISI fixes each cell and determines the origin of the neighbouring cells. If these cells come from the same batch group as the fixed cell, then a low score is assigned. However, if the surrounding cells come from different batches, then high scores are assigned based on how many batch groups are detected. The same process is repeated for all cells in the low-dimensional embedding. The output of LISI is a distribution which, theoretically, is supposed to be peaked at a value that corresponds to the total number of batch groups in the data if integration/batch correction has been successful. Otherwise, the distribution will peak at 1 when batch correction has failed. However, these conclusions only make sense under the assumption that there are equal numbers of cells within each batch. If one batch has significantly more cells, the LISI distribution will be shifted to the lower end because significant numbers of cells from the over-represented batch will inevitably surround each other. A reasonable way of addressing this problem for sufficiently large datasets is to run the LISI algorithm on down-sampled data in which there are similar numbers of cells per batch.

After inspecting the clusters on the UMAP and leveraging the LISI distributions, we decided to correct for cell cycle stage and study for the mouse dataset. In the human Treg meta-atlas, we corrected for individual subjects in addition to cell cycle stage and study variables.

### Cell cycle and module/signature scoring

In scRNA-seq analysis, different types of proliferating cells tend to cluster together. Therefore, it is difficult to extract additional biological information from these cells in addition to proliferation.

To regress out the effect of cell cycling, we needed to score all cells in the data to identify the cells that were in the synthesis stage (S-phase) and the G2M cell cycle arrest phase. This was accomplished by calculating the normalised expression of genes of the

S-phase and G2M-phase in all cells using established sets of S-phase and G2M-phase genes in humans (Tirosh et al., 2016). For mice, cell cycle scoring was performed using the corresponding murine orthologs.

In our pipeline, we used the previously stored instance of data with all normalised and scaled genes described towards the end of Subsection 4.3.4 instead of the instance with highly variable genes only. This ensured that some cell cycle genes that had been filtered out as less variable in different cells were present to more accurately score the cells.

Apart from cell cycle scoring, we also performed gene signature/module scoring. This was similarly accomplished through calculating the average normalised expression of a collection of genes, which make up the module or gene signature of interest. For both cell cycle and module scoring, the Scanpy function scanpy.tl.score_genes was used (Wolf et al., 2018).

### Doublet removal

Following cell cycle scoring, we applied Single Cell Remover of Doublets (Scrublet), a method that is used to detect doublets in the data (Wolock et al., 2019). Doublets arise when two cells are captured in an oil droplet or well during the experimental setup of a sequencing run. Thus, when the cell by gene count matrix is generated after sequencing, the transcriptomes of two independent cells are registered under an individual cell referred to as a doublet. The presence of doublets leads to inaccurate identification of cell subtypes and their biological states (Wolock et al., 2019).

To identify doublets, Scrublet takes in the raw count data matrix, performs library size normalisation, identifies highly variable genes, standardises the data, and runs unweighted PCA. Following these steps, Scrublet simulates doublets using the observed data. This is simply accomplished by randomly adding up the unnormalised expression values of any two cells in the data. The key assumption here is that doublets or multiplets are rare, so it is less likely to inadvertently simulate doublets from cells that are already doublets to begin with.

The simulated doublets are pre-processed in the same way as the original data as described above. Scrublet then embeds the doublets into the same PCA space as the original data using the eigenvectors from the previous PCA run (Wolock et al., 2019). It then clusters both the observed data and the simulated doublets on a k-nearest neighbour graph using the principal components. The K-nearest neighbours algorithm accepts a parameter, $k_{adj}$ which corresponds to the number of nearest neighbours and is set to:

$$k_{adj} = \text{round}(f + (1 + r)) \quad \text{where} \quad f = \text{round}(0.5 \times \sqrt{\text{total number of cells}}), \tag{4.4}$$

and $r$ is the ratio of the simulated doublets to the observed data (Wolock et al., 2019).

The cells are then assigned doublet scores based on their proximity to the simulated doublets on the k-nearest neighbour graph. For a cell $i$ with $k_d(i)$ neighbouring doublets, the doublet score, $\mathcal{L}_i$, is calculated as follows:

$$\mathcal{L}_i = \frac{q_i \hat{\rho}/r}{1 - \hat{\rho} - q_i(1 - \hat{\rho} - \hat{\rho}/r)} \quad \text{with} \quad q_i = \frac{k_d(i) + 1}{k_{adj} + 2}, \tag{4.5}$$

where $\hat{\rho}$ is the estimated doublet rate of approximately 5% (Wolock et al., 2019). Doublet scores associated with the simulated doublets are also calculated, and their distribution is used to inform the threshold that separates singlets from doublets. Cells that have a doublet score above this threshold are labelled as doublets and removed from the data (Wolock et al., 2019).

### Regressing out sources of unwanted biological variation

After cell cycle scoring and doublet removal, the dataset exists as a normalised and scaled gene expression matrix with all genes. Like before, we proceeded to identify highly variable genes and reduce the dimensionality of the dataset. Next, we regressed out the artefacts that are caused by differences in the total number of gene counts, the percentage of mitochondrial genes, and the cell cycle scores for each cell. This was done by fitting a generalised linear model to the data matrix and using the model to remove the contribution of these variables from the gene expression matrix (Wolf et al., 2018).

Following this correction, we scaled the dataset and ran PCA to reduce the dimensionality. Since from Subsection 4.3.4, we had identified the variables to integrate the data over, we applied the Harmony algorithm (Korsunsky et al., 2019a) to correct for the artefacts caused by the fact that the data originated from different studies and the inter-individual batch effects seen in human data. We then embedded the data into a 2-dimensional UMAP plot and evaluated the success of data integration using LISI scores.

### 4.3.5 Batch correction using Harmony

Currently, more than 49 batch correction algorithms have been developed (Luecken et al., 2022). Some of the popular methods include Harmony (Korsunsky et al., 2019a), Batch-balanced K-Nearest Neighbours (BBKNN) (Polański et al., 2020), Mutual Nearest Neighbours (MNN) (Haghverdi et al., 2018) and Count-adapted Regularised Deep Embedded Clustering (CarDEC) (Lakkis et al., 2021).

To correct for batch effects during the creation of Treg meta-atlases, we explored the use of BBKNN and Harmony. Upon inspection, Harmony, but not BBKNN, was able to effectively correct for study-specific and inter-individual variations in the atlases. Below, we briefly explain how Harmony works.

Harmony corrects for batch effects by modifying the principal component (PC) embeddings associated with each cell. This implies that scRNA-seq data needs to be preprocessed before Harmony can be applied. The required preprocessing steps include library normalisation, log transformation, scaling, and Principal Component Analysis (PCA). Thereafter, the principal components and a dataframe with categorical variables to be 'harmonised' over are used as input for the Harmony algorithm.

Harmony applies L2 normalisation to the PCs to determine cell-to-cell similarity using cosine distances. The algorithm then runs k-nearest neighbours 10 times with random restarts to identify initial cluster centroids for the L2 normalised PCs (Korsunsky et al., 2019b). Next, each cell is assigned a probabilistic membership in each of the clusters based on how close the cell is to the cluster centroids.

Once the cells have been probabilistically clustered, Harmony evaluates how diverse the cells in each cluster are. At this step, Harmony attempts to improve intra-cluster batch diversity by reassigning cells to nearby cluster centroids while penalising cell assignments that do not differ by batch factor. Thereafter, Harmony recomputes the new cluster centroids and corrects the original principal component embeddings to reflect the intra-cluster batch correction/diversification. This is achieved through the use of a machine learning model known as the Mixture of Experts (MoE) model. In short, this is an ensemble learning technique that splits data into a number of subdatasets. Each subdataset is then assigned to a specialised statistical model, known as an expert or learner, that is well adapted for processing that particular data subset.

In the mixture of experts model that Harmony uses, each cluster is considered to be an expert and is assigned a linear model that determines the contribution of cell states and batch effects to the original PCs. Once the factors that contribute to the original PCs have been determined, Harmony subtracts the batch-specific factors to remove batch effects while preserving cell-specific/biological effects. This results in the correction of the PC embeddings (Korsunsky et al., 2019b).

The steps outlined above are repeated until a state of convergence is reached in which no additional changes in the corrected PC components are seen. Schematically, the Harmony algorithm is illustrated below.

## 4.4 Results

### 4.4.1 Integrating mouse Tregs

We constructed an scRNA-seq Treg meta-atlas to explore mouse Treg heterogeneity in health and disease. scRNA-seq datasets from the public domain representing different murine tissue (Fig. 4.3A-B) were collected, cleaned and integrated. To identify sources of technical variation, also known as batch effects, we first clustered the combined datasets before performing batch correction. The LISI distribution, which measures

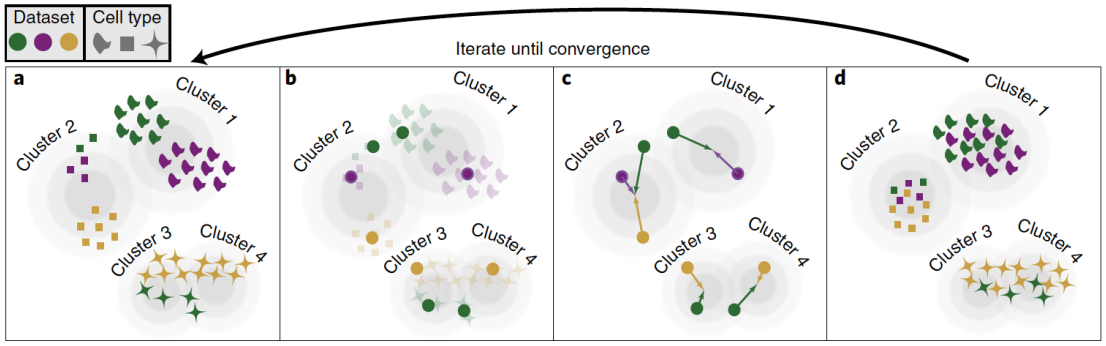



**Figure 4.2: Illustration of steps taken by the Harmony algorithm**. A: Harmony inspects the PC embeddings by dataset and performs diverse assignment of cells to different clusters. Dataset/batch-specific centroids are determined (B). Harmony learns correction factors that translate cells from individual datasets so that their centroids approach the local cluster centroid (C). D: Harmony assigns the cells to the new locations. The algorithm is then repeated until convergence is reached. The figure was taken from the original Harmony publication (Korsunsky et al., 2019a).

the extent of study-specific batch effects within scRNA-seq meta-atlases, was centered at unity (Fig. 4.3C). This indicated that the Tregs tended to cluster according to the study of origin rather than gene expression, contrary to what would be expected (Fig. 4.3D). Furthermore, highly proliferative cells clustered together (Fig. 4.3E).

To correct for the study-specific batch effects, we used the Harmony algorithm (Korsunsky et al., 2019a). After batch correction, we downsampled the dataset to ensure that there were equal Treg numbers in each study then determined the LISI distribution. The LISI distribution shifted in the positive direction and was peaked at 8, suggesting an improvement in data integration (Fig. 4.3F). Upon data visualisation on the UMAP, study-specific and proliferative cell clusters were no longer visible (Fig. 4.3G-H). Summing these observations, we concluded that the Treg datasets from different studies had been successfully integrated.

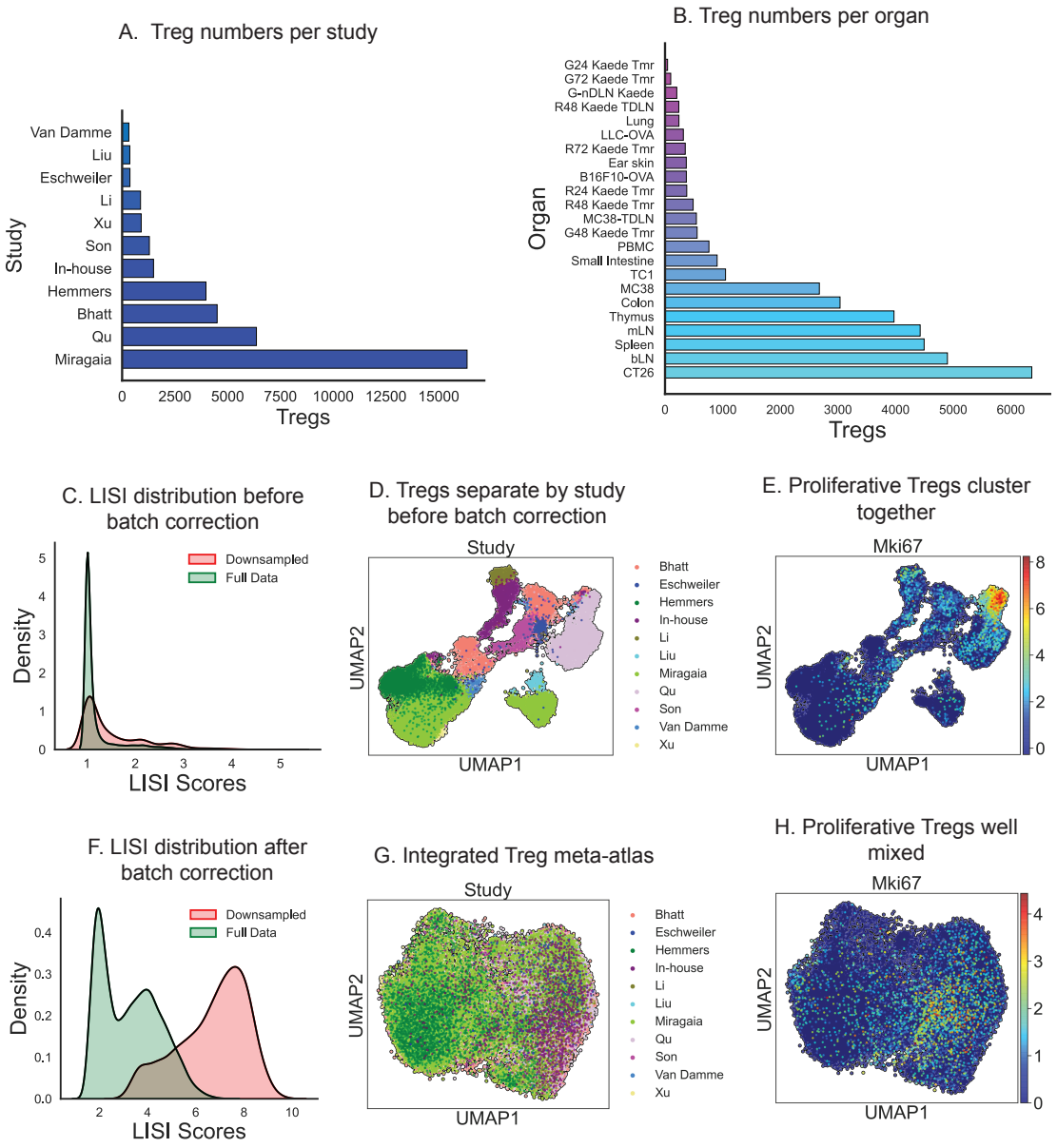



**Figure 4.3: Integrating mouse Tregs**. A: Treg numbers per study. B: Treg numbers per organ. C: LISI distributions calculated from either the full or downsampled dataset before batch correction. D: UMAP showing Tregs clustering by batch/study. E: UMAP showing the expression of Mki67 before batch correction. F: LISI distributions determined using either the full or downsampled dataset after batch correction. G: UMAP showing the integrated mouse Treg meta-atlas. H: UMAP showing the expression of Mki67 after batch correction.

### 4.4.2 Identifying Treg subpopulations using the mouse Treg meta-atlas

To identify Treg communities with similar transcriptional profiles, we proceeded to cluster the integrated mouse Treg meta-atlas using the Leiden community-detection algorithm (Traag et al., 2019). We identified 7 Treg subclusters namely Ccr7$^+$, Srm$^+$, Itgb1$^+$, Isg15$^+$, non-lymphoid (NLT), non-lymphoid Ccr7$^+$ (NLT Ccr7) and activated Tregs (Fig. 4.4A).

Ccr7$^+$ Tregs expressed markers such as Ccr7, Lef1, Tcf7 and Sell, which are associated with a naive, stem-like or central memory T cell signature. Srm$^+$ Tregs upregulated Srm, which encodes for Spermidine Synthase, an enzyme that plays a critical role in polyamine metabolism by converting putrescine to spermidine. These Srm$^+$ Tregs also upregulated Cdk4, a cyclin-dependent kinase, that is involved in cell proliferation. Itgb1$^+$ Tregs upregulated the integrins Itgb1 and Itga4. They also over expressed Nrp1 and Nt5e, an ectonucleotidase, which is associated with adinosine-mediated immunosuppression. Isg15$^+$ Tregs upregulated cytokine response genes such as Isg15, Stat1, Ifit1 and Socs1.

NLT Tregs, which mostly came from the skin and colon, were marked by the expression of Cd83 and transcriptional factors such as Batf, Rora and Gata3. NLT Ccr7$^+$ Tregs clustered close to the NLT Tregs and expressed markers associated with naive/central memory phenotype such as Ccr7 and Lef1. Finally, activated Tregs upregulated markers associated with a strong immunosuppressive potential such as Gzmb and the ectonucleotidase, Entpd1. They also expressed Lag3, which we previously identified as one of the markers of tumour-resident Tregs in Chapter 3, and Ccr8, which has been previously reported as a marker of tumour-infiltrating Tregs (Whiteside et al., 2021) (Fig. 4.4B).

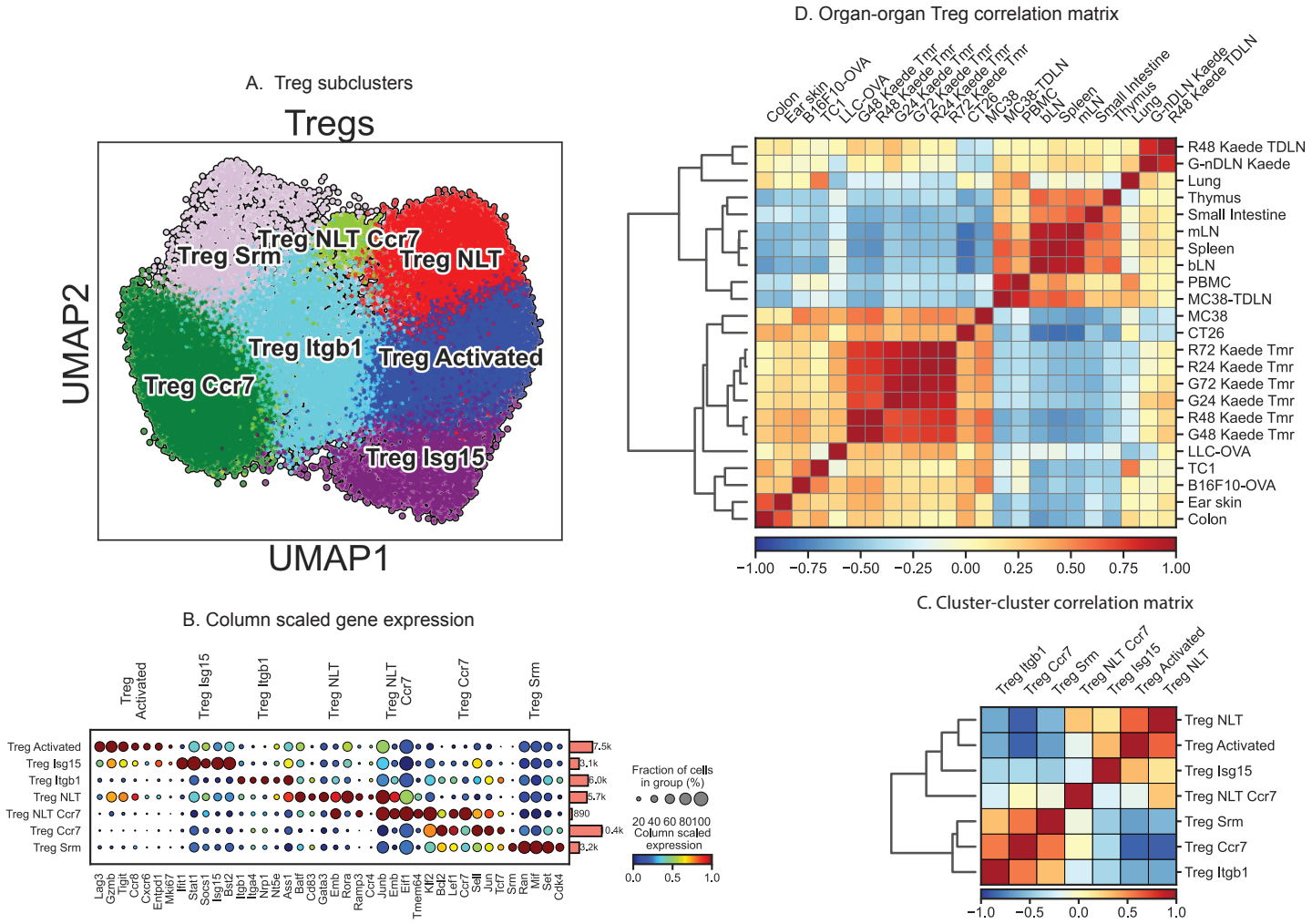



**Figure 4.4: Clustering the mouse Treg meta-atlas**. A: Treg meta-atlas subclusters. B: Dotplot showing the column scaled expression patterns of different genes in different Treg clusters. Correlation matrices showing Treg clusters (C) and tissue Tregs (D) with similar gene expression patterns. NLT – Non-Lymphoid Tissue

To explore inter-cluster relationships, we performed hierarchical clustering which revealed two groupings of the Treg subclusters within the meta-atlas. $Srm^+$, $Ccr7^+$ and $Itgb1^+$ Treg clusters were grouped together while the NLT, activated, $Isg15^+$ and NLT $Ccr7^+$ Treg clusters formed a separate group (Fig. 4.4C). Interestingly, this analysis suggested that NLT and activated Tregs were closely related by gene expression (Fig. 4.4C).

Similarly, we examined overall inter-tissue Treg gene expression relationships. Again, hierarchical clustering revealed two different tissue Treg groupings. Broadly, Tregs from healthy tissue separated from Tregs from tumours, with the exception of Tregs from the ear skin and colon, which were grouped together with Tregs from tumours (Fig. 4.4D). Collectively, these findings suggested a similarity in gene expression patterns between tumour Tregs and NLT Tregs, which could potentially complicate the development of therapeutics that specifically target tumour-resident Tregs without affecting Tregs resident in non-lymphoid tissue.

### 4.4.3 Compositional analysis of mouse Tregs

To further explore relationships between tissue-specific Tregs, we plotted sample-level Treg centroids. This allowed us to broadly visualise where Tregs from individual mice/samples localised on the UMAP embedding. Generally, Tregs from tumours separated from Tregs from healthy tissue (Fig. 4.5A). However, as previously noted, Tregs from non-lymphoid tissue (NLT) exhibited extreme heterogeneity. While some NLT Tregs clustered together with Tregs from lymphoid tissue, others (ear skin and colon Tregs) clustered closely with tumour Tregs (Fig. 4.5A). This was similarly observed when we plotted density plots showing where lymphoid, non-lymphoid and tumour Tregs localised on the UMAP (Fig. 4.5B-D).

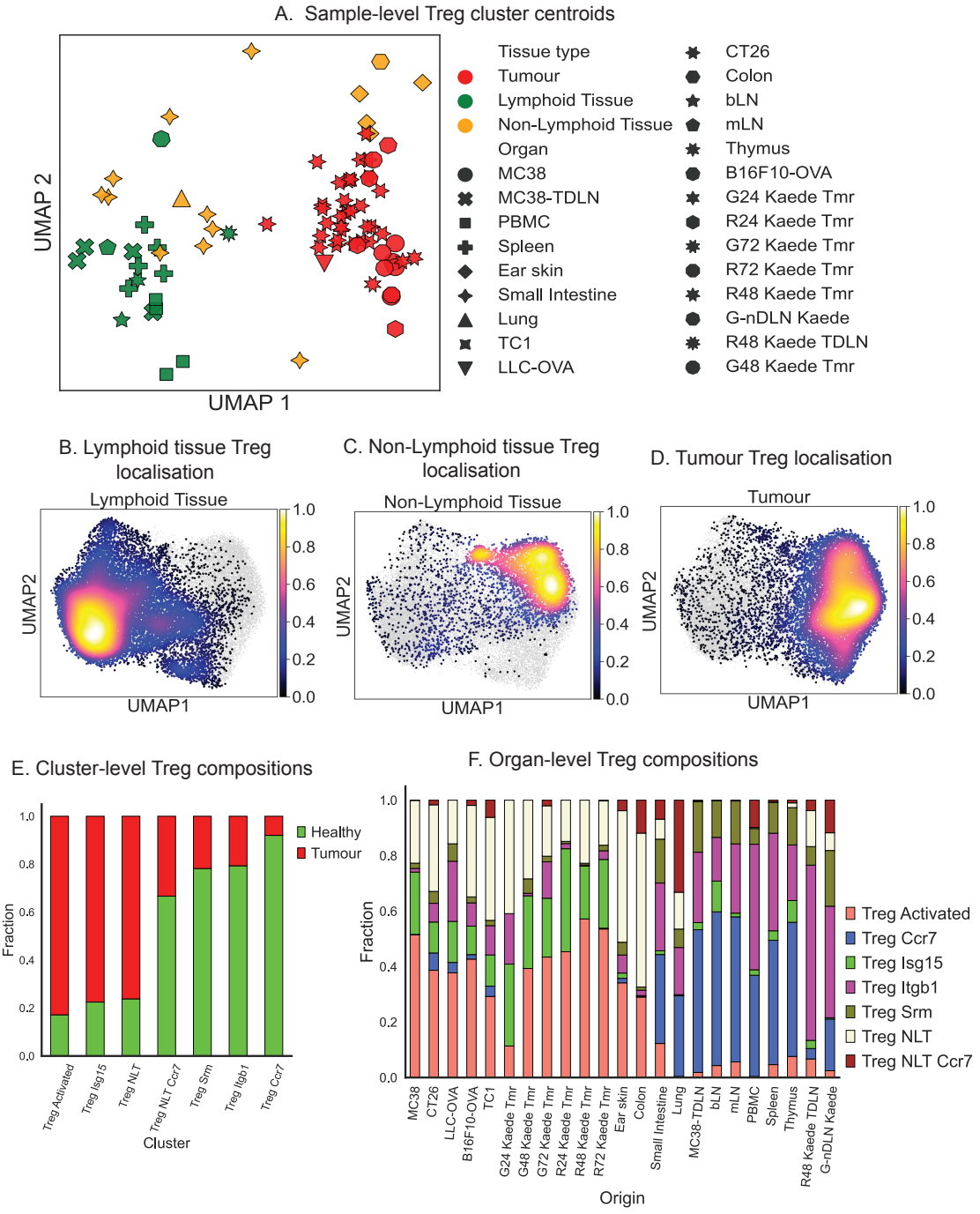



**Figure 4.5: Compositional analysis of mouse Treg meta-atlas**. A: UMAP showing Treg centroids per mouse or sample. UMAPs showing regions with the highest densities of lymphoid tissue (B), non-lymphoid tissue (C) and tumour Tregs (D). E: Barplot showing the fractions of Tregs originating from healthy tissue and tumours per cluster. For this analysis, the dataset was downsampled so that there were equal numbers of Tregs (12 696) from healthy tissue and tumours. F: Barplot showing the compositional phenotypes of Tregs per organ.

We then performed compositional analysis of each Treg subcluster to identify clusters that had high fractions of Tregs from tumours. This analysis required equal numbers of Tregs from healthy tissue and tumours. Therefore, to match these Treg numbers, we downsampled the dataset, resulting in 12 696 Tregs from each condition. Compositional analysis with the downsampled dataset showed that there were higher fractions of tumour Tregs in the activated, Isg15$^+$ and NLT Treg subclusters in contrast to the NLT Ccr7, Srm, Itgb1, and Ccr7 Treg subclusters, which mostly consisted of Tregs from healthy tissue (Fig. 4.5E).

To investigate tissue-level Treg compositions, we used the full dataset to visualise the fractions of each of the Treg subclusters within Tregs from each tissue. Tregs from tumours mostly consisted of activated Tregs and, to varying extents, NLT and Isg15$^+$ Tregs. Insignificant fractions of Ccr7$^+$ Tregs were seen in tumours (Fig. 4.5F). Tregs from the ear skin and the colon also consisted of considerable fractions of activated and NLT Tregs, which could explain why they clustered together with tumour Tregs in UMAP space (Fig. 4.5F). On the other hand, Tregs from healthy tissue mostly consisted of Ccr7$^+$ and Itgb1$^+$ Tregs. Barely any activated Tregs were found within healthy tissue (Fig. 4.5F).

To further explore these findings, we determined the fractions of Tregs from each of the identified Treg subclusters per individual mouse. In order to be able to perform statistical analysis, we needed datasets that represented at least 3 mice. Thus, we excluded organs from which we could not trace the mouse origin of the Tregs. We were left with Tregs from MC38, CT26 and B16F10-OVA tumours as well as the ear skin, small intestines, MC38-TDLN, spleen and PBMC. Analysing this data subset, we confirmed that tumours and the ear skin mostly consisted of high fractions of activated Tregs and NLT Tregs (Fig. 4.6A and D). Furthermore, Isg15$^+$ Tregs were mostly derived from tumours (Fig. 4.6C). In contrast, Ccr7$^+$ and Itgb1$^+$ Tregs were primarily from healthy tissue (Fig. 4.6B and F). We did not see significant differences between healthy tissue and tumours when considering NLT Ccr7$^+$ Tregs (Fig. 4.6E). Srm$^+$ Tregs appeared to be slightly higher in some of the healthy tissue in contrast to tumours (Fig. 4.6G).

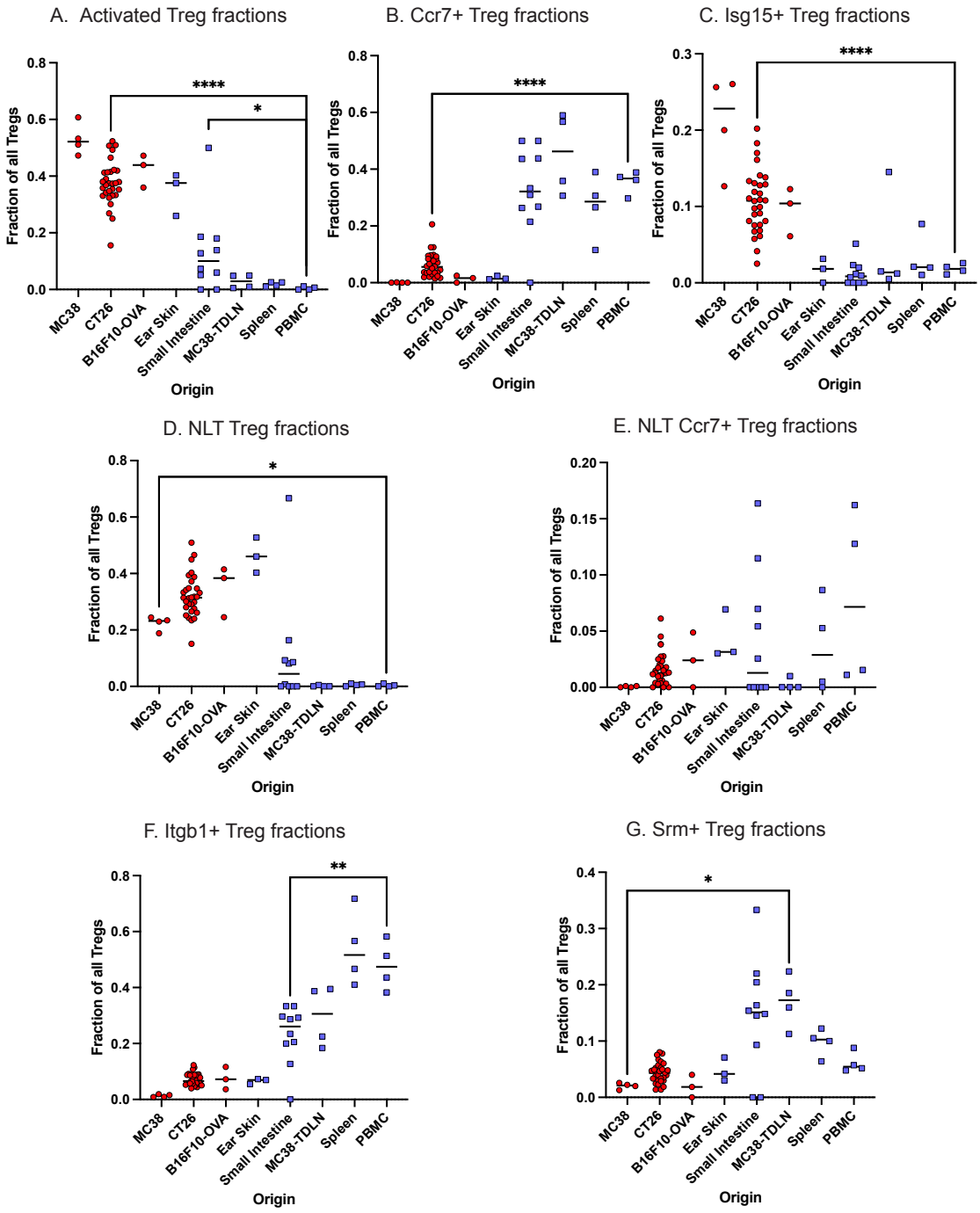



**Figure 4.6: Mouse-level compositional analysis**. Fractions of activated (A), Ccr7$^+$ (B), Isg15$^+$ (C), NLT (D), NLT Ccr7$^+$ (E), Itgb1$^+$ (F) and Srm$^+$ (G) Tregs of all Tregs per individual mouse. The red circles correspond to tumour Treg fractions per mouse while purple boxes correspond to healthy tissue Treg fractions per mouse. Black horizontal lines depict average fractions. The Mann-Whitney U-test was used to compare means. Calculated p-values were as follows: *$p < 0.05$, **$p < 0.01$, ***$p < 0.001$, ****$p < 0.0001$.

Apart from analysing Treg cluster compositions, we also performed signature/module scoring to assess the extent to which Tregs from different tissue express tumour-resident and transient Treg genes/signatures. Using genes that differentially differ between tumour-resident and transient Tregs that were identified from Chapter 3, we observed that Tregs from tumours had lower tumour-transient scores that Tregs from healthy tissue (Fig. 4.7A, B).

Conversely, Tregs from tumours had higher tumour-resident scores than Tregs from healthy tissue (Fig. 4.7C, D). These findings suggested that varying levels of tumour-resident Tregs might also be found in other murine tumour models such as TC1, LLC-OVA and B16F10-OVA.

Given the significant fractions of NLT Tregs identified in tumours, we considered whether tumour Tregs would exhibit a strong tissue Treg signature. Therefore, we scored the Treg meta-atlas for tissue modules using established gene sets for tissue Tregs (Muñoz-Rojas and Mathis, 2021). We found that tumour Tregs had elevated tissue Treg signatures in contrast to Tregs from lymphoid tissue (Supplementary Fig. C.1A, B). Tregs from non-lymphoid tissue such as the colon, ear skin and lung also displayed high tissue Treg signatures (Supplementary Fig. C.1B). Interestingly, the tissue Treg genes minimally overlapped with tumour-resident and transient Treg genes (Supplementary Fig. C.1C).

In summary, we concluded that tumour Tregs mostly consisted of activated and NLT Treg subclusters while healthy tissue Tregs mostly came from $Ccr7^{+}$ and $Itgb1^{+}$ Treg subclusters. Furthermore, tumour-resident Tregs might also be present in other mouse tumour models, such as TC1, LLC-OVA and B16F10-OVA, which have been considered in the mouse Treg meta-atlas. Finally, though tumour Tregs have a strong tissue signature, using tumour-resident and transient Treg modules results in better separation between tumour and healthy tissue Tregs than using tissue Treg signatures.

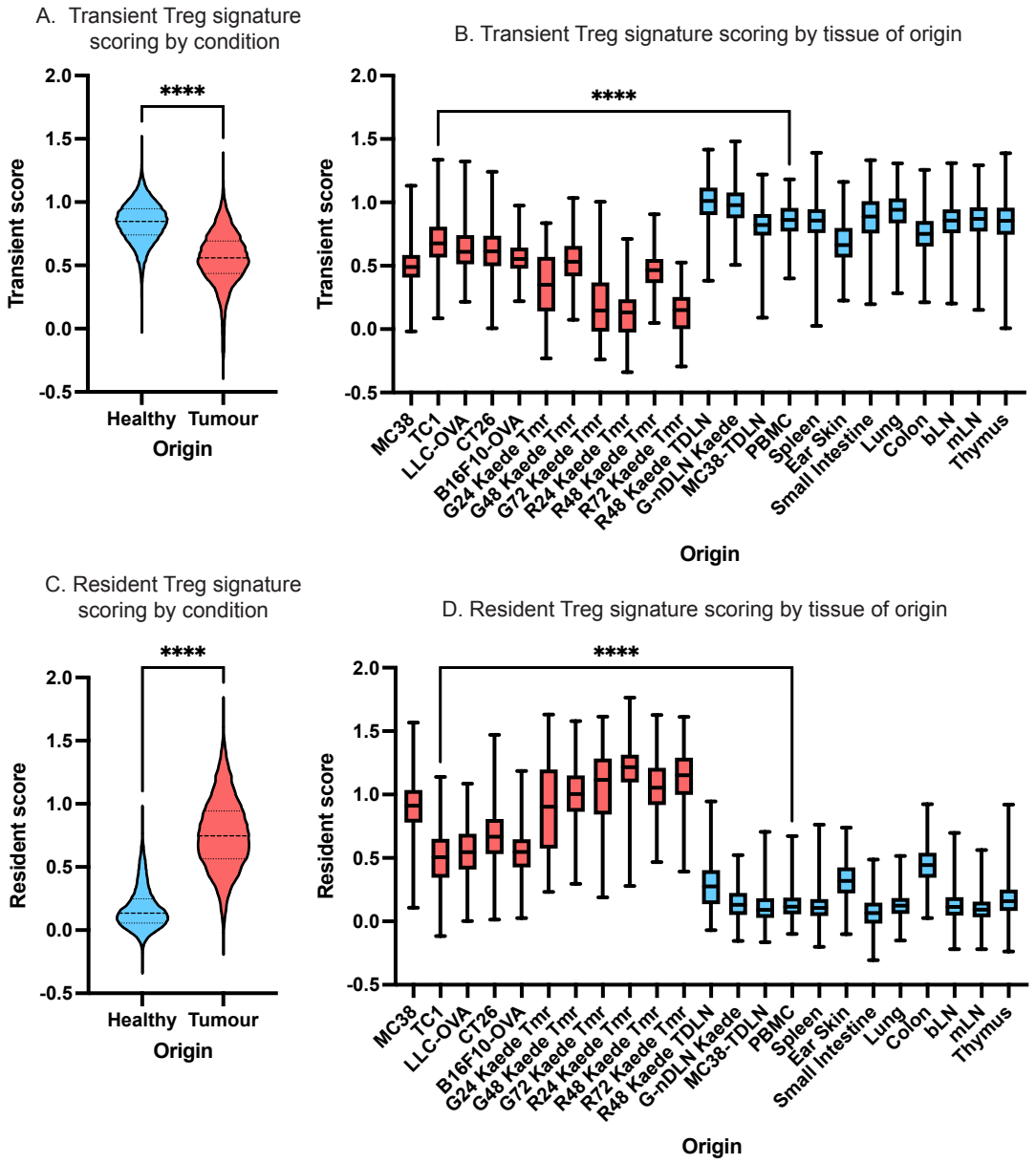



**Figure 4.7: Resident and transient signature/module scoring in mice**. A: Transient Treg module scoring for Tregs from healthy mouse tissue and tumours. B: Transient Treg module scoring for Tregs from individual mouse organs/tumours. C: Resident Treg scoring for Tregs from healthy mouse tissue and tumours. D: Resident Treg module scoring for Tregs from individual mouse organs/tumours. Whiskers show the minimum and maximum score ranges per organ. The Mann-Whitney U-test was used to compare means. Calculated p-values were as follows: *p $<$ 0.05, **p $<$ 0.01, ***p $<$ 0.001, ****p $<$ 0.0001.

### 4.4.4 Lag3 expression differentiates tumour Tregs from non-lymphoid tissue Tregs

In Chapter 3, we identified Lag3, Tnfrsf18 and Tnfrsf9 as top surface markers that are upregulated in MC38 tumour-resident Kaede Tregs. In Section 4.4.3, we observed similarities between Tregs in the tumour and non-lymphoid tissue (colon and ear skin). Therefore, to determine markers that can be used to uniquely target tumour-resident Tregs, it is imperative to assess whether Lag3, Tnfrsf18 and Tnfrsf9 are unique to tumour Tregs or they are also expressed in non-lymphoid tissue Tregs. In addition to these markers, we also considered Ccr8, which has been shown to mark tumour-infiltrating Tregs (Whiteside et al., 2021) but was poorly expressed in the Kaede system.

To investigate the expression patterns of Lag3, Ccr8, Tnfrsf18 and Tnfrsf9, we partitioned the mouse meta-atlas into tumour, lymphoid tissue and non-lymphoid tissue Tregs. Tumour Tregs exhibited high expression of Lag3, Ccr8, Tnfrsf18 and Tnfrsf9 (Fig. 4.8A). Lymphoid tissue Tregs did not highly express Lag3 and Ccr8 but displayed moderate Tnfrsf18 and Tnfrsf9 expression (Fig. 4.8B). Similarly, non-lymphoid tissue Tregs lowly expressed Lag3 and Ccr8 but highly expressed Tnfrsf18 and Tnfrsf9 (Fig. 4.8C). Next, we visualised gene expression in different tissue Tregs (Fig. 4.8D). Tumour Tregs highly expressed all 4 markers. As previously mentioned, Tregs from MC38-implanted Kaede mice poorly expressed Ccr8 though Ccr8 was highly expressed in MC38 tumours from non-Kaede mouse backgrounds. Considering Tregs from healthy tissue, we observed that Lag3 and Ccr8 expression was low while Tnfrsf18 and Tnfrsf9 expression was elevated (Fig. 4.8D).

Given that we previously observed strong similarities between tumour Tregs and non-lymphoid tissue Tregs (Sections 4.4.2, 4.4.3), we decided to perform differential gene expression analysis comparing Tregs from the colon and MC38 tumours using MAST (Finak et al., 2015). Colonic Tregs upregulated Ccr7, Gramd3, Cd83, Il1rl1 and Dusp10. On the contrary, MC38 Tregs upregulated Nkg7, Tigit and Lag3. Lag3 was the most significantly upregulated gene in MC38 tumours (Figure 4.8E and Table 4.4). Thus,

we concluded that of all the 3 markers that were upregulated in tumour-resident Tregs from Chapter 3, Lag3 uniquely marks tumour Tregs.

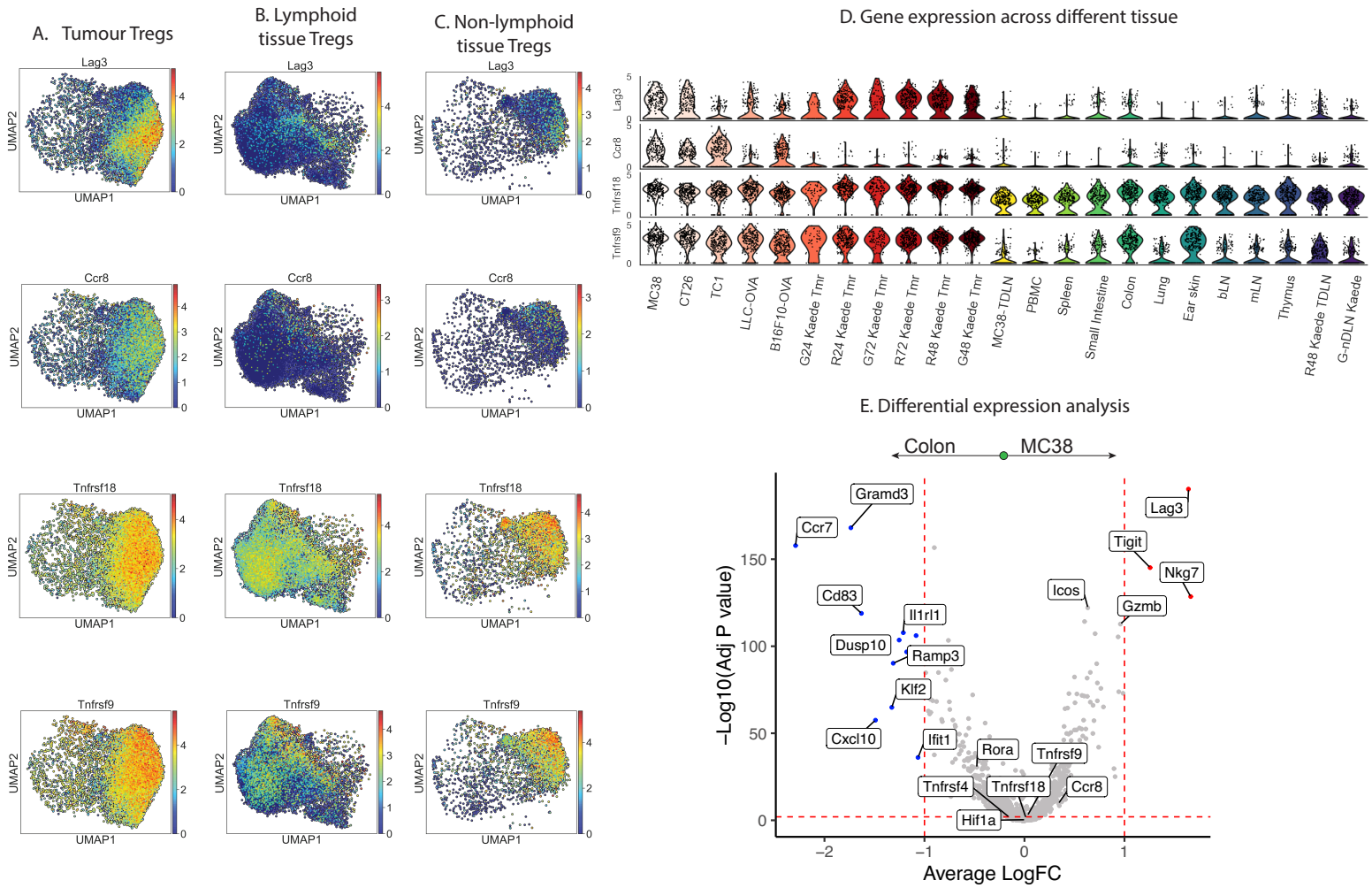



**Figure 4.8: Transcriptional comparison of Tregs across organs**. Gene expression in tumour (A), lymphoid (B) and NLT tissue (C) Tregs. D: Violin plots showing gene expression in tumour (red) and healthy tissue (green) Tregs. E: Volcano plot showing differentially expressed genes between colon (non-lymphoid tissue) and MC38 (tumour) Tregs. Average LogFC – average base 2 logarithmic fold change.

**Table 4.4: Table showing some of the genes that are differentially expressed between Tregs from MC38 tumours (2678 Tregs) and the colon (3037 Tregs)**. Genes that are positively regulated in MC38 Tregs are ordered by decreasing average LogFC while negatively regulated genes are ordered by increasing average LogFC. Average LogFC – average base 2 logarithmic fold change.

| Genes upregulated in MC38 Tregs | | | Genes downregulated in MC38 Tregs | | |
|---|---|---|---|---|---|
| Gene | Average LogFC | Adjusted p-val | Gene | Average LogFC | Adjusted p-val |
| Nkg7 | 1.662421 | 3.244571e-129 | Ccr7 | -2.289129 | 1.476622e-158 |
| Lag3 | 1.640617 | 6.277387e-191 | Gramd3 | -1.735517 | 8.220144e-169 |
| Tigit | 1.256917 | 7.027662e-146 | Cd83 | -1.629744 | 1.292486e-119 |
| Cxcr6 | 0.985881 | 1.165469e-73 | Cxcl10 | -1.490735 | 3.124296e-58 |
| Gzmb | 0.959967 | 1.664576e-113 | Klf2 | -1.327008 | 1.310995e-65 |
| Sv2c | 0.941549 | 1.358603e-74 | Dusp10 | -1.253371 | 2.979013e-104 |
| Cst7 | 0.935429 | 3.628130e-106 | Il1rl1 | -1.212604 | 1.789658e-108 |
| Ccl4 | 0.905969 | 9.105888e-26 | Ifit1 | -1.063820 | 8.092026e-37 |
| Ccl5 | 0.896167 | 1.802240e-30 | Map3k8 | -0.960904 | 1.698399e-63 |
| Pglyrp1 | 0.790489 | 8.329417e-66 | Ms4a4b | -0.948084 | 8.606830e-62 |
| Ccr5 | 0.764286 | 1.549281e-76 | Gm2000 | -0.941430 | 2.963557e-70 |
| Oxsr1 | 0.742730 | 9.119954e-43 | Gata3 | -0.937689 | 9.035368e-63 |
| Ctsd | 0.729917 | 2.344813e-69 | Fas | -0.917718 | 1.945879e-69 |
| Fgl2 | 0.727837 | 1.040328e-79 | Gadd45b | -0.859248 | 1.293470e-85 |
| Ccr2 | 0.723460 | 1.102114e-90 | Kdm6b | -0.828736 | 1.053741e-58 |
| Maf | 0.706884 | 7.076043e-108 | Gadd45g | -0.807566 | 1.738358e-47 |
| Litaf | 0.695056 | 5.562629e-58 | Bcl2 | -0.793160 | 3.111840e-51 |
| Entpd1 | 0.685485 | 9.954322e-67 | Emb | -0.787982 | 2.727844e-81 |
| Ddit4 | 0.684604 | 1.471804e-50 | Isg15 | -0.765663 | 7.154600e-44 |
| Ly6a | 0.659326 | 1.144480e-85 | Ier5 | -0.751118 | 7.177310e-69 |
| Anxa2 | 0.658795 | 1.263740e-68 | Gm11808 | -0.717134 | 2.742736e-58 |
| Icos | 0.634080 | 7.636474e-123 | Faim | -0.691042 | 6.640122e-36 |
| S100a6 | 0.628134 | 6.419216e-72 | Cd69 | -0.652225 | 3.320824e-50 |
| Ctsb | 0.626268 | 2.035653e-82 | Bhlhe40 | -0.644136 | 1.235086e-43 |
| Ifi27l2a | 0.614945 | 1.271856e-47 | Bzw2 | -0.633305 | 8.534368e-41 |
| Lbh | 0.614599 | 3.661475e-53 | Batf | -0.602440 | 5.579122e-35 |

### 4.4.5 Exploring gene expression patterns across T and NK cells

In the previous section, we explored the expression patterns of Lag3, Ccr8, Tnfrsf18 and Tnfrsf9 in Tregs. However, there are many potential candidate markers currently being studied to target intratumoral Tregs that also need to be explored using Treg meta-atlases. Furthermore, a key challenge in immuno-oncology is that of identifying drug targets that are unique to tumour Tregs and lowly expressed on conventional T cells as well as NK cells,

which play critical roles in tumour restriction. This would help inform the development of Treg-targeting immunotherapeutics with high specificity and low side-effects.

We used the Treg meta-atlas to explore the inter-tissue expression of immune checkpoint markers, costimulatory molecules, cytokine receptors, chemokine receptors, integrins and other molecules (Fig. 4.9A). The analysis showed that additional markers such as Tigit, Entpd1, Ccrl2, Ccr5, Cxcr3, Itgb8 and Sdf4 were also highly expressed in tumour Tregs and minimally expressed in healthy tissue Tregs. Therefore, further research into targeting mouse tumour Tregs using some of these markers is warranted (Fig. 4.9A).

To explore the expression patterns of the primary markers of interest, Lag3, Ccr8, Tnfrsf18 and Tnfrsf9, in other immune cells namely conventional T cells and NK cells, we used the data that we had collected for the Treg meta-atlas to generate a mouse T and NK cell meta-atlas. Before batch correction, the data separated by study of origin as expected (Fig. 4.9B). However, after batch correction using the Harmony algorithm, we identified biologically relevant T and NK cell clusters (Fig. 4.9C).

$CD4^+$ T cells expressed Cd4, CD8 T cells were identified by the expression of Cd8a and Cd8b1, and NK cells expressed markers such as Ncr1. Tumour-resident Tregs were identified by the expression of Lag3 as previously discussed (Fig. 4.9D). Using the T and NK cell meta-atlas, we visualised the expression of markers of interest. We observed that Lag3 was not only expressed in tumour-resident Tregs, but was also expressed in exhausted CD8 T cells. Ccr8 was also expressed in tumour-resident Tregs and, to a lesser extent than Lag3, in exhausted CD8 T cells (Fig. 4.9D-E). On the contrary, Tnfrsf18 and Tnfrsf9 were expressed in multiple cell types and thus, less specific than Lag3 and Ccr8 (Fig. 4.9D-E).

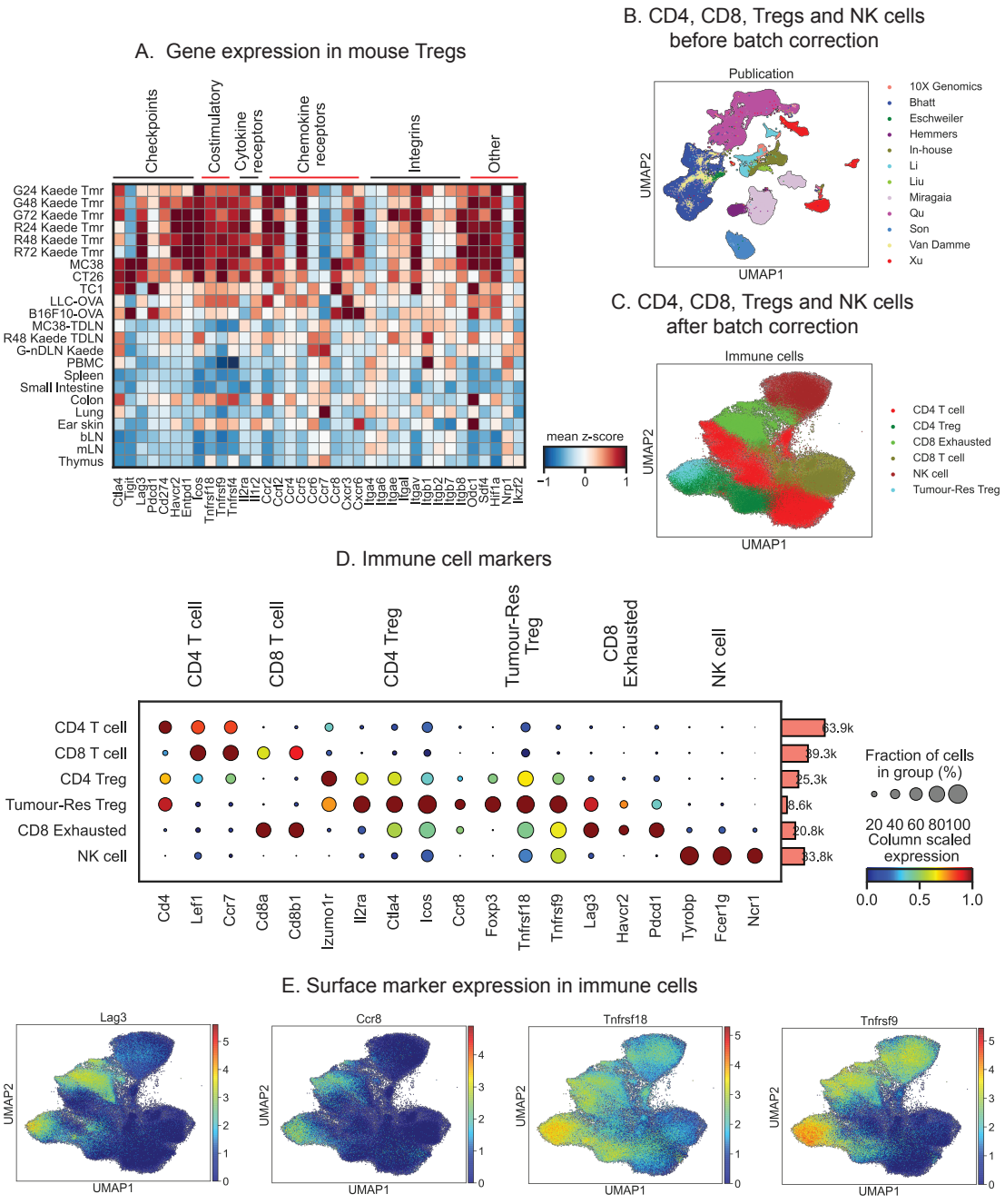



**Figure 4.9: Exploring gene expression patterns across T and NK cells**. A: Heatmap showing the expression patterns of immune checkpoint markers, costimulatory molecules, cytokine receptors, chemokine receptors, integrins and other relevant molecules in Tregs. T cell and NK cell scRNA-seq meta-atlas before (B) and after (C) batch correction. D: Dotplot showing genes expressed in cell clusters. E: UMAPs showing the expression of Lag3, Ccr8, Tnfrsf18 and Tnfrsf9. Tumour-Res Tregs – Tumour-resident Tregs.

In summary, we concluded that, given the expression of Lag3 in both tumour-resident and exhausted CD8 T cells, inhibitory rather than depletory anti-Lag3 antibodies may be better suited for targeting intratumoral Tregs without negatively affecting exhausted CD8 T cells in mice. With caution, $Ccr8^{+}$ Tregs in mouse tumour models could potentially be targeted using antibodies that deplete cells via antibody-dependent cellular cytotoxicity (ADCC) activity. However, whether the same propositions can be made for humans remains unclear as the results thus far only consider mouse models.

### 4.4.6 Inter-species comparison: Developing a human Treg meta-atlas

One of the key challenges facing cancer drug development is the poor translation between mouse tumour models and humans. In many cases, experimental drugs work fairly well in mouse models but fail to achieve efficacy once they reach clinical trials. Inter-species differences, among other factors, could be contributing towards driving the observed attrition rates in cancer immunotherapy trials. Therefore, in the context of our study, it is critical to compare and contrast mouse and human Tregs to identify targets that translate well between species. With this goal in mind, we developed a human Treg meta-atlas and used it to assess the expression patterns of markers of interest.

Similar to the mouse Treg meta-atlas, we identified human Treg datasets covering different tissue from the public domain (Fig. 4.10A-B). We then combined the Tregs and assessed the meta-atlas for sources of technical variation. Before batch correction, LISI distributions were peaked at unity (Fig. 4.10C) and the Tregs clustered by study (Fig. 4.10D) as well as individual patients within each study (Fig. 4.10E). This indicated that, to successfully integrate the datasets, we needed to correct for batch effects at both the study and patient level. Following batch correction, LISI distributions for the study size matched (downsampled) sub dataset shifted towards the right and was peaked at 10 (Fig. 4.10F). Furthermore, the Tregs no longer clustered into study or subject-specific groups (Fig. 4.10G-H).

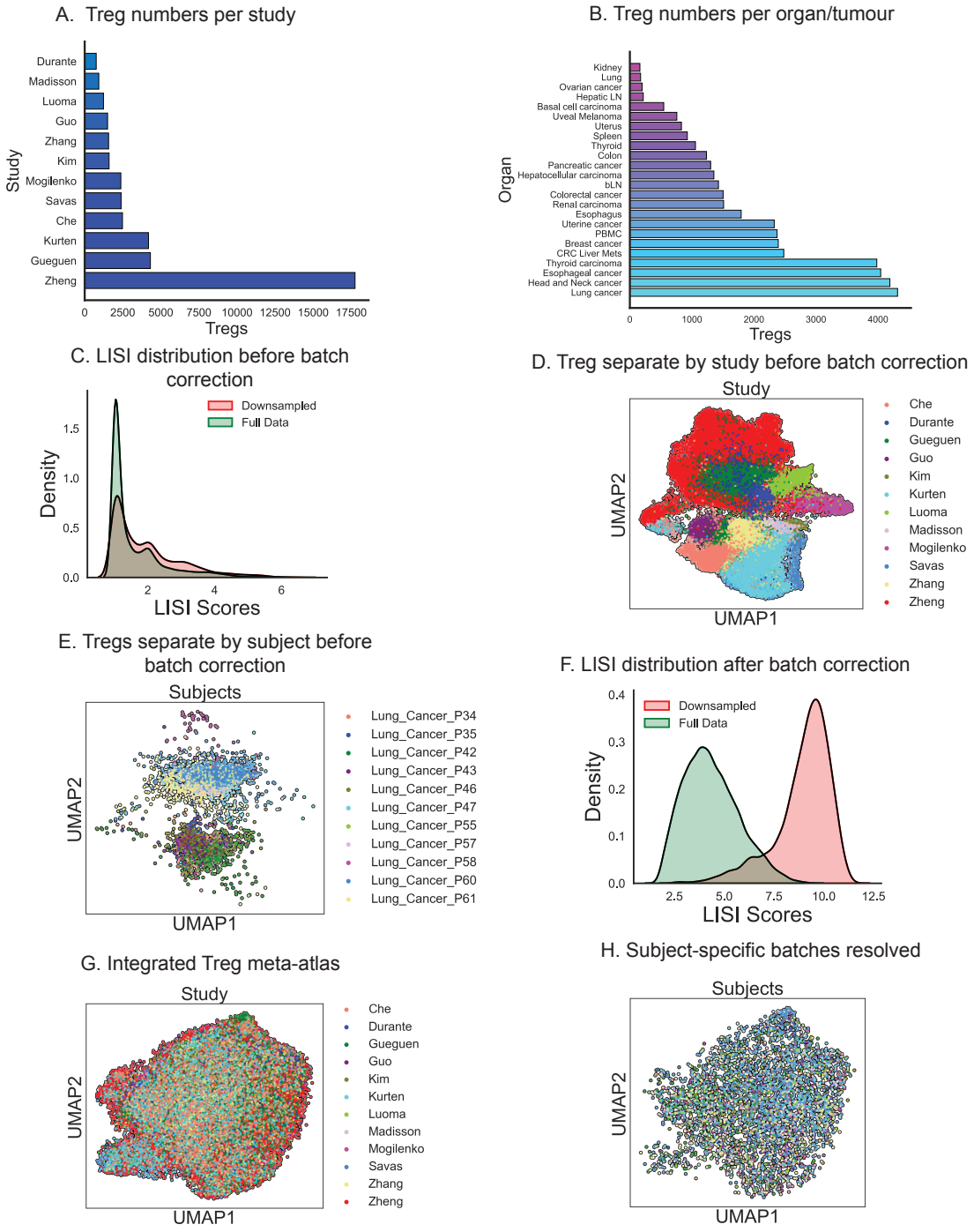



**Figure 4.10: Integrating human Tregs**. A: Treg numbers present in each study. B: Numbers of Tregs in respective tissue. C: LISI distributions computed from the complete and downsampled datasets before batch correction. D: UMAP showing Tregs clustering in a study-specific manner before batch correction. E: UMAP of a selected dataset with lung cancer Tregs showing that inter-patient differences constitute an additional batch effect. F: LISI distributions from the complete or study size matched datasets after batch correction. G: UMAP showing the integrated/batch-corrected human Treg meta-atlas. H: UMAP showing the batch-corrected lung cancer sub dataset within the human Treg meta-atlas. LN – Lymph node, bLN – brachial lymph node, PBMC – blood, CRC Liver Mets – Colorectal cancer liver metastases.

### 4.4.7 Identifying human Treg subclusters

We analysed the batch-corrected human Treg meta-atlas to identify unique Treg subpopulations. The Leiden community detection algorithm (Traag et al., 2019) identified 4 Treg subclusters namely, proliferating, CCR7$^+$, ISG15$^+$ and activated Tregs (Fig. 4.11A). These Treg subclusters were very similar to the ones we identified in mice in Section 4.4.2.

CCR7$^+$ Tregs exhibited a naive/central memory phenotype, upregulating markers such as CCR7, LEF1 and KLF2. Activated Tregs expressed markers of cell activation such as TNFRSF18, TNFRSF9, TNFSR4 and TIGIT, as well as the chemokine receptor, CCR8. ISG15$^+$ Tregs displayed a cytokine responsive phenotype, expressing markers such as IFIT1, ISG15 and IFIT3. Finally, proliferative Tregs upregulated MKI67, STMN1 and TOP2A (Fig. 4.11B).

To explore the broad relationships between the Treg clusters in terms of gene expression, we performed hierarchical clustering. Proliferating, ISG15$^+$ and activated Tregs were clustered separately from CCR7$^+$ Tregs (Fig. 4.11C). Hierarchical clustering also revealed relationships between Tregs derived from different tissue. Tregs from lymphoid organs such as the brachial lymph node and the spleen were clustered together suggesting that they had similar gene expression programs. Tumour Tregs were mostly grouped together although there was some degree of mixing with Tregs from non-lymphoid tissue (Fig. 4.11D).

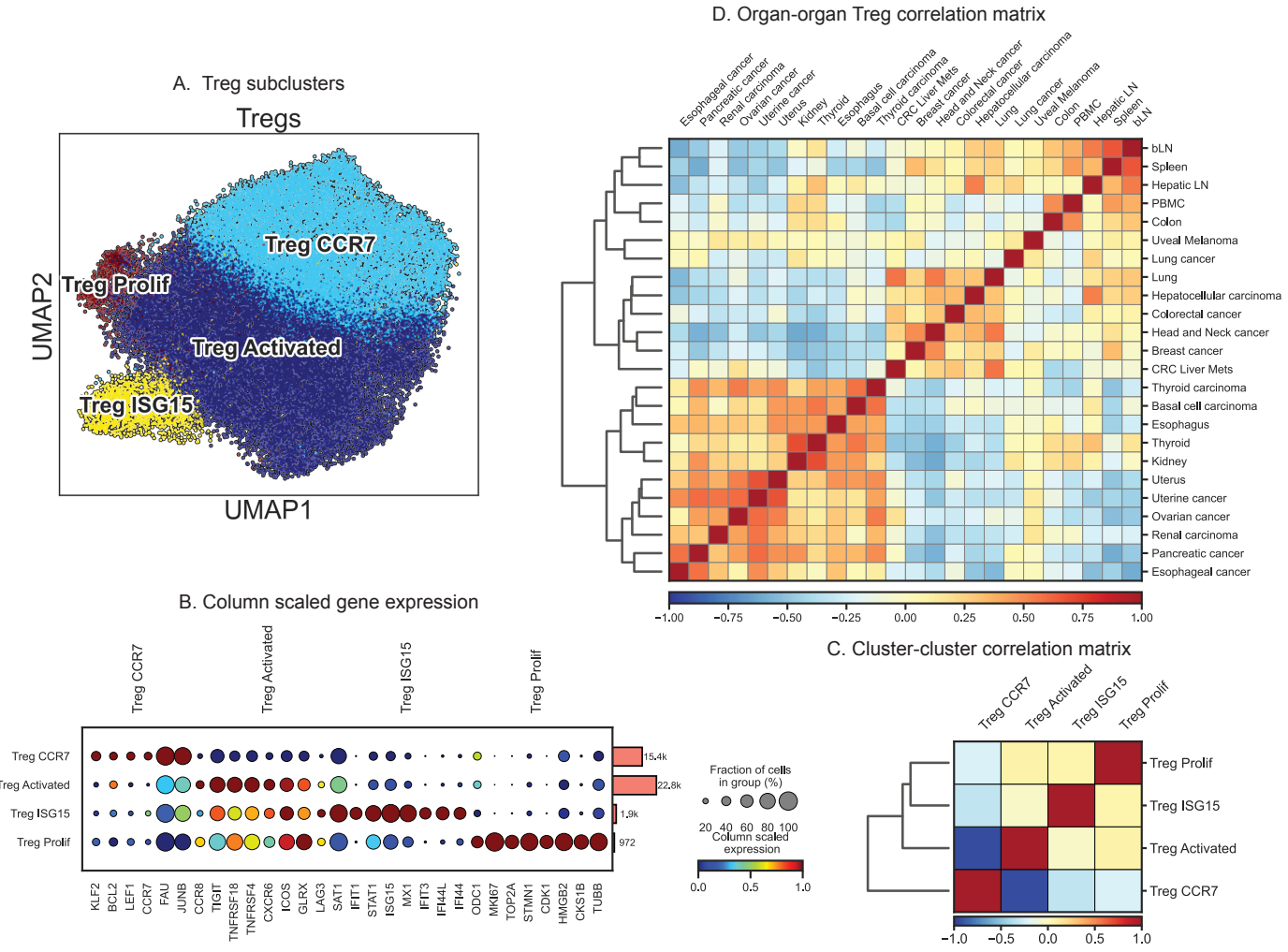



**Figure 4.11: Clustering human Tregs**. A: UMAP showing different human Treg subpopulations. B: Dotplot showing the expression of selected genes within each Treg subpopulation. Heatmaps showing broad gene expression relationships between Treg subclusters (C) and Tregs in different tissue or tumours (D).

### 4.4.8 Compositional analysis of human Tregs

To further explore the relationships between Tregs from different tissue and conditions, we visualised the subject-level Treg centroids in low dimensional space. Broadly, we observed that Tregs from lymphoid tissue clustered separately from tumour Tregs. However, similar to mouse Tregs from Section 4.4.3, human non-lymphoid tissue Tregs exhibited extensive heterogeneity and could be found in both lymphoid tissue and tumour Treg regions (Fig. 4.12A). Density plots showing lymphoid tissue, non-lymphoid tissue and tumour Treg localisation also evoked similar results, with non-lymphoid tissue found at the intersection of lymphoid tissue and tumour Treg cluster regions (Fig. 4.12B,C,D).

Next, we examined the compositional contributions of Tregs from healthy tissue and tumours within each Treg subcluster. After matching the numbers of healthy tissue and tumour Tregs, we observed that tumour Tregs dominated the activated, ISG15$^+$ and proliferative Treg subclusters. On the contrary, Tregs from healthy tissue were mostly naive/central memory (Fig. 4.12E). We then quantified the fractions of each Treg subcluster within Tregs from each tissue. The general trend that we observed was that tumour Tregs mostly consisted of high activated Treg fractions. As we moved from tumour to healthy tissue Tregs, there was an increase in the fractions of CCR7$^+$ Tregs. However, there were some exceptions. Tregs from the lung and uterus appeared to have high fractions of activated Tregs just like most of the tumour Tregs (Fig. 4.12F).

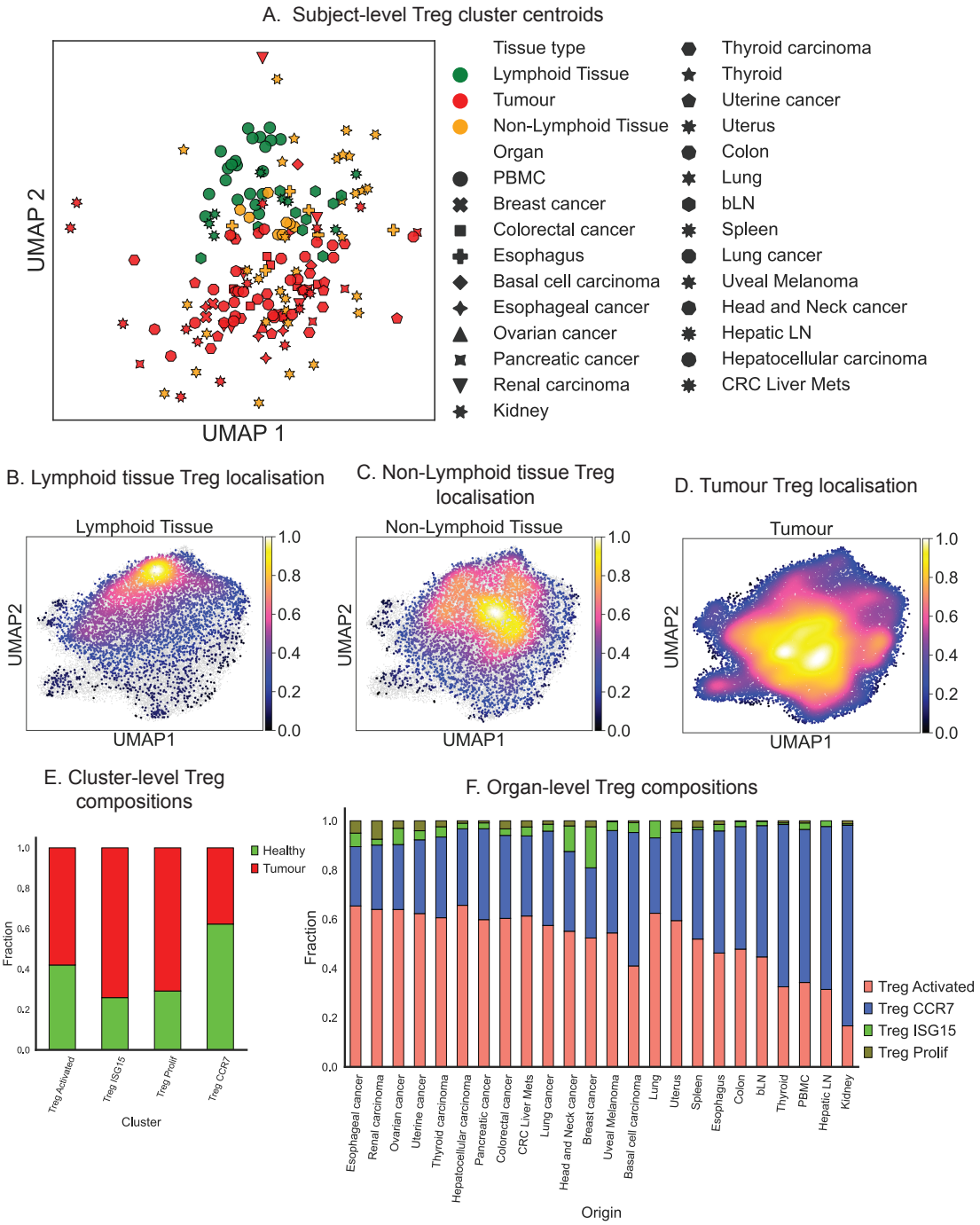



**Figure 4.12: Compositional analysis of human Tregs**. A: UMAP showing subject-level Treg centroids, stratified by tissue of origin. UMAP density plots showing the localisation of Tregs from lymphoid tissue (B), non-lymphoid tissue (C) and tumours (D). The bright orange colour depicts regions of the UMAP where a higher density of cells localise in contrast to the dark blue colour which shows UMAP regions with fewer cell numbers/densities. E: Barplot highlighting the compositions of each Treg subcluster by healthy or tumour tissue type. To conduct this analysis, the dataset was downsampled to match Treg numbers from tumours and healthy tissue. In the end, 10 258 Tregs from each condition were used. F: Barplot showing the composition of each tissue by Treg subcluster.

Finally, we determined the fractions of each of the 4 Treg subpopulations within each subject. To perform this analysis, we only used datasets representative of at least 3 subjects. Thus, we excluded the ovarian cancer, breast cancer and basal cell carcinoma datasets from the analysis (Fig. 4.13A). We found that, on a subject-level basis, Tregs from tumours had higher activated Treg fractions in comparison to most Tregs from healthy tissue (Fig. 4.13B). On the contrary, Tregs from healthy tissue had higher fractions of CCR7$^+$ Treg subpopulations than Tregs from most tumours (Fig. 4.13C). ISG15$^+$ and proliferating Tregs did not show drastic differences between tumour and healthy tissue Tregs per subject (Fig. 4.13D-E).

Collectively, these findings suggested that tumour Tregs are mostly composed of activated Tregs, with small fractions of naive/central memory CCR7$^+$ Tregs. Furthermore, Tregs from some of the non-lymphoid tissue have similar gene expression patterns and compositions as tumour Tregs, an observation which complicates the identification of therapeutic markers that are specific for tumour Tregs.

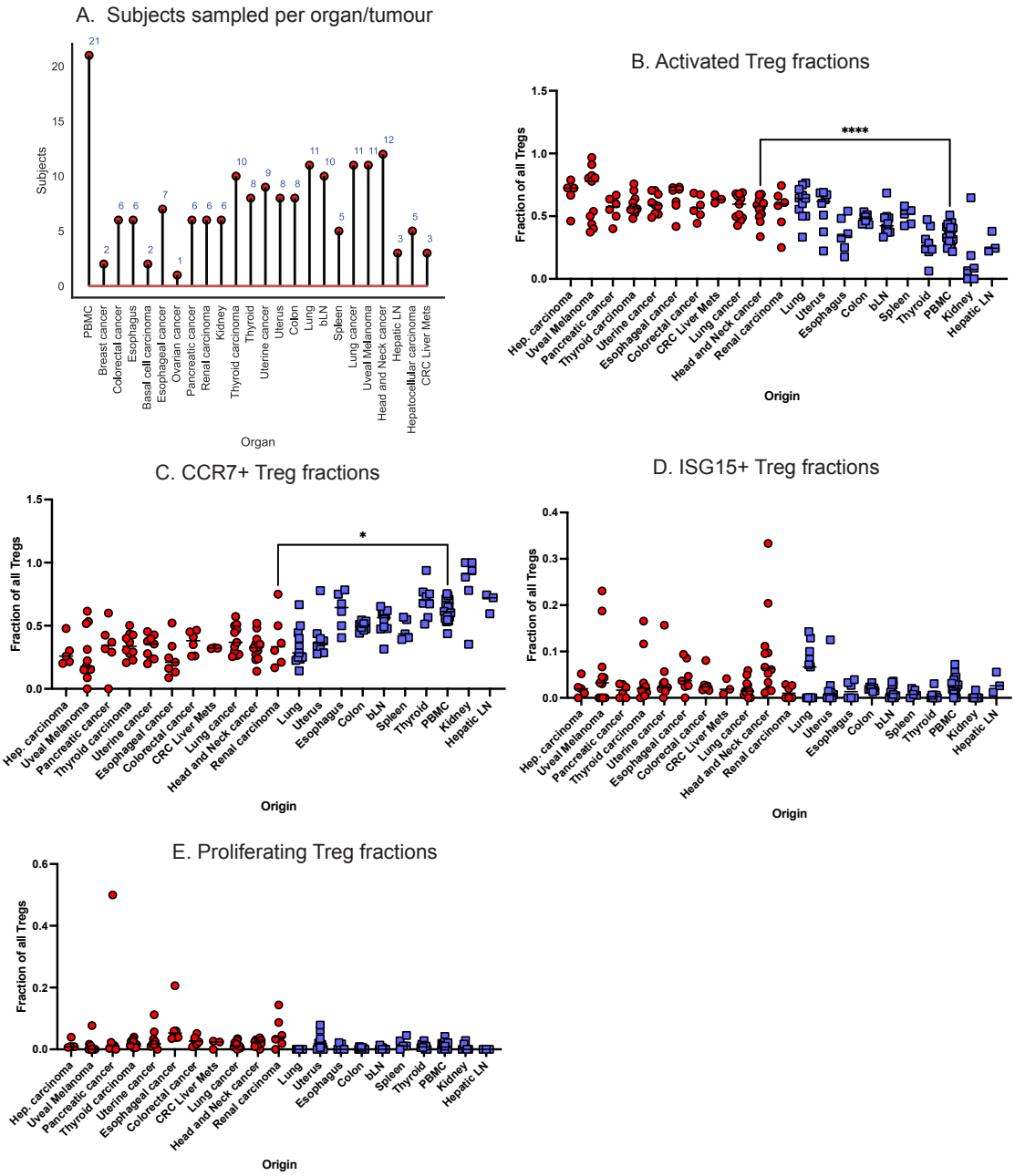



**Figure 4.13: Subject-level Treg compositions**. A: Plot showing the numbers of subjects from which Tregs were isolated. Individual value plots showing the fractions of activated (B), CCR7$^+$ (C), ISG15$^+$ (D) and proliferating (E) Tregs of all Tregs per subject. The red circles correspond to tumour Treg fractions per subject while purple boxes correspond to healthy tissue Treg fractions per subject. Black horizontal lines depict average fractions. The Mann-Whitney U-test was used to compare means. Calculated p-values were as follows: *p $<$ 0.05, **p $<$ 0.01, ***p $<$ 0.001, ****p $<$ 0.0001. Hep. carcinoma – Hepatocellular carcinoma.

### 4.4.9 Human tumour Tregs highly express CCR8

Section 4.4.4 revealed that Lag3 specifically marks mouse tumour-resident Tregs. In Section 4.4.5, we saw that Ccr8 and Lag3 were expressed on mouse tumour Tregs and to some degree, exhausted CD8 T cells. In this section, our aim was to conduct inter-species comparisons by assessing the expression of LAG3, CCR8, TNFRSF18 (GITR) and TNFRSF9 (4-1BB) on human Tregs, conventional T cells and NK cells. Understanding potential differences in marker expression between mouse tumour models and human tumours is critical for clinical translation of Treg targeting immunotherapy.

Using the human Treg meta-atlas, we visualised the expression of LAG3, CCR8, TNFRSF18 and TNFRSF9 in different organs. Unexpectedly, LAG3 was not highly expressed in human tumour Tregs, whereas CCR8 was highly expressed in most of the tumour Tregs but minimally expressed in Tregs from healthy tissue with the exception of a few organs particularly the esophagus and uterus. The expression of TNFRSF18 (GITR) and TNFRSF9 (4-1BB) did not vary much between tumour and healthy tissue Tregs (Fig. 4.14A). These finds suggested potential inter-species differences in the expression of LAG3 on tumour Tregs.

We extended our analysis of human tumour Tregs by visualising the expression patterns of many markers that have potential therapeutic applications. These included immune checkpoint markers, costimulatory molecules, cytokine receptors, integrins and other relevant genes (Fig. 4.14B). Again, CCR8 showed the strongest signal in Tregs from some, but not all, of the tumours (Fig. 4.14B). These findings suggested that CCR8 may be a better marker for human tumour Tregs in comparison to LAG3, TNFRSF18 (GITR) and TNFRSF9 (4-1BB).

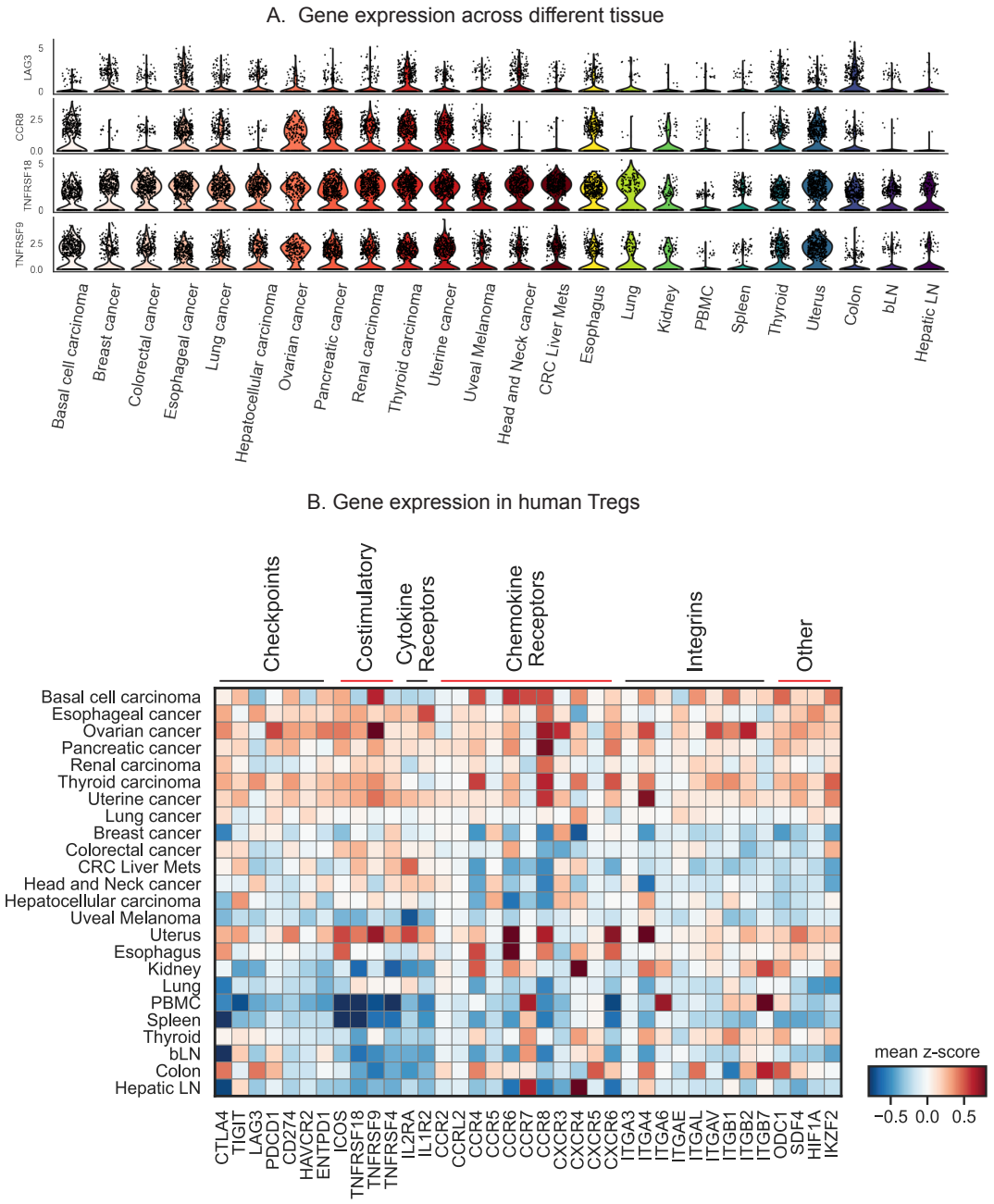



**Figure 4.14: CCR8 is highly expressed on human tumour Tregs**. A: Violin plots showing gene expression patterns in different tissue. B: Heatmap showing the expression of relevant molecules in Tregs in different tissue.

To further explore the specificity of CCR8 to human tumour Tregs, we generated human CD4 and CD8 T cell meta-atlases (Fig. 4.15 and Supplementary Fig. C.2). We assessed them for batch effects and appropriately corrected the datasets (Figs. 4.15A, B, D and E). CCR8 was not highly expressed in both human CD4 and CD8 T cells regardless of the presence or absence of cancer. On the contrary, LAG3, TNFRSF18 (GITR) and TNFRSF9 (4-1BB) were upregulated in CD4 and CD8 T cells from human tumours (Fig. 4.15C,F). Overall, these analyses emphasised the unique expression of CCR8 human tumour Tregs.

Given that the immune system consists of many cell types beyond CD4 and CD8 T cells, we investigated the expression of CCR8, LAG3, TNFRSF18 and TNFRSF9 on numerous immune cell types. To accomplish this, we made use of an integrated public scRNA-seq meta-atlas of immune cells from several human cancer types (Fig. 4.16A) (Nieto et al., 2021). The meta-atlas revealed that CCR8 is specific to human tumour Tregs while LAG3, TNFRSF18 and TNFSRF9 were expressed on multiple immune cell types (Fig. 4.16B). Thus, we concluded that, given the specificity of CCR8 to human tumour Tregs, anti-CCR8 antibodies with ADCC activity could potentially be used to deplete intratumoral Tregs in humans. However, great caution would need to be taken considering that Tregs resident in few organs, in particular the uterus and esophagus, were found to highly express CCR8 as well.

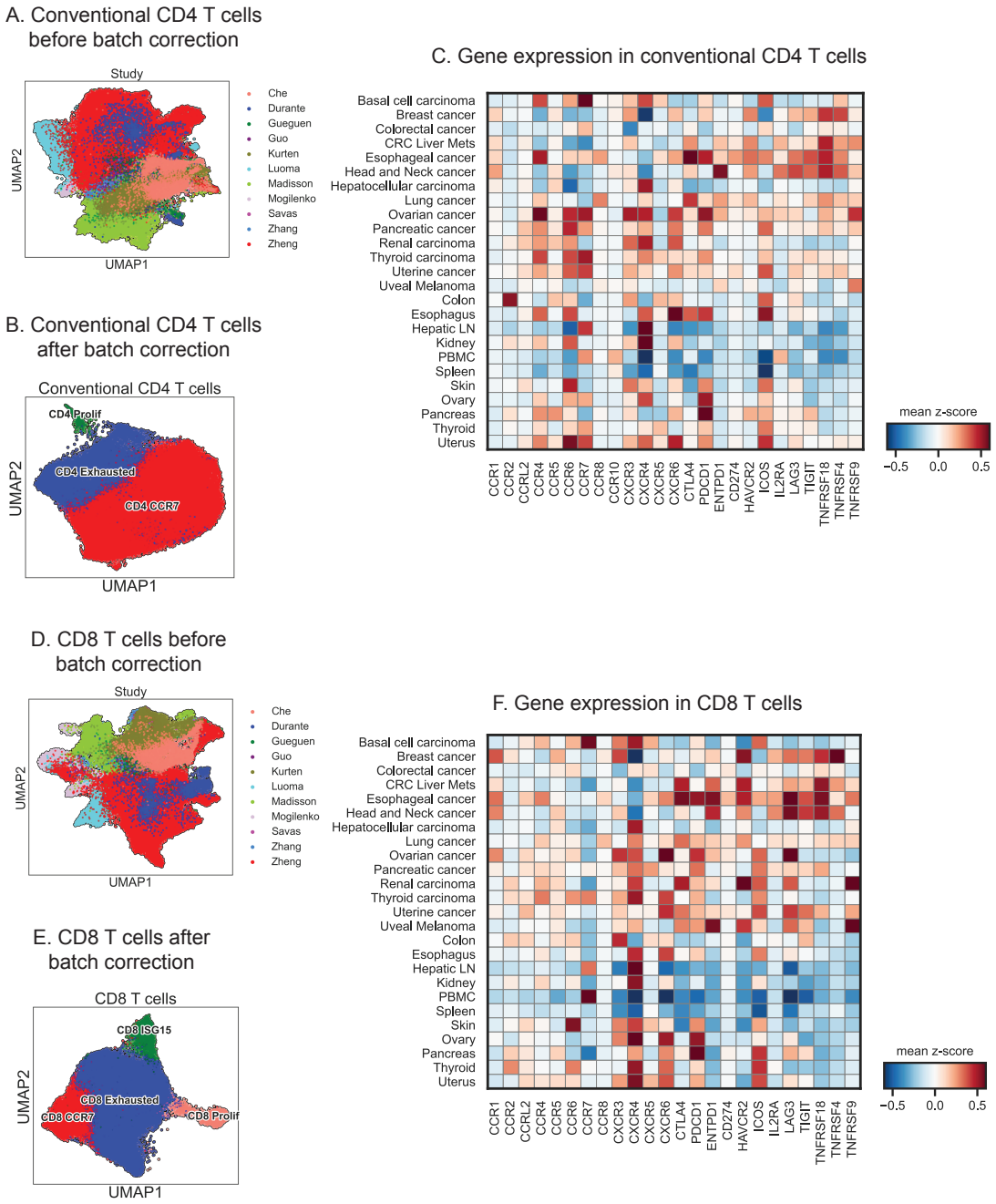



**Figure 4.15: CCR8 is not highly expressed on conventional T cells**. Human CD4 T cell meta-atlas before (A) and after (B) batch correction. C: Heatmap showing gene expression in CD4 T cells. Human CD8 T cell meta-atlas before (D) and after (E) batch correction. F: Heatmap showing gene expression in CD8 T cells.

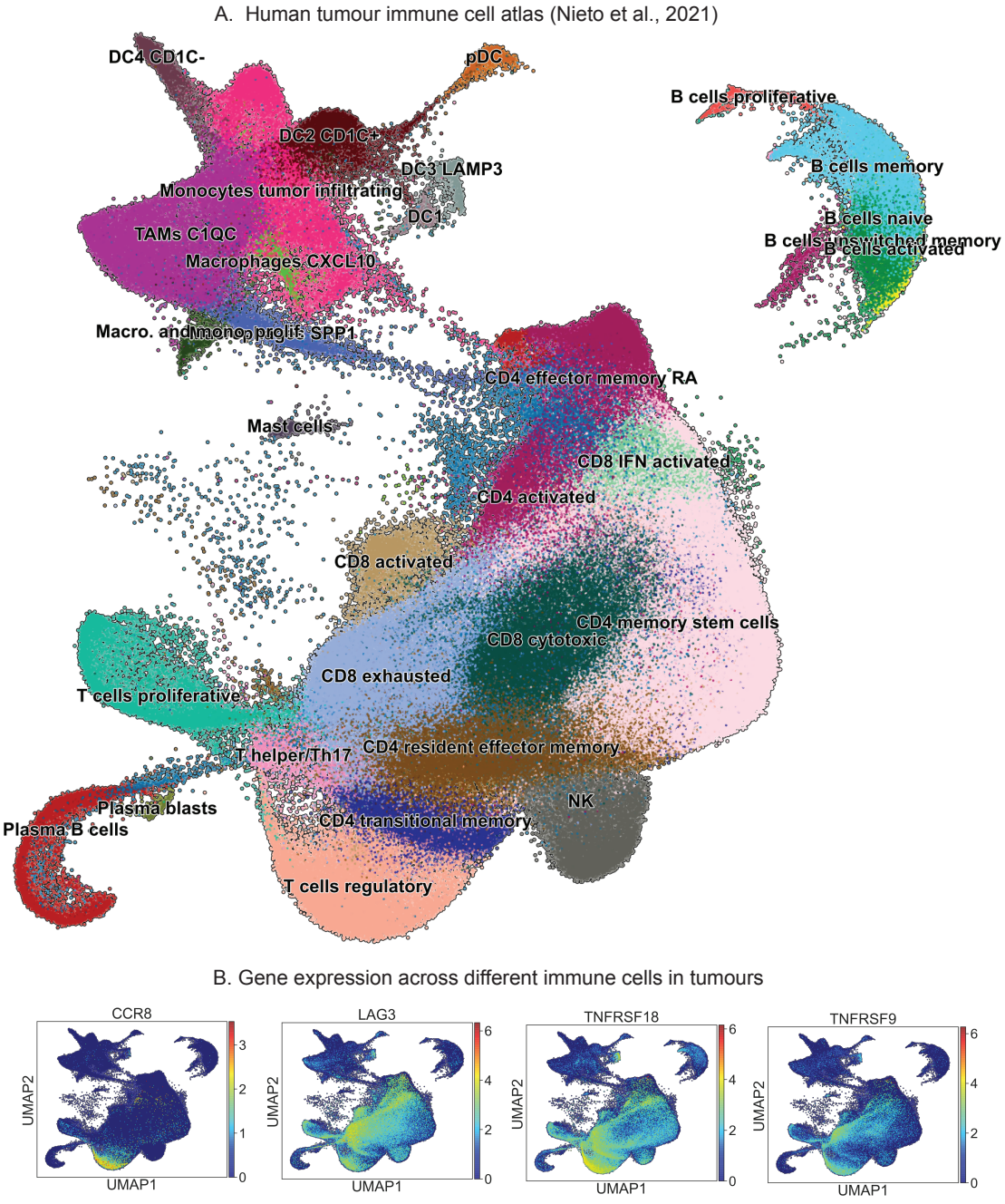



**Figure 4.16: Using a human immune cell mega meta-atlas to confirm the specificity of CCR8 on tumour Tregs**. A: A fully integrated and batch-corrected public tumour immune cell meta-atlas (Nieto et al., 2021). B: The expression of CCR8, LAG3, TNFRSF18 (GITR) and TNFRSF9 (4-1BB) on immune cells within the meta-atlas.

## 4.5 Discussion

It is well known that Tregs exhibit significant inter-tissue heterogeneity. For example, peroxisome proliferator-activated receptor gamma low (PPAR$\gamma^{lo}$) Tregs in the spleen have been shown to give rise to visceral adipose tissue (VAT) Treg subsets (Li et al., 2021). Amphiregulin (Areg) has been associated with skeletal muscle Tregs (Burzyn et al., 2013) while the Batf transcription factor has been shown to drive the differentiation of various non-lymphoid tissue Treg subsets (Delacher et al., 2020).

In addition to inter-tissue variability, Tregs display cross-species phenotypic differences. Most mouse studies involve juvenile mice that are typically grown in germ-free environments. Thus, Tregs from these mice are often classified as mostly naive whereas Tregs in humans are highly heterogeneous with significant numbers of effector or memory Treg subplopulations (Akimova and Hancock, 2018). These inter-tissue and inter-species differences contribute to the difficulty associated with developing tumour-specific and translationally-relevant Treg-targeting cancer therapeutics.

With these differences in mind, the goal of this chapter has been to explore Treg heterogeneity between organs and species to identify markers that are specific to intratumoral Tregs and translatable between species. In Chapter 3, we used an MC38-bearing Kaede mouse model in conjunction with scRNA-seq data analysis to show that tumour-resident Tregs are highly immunosuppressive and upregulate "druggable" surface markers such as Lag3, Tnfrsf18 and Tnfrsf9. However, because the study did not consider the characteristics of Tregs in other organs and in humans, there was no way of knowing which of these markers was specifically upregulated on Tregs present in both murine and human tumours but not healthy tissue.

To investigate the expression of Lag3, Tnfrsf18 and Tnfrsf9 on Tregs in different mouse organs, we developed a mouse Treg scRNA-seq meta-atlas using public datasets. We identified 7 Treg subpopulations which included Ccr7$^{+}$, Isg15$^{+}$, NLT and activated Tregs. Tregs from lymphoid tissue were transcriptionally distinct from Tregs from tumours. However, non-lymphoid tissue (NLT) Tregs showed extensive heterogeneity.

Some of the NLT Tregs clustered with lymphoid tissue Tregs while colon and ear skin Tregs co-clustered with tumour Tregs. Compositional analysis revealed that Tregs from lymphoid tissue were mostly Ccr7$^{+}$ while tumour Tregs consisted of mostly Tregs from the activated, NLT and Isg15$^{+}$ clusters. Interestingly, Tregs from the colon and ear skin were comprised of significant fractions of activated and NLT Tregs, similar to tumour Tregs. These phenotypic similarities suggested that there could also be extensive transcriptional resemblances in the expression of Lag3, Tnfrsf18 and Tnfrsf9, the key markers of activated Tregs we previously associated with tumour-resident Tregs. As a result, we systematically compared the expression patterns of Lag3, Ccr8, Tnfrsf18 and Tnfrsf9 in lymphoid, non-lymphoid tissue and tumour Tregs. Although it was not highly expressed in tumour-resident Tregs from the Kaede system, Ccr8 was included in the comparison due to multiple emerging studies that have highlighted the upregulated expression of Ccr8 in Tregs from tumours (Van Damme et al., 2021; Whiteside et al., 2021; Bhatt et al., 2021; Plitas et al., 2016). Therefore, we hypothesised that the Kaede background might have been masking Ccr8 expression and making it seem as though it were not a relevant marker.

Our analysis revealed that while Lag3 and Ccr8 were mainly expressed on tumour Tregs, Tnfrsf18 and Tnfrsf9 were expressed on tumour, lymphoid and non-lymphoid tissue Tregs. We then compared NLT and tumour Tregs by performing differential expression analysis using colon and MC38 Tregs. Lag3 emerged as the top marker that differentiates NLT and tumour Tregs within our dataset. Therefore, we concluded that Lag3 is an appropriate marker of murine tumour-resident Tregs and is not highly expressed in non-lymphoid tissue Tregs.

Preclinical models have shown the therapeutic potential of targeting both Lag3 and PD1 (Woo et al., 2012). Interestingly, blocking Lag3 alone failed to reverse the growth of 4T1 mouse tumours (Lauder et al., 2020, 2021). Instead, tumour regression was achieved when anti-Lag3 treatment was administered in mice after systemic Treg depletion using Pi3k$\delta$ inhibitors (Lauder et al., 2020, 2021). In humans, the combination of Relatlimab

(anti-LAG3) and Nivolumab (anti-PD1) has been shown to promote progression-free survival in treatment-naive patients with metastatic melanoma (Tawbi et al., 2022).

However, in addition to its binding to the peptide-major histocompatibility complex class II (MHC class II) complex (MacLachlan et al., 2021), the mechanistic function of Lag3 remains a mystery, in part, due to the lack of comprehensive knowledge about its ligands (Burnell et al., 2022). An early study looking at Lag3$^+$ Tregs suggested that Lag3 plays a role in Treg-mediated suppression of conventional CD4 T cells (Huang et al., 2004). In an in vitro suppression assay, Tregs that were treated with Lag3 blocking antibodies exhibited a decreased immunosuppressive capacity on CD4 T cells (Huang et al., 2004). However, other studies suggested that Lag3 expression inhibited the suppressive role of Tregs, further mystifying the function of Lag3 on Tregs (Zhang et al., 2017). Therefore, in light of the findings presented here, more studies are warranted to investigate the role of Lag3$^+$ Tregs enriched in mouse tumour Tregs. One way to investigate this would be to photoconvert MC38 tumours in Kaede mice, treat mice with Lag3-blocking antibodies, and quantify the differences between tumour-resident Treg numbers in the presence and absence of treatment.

Most therapeutics fail to achieve efficacy during clinical trials despite having demonstrated promise in preclinical models. Inter-species differences, the mismatch between syngeneic cancer cell lines and human tumours and significant inter-patient variability likely contribute to the extensive attrition rates in clinical trials (Mak et al., 2014). To assess whether Lag3 is highly expressed on human tumour Tregs, we developed a human Treg meta-atlas.

Comparable to mouse Tregs, we identified activated, ISG15$^+$, CCR7$^+$ and proliferative Tregs. Most tumour Tregs consisted of activated Treg fractions, while healthy tissues were composed of variable fractions of CCR7$^+$ and activated Tregs. Lymphoid tissue Tregs clustered separately from tumour Tregs, in contrast to non-lymphoid tissue Tregs which were found in both tumour and lymphoid tissue Treg clusters. This indicated that some non-lymphoid tissue Tregs shared transcriptional profiles with tumour Tregs, similar to what was observed in the mouse Treg meta-atlas. However,

when we assessed the expression of LAG3, CCR8, TNFRSF18 and TNFSR9 in human Tregs, we observed interesting inter-species differences. In contrast to mouse tumour Tregs, human tumour Tregs did not highly express LAG3. Tregs in multiple types of tumours and non-lymphoid tissue, particularly oesophagus, lung, thyroid, uterus and colon, highly expressed TNFRSF18 and TNFRSF9. LAG3, TNFRSF18, and TNFRSF9 were also expressed in multiple types of immune cells of tumours, including exhausted CD8 T cells. Interestingly, CCR8 was highly expressed in Tregs from various human tumours, but minimally expressed in healthy tissue Tregs except for the uterus and esophagus. Furthermore, CCR8 was not highly expressed on other non-Treg immune cells from different tumours. This suggested that CCR8 may be an appropriate marker for targeting tumour Tregs although great care should be taken as Tregs in a few healthy tissue may also express CCR8.

These results do not imply that LAG3 is not an appropriate therapeutic target, but reflect that the mechanism of action associated with anti-LAG3 antibodies may not primarily focus on silencing intratumoral Tregs. LAG3 blockade may, for example, be inhibiting CD8 T cell exhaustion thereby contributing towards the demonstrated progression-free survival (Tawbi et al., 2022).

Regarding CCR8, several studies have demonstrated the therapeutic potential for depleting intratumoral Tregs using anti-CCR8 antibodies (Kidani et al., 2022; Weaver et al., 2022; Bhatt et al., 2021; Whiteside et al., 2021; Van Damme et al., 2021). However, the role of CCR8 on intratumoral Tregs has not been fully evaluated. Mouse studies suggest that though intratumoral Tregs upregulate Ccr8, it is dispensable for tumour infiltration and Treg effector function (Whiteside et al., 2021; Magnuson et al., 2018). Depletion rather than blockade of intratumoral Ccr8+ Tregs confers a therapeutic benefit in mouse models (Campbell et al., 2021; Bhatt et al., 2021). At the same time, other studies suggest that the CCL1-CCR8 axis is important for effector Treg function (Kuehnemuth et al., 2018; Barsheshet et al., 2017). However, despite these differences, it is clear that CCR8 has drawn much attention in recent years as a potential target for intratumoral Treg depletion.

The study presented here has several limitations. scRNA-seq provides mRNA counts, which do not inform us about the extent to which markers are expressed on the cell surface. Therefore, our results need to be experimentally validated using laboratory methods such as flow cytometry. Secondly, it is known that tumours are highly heterogeneous in different individuals. Therefore, the gene expression patterns presented here may not be universal but rather specific to the datasets used. It would not be surprising to see slightly different results if Tregs from a different cohort of cancer patients were analysed. Thirdly, Treg depletion does not apply as an effective treatment modality to all cancers. In fact, studies have shown that depleting Tregs in pancreatic cancer models worsens tumour progression (Zhang et al., 2020a). In such causes, alternative treatment options such as targeting exhausted CD8 T cells may be more viable. However, despite these limitations, our study effectively demonstrates how data-driven approaches can be used to rationally identify or rule out therapeutic markers for targeting intratumoral Tregs, in a way that is conscious about potential biases in translation between mouse models and human tumours.

### 4.5.1 Conclusion and future work

In this chapter, we have generated mouse and human scRNA-seq Treg meta-atlases with the objective of identifying surface markers that are unique to tumour-resident Tregs and consistently expressed between species. In mice, our study revealed that Lag3 was not only highly expressed on tumour Tregs, but was minimally expressed in Tregs resident in lymphoid and non-lymphoid tissue considered. However, the role of Lag3 in Tregs is poorly understood. Therefore, further studies should focus on dissecting the molecular mechanisms associated with Lag3 expression on tumour-resident Tregs.

The Kaede mouse model would provide a fantastic opportunity for studying whether Lag3-blockade perturbs tumour-resident Treg densities, suppressive potential, tumour infiltration and tumour retention. In parallel, the effect of Lag3 blockade on other critical immune cell subsets in the tumour, such as CD8 T cells, may be investigated to understand the role of anti-Lag3 on T cell exhaustion in mouse models. Such studies

may help generate hypotheses that can be further tested in human cells to provide a mechanistic understanding of how emerging treatments such as Relatlimab (human anti-LAG3) contribute towards extending progression-free survival in humans.

The unexpected low expression of LAG3 on human tumour Tregs highlighted the importance of evaluating inter-species differences when searching for therapeutic markers. To validate this finding, further studies should experimentally profile human tumour Tregs and quantify the extent of surface LAG3 expression using methods such as flow cytometry. Furthermore, the role of LAG3 in human Tregs, as well as the identification of associated ligands need further investigation.

Increased expression of CCR8 on Tregs from human tumours solidified the proposed potential for depleting human tumour Tregs using CCR8-antibodies. Though several studies have identified $CCR8^{+}$ Tregs in human tumours, additional studies need to be conducted with Tregs from more diverse cancer types to establish the potential limitations of anti-CCR8 treatment in depleting tumour Tregs. Furthermore, there are many immunosuppressive cell types in humans including Type 1 Tregs (Tr1) and Myeloid-derived suppressor cells (MDSCs) which we have not examined in this study. Therefore, CCR8 expression on these immunosuppressive cells should be evaluated to determine whether anti-CCR8-mediated depletion also affects these cells in the tumour.

# 5

# Thesis discussion

Contents


5.1 Research summary . . . . . 205
5.2 Context . . . . . 208
5.3 Future work . . . . . 213


In this thesis, we have applied data-driven approaches to study intratumoral Tregs. Our aim has been to explore intratumoral Treg trafficking behaviour in mice, and compare Tregs in tumours and healthy tissue across species to identify molecular markers that can be used to therapeutically target tumour-resident Tregs with minimum risk of inducing severe side-effects. In this current chapter, we will summarise the findings from this thesis and discuss how these findings fit in the context of the current knowledge in the field of immuno-oncology. Finally, we will describe potential studies that can be carried out to further investigate the results presented in this thesis.

## 5.1 Research summary

In Chapter 1, we gave a brief overview of the hallmarks of the tumour microenvironment and the role of the immune system in recognising and eliminating cancer cells. We

highlighted that immunosuppressive cells, particularly Tregs, accumulate in solid tumours where they contribute to the inhibition of anti-tumour responses, resulting in immune evasion. We described some of the mechanisms that Tregs employ to suppress the immune system and briefly outlined molecular markers that are enriched on the surfaces of highly immunosuppressive Tregs. We concluded the chapter by highlighting that though targeting intratumoral Tregs is a promising cancer treatment strategy, its mainstream application in the clinic is hindered by the lack of efficacy and induction of adverse events associated with a loss of immune homeostasis. Therefore, defining the therapeutic window associated with Treg-targeting cancer immunotherapy remains a fundamental challenge in the field of immuno-oncology. To contribute towards the identification of the therapeutic window, we underscored the importance of understanding the trafficking dynamics of intratumoral Tregs, biological processes that differ between tumour-resident and transient Tregs, and using scRNA-seq data to identify tumour Treg targets that are translatable between mice and humans.

In Chapter 2, we developed an ODE mathematical model describing the trafficking of red-labelled Tregs from MC38 and CT26 tumours in the Kaede mouse system. Through Bayesian parameter estimation, we explored potential mechanisms of intratumoral Treg migration out of the tumour (Fig. 1.7A). Our key hypothesis was that intratumoral Tregs are dynamically heterogeneous, consisting of resident and transient Tregs. This mechanism was inspired by flow cytometry analyses that have been conducted by other groups using photoconvertible mouse systems (Li et al., 2022; Ikebuchi et al., 2021). We also compared MC38 and CT26 Treg migration rates to investigate inter-tumour Treg trafficking heterogeneity. Although prior mathematical models involving Tregs have been described, they did not quantify tumour-specific Treg trafficking rates nor did they consider the prospect of tumour-resident and transient Tregs—all tumour Tregs were assumed to be dynamically homogeneous (Milanez-Almeida et al., 2015; Ji et al., 2023; Coletti et al., 2020; Wang et al., 2020c).

Unlike previous mathematical models, our model was constructed for the inference of intratumoral Treg trafficking mechanisms and trafficking rates, the latter of which may

be used to parameterise predictive PKPD models in the future. Our study suggested that there are resident and transient Tregs in both MC38 and CT26 tumours. Resident Tregs were predicted to be less proliferative than transient Tregs, consistent with prior work involving 4T1 tumours (Lauder et al., 2021). Furthermore, the mathematical model suggested that CT26 Tregs accumulate in the TDLN and spleen to a larger extent than MC38 Tregs, indicative of inter-tumour Treg dynamical differences.

In Chapter 3, we used both in-house and public scRNA-seq data to **1.)** compare MC38 and CT26 Tregs and **2.)** tumour-resident and transient Tregs. Our hypothesis was that the previously observed dynamical differences between MC38 and CT26, and resident and transient Tregs, could be a consequence of underlying transcriptional differences within these Treg subsets. The transcriptional profiling of MC38 and CT26 Tregs revealed that CT26 Tregs exhibit a mostly naive/central memory phenotype with the upregulation of Ccr7 and Cxcr4. These chemokine receptors play a key role in directing Treg migration towards lymph nodes and lymphoid organs such as the bone marrow (Menning et al., 2007; Zou et al., 2004). Therefore, these findings provided a transcriptional basis for the observed higher accumulation of CT26 Tregs in the TDLN and spleen in contrast to MC38 Tregs.

Transcriptional analysis of resident and transient MC38 Tregs showed that resident Tregs upregulate Lag3, Tnfrsf18 (GITR) and Tnfrsf9 (4-1BB) while transient Tregs highly express Ccr7. The expression of Lag3 on tumour Tregs was consistent with previous studies involving different murine tumour models (Li et al., 2022; Ikebuchi et al., 2021; Lauder et al., 2020, 2021). Gene set enrichment analysis highlighted that, compared to transient Tregs, tumour-resident Tregs highly activate biological pathways associated with immunosuppression and cytokine response but downregulate cellular metabolism, amide metabolism and cell proliferation. The downregulated cell proliferation in tumour-resident Tregs agreed with the mathematical modelling framework from Chapter 2 and was consistent with previous work, albeit in a different tumour model (Lauder et al., 2021, 2020). Metabolic differences between tumour-resident and transient Tregs were further explored through running metabolic simulations using Compass (Wagner

et al., 2021). The simulations suggested that metabolic reactions of the tricarboxylic acid cycle, oxidative phosphorylation, amino acid metabolism and fatty acid oxidation were downregulated in tumour-resident Tregs. Glycolysis did not significantly differ between tumour-resident and transient Tregs. Overall, results from this chapter were in agreement with the our hypothesis as MC38 and CT26, and tumour-resident and transient mouse Tregs exhibited significant transcriptional differences.

In Chapter 4, we tested two hypotheses. The first hypothesis was that some of the tumour-resident Treg markers identified in Chapter 3 namely, Lag3, Tnfrsf18 and Tnfrsf9, may not be unique to tumour Tregs but could also be expressed on Tregs in healthy mouse organs. The second hypothesis was that, owing to inter-species differences, tumour Treg markers identified in mice could be absent or expressed at low levels on tumour Tregs in humans. To test these hypotheses, we developed mouse and human Treg scRNA-seq meta-atlases using both in-house and public datasets. The generation of scRNA-seq meta-atlases was not unique to our study but has been used to study gene expression patterns in unrelated previous studies (Swamy et al., 2021; Nakayama and Yamamoto, 2021; Nieto et al., 2021).

In mice, we found that Lag3 is uniquely upregulated on tumour (MC38) Tregs while Tnfrsf9 and Tnfrsf18 are also expressed on Tregs in the skin and colon. However, we did not observe notable LAG3 expression in human tumour Tregs. This suggested that there could be inter-species differences in the extent to which LAG3 is expressed on tumour Tregs. Instead, CCR8 appeared to be highly expressed on Tregs from several human tumours. The upregulation of CCR8 on human tumour Tregs was consistent with previous studies (Plitas et al., 2016; Haruna et al., 2022) and supports further clinical development of CCR8-antibodies for depleting human tumour Tregs (Weaver et al., 2022).

## 5.2 Context

The development of Treg-targeting immunotherapies for solid tumours is primarily hindered by severe drug-induced toxicities. Approaches aimed at reducing these life-

threatening side-effects while maintaining drug efficacy are a current priority. Broadly, the objective of this thesis has been to identify molecular markers that could be used to deplete/inhibit tumour Tregs without affecting other immune cell types and Tregs in healthy organs. We accomplished this by investigating mechanisms of Treg accumulation in mouse tumours, which revealed the presence of tumour-resident and transient Tregs. In mice, we then determined markers that are enriched on tumour-resident but not transient Tregs, and assessed whether these markers are expressed on Tregs found in healthy organs. Finally, we tested the translatability of potential tumour Treg markers from mouse models to human tumours. By so doing, we hoped to contribute to the identification of the therapeutic window associated with Treg-targeting immunotherapy.

Treg dynamics in the tumour have not yet been adequately investigated. To our knowledge, only two studies have investigated Treg migration from tumours using photoconvertible mouse experimental models (Li et al., 2022; Ikebuchi et al., 2021). The rates at which Tregs leave the tumour and migrate to the TDLN and spleen are also unknown. Understanding the mechanisms of Treg accumulation in tumours and determining their migration rates is critical for developing PKPD models for early stage Treg-targeting drug development.

In Chapter 2, we applied mathematical modelling to show that the Treg profiles in MC38 and CT26 tumours fit a model in which there are tumour-resident and transient Tregs. Whether this mechanism holds for human tumour Tregs is unknown and likely difficult to determine for ethical reasons. However, most mathematical models of cancer-immune cell dynamics aimed at simulating dose-response oversimplify the mechanisms of Treg accumulation in tumours by not taking into account the prospect of resident and transient Tregs (Wang et al., 2020c; Coletti et al., 2020; Ma et al., 2020). These models could be improved by incorporating a more biologically accurate mechanism with resident and transient tumour Tregs and making use of Treg-specific parameters that we have estimated.

Another key finding from our mathematical model was that Treg migration rates differ depending on the tumour of origin. On average, CT26 Tregs egressed from the tumour

faster and significantly accumulated in the TDLN and spleen in comparison to MC38 Tregs. These findings were consistent with prior studies that highlighted that unlike MC38, CT26 tumours appear to repel Tregs over time (Taylor et al., 2019). In Chapter 3, we found that compared to MC38, CT26 Tregs upregulate Ccr7 and Cxcr4 which are associated with Treg migration to lymph nodes and lymphoid organs, respectively (Menning et al., 2007; Zou et al., 2004). This explained the observed increased egress of CT26 Tregs from tumours and their accumulation in the TDLN and the spleen.

Diverging Treg dynamics across different tumour models imply that great caution needs to be taken when evaluating Treg-targeting immunotherapeutics in mouse syngeneic models. In humans, variations of Treg dynamics in different tumours and patients could be contributing to tumour heterogeneity observed in the clinic. Treg depletion/inhibition might not be a universal cancer treatment strategy, especially for tumours that are mostly devoid of Tregs, which could be exploiting other mechanisms to evade the immune system.

In Chapter 3, we bioinformatically compared MC38 tumour-resident and transient Tregs. Our key objective was to identify markers and biological pathways that differ between tumour-resident and transient Tregs. We reasoned that because they are significantly retained in the tumour, resident Tregs should be functionally critical for sustaining tumour growth. Therefore, specifically targeting these tumour-resident Tregs could help reverse immunosuppression in the tumour and enhance anti-tumour responses.

We found that tumour-resident mouse Tregs are highly immunosuppressive, responsive to cytokines, less proliferative and metabolically quiescent in comparison to transient Tregs. The low proliferative capacity of tumour-resident Tregs was consistent with prior studies looking at Tregs that were enriched in the tumour following systemic Treg depletion (Lauder et al., 2020, 2021). The downregulation of various metabolic processes, particularly amide synthesis, was consistent with the hypoproliferative status of tumour-resident Tregs, as amide metabolism is crucial for cell division. Interestingly, genes involved in the production of putrescine, a precursor of the polyamine metabolic pathway, were upregulated in tumour-resident Tregs, though metabolic simulations

predicted that the actual reactions catalysed by the gene-products were downregulated. However, it would still be interesting to inhibit Odc1 and Sat1, enzymes involved in putrescine production, and assess how this affects tumour-resident Treg numbers and tumour growth in Kaede mice.

As they do not highly proliferate, tumour-resident Tregs would be expected to upregulate pathways that enhance their survival fitness in the tumour. Indeed, we found that tumour-resident Tregs upregulated interferon-response genes which enable them to evade cytokine-induced cell death within the potentially cytokine-rich tumour microenvironment (TME) (Pacella et al., 2020, 2016).

Due to oxygen-deficiency in the TME, tumour-resident Tregs downregulated oxygen-dependent metabolic pathways such as oxidative phosphorylation and fatty acid oxidation. At the same time, glycolysis remained unhindered in tumour-resident Tregs. The upregulation of Hif1-$\alpha$ in tumour-resident Tregs suggests that they undergo metabolic reprogramming, becoming glycolytic, which is typical of mammalian cells growing under hypoxia. Collectively, tumour-resident Tregs appear to be modulating their metabolic fitness to continue contributing towards immunosuppression without succumbing to the intense conditions of the TME, unlike conventional T cells.

The comparison of Kaede red and green MC38 tumour Tregs indicated that green Tregs (newly arriving in the tumour) upregulate Ccr7. Differential expression analysis of tumour-resident and transient Tregs revealed that resident Tregs upregulate Lag3, Tnfrsf18 and Tnfrsf9 in contrast to Ccr7-expressing transient Tregs. In Chapter 4, we observed that Lag3 is a better marker of tumour-resident Tregs than Tnfrsf18 and Tnfrsf9, which are also expressed in non-lymphoid tissue Tregs. Thus, consolidating findings from this work, we devised a schematic mouse model of Treg accumulation and migration in the tumour (Fig. 5.1). In this model, Ccr7$^+$ Tregs infiltrate the tumour. Some of them are differentiated into Lag3$^+$ and Isg15$^+$ resident Tregs. Finally, Ccr7$^+$ Tregs that are not converted into tumour-resident Tregs become transient Tregs and migrate to the TDLN and other organs.

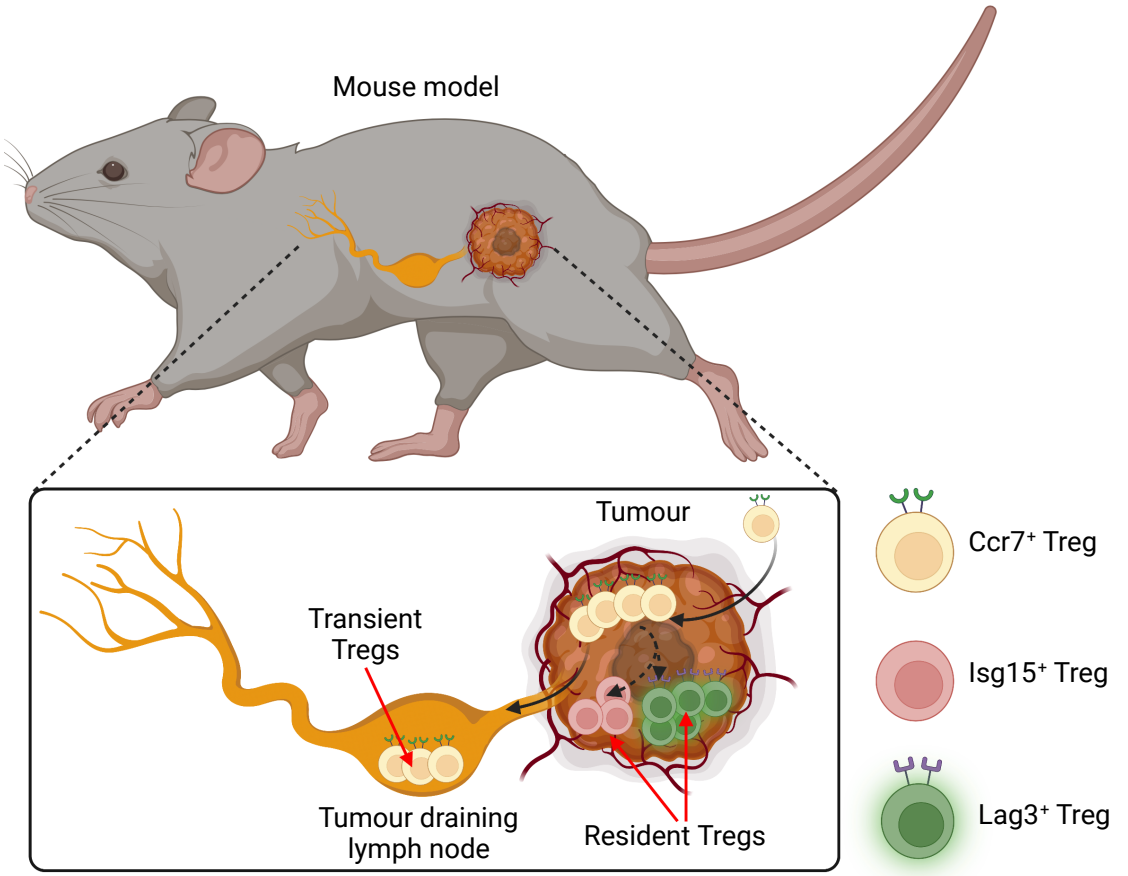



**Figure 5.1: Mechanism of Treg accumulation and trafficking in the tumour**. Ccr7$^+$ Tregs infiltrate the tumour and some of them are converted to Lag3$^+$ and Isg15$^+$ resident Tregs. Ccr7$^+$ Tregs that are not converted into a resident phenotype migrate out of the tumour as transient Tregs. The figure was created using Biorender.

The upregulation of Lag3 on tumour-resident Tregs was consistent with prior studies (Li et al., 2022; Ikebuchi et al., 2021; Lauder et al., 2020). However, the role of Lag3 on Tregs still remains unknown. Lag3 blockade alone does not have a significant effect on tumour growth (Lauder et al., 2021, 2020). However, in a recent clinical trial, the combination of anti-LAG3 and anti-PD1 therapy conferred enhanced clinical benefit to patients with unresectable melanoma compared to anti-PD1 treatment alone (Tawbi et al., 2022). Because LAG3 is highly expressed on exhausted CD8 Tregs, anti-LAG3 therapy possibly works by inhibiting CD8 T cell exhaustion in contrast to inhibiting intratumoral Tregs.

Our studies highlighted that human tumour Tregs did not highly express LAG3. Instead, they upregulated CCR8. This finding further supports the growing interest in developing anti-CCR8 antibodies to deplete tumour Tregs in humans (Weaver et al., 2022; Plitas

et al., 2016; Haruna et al., 2022; Kidani et al., 2022). The discrepancy in the expression of LAG3 was consistent with our hypothesis, which stated that inter-species differences could result in a lack of translatability of tumour Treg markers as we move from mice to humans. This emphasises the importance of practising caution when interpreting results from preclinical models as differences in biology across species may confound cancer drug development and ultimately engender severe side-effects.

## 5.3 Future work

### 5.3.1 Integrating mathematical modelling with transcriptomics

Immunology is a mechanism-heavy field involving complex interactions between different cell types. Understanding these complex mechanisms can play a paramount role in revealing processes that underpin disease pathogenesis, and the knowledge can be ultimately used in designing therapies and informing drug administration schedules. Over the past decade, single cell sequencing has transformed biomedical research, providing scientists with the lens through which they can examine differences in gene expression and cellular compositions in both health and disease. On the other hand, mathematical modelling has started gaining traction in biomedical research as a way of uncovering and simulating complex cellular interactions.

Accurate mathematical models require existing parameters that describe cellular behaviour or longitudinal experimental datasets from which the relevant parameters can be inferred. Often, the generated longitudinal data has few time points, is noisy and can be inadequate to provide the necessary information required to parameterise the mathematical models. Easily accessible public scRNA-seq data can be leveraged to aid the development of mathematical models that are biologically relevant. Thus, the integration of multi-scale mathematical modelling and multi-omics data is predicted to play a critical role in the future of precision oncology. However, exactly how this integration of multi-scale mathematical modelling and multi-omics data can be achieved remains a fundamental challenge (Lazarou et al., 2020; Zhang et al., 2020b).

A key strength of our study has been an illustration of how mathematical modelling can be synergistically combined with scRNA-seq data to reveal key biological insights to aid the development of Treg-targeting immunotherapy. In our study, we used scRNA-seq data to learn about the proliferative capacity of tumour-transient Tregs which in turn informed our mathematical model. To further incorporate scRNA-seq data in understanding intratumoral Treg dynamics, future preclinical studies may apply mathematical modelling directly to longitudinal scRNA-seq datasets, instead of flow cytometry cell counts, to model both red and green tumour Tregs, infer the rates at which newly arriving tumour Tregs are converted to resident Tregs and incorporate other Treg subpopulations such as Isg15$^+$ in the mathematical models. These mathematical models can then be further developed into PKPD models that can be used to perform simulations and predict the effect of various concentrations of Treg-targeting antibodies on tumour-resident Tregs and tumour growth.

### 5.3.2 Reducing the level of parameter uncertainty

Intratumoral Treg migration parameter distributions determined in Chapter 2 were associated with significant uncertainty. This was likely due to a limited number of time points and high variability in Treg counts quantified across individual mice. To obtain more accurate parameters, additional Kaede photoconversion and Treg quantification experiments involving more time points and mice may be conducted, and the generated data used to re-parameterise the mathematical model.

### 5.3.3 Are resident and transient Tregs present in other syngeneic mouse tumour models?

A key conclusion of Chapter 2 was that there are resident and transient Tregs in both MC38 and CT26 tumour models. However, whether the same phenomenon is true for other commonly used tumour models such as Renca (kidney), 4T1 (lung), TC1 (lung), LLC (lung) and B16F10 (melanoma) is unknown. Conducting Kaede photoconversion

experiments with these tumour models and applying mathematical modelling can reveal whether resident and transient Tregs are present in these tumour models as well.

One of the current challenges in the preclinical development of cancer immunotherapies is that there is no proper way of selecting which syngeneic mouse model to test the drug in. Understanding Treg dynamics in different tumour types can provide information on whether there is Treg-specific heterogeneity across mouse tumour experimental models, which can provide a basis for selecting specific mouse tumour models to test Treg-targeting therapeutics.

### 5.3.4 Experimental validation and spatio-temporal analysis of tumour Tregs

In Chapter 3, we observed that tumour-resident Tregs upregulate Lag3, Tnfrsf18, and Tnfrsf9 but downregulate Ccr7. As these conclusions were made using mRNA expression data, which may not translate well to surface protein expression, future work should focus on validating the surface expression of these markers on MC38 and CT26 tumour-resident Tregs. David Withers' group, our collaborators, have started quantifying the surface expression patterns of these markers using flow cytometry. Similarly, using samples from different human tumours, the observed high expression of CCR8 and low expression of LAG3 can be validated via flow cytometry.

An interesting question that arises from Chapters 3 and 4 is whether $Lag3^+$ resident Tregs in mouse tumours localise deep in the core of the tumour (thus becoming trapped) while $Ccr7^+$ transient Tregs are found on the boundary of the tumour and healthy tissue (and can easily escape to other organs). Understanding the localisation of tumour-resident and transient Tregs may provide mechanistic insights underlying the residency/transience of Tregs within tumours. This question can be addressed by staining, imaging the tumour and applying spatial analysis. David Withers' group is currently conducting the relevant microscopy studies on MC38 and CT26 tumours.

### 5.3.5 Can tumour-resident Tregs be metabolically targeted?

Bioinformatic analyses revealed that, tumour-resident Tregs are glycolytic but down-regulate oxidative phosphorylation, the tricarboxylic acid cycle, amide metabolism and fatty acid oxidation. Though it is difficult to measure metabolism *in vivo*, resident and transient Tregs may be isolated from the tumour and their metabolism measured using Seahorse assays (Caines et al., 2022). However, a potential challenge arising from using such a technique may be the metabolic changes that might take place when resident Tregs are isolated from the hypoxic and acidic TME into cell cultures which may have different conditions.

In Chapter 3, scRNA-seq analysis underscored that tumour-resident Tregs upregulate Odc1 and Sat1, which are involved in the production of putrescine, a precursor of the polyamine synthesis pathway. It would be interesting to inhibit Odc1 and Sat1 using difluoromethylornithine (DFMO) and Diminazene aceturate (DIZE) respectively (Wagner et al., 2021), and assess how these treatments affect tumour-resident Treg numbers and tumour growth in the Kaede system. Being able to metabolically target tumour-resident Tregs would provide a supplementary treatment avenue that can be easily explored through dietary modifications, for example feeding mice with spermine and spermidine-rich food, and using existing metabolism modulating agents.

### 5.3.6 Investigating the role of Lag3 in Tregs

We found that Lag3 is a good marker of mouse tumour-resident Tregs. However, the role of Lag3 on Tregs is contentious. In previous studies, Lag3 blockade alone did not inhibit tumour growth. However, Lag3 blockade after systemic Treg depletion inhibited 4T1 tumours (Lauder et al., 2020, 2021). It would be interesting to administer Lag3-blocking antibodies and quantify how this treatment affects the accumulation and retention of tumour-resident Tregs in the Kaede system. Our collaborators are currently conducting Lag3-blockade experiments and assessing how it impacts resident Tregs in MC38 and CT26 tumours.

Though we found that LAG3 was lowly expressed in human tumour Tregs, anti-LAG3 and anti-PD1 combination treatment has shown benefit in melanoma patients (Tawbi et al., 2022). Thus, understanding the role of Lag3 on Tregs may provide insights that could ultimately play a role in the exploration of different hypothesis revolving around the mechanism of action associated with anti-LAG3 therapy in humans.

### 5.3.7 Is there even a therapeutic window associated with Treg-targeting immunotherapy?

Much of the work in this thesis focused on mice, due to data availability. In humans, we were unable to do robust bioinformatic analyses to statistically identify markers that are upregulated on Tregs due to extensive nested batch-effects across studies and individuals. If we had scRNA-seq data from one well-designed study covering multiple tumour types, we could have applied differential expression analysis and additional statistical methods such as the partial least regression methods (Datta, 2001) to identify markers that are broadly upregulated on human tumour Tregs. With the availability of more data, such avenues may be explored in the future.

Though targeting Tregs has shown great promise in mice, its failure in clinical trials brings to question whether a tumour Treg-targeting therapeutic window exists in humans. In part, the high heterogeneity observed in cancer patients could be a significant contributing factor to the observed failures.

Extensive characterisation of the immune cells present in the human TME needs to be conducted to understand the heterogeneous immune cell characteristics in different patients, which will then impact clinical decision-making pertaining to the type of immunotherapy to administer. For instance, many Treg-depleting immunotherapies under investigation rely on ADCC, which in turn requires that there be enough NK cells in the TME to deplete intratumoral Tregs. Undoubtedly, such therapies would fail to achieve efficacy in patients whose tumours are poorly infiltrated by NK cells. Thus antibodies with different mechanisms of Treg depletion such as antibody-drug conjugates

(Zammarchi et al., 2020) may be indicated in such situations. Furthermore, bi-specific antibodies targeting not one, but two markers that are uniquely enriched on tumour Tregs may be explored as a platform for potentially restricting depletion to tumour Tregs.

In conclusion, tumour Treg-targeting is a promising cancer treatment strategy but much work still has to be done before human tumour Tregs can be targeted safely and effectively.

# Appendices

# A

# Mathematical Modelling Appendix

Our collaborators, David Withers' lab, used flow cytometry to quantify red and green Tregs from tumour-bearing Kaede mice. Figure A.1 gives an example of the gating strategy that was used to quantify Tregs isolated from CT26 tumours at different times after tumour photoconversion. MC38 tumour Tregs were also quantified similarly.

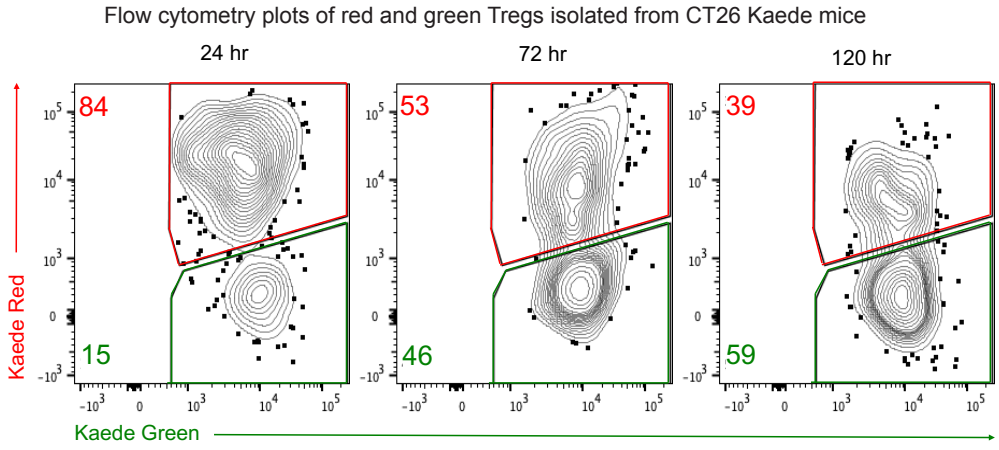



**Figure A.1: Quantification of red and green tumour Tregs**. Flow cytometry plots showing red and green Tregs that were isolated from CT26 tumours at different time points. Red and green boxes show the gating strategy for red and green Kaede Tregs respectively. Percentages of red and green Tregs are written next to each gate.

After running MCMC to estimate parameters for the CT26 and MC38 mathematical models, we assessed chain convergence using the Gelman-Rubin convergence statistic, $\hat{R}$. All parameters in both the CT26 and MC38 mathematical models had $\hat{R}$ values of approximately unity, suggesting good chain convergence (Table. A.1).

**Table A.1: Assessing MCMC chain mixing**. Table showing $\hat{R}$ metrics for the MC38 and CT26 mathematical models. Resident$_0$ – Initial resident Tregs, Transient$_0$ – Initial transient Tregs, Mass_TmrP$_0$ – Initial tumour mass following tumour photoconversion, Mass_TDLNP$_0$ – Initial tumour mass following TDLN photoconversion, TDLN_TDLNP$_0$ – Initial TDLN Tregs following the photoconversion of the TDLN.

| MC38 mathematical model | | CT26 mathematical model | |
|---|---|---|---|
| Parameter | $\hat{R}$ | Parameter | $\hat{R}$ |
| $\alpha$ | 1.001308 | $\alpha$ | 1.002631 |
| $\beta$ | 1.002833 | $\beta$ | – |
| $\delta$ | 1.002209 | $\delta$ | 1.015126 |
| $\gamma$ | 1.004344 | $\gamma$ | 1.021144 |
| $\rho$ | 1.002336 | $\rho$ | 1.002822 |
| $\tau$ | 1.003789 | $\tau$ | – |
| $\zeta$ | 1.001902 | $\zeta$ | 1.011783 |
| Resident$_0$ | 1.001446 | Resident$_0$ | 1.002700 |
| Transient$_0$ | 1.003168 | Transient$_0$ | 1.025390 |
| Mass_TmrP$_0$ | 1.002195 | Mass_TmrP$_0$ | 1.002496 |
| Mass_TDLNP$_0$ | 1.000970 | – | – |
| TDLN_TDLNP$_0$ | 1.002292 | – | – |

To fit the MC38 Treg trafficking model (Fig. A.2A), we excluded the 120 hour tumour Treg time point as it deviated from expected behaviour. Including this time point resulted in poor model fitting to the second, and more biologically plausible, time point (Fig. A.2B).

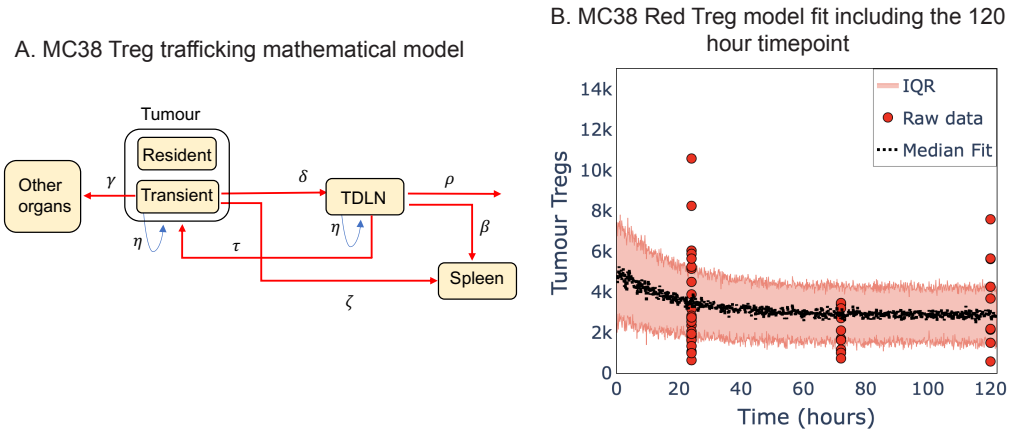



**Figure A.2: Fitting the MC38 Treg mathematical model to all data points**. A: MC38 Treg trafficking mathematical model. B: Fitting the MC38 Treg trafficking model to all data points, including the 120 hour Treg data. Black lines correspond to the median data fit, red dots are red Tregs quantified per mouse and the red shaded region is the interquartile range of the model fit. IQR – Inter-quartile range.

We modelled the migration of Tregs from CT26 and MC38 tumours with the absence of a resident Treg compartment (Fig. A.3A,D).Though the model could reasonably fit the red Tregs in CT26 tumours (Fig. A.3B), it failed to reproduce the dynamics associated with red Tregs that migrated from CT26 tumours to the spleen (Fig. A.3C). The MC38 mathematical model lacking a resident Treg compartment could not capture the non-zero red tumour Tregs at 120 hours (Fig. A.3E).

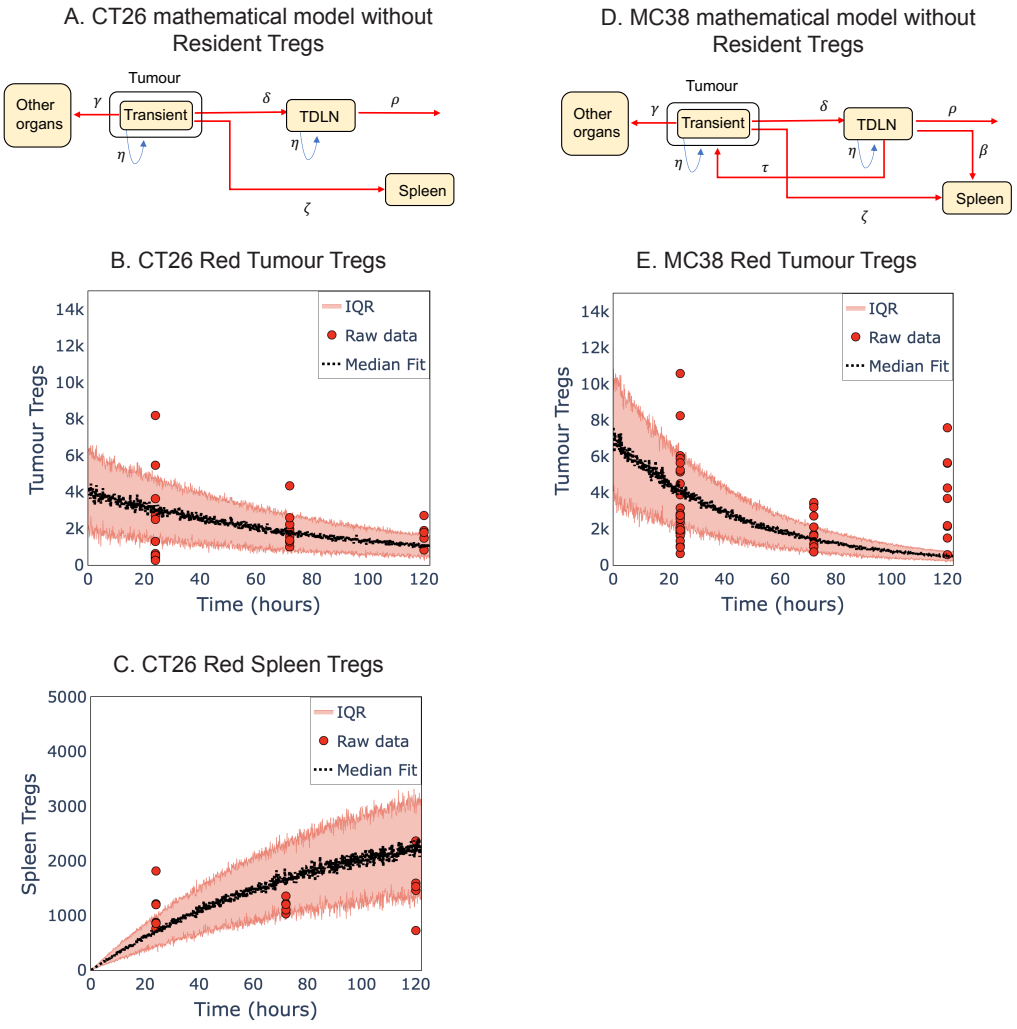



**Figure A.3: Treg trafficking mathematical models without resident Tregs**. A: CT26 Treg mathematical model without a resident Treg compartment. B: Fitting the CT26 Treg mathematical model to red Tregs from CT26 tumours. C: Fitting the CT26 Treg mathematical model to red Tregs that migrated from CT26 tumours to the spleen. D: MC38 Treg trafficking mathematical model without a resident Treg compartment. E: Fitting the MC38 Treg trafficking model to red MC38 Tregs. Black lines correspond to the median data fit, red dots are red Tregs quantified per mouse and the red shaded region is the interquartile range of the model fit. IQR – Inter-quartile range.

Mathematical models that do not consider Treg proliferation in the Transient and TDLN compartments (Fig. A.4A,C) resulted in high predicted initial red Treg numbers in CT26 tumours (Fig. A.4B) and were practically unidentifiable for MC38 Treg data (Fig. A.4D).

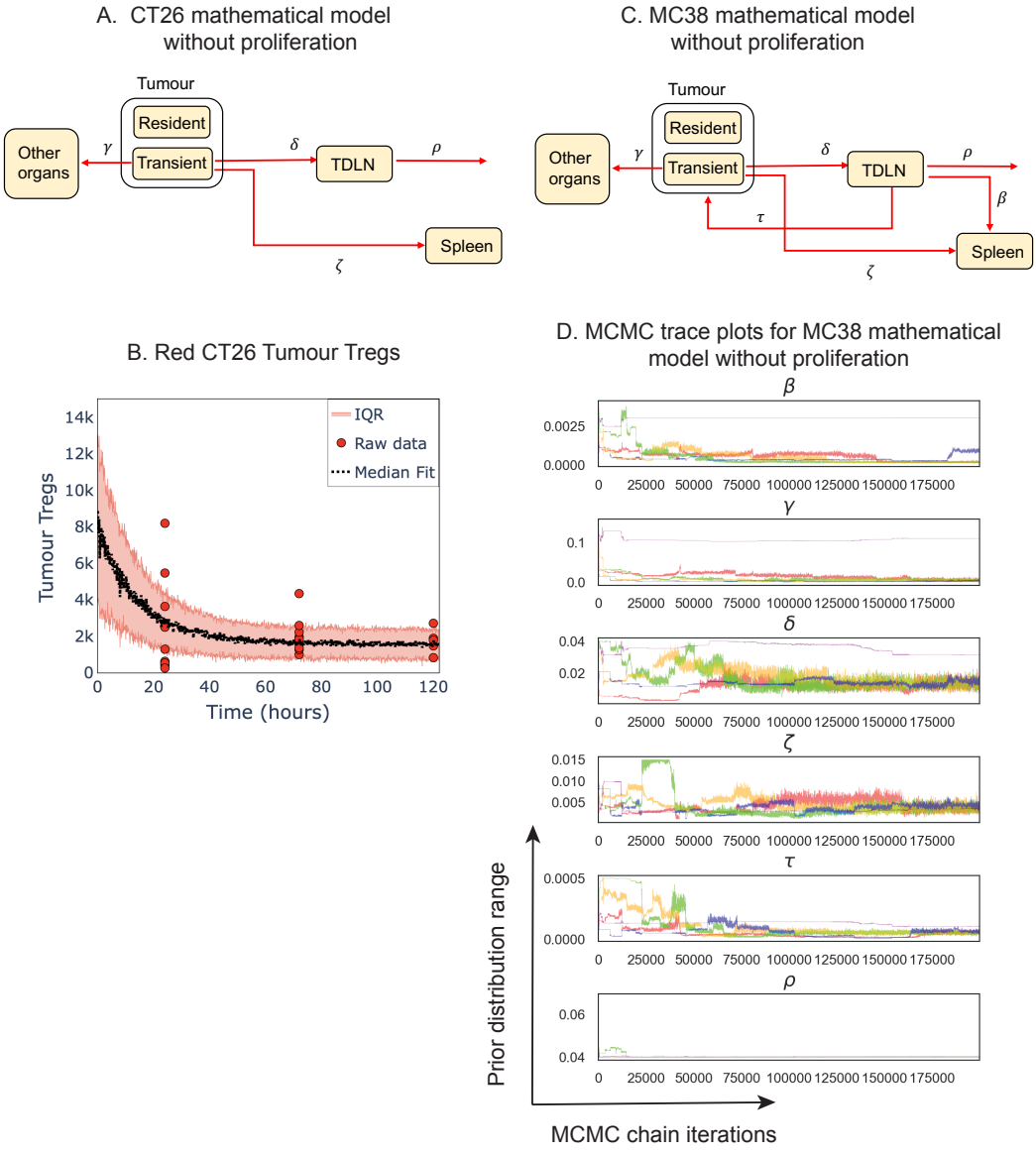



**Figure A.4: Treg trafficking mathematical models without Treg proliferation**. A: CT26 mathematical model with no Treg proliferation. B: Fitting the CT26 mathematical model to red CT26 Tregs. Black lines correspond to the median data fit, red dots are red Tregs quantified per mouse and the red shaded region is the interquartile range of the model fit. C: MC38 mathematical model with no Treg proliferation. D: MCMC trace plots for parameter inference on the MC38 mathematical model lacking Treg proliferation. Different colours in the trace plots represent independent MCMC chains. IQR – Inter-quartile range, MCMC – Markov Chain Monte Carlo.

# B

# Transcriptional Characterisation Appendix

We assessed the proliferative capacity of red and green Tregs using both scRNA-seq data and flow cytometry. Red Tregs that migrated from MC38 tumours to the TDLN at 48 hours after tumour photoconversion expressed higher Mki67 than all other Treg subsets (Fig. B.1A). Flow cytometry experiments conducted by our collaborators highlighted that there was a higher fraction of proliferative Tregs in the green Treg sample at 24 hours than red and green Tregs at 72 hours post MC38 tumour photoconversion (Fig. B.1B). Following the photoconversion of the TDLN in CT26-bearing Kaede mice, there were more proliferative Tregs in the TDLN than in CT26 tumours (Fig. B.1C). Overall, these results indicated that resident Tregs are less proliferative than transient or TDLN Tregs.

To perform metabolic simulations within a reasonable amount of time, we created micropools of resident and transient Tregs from the Kaede scRNA-seq datasets B.2. This reduced the dimensionality of the dataset from 1136 cells to 45 Treg micropools, with approximately 25 Tregs per micropool. We then determined which micropools resembled resident and transient Tregs by calculating the fraction of resident Tregs per micropool. Finally, we ran Compass using the Treg micropools as recommended in Wagner et al. (2021).

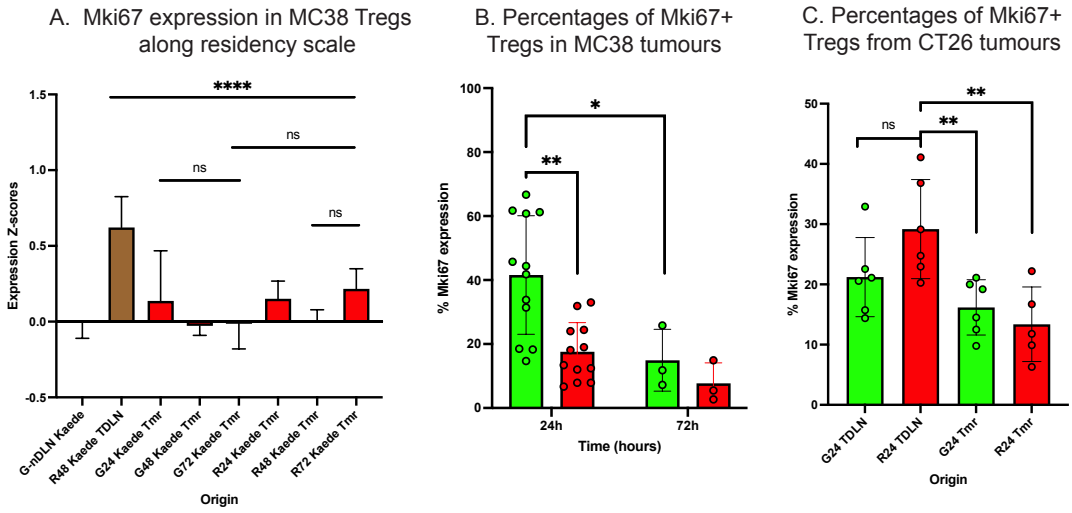



**Figure B.1: Mki67 expression in Tregs**. A: Scaled Mki67 scRNA-seq expression in red and green Tregs from MC38-implanted Kaede mice. B: The percentages of Mki67$^+$ Tregs from MC38 tumours determined using flow cytometry. C: Flow cytometry percentages of Mki67$^+$ Tregs from CT26 tumours and TDLNs following TDLN photoconversion determined using flow cytometry. TDLN – Tumour draining lymph node, Tmr – Tumour, R24 – Red Tregs at 24 hours after photoconversion, G72 – Green Tregs at 72 hours after photoconversion.

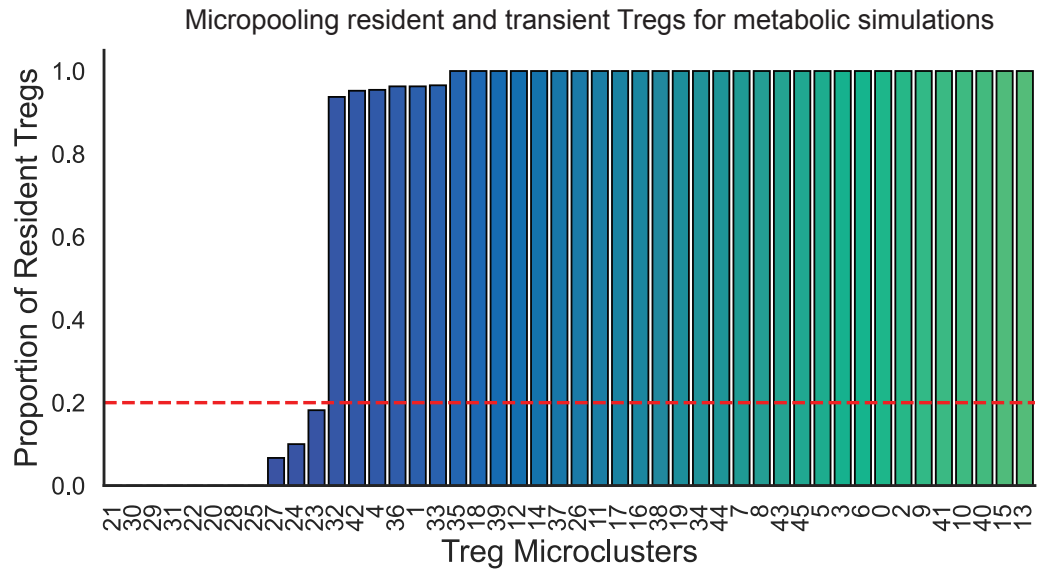



**Figure B.2: Micropooling resident and transient Tregs for metabolic simulations** Metabolic simulations were run with micropooled Treg clusters. Clusters with resident Treg proportions of less than 0.2 (under the red horizontal line) were annotated as transient Tregs while Tregs with resident Treg proportions above 0.2 were regarded as resident Tregs. Resident Treg proportions were calculated as the fraction of resident Tregs within a Treg microcluster out of all the Tregs in the same microcluster.

# C

# Treg Meta-atlases Appendix

In Chapters 2 and 3, we proposed the presence of resident and transient Tregs, and transcriptionally profiled these Treg subpopulations using MC38 Treg scRNA-seq data. Here, we used a public gene set associated with tissue Tregs from the muscle, visceral adipose tissue (VAT), intestines and the brain (Muñoz-Rojas and Mathis, 2021) to score Tregs in the mouse Treg meta-atlas for tissue Treg signatures/modules. In other words, we determine the average combined expression of genes associated with tissue Tregs across conditions and mouse tissue. This was performed to infer whether tumour Tregs exhibit a strong tissue signal, given that we observed high fractions of NLT Tregs in tumours when we performed compositional analysis of the Treg meta-atlas subclusters in Chapter 3.

We found that, on average, Tregs from tumours had a stronger tissue signature than Tregs from healthy lymphoid tissue (Fig. C.1A, B). Tregs from non-lymphoid tissue, such as the ear skin, lung and colon had high tissue Treg signatures as expected (Fig. C.1B). Tissue Treg genes shared minimum overlap with resident and transient Treg genes identified in Chapter 3 (Fig. C.1B).

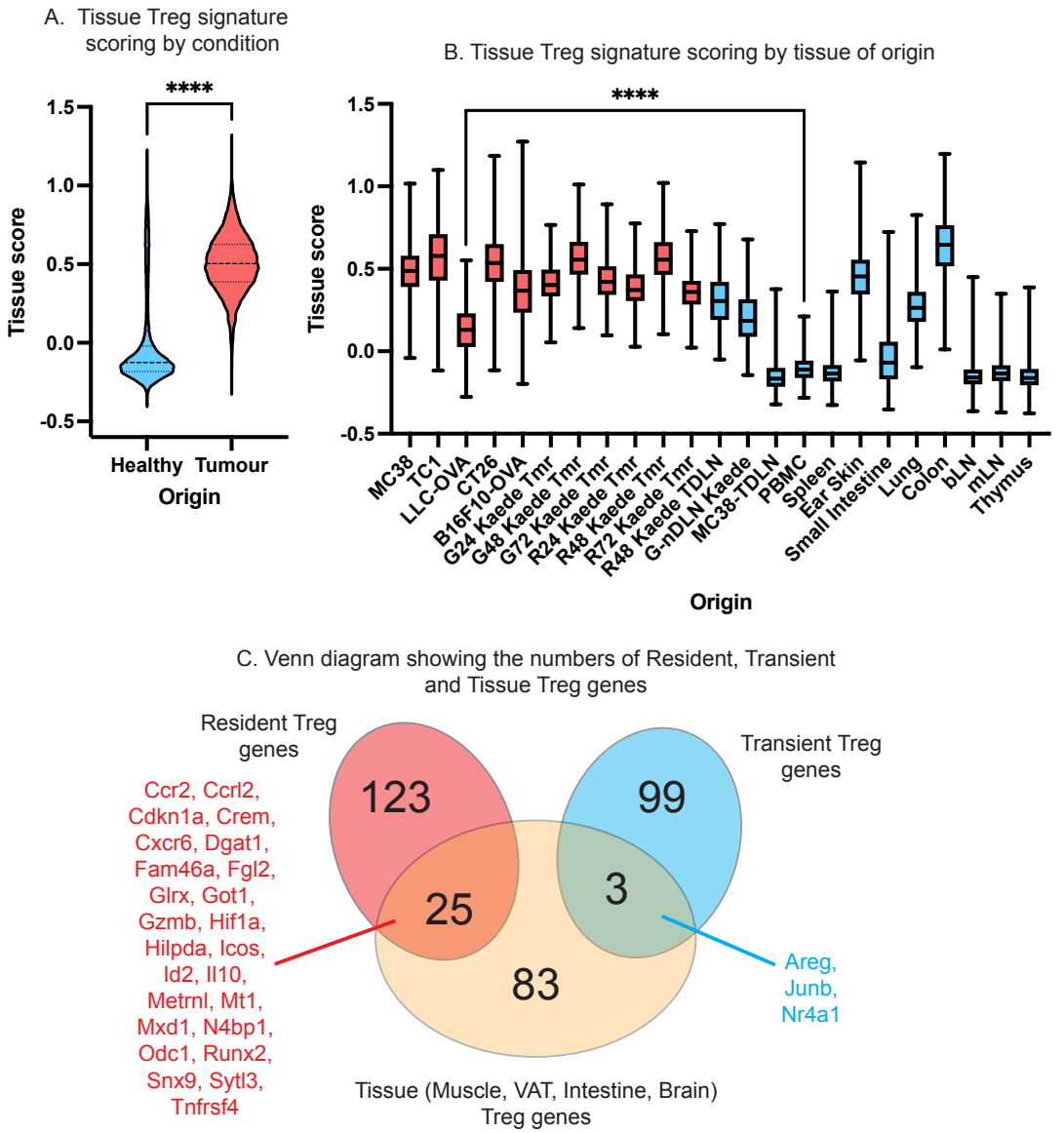



**Figure C.1: Tissue Treg signature/module scoring in mice**. A: Tissue Treg module scoring for Tregs from healthy mouse tissue and tumours. B: Tissue Treg module scoring for Tregs from individual mouse organs/tumours. C: A Venn diagram showing the degree of overlap of tissue Treg genes with genes associated with resident and transient Tregs in mice. VAT – Visceral Adipose Tissue.

We generated human CD4 non-Treg and CD8 T cell meta-atlases to assess the specificity of different markers that were upregulated on tumour Tregs. Here, we show the numbers of CD4 and CD8 T cells in the human meta-atlases (Fig. C.2A,B) together with the scaled expression of different markers associated with the T cells (Fig. C.2C,D).

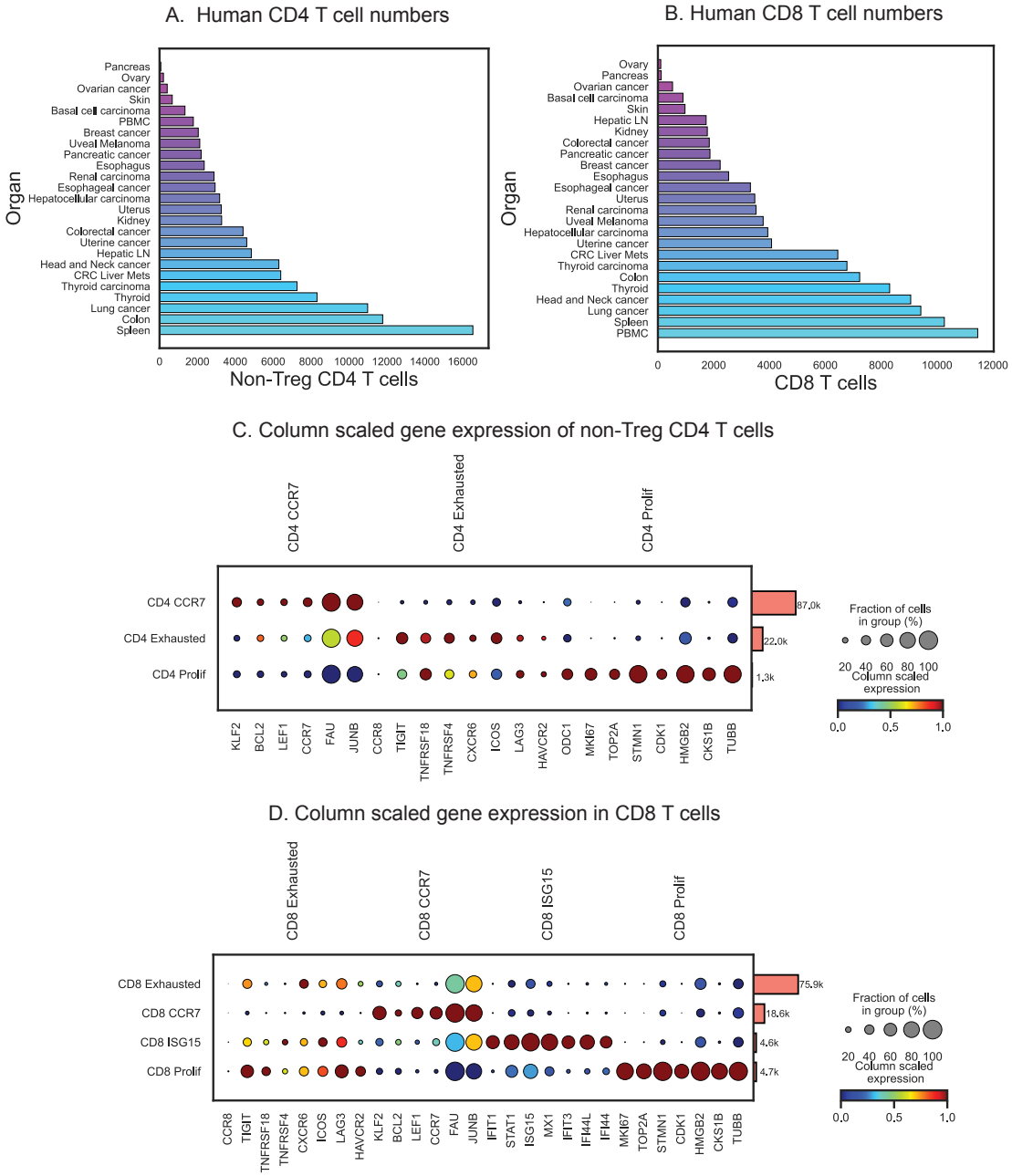



**Figure C.2: Human CD4 non-Treg and CD8 T cell meta-atlases**. Numbers of T cells used to generate the human CD4 (A) and CD8 (B) T cell meta-atlases. Scaled gene expression Dot plots showing markers associated with different T cell subpopulations (C, D).

# Bibliography


Jonathan M Kocarnik, Kelly Compton, Frances E Dean, Weijia Fu, Brian L Gaw, James D Harvey, Hannah Jacqueline Henrikson, Dan Lu, Alyssa Pennini, Rixing Xu, et al. Cancer incidence, mortality, years of life lost, years lived with disability, and disability-adjusted life years for 29 cancer groups from 2010 to 2019: A systematic analysis for the global burden of disease study 2019. *JAMA Oncology*, 8(3):420–444, 2022.

Kyle J Foreman, Neal Marquez, Andrew Dolgert, Kai Fukutaki, Nancy Fullman, Madeline McGaughey, Martin A Pletcher, Amanda E Smith, Kendrick Tang, Chun-Wei Yuan, et al. Forecasting life expectancy, years of life lost, and all-cause and cause-specific mortality for 250 causes of death: Reference and alternative scenarios for 2016–40 for 195 countries and territories. *The Lancet*, 392(10159):2052–2090, 2018.

Yuanyuan Zhang and Zemin Zhang. The history and advances in cancer immunotherapy: Understanding the characteristics of tumor-infiltrating immune cells and their therapeutic implications. *Cellular & Molecular Immunology*, 17(8):807–821, 2020.

Yan Tie, Fan Tang, Yu-quan Wei, and Xia-wei Wei. Immunosuppressive cells in cancer: Mechanisms and potential therapeutic targets. *Journal of Hematology & Oncology*, 15(1): 61, 2022.

Daniil Shevyrev and Valeriy Tereshchenko. Treg heterogeneity, function, and homeostasis. *Frontiers in Immunology*, 10:3100, 2020.

Isabella WY Mak, Nathan Evaniew, and Michelle Ghert. Lost in translation: Animal models and clinical trials in cancer treatment. *American Journal of Translational Research*, 6(2): 114, 2014.

Arthur W Lambert, Diwakar R Pattabiraman, and Robert A Weinberg. Emerging biological principles of metastasis. *Cell*, 168(4):670–691, 2017.

CDC. How tobacco smoke causes disease: The biology and behavioral basis for smoking-attributable disease: A report of the surgeon general. *Atlanta, GA: US Department of Health and Human Services*, 500:647–54, 2010.

Clarke Brian Blackadar. Historical review of the causes of cancer. *World Journal of Clinical Oncology*, 7(1):54, 2016.

Sam Behjati, Gunes Gundem, David C Wedge, Nicola D Roberts, Patrick S Tarpey, Susanna L Cooke, Peter Van Loo, Ludmil B Alexandrov, Manasa Ramakrishna, Helen Davies, et al. Mutational signatures of ionizing radiation in second malignancies. *Nature Communications*, 7(1):12605, 2016.

Brian E Henderson and Heather Spencer Feigelson. Hormonal carcinogenesis. *Carcinogenesis*, 21(3):427–433, 2000.

Mark Schiffman, Philip E Castle, Jose Jeronimo, Ana C Rodriguez, and Sholom Wacholder. Human papillomavirus and cervical cancer. *The Lancet*, 370(9590):890–907, 2007.

Geoffrey M Cooper and Roberte Hausman. A molecular approach. *The Cell. 2nd ed. Sunderland, MA: Sinauer Associates*, 2000.

Douglas Hanahan and Robert A Weinberg. Hallmarks of cancer: The next generation. *Cell*, 144(5):646–674, 2011.

Henk MW Verheul and Herbert M Pinedo. The role of vascular endothelial growth factor (VEGF) in tumor angiogenesis and early clinical development of VEGF Receptor kinase inhibitors. *Clinical Breast Cancer*, 1:S80–S84, 2000.

Maria V Liberti and Jason W Locasale. The Warburg effect: How does it benefit cancer cells? *Trends in Biochemical Sciences*, 41(3):211–218, 2016.

Joy X Wang, Stephen YC Choi, Xiaojia Niu, Ning Kang, Hui Xue, James Killam, and Yuzhuo Wang. Lactic acid and an acidic tumor microenvironment suppress anticancer immunity. *International Journal of Molecular Sciences*, 21(21):8363, 2020a.

Jean S Marshall, Richard Warrington, Wade Watson, and Harold L Kim. An introduction to immunology and immunopathology. *Allergy, Asthma & Clinical Immunology*, 14(2):1–10, 2018.

Maelig G Morvan and Lewis L Lanier. NK cells and cancer: You can teach innate cells new tricks. *Nature Reviews Cancer*, 16(1):7–19, 2016.

Daniel S Chen and Ira Mellman. Oncology meets immunology: The cancer-immunity cycle. *Immunity*, 39(1):1–10, 2013.

Paola Bonaventura, Tala Shekarian, Vincent Alcazer, Jenny Valladeau-Guilemond, Sandrine Valsesia-Wittmann, Sebastian Amigorena, Christophe Caux, and Stéphane Depil. Cold tumors: A therapeutic challenge for immunotherapy. *Frontiers in Immunology*, 10:168, 2019.

Y Jiang, Y Li, and B Zhu. T-cell exhaustion in the tumor microenvironment. *Cell Death & Disease*, 6(6):e1792–e1792, 2015.

Shimon Sakaguchi, Noriko Sakaguchi, Masanao Asano, Misako Itoh, and Masaaki Toda. Immunologic self-tolerance maintained by activated T cells expressing IL-2 receptor alpha-chains (CD25). Breakdown of a single mechanism of self-tolerance causes various autoimmune diseases. *Journal of Immunology (Baltimore, Md.: 1950)*, 155(3):1151–1164, 1995.

Shimon Sakaguchi, Tomoyuki Yamaguchi, Takashi Nomura, and Masahiro Ono. Regulatory T cells and immune tolerance. *Cell*, 133(5):775–787, 2008.

Angela M Thornton and Ethan M Shevach. Suppressor effector function of CD4+ CD25+ immunoregulatory T cells is antigen nonspecific. *The Journal of Immunology*, 164(1): 183–190, 2000.

Piotr Trzonkowski, Ewa Szmit, Jolanta Myśliwska, Anita Dobyszuk, and Andrzej Myśliwski. CD4+ CD25+ T regulatory cells inhibit cytotoxic activity of T CD8+ and NK lymphocytes in the direct cell-to-cell interaction. *Clinical Immunology*, 112(3):258–267, 2004.

Madhav D Sharma, Babak Baban, Phillip Chandler, De-Yan Hou, Nagendra Singh, Hideo Yagita, Miyuki Azuma, Bruce R Blazar, Andrew L Mellor, David H Munn, et al. Plasmacytoid Dendritic cells from mouse tumor-draining lymph nodes directly activate mature Tregs via indoleamine 2, 3-dioxygenase. *The Journal of Clinical Investigation*, 117 (9):2570–2582, 2007.

Nicholas C DeVito, Michael P Plebanek, Bala Theivanthiran, and Brent A Hanks. Role of tumor-mediated dendritic cell tolerization in immune evasion. *Frontiers in Immunology*, 10: 2876, 2019.

Yueyun Pan, Yinda Yu, Xiaojian Wang, and Ting Zhang. Tumor-associated macrophages in tumor immunity. *Frontiers in Immunology*, 11:583084, 2020.

Claire E Lewis and Jeffrey W Pollard. Distinct role of macrophages in different tumor microenvironments. *Cancer Research*, 66(2):605–612, 2006.

Yibing Chen, Yucen Song, Wei Du, Longlong Gong, Haocai Chang, and Zhengzhi Zou. Tumor-associated Macrophages: An accomplice in solid tumor progression. *Journal of Biomedical Science*, 26(1):1–13, 2019a.

Young-June Kim, Su-Jung Park, and Hal E Broxmeyer. Phagocytosis, a potential mechanism for Myeloid-derived suppressor cell regulation of CD8+ T cell function mediated through Programmed cell death-1 and Programmed cell death-1 ligand interaction. *The Journal of Immunology*, 187(5):2291–2301, 2011.

Julie R Brahmer, Charles G Drake, Ira Wollner, John D Powderly, Joel Picus, William H Sharfman, Elizabeth Stankevich, Alice Pons, Theresa M Salay, Tracee L McMiller, et al. Phase I study of single-agent anti–programmed death-1 (MDX-1106) in refractory solid tumors: Safety, clinical activity, pharmacodynamics, and immunologic correlates. *Journal of Clinical Oncology*, 28(19):3167, 2010.

Kei Muro, Yung-Jue Bang, Veena Shankaran, Ravit Geva, Daniel Virgil Thomas Catenacci, Shilpa Gupta, Joseph Paul Eder, Raanan Berger, Edward J Gonzalez, Archana Ray, et al. Relationship between PD-L1 expression and clinical outcomes in patients (Pts) with advanced gastric cancer treated with the anti-PD-1 monoclonal antibody pembrolizumab (Pembro; MK-3475) in KEYNOTE-012., 2015.

Peter H O'Donnell, Elizabeth R Plimack, Joaquim Bellmunt, Raanan Berger, Robert B Montgomery, Karl Heath, Marisa Dolled-Filhart, Kumudu Pathiraja, Christine K Gause, Jonathan D Cheng, et al. Pembrolizumab (Pembro; MK-3475) for advanced urothelial cancer: Results of a phase IB study., 2015.

Steven J O'Day, Michele Maio, Vanna Chiarion-Sileni, Thomas F Gajewski, Hubert Pehamberger, Igor N Bondarenko, P Queirolo, Lotta Lundgren, Sergei Mikhailov, Laslo Roman, et al. Efficacy and safety of Ipilimumab monotherapy in patients with pretreated advanced melanoma: A multicenter single-arm phase II study. *Annals of Oncology*, 21(8): 1712–1717, 2010.

Jedd D Wolchok, Bart Neyns, Gerald Linette, Sylvie Negrier, Jose Lutzky, Luc Thomas, William Waterfield, Dirk Schadendorf, Michael Smylie, Troy Guthrie, et al. Ipilimumab monotherapy in patients with pretreated advanced melanoma: A randomised, double-blind, multicentre, phase 2, dose-ranging study. *The Lancet Oncology*, 11(2):155–164, 2010.

Padmanee Sharma, Siwen Hu-Lieskovan, Jennifer A Wargo, and Antoni Ribas. Primary, adaptive, and acquired resistance to cancer immunotherapy. *Cell*, 168(4):707–723, 2017.

C Schaefer, GG Kim, A Albers, K Hoermann, EN Myers, and TL Whiteside. Characteristics of CD4+ CD25+ regulatory T cells in the peripheral circulation of patients with head and neck cancer. *British Journal of Cancer*, 92(5):913–920, 2005.

Udaya K Liyanage, Todd T Moore, Hong-Gu Joo, Yoshiyuki Tanaka, Virginia Herrmann, Gerard Doherty, Jeffrey A Drebin, Steven M Strasberg, Timothy J Eberlein, Peter S Goedegebuure, et al. Prevalence of regulatory T cells is increased in peripheral blood and tumor microenvironment of patients with pancreas or breast adenocarcinoma. *The Journal of Immunology*, 169(5):2756–2761, 2002.

Anna Maria Wolf, Dominik Wolf, Michael Steurer, Guenther Gastl, Eberhard Gunsilius, and Beatrix Grubeck-Loebenstein. Increase of regulatory T cells in the peripheral blood of cancer patients. *Clinical Cancer Research*, 9(2):606–612, 2003.

Lars A Ormandy, Tina Hillemann, Heiner Wedemeyer, Michael P Manns, Tim F Greten, and Firouzeh Korangy. Increased populations of regulatory T cells in peripheral blood of patients with hepatocellular carcinoma. *Cancer Research*, 65(6):2457–2464, 2005.

Nobuyoshi Hiraoka, Kaoru Onozato, Tomoo Kosuge, and Setsuo Hirohashi. Prevalence of FOXP3+ regulatory T cells increases during the progression of pancreatic ductal adenocarcinoma and its premalignant lesions. *Clinical Cancer Research*, 12(18):5423–5434, 2006.

Tyler J Curiel, George Coukos, Linhua Zou, Xavier Alvarez, Pui Cheng, Peter Mottram, Melina Evdemon-Hogan, Jose R Conejo-Garcia, Lin Zhang, Matthew Burow, et al. Specific recruitment of regulatory T cells in ovarian carcinoma fosters immune privilege and predicts reduced survival. *Nature Medicine*, 10(9):942–949, 2004.

Stephen B Bates, Gaynor J Fox, Russell D Han, Cheng Leek, Adrian L Garcia, Jose F Harris, and Alison H Banham. Quantification of regulatory T cells enables the identification of high-risk breast cancer patients and those at risk of late relapse. *Journal of Clinical Oncology*, 24(34):5373–5380, 2006.

Tetsuro Sasada, Motohide Kimura, Yuka Yoshida, Michiyuki Kanai, and Arimichi Takabayashi. CD4+ CD25+ regulatory T cells in patients with gastrointestinal malignancies: Possible involvement of regulatory T cells in disease progression. *Cancer: Interdisciplinary International Journal of the American Cancer Society*, 98(5):1089–1099, 2003.

Sundee Dees, Rajkumar Ganesan, Sanjaya Singh, and Iqbal S Grewal. Regulatory T cell targeting in cancer: Emerging strategies in immunotherapy. *European Journal of Immunology*, 51(2):280–291, 2021.

Séverine Le Bras, Raif S Geha, et al. IPEX and the role of Foxp3 in the development and function of human Tregs. *The Journal of clinical investigation*, 116(6):1473–1475, 2006.

Audrey Nosbaum, Nicolas Prevel, Hong-An Truong, Pooja Mehta, Monika Ettinger, Tiffany C Scharschmidt, Niwa H Ali, Mariela L Pauli, Abul K Abbas, and Michael D Rosenblum. Cutting edge: Regulatory T cells facilitate cutaneous wound healing. *The Journal of Immunology*, 196(5):2010–2014, 2016.

Mary E Brunkow, Eric W Jeffery, Kathryn A Hjerrild, Bryan Paeper, Lisa B Clark, Sue-Ann Yasayko, J Erby Wilkinson, David Galas, Steven F Ziegler, and Fred Ramsdell. Disruption of a new forkhead/winged-helix protein, scurfin, results in the fatal lymphoproliferative disorder of the scurfy mouse. *Nature Genetics*, 27(1):68–73, 2001.

Craig L Bennett, Jacinda Christie, Fred Ramsdell, Mary E Brunkow, Polly J Ferguson, Luke Whitesell, Thaddeus E Kelly, Frank T Saulsbury, Phillip F Chance, and Hans D Ochs. The immune dysregulation, polyendocrinopathy, enteropathy, X-linked syndrome (IPEX) is caused by mutations of FOXP3. *Nature Genetics*, 27(1):20–21, 2001.

Johan Verhagen, Mübeccel Akdis, Claudia Traidl-Hoffmann, Peter Schmid-Grendelmeier, DirkJan Hijnen, Edward F Knol, Heidrun Behrendt, Kurt Blaser, and Cezmi A Akdis. Absence of T-regulatory cell expression and function in atopic dermatitis skin. *Journal of Allergy and Clinical Immunology*, 117(1):176–183, 2006.

Xiaomei Li, Xiangpei Li, Long Qian, Guosheng Wang, Hong Zhang, Xiaoqiu Wang, Ke Chen, Zhimin Zhai, Qing Li, Yiping Wang, et al. T regulatory cells are markedly diminished in diseased salivary glands of patients with primary sjögren's syndrome. *The Journal of Rheumatology*, 34(12):2438–2445, 2007.

Li-jun Chi, Hua-bing Wang, Ying Zhang, and Wei-zhi Wang. Abnormality of circulating CD4+ CD25+ regulatory T cell in patients with Guillain–Barré syndrome. *Journal of Neuroimmunology*, 192(1-2):206–214, 2007.

Yifang Hu, Lijuan Zhang, Huanhuan Chen, Xiaoyun Liu, Xuqin Zheng, He Shi, Lin Jiang, and Dai Cui. Analysis of regulatory T cell subsets and their expression of Helios and PD-1 in patients with Hashimoto thyroiditis. *International Journal of Endocrinology*, 2019, 2019.

Wonyong Lee and Gap Ryol Lee. Transcriptional regulation and development of regulatory T cells. *Experimental & Molecular Medicine*, 50(3):e456–e456, 2018.

Nicola Gagliani, Chiara F Magnani, Samuel Huber, Monica E Gianolini, Mauro Pala, Paula Licona-Limon, Binggege Guo, De'Broski R Herbert, Alessandro Bulfone, Filippo Trentini, et al. Coexpression of CD49b and LAG-3 identifies human and mouse T regulatory type 1 cells. *Nature Medicine*, 19(6):739–746, 2013.

Rianne Opstelten, Sander de Kivit, Manon C Slot, Maartje van den Biggelaar, Dorota Iwaszkiewicz-Grześ, Mateusz Gliwiński, Andrew M Scott, Bianca Blom, Piotr Trzonkowski, Jannie Borst, et al. GPA33: A marker to identify stable human regulatory T cells. *The Journal of Immunology*, 204(12):3139–3148, 2020.

Mahesh Yadav, Cedric Louvet, Dan Davini, James M Gardner, Marc Martinez-Llordella, Samantha Bailey-Bucktrout, Bryan A Anthony, Francis M Sverdrup, Richard Head, Daniel J Kuster, et al. Neuropilin-1 distinguishes natural and inducible regulatory T cells among regulatory T cell subsets in vivo. *Journal of Experimental Medicine*, 209(10): 1713–1722, 2012.

Pierre Milpied, Amédée Renand, Julie Bruneau, Daniella A Mendes-Da-Cruz, Sébastien Jacquelin, Vahid Asnafi, Marie-Thérèse Rubio, Elizabeth MacIntyre, Yves Lepelletier, and Olivier Hermine. Neuropilin-1 is not a marker of human Foxp3+ Treg. *European Journal of Immunology*, 39(6):1466–1471, 2009.

Kailash Singh, Marcus Hjort, Lina Thorvaldson, and Stellan Sandler. Concomitant analysis of Helios and Neuropilin-1 as a marker to detect thymic derived regulatory T cells in naive mice. *Scientific Reports*, 5(1):7767, 2015.

Tatiana Akimova, Ulf H Beier, Liqing Wang, Matthew H Levine, and Wayne W Hancock. Helios expression is a marker of T cell activation and proliferation. *PloS One*, 6(8):e24226, 2011.

Alvin Pratama, Alexandra Schnell, Diane Mathis, and Christophe Benoist. Developmental and cellular age direct conversion of CD4+ T cells into ROR$\gamma$+ or Helios+ colon Treg cells. *Journal of Experimental Medicine*, 217(1), 2020.

Maurus de la Rosa, Sascha Rutz, Heike Dorninger, and Alexander Scheffold. Interleukin-2 is essential for CD4+ CD25+ regulatory T cell function. *European Journal of Immunology*, 34(9):2480–2488, 2004.

Pushpa Pandiyan, Lixin Zheng, Satoru Ishihara, Jennifer Reed, and Michael J Lenardo. CD4+ CD25+ Foxp3+ regulatory T cells induce cytokine deprivation–mediated apoptosis of effector CD4+ T cells. *Nature Immunology*, 8(12):1353–1362, 2007.

Dong-Mei Zhao, Angela M Thornton, Richard J DiPaolo, and Ethan M Shevach. Activated CD4+ CD25+ T cells selectively kill B lymphocytes. *Blood*, 107(10):3925–3932, 2006.

Xuefang Cao, Sheng F Cai, Todd A Fehniger, Jiling Song, Lynne I Collins, David R Piwnica-Worms, and Timothy J Ley. Granzyme B and perforin are important for regulatory T cell-mediated suppression of tumor clearance. *Immunity*, 27(4):635–646, 2007.

Maykel Arias, Luis Martinez-Lostao, Llipsy Santiago, Angel Ferrandez, David J Granville, and Julian Pardo. The untold story of granzymes in oncoimmunology: Novel opportunities with old acquaintances. *Trends in Cancer*, 3(6):407–422, 2017.

Akio Ohta and Michail Sitkovsky. Extracellular adenosine-mediated modulation of regulatory T cells. *Frontiers in Immunology*, 5:304, 2014.

Bo-Jin Chen, Jing-Wen Zhao, Da-Hong Zhang, Ai-Hong Zheng, and Guo-Qing Wu. Immunotherapy of cancer by targeting regulatory T cells. *International Immunopharmacology*, 104:108469, 2022.

Joshua M Moreau, Maria Velegraki, Chelsea Bolyard, Michael D Rosenblum, and Zihai Li. Transforming growth factor–$\beta$1 in regulatory T cell biology. *Science Immunology*, 7(69): eabi4613, 2022.

Ashutosh Chaudhry, Robert M Samstein, Piper Treuting, Yuqiong Liang, Marina C Pils, Jan-Michael Heinrich, Robert S Jack, F Thomas Wunderlich, Jens C Brüning, Werner Müller, et al. Interleukin-10 signaling in regulatory T cells is required for suppression of Th17 cell-mediated inflammation. *Immunity*, 34(4):566–578, 2011.

Lauren W Collison, Creg J Workman, Timothy T Kuo, Kelli Boyd, Yao Wang, Kate M Vignali, Richard Cross, David Sehy, Richard S Blumberg, and Dario AA Vignali. The inhibitory cytokine IL-35 contributes to regulatory T-cell function. *Nature*, 450(7169):566–569, 2007.

Lukas Cederbom, Håkan Hall, and Fredrik Ivars. CD4+ CD25+ regulatory T cells down-regulate co-stimulatory molecules on antigen-presenting cells. *European Journal of Immunology*, 30(6):1538–1543, 2000.

Murat Tekguc, James Badger Wing, Motonao Osaki, Jia Long, and Shimon Sakaguchi. Treg-expressed CTLA-4 depletes CD80/CD86 by trogocytosis, releasing free PD-L1 on antigen-presenting cells. *Proceedings of the National Academy of Sciences*, 118(30): e2023739118, 2021.

Ursula Grohmann, Ciriana Orabona, Francesca Fallarino, Carmine Vacca, Filippo Calcinaro, Alberto Falorni, Paola Candeloro, Maria L Belladonna, Roberta Bianchi, Maria C Fioretti, et al. CTLA-4–Ig regulates tryptophan catabolism in vivo. *Nature Immunology*, 3(11): 1097–1101, 2002.

Maria Laura Belladonna, Paolo Puccetti, Ciriana Orabona, Francesca Fallarino, Carmine Vacca, Claudia Volpi, Stefania Gizzi, Maria Teresa Pallotta, Maria Cristina Fioretti, and Ursula Grohmann. Immunosuppression via tryptophan catabolism: The role of kynurenine pathway enzymes. *Transplantation*, 84(1):S17–S20, 2007.

Martina Lubrano di Ricco, Emilie Ronin, Davi Collares, Jordane Divoux, Sylvie Grégoire, Harald Wajant, Tomás Gomes, Yenkel Grinberg-Bleyer, Véronique Baud, Gilles Marodon, et al. Tumor necrosis factor receptor family costimulation increases regulatory T-cell activation and function via NF-$\kappa$B. *European Journal of Immunology*, 50(7):972–985, 2020.

Ajithkumar Vasanthakumar, Yang Liao, Peggy Teh, Maria F Pascutti, Anna E Oja, Alexandra L Garnham, Renee Gloury, Jessica C Tempany, Tom Sidwell, Eloy Cuadrado, et al. The TNF receptor superfamily-NF-$\kappa$B axis is critical to maintain effector regulatory T cells in lymphoid and non-lymphoid tissues. *Cell Reports*, 20(12):2906–2920, 2017.

Galina Zhulai and Eugenia Oleinik. Targeting regulatory T cells in anti-PD-1/PD-L1 cancer immunotherapy. *Scandinavian Journal of Immunology*, 95(3):e13129, 2022.

Jian Wang, Taku Yoshida, Fumio Nakaki, Hiroshi Hiai, Taku Okazaki, and Tasuku Honjo. Establishment of NOD-Pdcd1-/-mice as an efficient animal model of type I diabetes. *Proceedings of the National Academy of Sciences*, 102(33):11823–11828, 2005.

Giorgia Fanelli, Marco Romano, Estefania Nova-Lamperti, Mariana Werner Sunderland, Alessandra Nerviani, Cristiano Scottà, Michele Bombardieri, Sergio A Quezada, Steven H Sacks, Randolph J Noelle, et al. PD-L1 signaling on human memory CD4+ T cells induces a regulatory phenotype. *PLoS Biology*, 19(4):e3001199, 2021.

Hyo Jin Park, Joon Seok Park, Yun Hee Jeong, Jimin Son, Young Ho Ban, Byoung-Hee Lee, Lieping Chen, Jun Chang, Doo Hyun Chung, Inhak Choi, et al. PD-1 upregulated on regulatory T cells during chronic virus infection enhances the suppression of CD8+ T cell immune response via the interaction with PD-L1 expressed on CD8+ T cells. *The Journal of Immunology*, 194(12):5801–5811, 2015.

Bruce J MacLachlan, Georgina H Mason, Alexander Greenshields-Watson, Frederic Triebel, Awen Gallimore, David K Cole, and Andrew Godkin. Molecular characterization of HLA class II binding to the LAG-3 T cell co-inhibitory receptor. *European Journal of Immunology*, 51(2):331–341, 2021.

Ching-Tai Huang, Creg J Workman, Dallas Flies, Xiaoyu Pan, Aimee L Marson, Gang Zhou, Edward L Hipkiss, Sowmya Ravi, Jeanne Kowalski, Hyam I Levitsky, et al. Role of LAG-3 in regulatory T cells. *Immunity*, 21(4):503–513, 2004.

Bitao Liang, Craig Workman, Janine Lee, Claude Chew, Benjamin M Dale, Lucrezia Colonna, Marcella Flores, Nianyu Li, Edina Schweighoffer, Steven Greenberg, et al. Regulatory T cells inhibit Dendritic cells by lymphocyte activation gene-3 engagement of MHC class II. *The Journal of Immunology*, 180(9):5916–5926, 2008.

Takumi Maruhashi, Daisuke Sugiura, Il-mi Okazaki, Kenji Shimizu, Takeo K Maeda, Jun Ikubo, Harunori Yoshikawa, Katsumi Maenaka, Naozumi Ishimaru, Hidetaka Kosako, et al. Binding of LAG-3 to stable peptide-MHC class II limits T cell function and suppresses autoimmunity and anti-cancer immunity. *Immunity*, 55(5):912–924, 2022.

Thomas Duhen, Rebekka Geiger, David Jarrossay, Antonio Lanzavecchia, and Federica Sallusto. Production of Interleukin 22 but not Interleukin 17 by a subset of human skin-homing memory T cells. *Nature Immunology*, 10(8):857–863, 2009.

Andrea Iellem, Margherita Mariani, Rosmarie Lang, Helios Recalde, Paola Panina-Bordignon, Francesco Sinigaglia, and Daniele D'Ambrosio. Unique chemotactic response profile and specific expression of chemokine receptors CCR4 and CCR8 by CD4+ CD25+ regulatory T cells. *The Journal of Experimental Medicine*, 194(6):847–854, 2001.

Blythe D Sather, Piper Treuting, Nikole Perdue, Mike Miazgowicz, Jason D Fontenot, Alexander Y Rudensky, and Daniel J Campbell. Altering the distribution of Foxp3+ regulatory T cells results in tissue-specific inflammatory disease. *The Journal of Experimental Medicine*, 204(6):1335–1347, 2007.

Shingo Maeda, Kohei Murakami, Akiko Inoue, Tomohiro Yonezawa, and Naoaki Matsuki. Ccr4 blockade depletes regulatory T cells and prolongs survival in a canine model of bladder cancer. *Cancer Immunology Research*, 7(7):1175–1187, 2019.

Koji Kurose, Yoshihiro Ohue, Eiichi Sato, Akira Yamauchi, Shingo Eikawa, Midori Isobe, Yumi Nishio, Akiko Uenaka, Mikio Oka, and Eiichi Nakayama. Increase in activated Treg in TIL in lung cancer and in vitro depletion of Treg by ADCC using an antihuman CCR4 mAb (KM2760). *Journal of Thoracic Oncology*, 10(1):74–83, 2015a.

Daisuke Sugiyama, Hiroyoshi Nishikawa, Yuka Maeda, Megumi Nishioka, Atsushi Tanemura, Ichiro Katayama, Sachiko Ezoe, Yuzuru Kanakura, Eiichi Sato, Yasuo Fukumori, et al. Anti-CCR4 mAb selectively depletes effector-type FoxP3+ CD4+ regulatory T cells, evoking antitumor immune responses in humans. *Proceedings of the National Academy of Sciences*, 110(44):17945–17950, 2013.

Koji Kurose, Yoshihiro Ohue, Hisashi Wada, Shinsuke Iida, Takashi Ishida, Takashi Kojima, Toshihiko Doi, Susumu Suzuki, Midori Isobe, Takeru Funakoshi, et al. Phase Ia study of FoxP3+ CD4 Treg depletion by infusion of a humanized anti-CCR4 antibody, KW-0761, in cancer patients. *Clinical Cancer Research*, 21(19):4327–4336, 2015b.

Yuka Maeda, Hisashi Wada, Daisuke Sugiyama, Takuro Saito, Takuma Irie, Kota Itahashi, Kodai Minoura, Susumu Suzuki, Takashi Kojima, Kazuhiro Kakimi, et al. Depletion of central memory CD8+ T cells might impede the antitumor therapeutic effect of Mogamulizumab. *Nature Communications*, 12(1):7280, 2021.

Onur Boyman and Jonathan Sprent. The role of Interleukin-2 during homeostasis and activation of the immune system. *Nature Reviews Immunology*, 12(3):180–190, 2012.

Rodrigo Nalio Ramos, Carine Ervolino Oliveira, Thais Helena Gasparoto, Tatiana Salles de Souza Malaspina, Eduardo Bertoli Belai, Karen Angélica Cavassani, Gustavo Pompermaier Garlet, João Santana da Silva, and Ana Paula Campanelli. CD25+ T cell depletion impairs murine squamous cell carcinoma development via modulation of antitumor immune responses. *Carcinogenesis*, 33(4):902–909, 2012.

Masanori Onda, Kazuto Kobayashi, and Ira Pastan. Depletion of regulatory T cells in tumors with an anti-CD25 immunotoxin induces CD8 T cell-mediated systemic antitumor immunity. *Proceedings of the National Academy of Sciences*, 116(10):4575–4582, 2019.

Karsten Mahnke, Kurt Schönfeld, Sabine Fondel, Sabine Ring, Svetlana Karakhanova, Katharina Wiedemeyer, Tanja Bedke, Theron Scott Johnson, Volker Storn, Sonja Schallenberg, et al. Depletion of CD4+ CD25+ human regulatory T cells in vivo: kinetics of Treg depletion and alterations in immune functions in vivo and in vitro. *International Journal of Cancer*, 120(12):2723–2733, 2007.

Frederick Arce Vargas, Andrew JS Furness, Isabelle Solomon, Kroopa Joshi, Leila Mekkaoui, Marta H Lesko, Enrique Miranda Rota, Rony Dahan, Andrew Georgiou, Anna Sledzinska, et al. Fc-optimized anti-CD25 depletes tumor-infiltrating regulatory T cells and synergizes with PD-1 blockade to eradicate established tumors. *Immunity*, 46(4):577–586, 2017.

Isabelle Solomon, Maria Amann, Anne Goubier, Frederick Arce Vargas, Dimitrios Zervas, Chen Qing, Jake Y Henry, Ehsan Ghorani, Ayse U Akarca, Teresa Marafioti, et al. CD25-Treg-depleting antibodies preserving IL-2 signaling on effector T cells enhance effector activation and antitumor immunity. *Nature Cancer*, 1(12):1153–1166, 2020.

Marit J Van Elsas, Johan MS Van der Schoot, Alexander Bartels, Kas Steuten, Duco Van Dalen, Zacharias Wijfjes, Carl G Figdor, Thorbald Van Hall, Sjoerd H Van der Burg, Martijn Verdoes, et al. Regulatory T cell depletion using a CRISPR Fc-optimized CD25 antibody. *International Journal of Molecular Sciences*, 23(15):8707, 2022.

Chuanwu Wang, Jee H Lee, and Chang H Kim. Optimal population of FoxP3+ T cells in tumors requires an antigen priming-dependent trafficking receptor switch. *PloS One*, 7(1): e30793, 2012.

Sarah K Whiteside, Francis M Grant, David S Gyori, Alberto G Conti, Charlotte J Imianowski, Paula Kuo, Rabab Nasrallah, Firas Sadiyah, Sergio A Lira, Frank Tacke, et al. CCR8 marks highly suppressive Treg cells within tumours but is dispensable for their accumulation and suppressive function. *Immunology*, 163(4):512–520, 2021.

Angela M Magnuson, Evgeny Kiner, Ayla Ergun, Jun Seok Park, Natasha Asinovski, Adriana Ortiz-Lopez, Aoife Kilcoyne, Elisa Paoluzzi-Tomada, Ralph Weissleder, Diane Mathis, et al. Identification and validation of a tumor-infiltrating Treg transcriptional signature conserved

across species and tumor types. *Proceedings of the National Academy of Sciences*, 115 (45):E10672–E10681, 2018.

Dev Bhatt, Boxi Kang, Deepali Sawant, Liangtao Zheng, Kristy Perez, Zhiyu Huang, Laura Sekirov, Dan Wolak, Julie Y Huang, Xian Liu, et al. STARTRAC analyses of scRNAseq data from tumor models reveal T cell dynamics and therapeutic targets. *Journal of Experimental Medicine*, 218(6):e20201329, 2021.

Joseph R Campbell, Bryan R McDonald, Paul B Mesko, Nathan O Siemers, Priti B Singh, Mark Selby, Tim W Sproul, Alan J Korman, Logan M Vlach, Jeff Houser, et al. Fc-optimized anti-CCR8 antibody depletes regulatory T cells in human tumor models. *Cancer Research*, 81(11):2983–2994, 2021.

Helena Van Damme, Bruno Dombrecht, Máté Kiss, Heleen Roose, Elizabeth Allen, Eva Van Overmeire, Daliya Kancheva, Liesbet Martens, Aleksandar Murgaski, Pauline Madeleine Rachel Bardet, et al. Therapeutic depletion of CCR8+ tumor-infiltrating regulatory T cells elicits antitumor immunity and synergizes with anti-PD-1 therapy. *Journal for Immunotherapy of Cancer*, 9(2), 2021.

Yujiro Kidani, Wataru Nogami, Yoshiaki Yasumizu, Atsunari Kawashima, Atsushi Tanaka, Yudai Sonoda, Yumi Tona, Kunitaka Nashiki, Reimi Matsumoto, Masaki Hagiwara, et al. CCR8-targeted specific depletion of clonally expanded Treg cells in tumor tissues evokes potent tumor immunity with long-lasting memory. *Proceedings of the National Academy of Sciences*, 119(7):e2114282119, 2022.

Yiftah Barsheshet, Gizi Wildbaum, Eran Levy, Alon Vitenshtein, Chika Akinseye, Jeremy Griggs, Sergio A Lira, and Nathan Karin. CCR8+ FOXP3+ Treg cells as master drivers of immune regulation. *Proceedings of the National Academy of Sciences*, 114(23):6086–6091, 2017.

George Plitas, Catherine Konopacki, Kenmin Wu, Paula D Bos, Monica Morrow, Ekaterina V Putintseva, Dmitriy M Chudakov, and Alexander Y Rudensky. Regulatory T cells exhibit distinct features in human breast cancer. *Immunity*, 45(5):1122–1134, 2016.

Benjamin Kuehnemuth, Ignazio Piseddu, Gabriela M Wiedemann, Michael Lauseker, Christina Kuhn, Simone Hofmann, Elisa Schmoeckel, Stefan Endres, Doris Mayr, Udo Jeschke, et al. CCL1 is a major regulatory T cell attracting factor in human breast cancer. *BMC Cancer*, 18(1):1–6, 2018.

Gang Yi, Shiwei Guo, Wenyu Liu, Huan Wang, Rendong Liu, Andy Tsun, Gang Jin, and Bin Li. Identification and functional analysis of heterogeneous FOXP3+ Treg cell subpopulations in human pancreatic ductal adenocarcinoma. *Science Bulletin*, 63(15): 972–981, 2018.

Tao Wang, Quan Zhou, Han Zeng, Hongyu Zhang, Zhaopei Liu, Jialiang Shao, Zewei Wang, Ying Xiong, Jiajun Wang, Qi Bai, et al. CCR8 blockade primes anti-tumor immunity through intratumoral regulatory T cells destabilization in muscle-invasive bladder cancer. *Cancer Immunology, Immunotherapy*, 69:1855–1867, 2020b.

Miya Haruna, Azumi Ueyama, Yoko Yamamoto, Michinari Hirata, Kumiko Goto, Hiroshi Yoshida, Naoko Higuchi, Tetsuya Yoshida, Yujiro Kidani, Yamami Nakamura, et al. The

impact of CCR8+ regulatory T cells on cytotoxic T cell function in human lung cancer. *Scientific Reports*, 12(1):5377, 2022.

Jérôme Giustiniani, Gabor Dobos, Hélène Moins-Teisserenc, Tiago Eustaquio, Maxime Battistella, Nicolas Ortonne, Caroline Ram-Wolff, Jean-David Bouaziz, Anne Marie-Cardine, Samia Mourah, et al. CCR8 is a new therapeutic target in cutaneous T-cell lymphomas. *Blood Advances*, 6(11):3507–3512, 2022.

Jessica D Weaver, Edward C Stack, Joshua A Buggé, Changyun Hu, Lara McGrath, Amy Mueller, Masie Wong, Boris Klebanov, Tanzila Rahman, Rosemary Kaufman, et al. Differential expression of CCR8 in tumors versus normal tissue allows specific depletion of tumor-infiltrating T regulatory cells by GS-1811, a novel Fc-optimized anti-CCR8 antibody. *OncoImmunology*, 11(1):2141007, 2022.

Nicholas M Durham, Christopher J Nirschl, Christopher M Jackson, Jimmy Elias, Christina M Kochel, Robert A Anders, and Charles G Drake. Lymphocyte Activation Gene 3 (LAG-3) modulates the ability of CD4 T-cells to be suppressed in vivo. *PloS One*, 9(11):e109080, 2014.

Stephanie EA Burnell, Lorenzo Capitani, Bruce J MacLachlan, Georgina H Mason, Awen M Gallimore, and Andrew Godkin. Seven mysteries of LAG-3: A multi-faceted immune receptor of increasing complexity. *Immunotherapy Advances*, 2(1):ltab025, 2022.

Creg J Workman and Dario AA Vignali. Negative regulation of T cell homeostasis by lymphocyte activation gene-3 (CD223). *The Journal of Immunology*, 174(2):688–695, 2005.

Emanuela I Sega, Dennis B Leveson-Gower, Mareike Florek, Dominik Schneidawind, Richard H Luong, and Robert S Negrin. Role of lymphocyte activation gene-3 (Lag-3) in conventional and regulatory T cell function in allogeneic transplantation. *PloS One*, 9(1): e86551, 2014.

Qianxia Zhang, Maria Chikina, Andrea L Szymczak-Workman, William Horne, Jay K Kolls, Kate M Vignali, Daniel Normolle, Maria Bettini, Creg J Workman, and Dario AA Vignali. LAG3 limits regulatory T cell proliferation and function in autoimmune diabetes. *Science Immunology*, 2(9):eaah4569, 2017.

Zhi Li, Zewen K Tuong, Isaac Dean, Claire Willis, Fabrina Gaspal, Rémi Fiancette, Suaad Idris, Bethany Kennedy, John R Ferdinand, Ana Peñalver, et al. In vivo labeling reveals continuous trafficking of TCF-1+ T cells between tumor and lymphoid tissue. *Journal of Experimental Medicine*, 219(6), 2022.

Ryoyo Ikebuchi, Taiki Moriya, Mizuki Ueda, Ippei Yasuda, Yutaka Kusumoto, Tatyana Chtanova, and Michio Tomura. Cutting edge: Recruitment, retention, and migration underpin functional phenotypic heterogeneity of regulatory T cells in tumors. *The Journal of Immunology*, 207(3):771–776, 2021.

Sarah N Lauder, Bart Vanhaesebroeck, and Awen Gallimore. Sequential targeting of PI3K$\delta$ and LAG3 as an effective anti-cancer approach. *British Journal of Cancer*, 125(4):467–469, 2021.

Sarah Nicol Lauder, Kathryn Smart, Veerle Kersemans, Danny Allen, Jake Scott, Ana Pires, Stefan Milutinovic, Michelle Somerville, Sean Smart, Paul Kinchesh, et al. Enhanced antitumor immunity through sequential targeting of PI3K$\delta$ and LAG3. *Journal for Immunotherapy of Cancer*, 8(2), 2020.

Seng-Ryong Woo, Meghan E Turnis, Monica V Goldberg, Jaishree Bankoti, Mark Selby, Christopher J Nirschl, Matthew L Bettini, David M Gravano, Peter Vogel, Chih Long Liu, et al. Immune inhibitory molecules LAG-3 and PD-1 synergistically regulate T-cell function to promote tumoral immune escape. *Cancer Research*, 72(4):917–927, 2012.

Chiara Camisaschi, Chiara Casati, Francesca Rini, Michela Perego, Annamaria De Filippo, Frédéric Triebel, Giorgio Parmiani, Filiberto Belli, Licia Rivoltini, and Chiara Castelli. LAG-3 expression defines a subset of CD4+ CD25 high Foxp3+ regulatory T cells that are expanded at tumor sites. *The Journal of Immunology*, 184(11):6545–6551, 2010.

Hussein A Tawbi, Dirk Schadendorf, Evan J Lipson, Paolo A Ascierto, Luis Matamala, Erika Castillo Gutiérrez, Piotr Rutkowski, Helen J Gogas, Christopher D Lao, Juliana Janoski De Menezes, et al. Relatlimab and Nivolumab versus Nivolumab in untreated advanced melanoma. *New England Journal of Medicine*, 386(1):24–34, 2022.

Julia Paik. Nivolumab plus Relatlimab: First approval. *Drugs*, 82(8):925–931, 2022.

Simona Ronchetti, Erika Ricci, Maria Grazia Petrillo, Luigi Cari, Graziella Migliorati, Giuseppe Nocentini, and Carlo Riccardi. Glucocorticoid-induced tumour necrosis factor receptor-related protein: A key marker of functional regulatory T cells. *Journal of Immunology Research*, 2015, 2015.

Jun Shimizu, Sayuri Yamazaki, Takeshi Takahashi, Yasumasa Ishida, and Shimon Sakaguchi. Stimulation of CD25+ CD4+ regulatory T cells through GITR breaks immunological self-tolerance. *Nature Immunology*, 3(2):135–142, 2002.

Laura Tsaknaridis, Leslie Spencer, Nicole Culbertson, Kevin Hicks, Dorian LaTocha, Yuan K Chou, Ruth H Whitham, Antony Bakke, Richard E Jones, Halina Offner, et al. Functional assay for human CD4+ CD25+ Treg cells reveals an age-dependent loss of suppressive activity. *Journal of Neuroscience Research*, 74(2):296–308, 2003.

Giuseppe Nocentini, Linda Giunchi, Simona Ronchetti, Ludovic Tibor Krausz, Andrea Bartoli, Rosalba Moraca, Graziella Migliorati, and Carlo Riccardi. A new member of the tumor necrosis factor/nerve growth factor receptor family inhibits T cell receptor-induced apoptosis. *Proceedings of the National Academy of Sciences*, 94(12):6216–6221, 1997.

Luis Vence, Samantha L Bucktrout, Irina Fernandez Curbelo, Jorge Blando, Bevin M Smith, Ashley E Mahne, John C Lin, Terrence Park, Edward Pascua, Tao Sai, et al. Characterization and comparison of GITR expression in solid tumors. *Clinical Cancer Research*, 25(21):6501–6510, 2019.

Simona Ronchetti, Ornella Zollo, Stefano Bruscoli, Massimiliano Agostini, Rodolfo Bianchini, Giuseppe Nocentini, Emira Ayroldi, and Carlo Riccardi. Frontline: GITR, a member of the TNF receptor superfamily, is costimulatory to mouse T lymphocyte subpopulations. *European Journal of Immunology*, 34(3):613–622, 2004.

Ronald W van Olffen, Nathalie Koning, Klaas PJM van Gisbergen, Felix M Wensveen, Robert M Hoek, Louis Boon, Jörg Hamann, Rene AW van Lier, and Martijn A Nolte. GITR triggering induces expansion of both effector and regulatory CD4+ T cells in vivo. *The Journal of Immunology*, 182(12):7490–7500, 2009.

Pengfei Zhou, Lawrence L'italien, Douglas Hodges, and Xiao Min Schebye. Pivotal roles of CD4+ effector T cells in mediating agonistic anti-GITR mAb-induced-immune activation and tumor immunity in CT26 tumors. *The Journal of Immunology*, 179(11):7365–7375, 2007.

Adam D Cohen, David A Schaer, Cailian Liu, Yanyun Li, Daniel Hirschhorn-Cymmerman, Soo Chong Kim, Adi Diab, Gabrielle Rizzuto, Fei Duan, Miguel A Perales, et al. Agonist anti-GITR monoclonal antibody induces melanoma tumor immunity in mice by altering regulatory T cell stability and intra-tumor accumulation. *PloS One*, 5(5):e10436, 2010.

David Coe, Shaima Begom, Caroline Addey, Matthew White, Julian Dyson, and Jian-Guo Chai. Depletion of regulatory T cells by anti-GITR mAb as a novel mechanism for cancer immunotherapy. *Cancer Immunology, Immunotherapy*, 59:1367–1377, 2010.

Ashley E Mahne, Smita Mauze, Barbara Joyce-Shaikh, Jane Xia, Edward P Bowman, Amy M Beebe, Daniel J Cua, and Renu Jain. Dual roles for regulatory T-cell depletion and costimulatory signaling in agonistic GITR targeting for tumor immunotherapy. *Cancer Research*, 77(5):1108–1118, 2017.

Kimberley M Heinhuis, Matteo Carlino, Markus Joerger, Massimo Di Nicola, Tarek Meniawy, Sylvie Rottey, Victor Moreno, Anas Gazzah, Jean-Pierre Delord, Luis Paz-Ares, et al. Safety, tolerability, and potential clinical activity of a glucocorticoid-induced TNF receptor–related protein agonist alone or in combination with nivolumab for patients with advanced solid tumors: A phase 1/2a dose-escalation and cohort-expansion clinical trial. *JAMA Oncology*, 6(1):100–107, 2020.

Sarina Piha-Paul, Ravit Geva, Tira Tan, Darren Wan-Teck Lim, Cinta Hierro Carbó, et al. First-in-human phase I/Ib open-label dose-escalation study of GWN323 (anti-GITR) as a single agent and in combination with Spartalizumab (anti-PD-1) in patients with advanced solid tumors and lymphomas. *Journal for ImmunoTherapy of Cancer*, 2021.

Diwakar Davar, Roberta Zappasodi, Hong Wang, Girish S Naik, Takami Sato, Todd Bauer, David Bajor, Olivier Rixe, Walter Newman, Jingjing Qi, et al. Phase IB study of GITR agonist antibody TRX518 singly and in combination with Gemcitabine, Pembrolizumab, or Nivolumab in patients with advanced solid tumors. *Clinical Cancer Research*, pages OF1–OF13, 2022.

Atsushi Tanaka and Shimon Sakaguchi. Targeting Treg cells in cancer immunotherapy. *European Journal of Immunology*, 49(8):1140–1146, 2019.

Guoxing Zheng, Bin Wang, and Aoshuang Chen. The 4-1BB costimulation augments the proliferation of CD4+ CD25+ regulatory T cells. *The Journal of Immunology*, 173(4): 2428–2434, 2004.

Mark R Alderson, Craig A Smith, Teresa W Tough, Terri Davis-Smith, Richard J Armitage, Ben Falk, Eileen Roux, Elizabeth Baker, Grant R Sutherland, Wenie S Din, et al.

Molecular and biological characterization of human 4-1BB and its ligands. *European Journal of Immunology*, 24(9):2219–2227, 1994.

Walter W Shuford, Kerry Klussman, Douglas D Tritchler, Deryk T Loo, Jan Chalupny, Anthony W Siadak, T Joseph Brown, John Emswiler, Hong Raecho, Christian P Larsen, et al. 4-1BB costimulatory signals preferentially induce CD8+ T cell proliferation and lead to the amplification in vivo of cytotoxic T cell responses. *The Journal of Experimental Medicine*, 186(1):47–55, 1997.

P Zhang, F Gao, Q Wang, X Wang, F Zhu, C Ma, W Sun, and L Zhang. Agonistic anti-4-1BB antibody promotes the expansion of natural regulatory T cells while maintaining Foxp3 expression. *Scandinavian Journal of Immunology*, 66(4):435–440, 2007.

Kenneth F May Jr, Lieping Chen, Pan Zheng, and Yang Liu. Anti-4-1BB monoclonal antibody enhances rejection of large tumor burden by promoting survival but not clonal expansion of tumor-specific CD8+ T cells. *Cancer Research*, 62(12):3459–3465, 2002.

Sarah L Buchan, Lang Dou, Marcus Remer, Steven G Booth, Stuart N Dunn, Chester Lai, Monika Semmrich, Ingrid Teige, Linda Mårtensson, Christine A Penfold, et al. Antibodies to costimulatory receptor 4-1BB enhance anti-tumor immunity via T regulatory cell depletion and promotion of CD8 T cell effector function. *Immunity*, 49(5):958–970, 2018.

Neil H Segal, Theodore F Logan, F Stephen Hodi, David McDermott, Ignacio Melero, Omid Hamid, Henrik Schmidt, Caroline Robert, Vanna Chiarion-Sileni, Paolo A Ascierto, et al. Results from an integrated safety analysis of Urelumab, an agonist Anti-CD137 monoclonal antibody. *Clinical Cancer Research*, 23(8):1929–1936, 2017.

Ya-Tao Wang, Wei-Dong Ji, Hong-Mei Jiao, Ang Lu, Kun-Feng Chen, and Qi-Bing Liu. Targeting 4-1BB for tumor immunotherapy from bench to bedside. *Frontiers in Immunology*, 13, 2022.

Aymara Sancho-Araiz, Victor Mangas-Sanjuan, and Iñaki F Trocóniz. The role of mathematical models in immuno-oncology: Challenges and future perspectives. *Pharmaceutics*, 13(7):1016, 2021.

Zhihui Wang and Thomas S Deisboeck. Mathematical modeling in cancer drug discovery. *Drug Discovery Today*, 19(2):145–150, 2014.

Pedro Milanez-Almeida, Michael Meyer-Hermann, Aras Toker, Sahamoddin Khailaie, and Jochen Huehn. Foxp3+ regulatory T-cell homeostasis quantitatively differs in murine peripheral lymph nodes and spleen. *European Journal of Immunology*, 45(1):153–166, 2015.

Lisette G de Pillis et al. Mathematical modeling of the regulatory T cell effects on renal cell carcinoma treatment. *Discrete and Continuous Dynamical Systems - Series B (DCDS-B)*, 18(4):915–943, 2013.

Huiming Peng, Weiling Zhao, Hua Tan, Zhiwei Ji, Jingsong Li, King Li, and Xiaobo Zhou. Prediction of treatment efficacy for prostate cancer using a mathematical model. *Scientific Reports*, 6(1):21599, 2016.

Hanwen Wang, Richard J Sové, Mohammad Jafarnejad, Sondra Rahmeh, Elizabeth M Jaffee, Vered Stearns, Evanthia T Roussos Torres, Roisin M Connolly, and Aleksander S Popel. Conducting a virtual clinical trial in HER2-negative breast cancer using a quantitative systems pharmacology model with an epigenetic modulator and immune checkpoint inhibitors. *Frontiers in Bioengineering and Biotechnology*, 8:141, 2020c.

Huilin Ma, Hanwen Wang, Richard J Sove, Mohammad Jafarnejad, Chia-Hung Tsai, Jun Wang, Craig Giragossian, and Aleksander S Popel. A quantitative systems pharmacology model of T cell engager applied to solid tumor. *The AAPS Journal*, 22:1–16, 2020.

Roberta Coletti, Lorena Leonardelli, Silvia Parolo, and Luca Marchetti. A QSP model of prostate cancer immunotherapy to identify effective combination therapies. *Scientific Reports*, 10(1):1–18, 2020.

Yan Ji, Kumpal Madrasi, Deborah A Knee, Lore Gruenbaum, Joshua F Apgar, John M Burke, and Bruce Gomes. Quantitative systems pharmacology model of GITR-mediated T cell dynamics in tumor microenvironment. *CPT: Pharmacometrics & Systems Pharmacology*, 2023.

Yuheng Yan, Lan Huang, Yiming Liu, Ming Yi, Qian Chu, Dechao Jiao, and Kongming Wu. Metabolic profiles of regulatory T cells and their adaptations to the tumor microenvironment: Implications for antitumor immunity. *Journal of Hematology & Oncology*, 15(1):104, 2022.

Seon Ah Lim, Jun Wei, Thanh-Long M Nguyen, Hao Shi, Wei Su, Gustavo Palacios, Yogesh Dhungana, Nicole M Chapman, Lingyun Long, Jordy Saravia, et al. Lipid signalling enforces functional specialization of Treg cells in tumours. *Nature*, 591(7849):306–311, 2021.

Paula Nieto, Marc Elosua-Bayes, Juan L Trincado, Domenica Marchese, Ramon Massoni-Badosa, Maria Salvany, Ana Henriques, Juan Nieto, Sergio Aguilar-Fernández, Elisabetta Mereu, et al. A single-cell tumor immune atlas for precision oncology. *Genome Research*, 31(10):1913–1926, 2021.

Brittany Rocque, Arianna Barbetta, Pranay Singh, Cameron Goldbeck, Doumet Georges Helou, Yong-Hwee Eddie Loh, Nolan Ung, Jerry Lee, Omid Akbari, and Juliet Emamaullee. Creation of a single cell RNASeq meta-atlas to define human liver immune homeostasis. *Frontiers in Immunology*, 12:679521, 2021.

Eiichi Sato, Sara H Olson, Jiyoung Ahn, Brian Bundy, Hiroyoshi Nishikawa, Feng Qian, Achim A Jungbluth, Denise Frosina, Sacha Gnjatic, Christine Ambrosone, et al. Intraepithelial CD8+ tumor-infiltrating lymphocytes and a high CD8+/regulatory T cell ratio are associated with favorable prognosis in ovarian cancer. *Proceedings of the National Academy of Sciences*, 102(51):18538–18543, 2005.

Ryoko Ando, Hiroshi Hama, Miki Yamamoto-Hino, Hideaki Mizuno, and Atsushi Miyawaki. An optical marker based on the UV-induced green-to-red photoconversion of a fluorescent protein. *Proceedings of the National Academy of Sciences*, 99(20):12651–12656, 2002.

Hideaki Mizuno, Tapas Kumar Mal, Kit I Tong, Ryoko Ando, Toshiaki Furuta, Mitsuhiko Ikura, and Atsushi Miyawaki. Photo-induced peptide cleavage in the green-to-red conversion of a fluorescent protein. *Molecular Cell*, 12(4):1051–1058, 2003.

Michio Tomura, Naoki Yoshida, Junko Tanaka, Satoshi Karasawa, Yoshihiro Miwa, Atsushi Miyawaki, and Osami Kanagawa. Monitoring cellular movement in vivo with photoconvertible fluorescence protein "kaede" transgenic mice. *Proceedings of the National Academy of Sciences*, 105(31):10871–10876, 2008.

Mario Castro and Rob J de Boer. Testing structural identifiability by a simple scaling method. *PLOS Computational Biology*, 16(11):e1008248, 2020.

Nicolette Meshkat, Christine Er-zhen Kuo, and Joseph DiStefano III. On finding and using identifiable parameter combinations in nonlinear dynamic systems biology models and COMBOS: a novel web implementation. *PloS One*, 9(10):e110261, 2014.

Khuloud Jaqaman and Gaudenz Danuser. Linking data to models: Data regression. *Nature Reviews Molecular Cell Biology*, 7(11):813–819, 2006.

Franz-Georg Wieland, Adrian L Hauber, Marcus Rosenblatt, Christian Tönsing, and Jens Timmer. On structural and practical identifiability. *Current Opinion in Systems Biology*, 25:60–69, 2021.

Nicholas Metropolis, Arianna W Rosenbluth, Marshall N Rosenbluth, Augusta H Teller, and Edward Teller. Equation of state calculations by fast computing machines. *The Journal of Chemical Physics*, 21(6):1087–1092, 1953.

W Keith Hastings. Monte Carlo sampling methods using Markov chains and their applications. *Biometrika*, page 97–109, 1970.

Heikki Haario, Eero Saksman, and Johanna Tamminen. An adaptive Metropolis algorithm. *Bernoulli*, pages 223–242, 2001.

Simon Duane, Anthony D Kennedy, Brian J Pendleton, and Duncan Roweth. Hybrid Monte Carlo. *Physics Letters B*, 195(2):216–222, 1987.

Stuart Geman and Donald Geman. Stochastic relaxation, Gibbs distributions, and the Bayesian restoration of images. *IEEE Transactions on Pattern Analysis and Machine Intelligence*, PAMI-6(6):721–741, 1984.

Ben Lambert. *A Student's Guide to Bayesian Statistics*. Sage, 2018. ISBN 1473916356.

Michael Clerx, Martin Robinson, Ben Lambert, Chon Lok Lei, Sanmitra Ghosh, Gary R Mirams, and David J Gavaghan. Probabilistic inference on noisy time series (PINTS). *ArXiv Preprint ArXiv:1812.07388*, 2018.

David Augustin. Chi - An open source Python package for treatment response modelling, 12 2021. URL https://github.com/DavAug/chi.

Michael Hucka, Frank T Bergmann, Claudine Chaouiya, Andreas Dräger, Stefan Hoops, Sarah M Keating, Matthias König, Nicolas Le Novère, Chris J Myers, Brett G Olivier, et al. The systems biology markup language (SBML): Language specification for level 3 version 2 core release 2. *Journal of Integrative Bioinformatics*, 16(2), 2019.

Andrew Gelman, Gareth O Roberts, Walter R Gilks, et al. Efficient Metropolis jumping rules. *Bayesian Statistics*, 5(599-608):42, 1996.

Michael Clerx, Pieter Collins, Enno De Lange, and Paul GA Volders. Myokit: A simple interface to cardiac cellular electrophysiology. *Progress in Biophysics and Molecular Biology*, 120(1-3):100–114, 2016.

Andrew Gelman and Donald B Rubin. Inference from iterative simulation using multiple sequences. *Statistical Science*, pages 457–472, 1992.

Andrea Saltelli, Stefano Tarantola, and KP-S Chan. A quantitative model-independent method for global sensitivity analysis of model output. *Technometrics*, 41(1):39–56, 1999.

Simeone Marino, Ian B Hogue, Christian J Ray, and Denise E Kirschner. A methodology for performing global uncertainty and sensitivity analysis in systems biology. *Journal of Theoretical Biology*, 254(1):178–196, 2008.

Andrea Saltelli, Stefano Tarantola, Francesca Campolongo, Marco Ratto, et al. Sensitivity analysis in practice: a guide to assessing scientific models. *Chichester, England*, 2004.

Andrea Saltelli and Ricardo Bolado. An alternative way to compute Fourier amplitude sensitivity test (FAST). *Computational Statistics & Data Analysis*, 26(4):445–460, 1998.

RI Cukier, CM Fortuin, Kurt E Shuler, AG Petschek, and JH Schaibly. Study of the sensitivity of coupled reaction systems to uncertainties in rate coefficients. I Theory. *The Journal of Chemical Physics*, 59(8):3873–3878, 1973.

Debalina Sarkar, Moanaro Biswas, Gongxian Liao, Howard R Seay, George Q Perrin, David M Markusic, Brad E Hoffman, Todd M Brusko, Cox Terhorst, and Roland W Herzog. Ex vivo expanded autologous polyclonal regulatory T cells suppress inhibitor formation in hemophilia. *Molecular Therapy-Methods & Clinical Development*, 1:14030, 2014.

Karyn F Siemasko, Jianping Gao, Virginia L Calder, Rebecca Hanna, Margarita Calonge, Stephen C Pflugfelder, Jerry Y Niederkorn, and Michael E Stern. In vitro expanded CD4+ CD25+ Foxp3+ regulatory T cells maintain a normal phenotype and suppress immune-mediated ocular surface inflammation. *Investigative Ophthalmology & Visual Science*, 49(12):5434–5440, 2008.

Ineke den Braber, Tendai Mugwagwa, Nienke Vrisekoop, Liset Westera, Ramona Mögling, Anne Bregje de Boer, Neeltje Willems, Elise HR Schrijver, Gerrit Spierenburg, Koos Gaiser, et al. Maintenance of peripheral naive T cells is sustained by thymus output in mice but not humans. *Immunity*, 36(2):288–297, 2012.

Rob J De Boer, Dirk Homann, and Alan S Perelson. Different dynamics of CD4+ and CD8+ T cell responses during and after acute lymphocytic choriomeningitis virus infection. *The Journal of Immunology*, 171(8):3928–3935, 2003.

Keegan E Hines, Thomas R Middendorf, and Richard W Aldrich. Determination of parameter identifiability in nonlinear biophysical models: A Bayesian approach. *Journal of General Physiology*, 143(3):401–416, 2014.

Takahiro Kamada, Yosuke Togashi, Christopher Tay, Danbee Ha, Akinori Sasaki, Yoshiaki Nakamura, Eiichi Sato, Shota Fukuoka, Yasuko Tada, Atsushi Tanaka, et al. PD-1+ regulatory T cells amplified by PD-1 blockade promote hyperprogression of cancer. *Proceedings of the National Academy of Sciences*, 116(20):9999–10008, 2019.

Hiroyoshi Nishikawa and Shimon Sakaguchi. Regulatory T cells in cancer immunotherapy. *Current Opinion in Immunology*, 27:1–7, 2014.

Justine Cinier, Margaux Hubert, Laurie Besson, Anthony Di Roio, Céline Rodriguez, Vincent Lombardi, Christophe Caux, and Christine Ménétrier-Caux. Recruitment and expansion of Tregs cells in the tumor environment—how to target them? *Cancers*, 13(8):1850, 2021.

Molly A Taylor, Adina M Hughes, Josephine Walton, Anna ML Coenen-Stass, Lukasz Magiera, Lorraine Mooney, Sigourney Bell, Anna D Staniszewska, Linda C Sandin, Simon T Barry, et al. Longitudinal immune characterization of syngeneic tumor models to enable model selection for immune oncology drug discovery. *Journal for Immunotherapy of Cancer*, 7(1):1–16, 2019.

Martin A Schneider, Josef G Meingassner, Martin Lipp, Henrietta D Moore, and Antal Rot. CCR7 is required for the in vivo function of CD4+ CD25+ regulatory T cells. *The Journal of Experimental Medicine*, 204(4):735–745, 2007.

Ivelina Gueorguieva, Ann L Cleverly, Anja Stauber, N Sada Pillay, Jordi A Rodon, Colin P Miles, Jonathan M Yingling, and Michael M Lahn. Defining a therapeutic window for the novel TGF-$\beta$ inhibitor LY 2157299 monohydrate based on a pharmacokinetic/pharmacodynamic model. *British Journal of Clinical Pharmacology*, 77 (5):796–807, 2014.

Wenyan Zhong, Jeremy S Myers, Fang Wang, Kai Wang, Justin Lucas, Edward Rosfjord, Judy Lucas, Andrea T Hooper, Sharon Yang, Lu Anna Lemon, et al. Comparison of the molecular and cellular phenotypes of common mouse syngeneic models with human tumors. *BMC Genomics*, 21(1):1–17, 2020.

Tommaso Torcellan, Henry R Hampton, Jacqueline Bailey, Michio Tomura, Robert Brink, and Tatyana Chtanova. In vivo photolabeling of tumor-infiltrating cells reveals highly regulated egress of T-cell subsets from tumors. *Proceedings of the National Academy of Sciences*, 114(22):5677–5682, 2017.

Myoung Jae Kang, Kyoung Min Kim, Jun Sang Bae, Ho Sung Park, Ho Lee, Myoung Ja Chung, Woo Sung Moon, Dong Geun Lee, and Kyu Yun Jang. Tumor-infiltrating PD1-positive lymphocytes and FoxP3-positive regulatory T cells predict distant metastatic relapse and survival of clear cell renal cell carcinoma. *Translational Oncology*, 6(3): 282–289, 2013.

Masahito Watanabe, Kent Kanao, Susumu Suzuki, Hiroyuki Muramatsu, Singo Morinaga, Keishi Kajikawa, Ikuo Kobayashi, Genya Nishikawa, Yoshiharu Kato, Kenji Zennami, et al. Increased infiltration of CCR4-positive regulatory T cells in prostate cancer tissue is associated with a poor prognosis. *The Prostate*, 79(14):1658–1665, 2019.

Hiroyuki Tao, Yusuke Mimura, Keisuke Aoe, Seiki Kobayashi, Hiromasa Yamamoto, Eisuke Matsuda, Kazunori Okabe, Tsuneo Matsumoto, Kazurou Sugi, and Hiroshi Ueoka. Prognostic potential of FOXP3 expression in non-small cell lung cancer cells combined with tumor-infiltrating regulatory T cells. *Lung Cancer*, 75(1):95–101, 2012.

Christine Ménétrier-Caux, Tyler Curiel, Julien Faget, Manuarii Manuel, Christophe Caux, and Weiping Zou. Targeting regulatory T cells. *Targeted Oncology*, 7(1):15–28, 2012.

JL Goggi, YX Tan, SV Hartimath, B Jieu, YY Hwang, L Jiang, R Boominathan, P Cheng, TY Yuen, HX Chin, et al. Granzyme B PET imaging of immune checkpoint inhibitor combinations in colon cancer phenotypes. *Molecular Imaging and Biology*, 22(5): 1392–1402, 2020.

McLane J Watson, Paolo DA Vignali, Steven J Mullett, Abigail E Overacre-Delgoffe, Ronal M Peralta, Stephanie Grebinoski, Ashley V Menk, Natalie L Rittenhouse, Kristin DePeaux, Ryan D Whetstone, et al. Metabolic support of tumour-infiltrating regulatory T cells by lactic acid. *Nature*, 591(7851):645–651, 2021.

Jeremy Ben-Shoshan, Sophia Maysel-Auslender, Adi Mor, Gad Keren, and Jacob George. Hypoxia controls CD4+ CD25+ regulatory T-cell homeostasis via hypoxia-inducible factor-1$\alpha$. *European Journal of Immunology*, 38(9):2412–2418, 2008.

Yan Qu, Ji Wen, Graham Thomas, Wenjing Yang, Weiwei Prior, Wenqian He, Purnima Sundar, Xiao Wang, Shobha Potluri, and Shahram Salek-Ardakani. Baseline frequency of inflammatory Cxcl9-expressing Tumor-associated Macrophages predicts response to Avelumab treatment. *Cell Reports*, 32(1):107873, 2020.

Grace XY Zheng, Jessica M Terry, Phillip Belgrader, Paul Ryvkin, Zachary W Bent, Ryan Wilson, Solongo B Ziraldo, Tobias D Wheeler, Geoff P McDermott, Junjie Zhu, et al. Massively parallel digital transcriptional profiling of single cells. *Nature Communications*, 8 (1):1–12, 2017.

F Alexander Wolf, Philipp Angerer, and Fabian J Theis. SCANPY: Large-scale single-cell gene expression data analysis. *Genome Biology*, 19(1):1–5, 2018.

Samuel L Wolock, Romain Lopez, and Allon M Klein. Scrublet: Computational identification of cell doublets in single-cell transcriptomic data. *Cell Systems*, 8(4):281–291, 2019.

Ilya Korsunsky, Nghia Millard, Jean Fan, Kamil Slowikowski, Fan Zhang, Kevin Wei, Yuriy Baglaenko, Michael Brenner, Po-ru Loh, and Soumya Raychaudhuri. Fast, sensitive and accurate integration of single-cell data with Harmony. *Nature Methods*, 16(12):1289–1296, 2019a.

Leland McInnes, John Healy, and James Melville. Umap: Uniform manifold approximation and projection for dimension reduction. *ArXiv Preprint ArXiv:1802.03426*, 2018.

Greg Finak, Andrew McDavid, Masanao Yajima, Jingyuan Deng, Vivian Gersuk, Alex K Shalek, Chloe K Slichter, Hannah W Miller, M Juliana McElrath, Martin Prlic, et al. Mast: A flexible statistical framework for assessing transcriptional changes and characterizing heterogeneity in single-cell RNA sequencing data. *Genome Biology*, 16(1):1–13, 2015.

Peter V Kharchenko, Lev Silberstein, and David T Scadden. Bayesian approach to single-cell differential expression analysis. *Nature Methods*, 11(7):740–742, 2014.

Mihails Delmans and Martin Hemberg. Discrete distributional differential expression (D3E)-a tool for gene expression analysis of single-cell RNA-seq data. *BMC Bioinformatics*, 17(1): 1–13, 2016.

Michael I Love, Wolfgang Huber, and Simon Anders. Moderated estimation of fold change and dispersion for RNA-seq data with DESeq2. *Genome Biology*, 15(12):1–21, 2014.

Mark D Robinson, Davis J McCarthy, and Gordon K Smyth. EdgeR: A Bioconductor package for differential expression analysis of digital gene expression data. *Bioinformatics*, 26(1): 139–140, 2010.

Jordan W Squair, Matthieu Gautier, Claudia Kathe, Mark A Anderson, Nicholas D James, Thomas H Hutson, Rémi Hudelle, Taha Qaiser, Kaya JE Matson, Quentin Barraud, et al. Confronting false discoveries in single-cell differential expression. *Nature Communications*, 12(1):1–15, 2021.

John G Cragg. Some statistical models for limited dependent variables with application to the demand for durable goods. *Econometrica: Journal of the Econometric Society*, pages 829–844, 1971.

Yoav Benjamini and Yosef Hochberg. Controlling the false discovery rate: A practical and powerful approach to multiple testing. *Journal of the Royal Statistical Society: Series B (Methodological)*, 57(1):289–300, 1995.

Yunshun Chen, Aaron TL Lun, and Gordon K Smyth. Differential expression analysis of complex RNA-seq experiments using EdgeR. *Statistical Analysis of Next Generation Sequencing Data*, pages 51–74, 2014.

Aravind Subramanian, Pablo Tamayo, Vamsi K Mootha, Sayan Mukherjee, Benjamin L Ebert, Michael A Gillette, Amanda Paulovich, Scott L Pomeroy, Todd R Golub, Eric S Lander, et al. Gene set enrichment analysis: A knowledge-based approach for interpreting genome-wide expression profiles. *Proceedings of the National Academy of Sciences*, 102 (43):15545–15550, 2005.

Guangchuang Yu, Li-Gen Wang, Yanyan Han, and Qing-Yu He. clusterProfiler: An R package for comparing biological themes among gene clusters. *Omics: A Journal of Integrative Biology*, 16(5):284–287, 2012.

Judith A. Blake et al. Creating the gene ontology resource: Design and implementation. *Genome Research*, 11(8):1425–1433, 2001.

Yan Tan, Jernej Godec, Felix Wu, Pablo Tamayo, Jill P Mesirov, and W Nicholas Haining. A method for downstream analysis of gene set enrichment results facilitates the biological interpretation of vaccine efficacy studies. *BioRxiv*, page 043158, 2016.

Yoav Benjamini, Dan Drai, Greg Elmer, Neri Kafkafi, and Ilan Golani. Controlling the false discovery rate in behavior genetics research. *Behavioural Brain Research*, 125(1-2): 279–284, 2001.

Anat Reiner, Daniel Yekutieli, and Yoav Benjamini. Identifying differentially expressed genes using false discovery rate controlling procedures. *Bioinformatics*, 19(3):368–375, 2003.

Cole Trapnell, Davide Cacchiarelli, Jonna Grimsby, Prapti Pokharel, Shuqiang Li, Michael Morse, Niall J Lennon, Kenneth J Livak, Tarjei S Mikkelsen, and John L Rinn. The dynamics and regulators of cell fate decisions are revealed by pseudotemporal ordering of single cells. *Nature Biotechnology*, 32(4):381–386, 2014.

Xiaojie Qiu, Andrew Hill, Jonathan Packer, Dejun Lin, Yi-An Ma, and Cole Trapnell. Single-cell mRNA quantification and differential analysis with Census. *Nature Methods*, 14 (3):309–315, 2017a.

Xiaojie Qiu, Qi Mao, Ying Tang, Li Wang, Raghav Chawla, Hannah A Pliner, and Cole Trapnell. Reversed graph embedding resolves complex single-cell trajectories. *Nature Methods*, 14(10):979–982, 2017b.

Junyue Cao, Malte Spielmann, Xiaojie Qiu, Xingfan Huang, Daniel M Ibrahim, Andrew J Hill, Fan Zhang, Stefan Mundlos, Lena Christiansen, Frank J Steemers, et al. The single-cell transcriptional landscape of mammalian organogenesis. *Nature*, 566(7745):496–502, 2019.

F Alexander Wolf, Fiona K Hamey, Mireya Plass, Jordi Solana, Joakim S Dahlin, Berthold Göttgens, Nikolaus Rajewsky, Lukas Simon, and Fabian J Theis. PAGA: Graph abstraction reconciles clustering with trajectory inference through a topology preserving map of single cells. *Genome Biology*, 20(1):1–9, 2019.

Kelly Street, Davide Risso, Russell B Fletcher, Diya Das, John Ngai, Nir Yosef, Elizabeth Purdom, and Sandrine Dudoit. Slingshot: Cell lineage and pseudotime inference for single-cell transcriptomics. *BMC Genomics*, 19(1):1–16, 2018.

Huidong Chen, Luca Albergante, Jonathan Y Hsu, Caleb A Lareau, Giosuè Lo Bosco, Jihong Guan, Shuigeng Zhou, Alexander N Gorban, Daniel E Bauer, Martin J Aryee, et al. Single-cell trajectories reconstruction, exploration and mapping of omics data with STREAM. *Nature Communications*, 10(1):1–14, 2019b.

Guoji Guo, Luca Pinello, Xiaoping Han, Shujing Lai, Li Shen, Ta-Wei Lin, Keyong Zou, Guo-Cheng Yuan, and Stuart H Orkin. Serum-based culture conditions provoke gene expression variability in mouse embryonic stem cells as revealed by single-cell analysis. *Cell Reports*, 14(4):956–965, 2016.

Benyamin Ghojogh, Ali Ghodsi, Fakhri Karray, and Mark Crowley. Locally linear embedding and its variants: Tutorial and survey. *ArXiv Preprint ArXiv:2011.10925*, 2020.

Luca Albergante, Evgeny Mirkes, Jonathan Bac, Huidong Chen, Alexis Martin, Louis Faure, Emmanuel Barillot, Luca Pinello, Alexander Gorban, and Andrei Zinovyev. Robust and scalable learning of complex intrinsic dataset geometry via ElPiGraph. *Entropy*, 22(3):296, 2020.

Allon Wagner, Chao Wang, Johannes Fessler, David DeTomaso, Julian Avila-Pacheco, James Kaminski, Sarah Zaghouani, Elena Christian, Pratiksha Thakore, Brandon Schellhaass, et al. Metabolic modeling of single Th17 cells reveals regulators of autoimmunity. *Cell*, 184 (16):4168–4185, 2021.

Ines Thiele, Neil Swainston, Ronan MT Fleming, Andreas Hoppe, Swagatika Sahoo, Maike K Aurich, Hulda Haraldsdottir, Monica L Mo, Ottar Rolfsson, Miranda D Stobbe, et al. A community-driven global reconstruction of human metabolism. *Nature Biotechnology*, 31 (5):419–425, 2013.

Francis M Grant, Jie Yang, Rabab Nasrallah, James Clarke, Firas Sadiyah, Sarah K Whiteside, Charlotte J Imianowski, Paula Kuo, Panagiota Vardaka, Tihomir Todorov, et al. BACH2 drives quiescence and maintenance of resting Treg cells to promote homeostasis and cancer immunosuppression. *Journal of Experimental Medicine*, 217(9), 2020.

Astrid Menning, Uta E Höpken, Kerstin Siegmund, Martin Lipp, Alf Hamann, and Jochen Huehn. Distinctive role of CCR7 in migration and functional activity of naive-and effector/memory-like treg subsets. *European Journal of Immunology*, 37(6):1575–1583, 2007.

Linhua Zou, Brian Barnett, Hana Safah, Vincent F LaRussa, Melina Evdemon-Hogan, Peter Mottram, Shuang Wei, Odile David, Tyler J Curiel, and Weiping Zou. Bone marrow is a reservoir for CD4+ CD25+ regulatory T cells that traffic through CXCL12/CXCR4 signals. *Cancer Research*, 64(22):8451–8455, 2004.

Luca Antonioli, Pál Pacher, E Sylvester Vizi, and György Haskó. CD39 and CD73 in immunity and inflammation. *Trends in Molecular Medicine*, 19(6):355–367, 2013.

Naihui Sun and Xing Zhao. Argininosuccinate synthase 1, arginine deprivation therapy and cancer management. *Frontiers in Pharmacology*, 13, 2022.

Dalia Burzyn, Wilson Kuswanto, Dmitriy Kolodin, Jennifer L Shadrach, Massimiliano Cerletti, Young Jang, Esen Sefik, Tze Guan Tan, Amy J Wagers, Christophe Benoist, et al. A special population of regulatory T cells potentiates muscle repair. *Cell*, 155(6):1282–1295, 2013.

Guang L Wang, Bing-Hua Jiang, Elizabeth A Rue, and Gregg L Semenza. Hypoxia-inducible factor 1 is a basic-helix-loop-helix-PAS heterodimer regulated by cellular $o_2$ tension. *Proceedings of the National Academy of Sciences*, 92(12):5510–5514, 1995.

Hélène Pendeville, Nick Carpino, Jean-Christophe Marine, Yutaka Takahashi, Marc Muller, Joseph A Martial, and John L Cleveland. The Ornithine Decarboxylase gene is essential for cell survival during early murine development. *Molecular and Cellular Biology*, 21(19): 6549–6558, 2001.

Ching-Huang Ho and Shih-Feng Tsai. Functional and biochemical characterization of a T cell-associated anti-apoptotic protein, GIMAP6. *Journal of Biological Chemistry*, 292(22): 9305–9319, 2017.

Kouta Yano, Christine Carter, Naofumi Yoshida, Takaya Abe, Akiko Yamada, Takeshi Nitta, Naozumi Ishimaru, Kensuke Takada, Geoffrey W Butcher, and Yousuke Takahama. Gimap3 and Gimap5 cooperate to maintain T-cell numbers in the mouse. *European Journal of Immunology*, 44(2):561–572, 2014.

Preeta Datta, Louise MC Webb, Inxhina Avdo, John Pascall, and Geoffrey W Butcher. Survival of mature T cells in the periphery is intrinsically dependent on GIMAP1 in mice. *European Journal of Immunology*, 47(1):84–93, 2017.

Silke Schnell, Corinne Démollière, Paul van den Berk, and Heinz Jacobs. Gimap4 accelerates T-cell death. *Blood*, 108(2):591–599, 2006.

Robert A Casero and Laurence J Marton. Targeting polyamine metabolism and function in cancer and other hyperproliferative diseases. *Nature Reviews Drug Discovery*, 6(5): 373–390, 2007.

Yuri P Rubtsov, Jeffrey P Rasmussen, Emil Y Chi, Jason Fontenot, Luca Castelli, Xin Ye, Piper Treuting, Lisa Siewe, Axel Roers, William R Henderson Jr, et al. Regulatory T cell-derived Interleukin-10 limits inflammation at environmental interfaces. *Immunity*, 28 (4):546–558, 2008.

Ilenia Pacella, Eleonora Timperi, Daniele Accapezzato, Carmela Martire, Giancarlo Labbadia, Eugenio N Cavallari, Gabriella D'Ettorre, Ludovica Calvo, Fabiana Rizzo, Martina Severa, et al. IFN-$\alpha$ promotes rapid human Treg contraction and late Th1-like Treg decrease. *Journal of Leukocyte Biology*, 100(3):613–623, 2016.

Arunakumar Gangaplara, Craig Martens, Eric Dahlstrom, Amina Metidji, Ameya S Gokhale, Deborah D Glass, Maria Lopez-Ocasio, Rachel Baur, Kishore Kanakabandi, Stephen F Porcella, et al. Type I interferon signaling attenuates regulatory T cell function in viral infection and in the tumor microenvironment. *PLoS Pathogens*, 14(4):e1006985, 2018.

Ilenia Pacella, Francesca Romana Spinelli, Martina Severa, Eleonora Timperi, Gloria Tucci, Marta Zagaglioni, Fulvia Ceccarelli, Fabiana Rizzo, Eliana M Coccia, Roosheel S Patel, et al. ISG15 protects human Tregs from interferon alpha-induced contraction in a cell-intrinsic fashion. *Clinical & Translational Immunology*, 9(12):e1221, 2020.

Jong W Yu, Sabyasachi Bhattacharya, Niranjan Yanamandra, David Kilian, Hong Shi, Sapna Yadavilli, Yuliya Katlinskaya, Heather Kaczynski, Michael Conner, William Benson, et al. Tumor-immune profiling of murine syngeneic tumor models as a framework to guide mechanistic studies and predict therapy response in distinct tumor microenvironments. *PloS One*, 13(11):e0206223, 2018.

Yuyin Fu, Yujia Peng, Shengyan Zhao, Jun Mou, Lishi Zeng, Xiaohua Jiang, Chengli Yang, Cheng Huang, Yuyan Li, Yin Lu, et al. Combination Foretinib and anti-PD-1 antibody immunotherapy for colorectal carcinoma. *Frontiers in Cell and Developmental Biology*, 9, 2021.

Mark J Selby, John J Engelhardt, Robert J Johnston, Li-Sheng Lu, Minhua Han, Kent Thudium, Dapeng Yao, Michael Quigley, Jose Valle, Changyu Wang, et al. Preclinical development of Ipilimumab and Nivolumab combination immunotherapy: Mouse tumor models, in vitro functional studies, and cynomolgus macaque toxicology. *PLoS One*, 11(9): e0161779, 2016.

Shin-ichi Koizumi and Hiroki Ishikawa. Transcriptional regulation of differentiation and functions of effector T regulatory cells. *Cells*, 8(8):939, 2019.

Varun Sasidharan Nair, Reem Saleh, Salman M Toor, Farhan S Cyprian, and Eyad Elkord. Metabolic reprogramming of T regulatory cells in the hypoxic tumor microenvironment. *Cancer Immunology, Immunotherapy*, 70(8):2103–2121, 2021.

Kazuhiro Nishimura, Fubito Nakatsu, Keiko Kashiwagi, Hiroshi Ohno, Takashi Saito, and Kazuei Igarashi. Essential role of S-adenosylmethionine decarboxylase in mouse embryonic development. *Genes to Cells*, 7(1):41–47, 2002.

Anthony E Pegg. Functions of polyamines in mammals. *Journal of Biological Chemistry*, 291 (29):14904–14912, 2016.

Clare Baecher-Allan, Vissia Viglietta, and David A Hafler. Human CD4+ CD25+ regulatory T cells. *Seminars in Immunology*, 16(2):89–98, 2004.

Chaoran Li, Andrés R Muñoz-Rojas, Gang Wang, Alexander O Mann, Christophe Benoist, and Diane Mathis. PPAR$\gamma$ marks splenic precursors of multiple nonlymphoid-tissue Treg compartments. *Proceedings of the National Academy of Sciences*, 118(13):e2025197118, 2021.

Michael Delacher, Charles D Imbusch, Agnes Hotz-Wagenblatt, Jan-Philipp Mallm, Katharina Bauer, Malte Simon, Dania Riegel, André F Rendeiro, Sebastian Bittner, Lieke Sanderink, et al. Precursors for nonlymphoid-tissue Treg cells reside in secondary lymphoid organs and are programmed by the transcription factor BATF. *Immunity*, 52(2):295–312, 2020.

Jung-Ho Kim, Beom Seok Kim, and Sang-Kyou Lee. Regulatory T cells in tumor microenvironment and approach for anticancer immunotherapy. *Immune Network*, 20(1), 2020a.

Frederick Arce Vargas, Andrew JS Furness, Kevin Litchfield, Kroopa Joshi, Rachel Rosenthal, Ehsan Ghorani, Isabelle Solomon, Marta H Lesko, Nora Ruef, Claire Roddie, et al. Fc effector function contributes to the activity of human anti-CTLA-4 antibodies. *Cancer Cell*, 33(4):649–663, 2018.

Anu Sharma, Sumit K Subudhi, Jorge Blando, Jorge Scutti, Luis Vence, Jennifer Wargo, James P Allison, Antoni Ribas, and Padmanee Sharma. Anti-CTLA-4 immunotherapy does not deplete FOXP3+ regulatory T Cells (Tregs) in human Cancers. *Clinical Cancer Research*, 25(4):1233–1238, 2019.

Amirali Karimi, Sanam Alilou, and Hamid Reza Mirzaei. Adverse events following administration of anti-CTLA4 antibody Ipilimumab. *Frontiers in Oncology*, 11:624780, 2021.

Daniel O Villarreal, Andrew L'Huillier, Susan Armington, Cristina Mottershead, Elena V Filippova, Brandon D Coder, Robert G Petit, and Michael F Princiotta. Targeting CCR8 induces protective antitumor immunity and enhances vaccine-induced responses in colon cancer. *Cancer Research*, 78(18):5340–5348, 2018.

Jun Nakayama and Yusuke Yamamoto. Single-cell meta-analysis of cigarette smoking lung atlas. *BioRxiv*, pages 2021–12, 2021.

Vinay S Swamy, Temesgen D Fufa, Robert B Hufnagel, and David M McGaughey. Building the mega single-cell transcriptome ocular meta-atlas. *GigaScience*, 10(10):giab061, 2021.

Emanuele Bosi, Lorella Marselli, Carmela De Luca, Mara Suleiman, Marta Tesi, Mark Ibberson, Decio L Eizirik, Miriam Cnop, and Piero Marchetti. Integration of single-cell datasets reveals novel transcriptomic signatures of $\beta$-cells in human type 2 diabetes. *NAR Genomics and Bioinformatics*, 2020.

Yale Liu, Christopher Cook, Andrew J Sedgewick, Shuyi Zhang, Marlys S Fassett, Roberto R Ricardo-Gonzalez, Paymann Harirchian, Sakeen W Kashem, Sho Hanakawa, Jacob R Leistico, et al. Single-cell profiling reveals divergent, globally patterned immune responses in murine skin inflammation. *iScience*, 23(10):101582, 2020.

Heping Xu, Jiarui Ding, Caroline BM Porter, Antonia Wallrapp, Marcin Tabaka, Sai Ma, Shujie Fu, Xuanxuan Guo, Samantha J Riesenfeld, Chienwen Su, et al. Transcriptional atlas of intestinal immune cells reveals that neuropeptide $\alpha$-CGRP modulates Group 2 Innate Lymphoid cell responses. *Immunity*, 51(4):696–708, 2019.

Jimin Son, Jae-Won Cho, Hyo Jin Park, Jihyun Moon, Seyeon Park, Hoyoung Lee, Jeewon Lee, Gamin Kim, Su-Myeong Park, Sergio A Lira, et al. Tumor-infiltrating regulatory T-cell accumulation in the tumor microenvironment is mediated by IL33/ST2 signaling. *Cancer Immunology Research*, 8(11):1393–1406, 2020.

Ricardo J Miragaia, Tomás Gomes, Agnieszka Chomka, Laura Jardine, Angela Riedel, Ahmed N Hegazy, Natasha Whibley, Andrea Tucci, Xi Chen, Ida Lindeman, et al. Single-cell transcriptomics of regulatory T cells reveals trajectories of tissue adaptation. *Immunity*, 50(2):493–504, 2019.

Saskia Hemmers, Michail Schizas, Elham Azizi, Stanislav Dikiy, Yi Zhong, Yongqiang Feng, Grégoire Altan-Bonnet, and Alexander Y Rudensky. IL-2 production by self-reactive CD4 thymocytes scales regulatory T cell generation in the thymus. *Journal of Experimental Medicine*, 216(11):2466–2478, 2019.

Simon Eschweiler, Ciro Ramírez-Suástegui, Yingcong Li, Emma King, Lindsey Chudley, Jaya Thomas, Oliver Wood, Adrian von Witzleben, Danielle Jeffrey, Katy McCann, et al. Intermittent PI3K$\delta$ inhibition sustains anti-tumour immunity and curbs irAEs. *Nature*, 605 (7911):741–746, 2022.

Liangtao Zheng, Shishang Qin, Wen Si, Anqiang Wang, Baocai Xing, Ranran Gao, Xianwen Ren, Li Wang, Xiaojiang Wu, Ji Zhang, et al. Pan-cancer single-cell landscape of tumor-infiltrating T cells. *Science*, 374(6574):abe6474, 2021.

Peter Savas, Balaji Virassamy, Chengzhong Ye, Agus Salim, Christopher P Mintoff, Franco Caramia, Roberto Salgado, David J Byrne, Zhi L Teo, Sathana Dushyanthen, et al. Single-cell profiling of breast cancer T cells reveals a tissue-resident memory subset associated with improved prognosis. *Nature Medicine*, 24(7):986–993, 2018.

Qiming Zhang, Yao He, Nan Luo, Shashank J Patel, Yanjie Han, Ranran Gao, Madhura Modak, Sebastian Carotta, Christian Haslinger, David Kind, et al. Landscape and dynamics of single immune cells in hepatocellular carcinoma. *Cell*, 179(4):829–845, 2019.

Wei Guo, Cuiyu Zhang, Xia Wang, Dandan Dou, Dawei Chen, and Jingxin Li. Resolving the difference between left-sided and right-sided colorectal cancer by single-cell sequencing. *JCI Insight*, 7(1), 2022.

Adrienne M Luoma, Shengbao Suo, Hannah L Williams, Tatyana Sharova, Keri Sullivan, Michael Manos, Peter Bowling, F Stephen Hodi, Osama Rahma, Ryan J Sullivan, et al. Molecular pathways of colon inflammation induced by cancer immunotherapy. *Cell*, 182(3): 655–671, 2020.

Li-Heng Che, Jing-Wen Liu, Jian-Ping Huo, Rong Luo, Rui-Ming Xu, Cai He, Yu-Qing Li, Ai-Jun Zhou, Piao Huang, Yong-Yu Chen, et al. A single-cell atlas of liver metastases of colorectal cancer reveals reprogramming of the tumor microenvironment in response to preoperative chemotherapy. *Cell Discovery*, 7(1):80, 2021.

Denis A Mogilenko, Oleg Shpynov, Prabhakar Sairam Andhey, Laura Arthur, Amanda Swain, Ekaterina Esaulova, Simone Brioschi, Irina Shchukina, Martina Kerndl, Monika Bambouskova, et al. Comprehensive profiling of an aging immune system reveals clonal GZMK+ CD8+ T cells as conserved hallmark of inflammaging. *Immunity*, 54(1):99–115, 2021.

E Madissoon, A Wilbrey-Clark, RJ Miragaia, K Saeb-Parsy, KT Mahbubani, N Georgakopoulos, P Harding, K Polanski, N Huang, K Nowicki-Osuch, et al. scRNA-seq assessment of the human lung, spleen, and esophagus tissue stability after cold preservation. *Genome Biology*, 21(1):1–16, 2020.

Paul Gueguen, Christina Metoikidou, Thomas Dupic, Myriam Lawand, Christel Goudot, Sylvain Baulande, Sonia Lameiras, Olivier Lantz, Nicolas Girard, Agathe Seguin-Givelet, et al. Contribution of resident and circulating precursors to tumor-infiltrating CD8+ T cell populations in lung cancer. *Science Immunology*, 6(55):eabd5778, 2021.

Cornelius HL Kürten, Aditi Kulkarni, Anthony R Cillo, Patricia M Santos, Anna K Roble, Sayali Onkar, Carly Reeder, Stephan Lang, Xueer Chen, Umamaheswar Duvvuri, et al. Investigating immune and non-immune cell interactions in head and neck tumors by single-cell rna sequencing. *Nature Communications*, 12(1):7338, 2021.

Nayoung Kim, Hong Kwan Kim, Kyungjong Lee, Yourae Hong, Jong Ho Cho, Jung Won Choi, Jung-Il Lee, Yeon-Lim Suh, Bo Mi Ku, Hye Hyeon Eum, et al. Single-cell RNA sequencing demonstrates the molecular and cellular reprogramming of metastatic lung adenocarcinoma. *Nature Communications*, 11(1):2285, 2020b.

Michael A Durante, Daniel A Rodriguez, Stefan Kurtenbach, Jeffim N Kuznetsov, Margaret I Sanchez, Christina L Decatur, Helen Snyder, Lynn G Feun, Alan S Livingstone, and J William Harbour. Single-cell analysis reveals new evolutionary complexity in uveal melanoma. *Nature Communications*, 11(1):496, 2020.

Jong Kyoung Kim, Aleksandra A Kolodziejczyk, Tomislav Ilicic, Sarah A Teichmann, and John C Marioni. Characterizing noise structure in single-cell RNA-seq distinguishes genuine from technical stochastic allelic expression. *Nature Communications*, 6(1):8687, 2015.

Malte D Luecken, Maren Büttner, Kridsadakorn Chaichoompu, Anna Danese, Marta Interlandi, Michaela F Müller, Daniel C Strobl, Luke Zappia, Martin Dugas, Maria Colomé-Tatché, et al. Benchmarking atlas-level data integration in single-cell genomics. *Nature Methods*, 19(1):41–50, 2022.

Rahul Satija, Jeffrey A Farrell, David Gennert, Alexander F Schier, and Aviv Regev. Spatial reconstruction of single-cell gene expression data. *Nature Biotechnology*, 33(5):495–502, 2015.

Isaac Virshup, Sergei Rybakov, Fabian J Theis, Philipp Angerer, and F Alexander Wolf. anndata: Annotated data. *BioRxiv*, 2021.

Geng Chen, Baitang Ning, and Tieliu Shi. Single-cell RNA-seq technologies and related computational data analysis. *Frontiers in Genetics*, page 317, 2019c.

Aaron TL Lun, Davis J McCarthy, and John C Marioni. A step-by-step workflow for low-level analysis of single-cell rna-seq data with Bioconductor. *F1000Research*, 5, 2016.

Robert L Thorndike. Who belongs in the family. In *Psychometrika*. Citeseer, 1953.

Laurens Van der Maaten and Geoffrey Hinton. Visualizing data using t-SNE. *Journal of Machine Learning Research*, 9(11), 2008.

Vincent A Traag, Ludo Waltman, and Nees Jan Van Eck. From Louvain to Leiden: Guaranteeing well-connected communities. *Scientific Reports*, 9(1):1–12, 2019.

Itay Tirosh, Benjamin Izar, Sanjay M Prakadan, Marc H Wadsworth, Daniel Treacy, John J Trombetta, Asaf Rotem, Christopher Rodman, Christine Lian, George Murphy, et al. Dissecting the multicellular ecosystem of metastatic melanoma by single-cell RNA-seq. *Science*, 352(6282):189–196, 2016.

Krzysztof Polański, Matthew D Young, Zhichao Miao, Kerstin B Meyer, Sarah A Teichmann, and Jong-Eun Park. BBKNN: Fast batch alignment of single cell transcriptomes. *Bioinformatics*, 36(3):964–965, 2020.

Laleh Haghverdi, Aaron TL Lun, Michael D Morgan, and John C Marioni. Batch effects in single-cell RNA-sequencing data are corrected by matching mutual nearest neighbors. *Nature Biotechnology*, 36(5):421–427, 2018.

Justin Lakkis, David Wang, Yuanchao Zhang, Gang Hu, Kui Wang, Huize Pan, Lyle Ungar, Muredach P Reilly, Xiangjie Li, and Mingyao Li. A joint deep learning model enables simultaneous batch effect correction, denoising, and clustering in single-cell transcriptomics. *Genome Research*, 31(10):1753–1766, 2021.

Ilya Korsunsky, Nghia Millard, Jean Fan, Kamil Slowikowski, Fan Zhang, Kevin Wei, Yuriy Baglaenko, Michael Brenner, Po-ru Loh, and Soumya Raychaudhuri. Detailed walkthrough of Harmony algorithm. https://portals.broadinstitute.org/harmony/advanced.html, April 2019b.

Andrés R Muñoz-Rojas and Diane Mathis. Tissue regulatory T cells: Regulatory chameleons. *Nature Reviews Immunology*, 21(9):597–611, 2021.

Tatiana Akimova and Wayne W Hancock. How little is known about the role of human FOXP3+ Tregs in tumors. *Expert Opinion on Therapeutic Targets*, 22(8):655–658, 2018.

Yaqing Zhang, Jenny Lazarus, Nina G Steele, Wei Yan, Ho-Joon Lee, Zeribe C Nwosu, Christopher J Halbrook, Rosa E Menjivar, Samantha B Kemp, Veerin R Sirihorachai, et al. Regulatory T-cell depletion alters the tumor microenvironment and accelerates pancreatic carcinogenesis. *Cancer Discovery*, 10(3):422–439, 2020a.

Georgia Lazarou, Vijayalakshmi Chelliah, Ben G Small, Michael Walker, Piet H van der Graaf, and Andrzej M Kierzek. Integration of omics data sources to inform mechanistic modeling of immune-oncology therapies: A tutorial for clinical pharmacologists. *Clinical Pharmacology & Therapeutics*, 107(4):858–870, 2020.

Jitao David Zhang, Lisa Sach-Peltason, Christian Kramer, Ken Wang, and Martin Ebeling. Multiscale modelling of drug mechanism and safety. *Drug Discovery Today*, 25(3):519–534, 2020b.

Jenna K Caines, David A Barnes, and Mark D Berry. The use of Seahorse XF assays to interrogate real-time energy metabolism in cancer cell lines. In *Cancer Cell Biology: Methods and Protocols*, pages 225–234. Springer, 2022.

Susmita Datta. Exploring relationships in gene expressions: A partial least squares approach. *Gene Expression The Journal of Liver Research*, 9(6):249–255, 2001.

Francesca Zammarchi, Karin Havenith, Francois Bertelli, Balakumar Vijayakrishnan, Simon Chivers, and Patrick H van Berkel. CD25-targeted antibody–drug conjugate depletes regulatory T cells and eliminates established syngeneic tumors via antitumor immunity. *Journal for ImmunoTherapy of Cancer*, 8(2), 2020.